

Copyright Undertaking

This thesis is protected by copyright, with all rights reserved.

By reading and using the thesis, the reader understands and agrees to the following terms:

- 1. The reader will abide by the rules and legal ordinances governing copyright regarding the use of the thesis.
- 2. The reader will use the thesis for the purpose of research or private study only and not for distribution or further reproduction or any other purpose.
- 3. The reader agrees to indemnify and hold the University harmless from and against any loss, damage, cost, liability or expenses arising from copyright infringement or unauthorized usage.

IMPORTANT

If you have reasons to believe that any materials in this thesis are deemed not suitable to be distributed in this form, or a copyright owner having difficulty with the material being included in our database, please contact lbsys@polyu.edu.hk providing details. The Library will look into your claim and consider taking remedial action upon receipt of the written requests.

ROBUST STATE ESTIMATION AND INTEGRITY MONITORING FOR INERTIAL-BASED MULTIPLE SENSORS NAVIGATION SYSTEM IN URBAN ENVIRONMENTS

SHAO JIANBO

PhD

The Hong Kong Polytechnic University

This programme is jointly offered by The Hong Kong Polytechnic
University and Harbin Institute of Technology

The Hong Kong Polytechnic University Department of Land Surveying and Geo-Informatics

Harbin Institute of Technology
School of Instrumentation Science and Engineering

Robust State Estimation and Integrity Monitoring for Inertial-Based Multiple Sensors Navigation System in Urban Environments

SHAO Jianbo

A thesis submitted in partial fulfilment of the requirements for the degree of Doctor of Philosophy

CERTIFICATE OF ORIGINALITY

I hereby declare that this thesis is my own work and that, to the best of my knowledge and belief, it reproduces no material previously publishedor written, nor material that has been accepted for the award of any other degree or diploma, except where due acknowledgement has been made in the text.

	(Signed)
Jianbo SHAO	(Name of student)

Abstract

The prosperous development of intelligent transportation has heightened the demand for precise positioning of autonomous vehicles in dense urban environments like building canyons and viaducts, where satellite signals are unavailable. Intelligent vehicles typically utilize navigation and positioning functions by employing an inertial-based multiple-sensor integrated system (INMS) for navigation, which combines inertial navigation with satellite systems, odometers, and optical sensors. However, the integration of more sensors increases the likelihood of data errors and outliers due to challenging urban conditions, impacting the performance of state estimation methods and noise statistics identification that rely on Gaussian noise assumptions. In addition to the accuracy, autonomous driving must evaluate the confidence of position solution to ensure quick system responses and safe mode switches when position solution is unreliable, thereby reducing accident risks and enhancing safety. Integrity is crucial for assessing position confidence, yet most current INMS integrity monitoring methods are derived from aviation satellite navigation techniques. Due to heavier-tailed noise distributions and higher outlier rates, the unique challenges of multi-failure, non-Gaussian integrity monitoring in urban environments have been insufficiently explored. Consequently, the following key issues have been addressed to improve navigation accuracy and reliability in an urban environment.

To address the problem of INMS state estimation performance degradation due to mismatched noise assumptions in urban environments, a robust resampling-free filtering algorithm based on the adaptive kernel-sizes maximum correntropy criterion is proposed. The cost function of the resampling-free update framework is constructed based on the maximum correntropy criterion, which effectively exploits the non-Gaussian moments of the state distribution caused by the non-closed mapping, ensuring the resampling-free estimation optimality and preventing the loss of the higher-order moment information from Gaussian reconstruction. Subsequently, an adaptive method for kernel size of correntropy is developed to realize the online optimal adjustment of the kernel size and ensure robustness against outliers. The simulation experiment demonstrates that the proposed algorithm can optimize the correntropy kernel size and improve the INMS state's estimation performance under non-Gaussian noise in urban environments compared with existing robust filters.

To mitigate outlier interference with the measurement noise covariance matrix (MNCM) estimation, a robust noise adaptation algorithm is proposed based on a posterior smoothing variational approximation. The inverse Wishart distribution is used as the conjugate

prior model of the MNCM, and a joint variational approximation analytical solution of the MNCM and smoothing state is derived. Then, the inverse Wishart distribution's inverse scale matrix is reconstructed based on the correntropy matrix to suppress the interference of measurement outliers on the MNCM estimation. The simulation experiment demonstrates that the proposed algorithm can effectively suppress the interference of measurement outliers on MNCM estimation and accurately identify the measurement noise statistics.

To quantitatively assess the reliability of INMS state estimates in urban environments, an autonomous integrity monitoring (IM) algorithm based on multiple fault-missing detection assumptions is proposed. A consistency factor in the state domain is calculated using the sequential probability ratio over sliding windows. Under the multi-fault missing detection assumption, the horizontal protection level is calculated based on the maximum eigenvalue combined with the consistency factor to quantitatively assess the confidence of the position solution. The simulation experiment demonstrates that the proposed algorithm can effectively quantitatively evaluate the confidence of the position solution and monitor the navigation integrity in the case of measurement outlier disturbance.

To validate the effectiveness of proposed algorithms in practical engineering, an invehicle experiment is conducted. The experimental results demonstrate that: 1) The proposed robust state estimation algorithm reduces the root mean square error (RMSE) of the horizontal position estimation by more than 5.0% compared with the existing robust estimation methods and has a higher robust state estimation accuracy in adverse urban areas; 2) The proposed noise adaptation algorithm provides a smoother and reliable MNCM estimation, which reduces the corresponding position RMSE by more than 13.6% compared to the existing methods and effectively suppresses the interference of measurement outliers on the MNCM adaptation; 3) Compared to the existing IM methods, the proposed IM algorithm has the higher reliability of protection level (99.85%) and does not produce any hazardous misleading events, which can effectively assess the position confidence and monitor the navigation integrity. Therefore, the experiment verifies the effectiveness of the proposed algorithm in practical engineering applications.

List of Publications

- [1] **Shao, J.**, Chen, W.*, Zhang, Y., Yu, F., & Wang, J. (2022). Adaptive maximum correntropy based robust CKF with variational Bayesian for covariance estimation. *Measurement*, 202, 111834. (SCI Index)
- [2] **Shao, J.**, Chen, W.*, Zhang, Y., Yu, F., & Chang, J. (2022). Adaptive multikernel size-based maximum correntropy cubature Kalman filter for the robust state estimation. *IEEE Sensors Journal*, 22(20), 19835-19844. (SCI Index)
- [3] **Shao, J.**, Zhang, Y., Yu, F., Fan, S., Sun, Q., & Chen, W. (2024). A novel resampling-free update framework-based cubature Kalman filter for robust estimation. *Signal Processing*, 221, 109507. (SCI Index)
- [4] **Shao, J.**, Yu, F., Zhang, Y., Sun, Q., Wang, Y., & Chen, W.* (2024). Robust sequential integrity monitoring for positioning safety in GNSS/INS integration. *IEEE Sensors Journal*, 24(9): 15145-15155. (SCI Index)
- [5] **Shao, J.**, Chen, W., Wang, J., Yu, F., Weng, D.*, & Zhang, Y. (2025). Sequential integrity monitoring with state-domain consistency detection for integrated navigation in adverse urban areas. *IEEE Transactions on Instrumentation and Measurement*, 74: 1-11. (SCI Index)

Acknowledgements

As I approach the completion of my PhD thesis, I am overwhelmed with gratitude. Reflecting on my academic research journey, I am keenly aware that every step has been supported by the kindness and guidance of those around me.

I am profoundly grateful to my supervisor, Professor Wu Chen, for his patient guidance and generous support. His rigorous and practical research approach, combined with his wealth of experience and insights, has provided me with invaluable professional direction that I truly admire. His continuous support and selfless advice have been truly invaluable, setting a remarkable example of what a good supervisor should be. I am very fortunate to be a student of Professor Wu Chen, and I will remember his kindness with sincere gratitude.

I am also deeply thankful to Professor Fei Yu of the Harbin Institute of Technology for his assistance and guidance. His extensive knowledge have been a model for my studies. He has always provided the necessary support whenever I sought help and guidance in my research or daily life. I am sincerely grateful and will never forget his kindness.

I would like to express my appreciation to Dr Duojie Weng and Dr Bingbo Cui for their guidance and assistance with my research topic, which was invaluable to me. I also sincerely appreciate the support and thorough review of my thesis by Professor Ya Zhang, Professor Qian Sun, and Dr Shiwei Fan from the Harbin Institute of Technology. Their help was invaluable to me.

I would like to thank my best friends from POLYU, including Drs Jingxian Wang, Chao Yang, Jiahuan Hu, Mengyu Ding, Yuanfan Deng, Bin Xu, Yan Wang, Jiaming Zhu, Ying Na, Hongsheng Huang, Ningyezi Peng, Xiaolong Mi etc., as well as other good friends of LSGI, for their kind help and shared experiences. I will never forget the pleasant times we spent together studying, discussing, having fun, and playing sports.

Finally, I would like to extend special thanks to my family, parents for their consistent understanding and support over the years. They were a tremendous support to me during challenging times. I will work hard in the future to honour their support.

Contents

Al	bstrac	et		ii
Li	st of l	Publica	tions	iv
A	cknov	vledgen	ients	v
Li	st of l	Figures		ix
Li	st of	Fables		xii
Li	st of A	Abbrevi	iations	xiii
1	Intr	oductio	o n	1
	1.1	Resear	rch Background and Motivation	1
	1.2	Review	w of Related Research	3
		1.2.1	Inertial-based Navigation State Estimation	3
		1.2.2	Navigation Autonomous Integrity Monitoring	9
	1.3	Resea	rch Objectives and Contributions	11
	1.4	Struct	ure of the Thesis	14
2	Rob	ust Sta	te Estimation Algorithm for INMS Noise Assumption Mismatch	17
	2.1	Introd	uction	17
	2.2	Analy	sis of the INMS State Estimation Problem	18
	2.3	Resam	npling-Free Gaussian Approximation Filter	21
		2.3.1	RFU Based on the Center Matrix of the Cubature Points	21
		2.3.2	Limitations Analysis for RFU in INMS	23
	2.4	Robus	t RFU Filter Based on Maximum Correntropy Criterion	23
		2.4.1	Maximum Correntropy Criterion	23
		2.4.2	A RFU Filtering Framework Based on MCC	25
		2.4.3	Adaptive Method for Correntropy Kernel Sizes	29
		2.4.4	Algorithm Performance and Complexity Analysis	32
	2.5	Simul	ation Verification Experiment	37
		2.5.1	Simulation Condition Setting	37
		2.5.2	Simulation Results and Analysis	41

	2.6	Summa	ary	48
3	Rob	ust Nois	se Adaptation Algorithm for Measuring Outliers Interference	49
	3.1	Introdu	action	49
	3.2	Analys	sis of the INMS Noise Adaptation Problem	50
	3.3	Variati	onal Bayes Based Noise Adaptation Method	51
		3.3.1	Conjugate distribution selection and joint variational approximation	51
		3.3.2	Limitations Analysis for VB in INMS	55
	3.4	Robust	t Smooth VB Noise Adaptation Based on MCC	56
		3.4.1	MNCM and Smoothing State Joint Variational Approximation	57
		3.4.2	IW distribution Reconstruction Based on Correntropy for GNSS	
			latitude Matrix	60
		3.4.3	Smooth Robust Adaptation Executed in INMS	62
		3.4.4	Algorithm Performance and Complexity Analysis	64
	3.5	Simula	ation Verification Experiment	66
		3.5.1	Simulation Condition Setting	66
		3.5.2	Simulation Results and Analysis	68
	3.6	Summa	ary	75
4	Auto	nomou	s State Integrity Monitoring Algorithm for Multiple Fault Assump	-
	tion			76
	4.1	Introdu	action	76
	4.2	Analys	sis of the INMS Integrity Monitoring Problem	77
	4.3	Integri	ty Monitoring Method With Biases Projections	80
		4.3.1	Protection Level Calculation Based on Maximum Slope	80
		4.3.2	Limitations Analysis for Integrity Monitoring in INMS	81
	4.4	Sequer	ntial Multiple Fault-Biases based Integrity Monitoring	82
		4.4.1	IM Regression Model Based on Consistent Estimation	83
		4.4.2	Estimation Consistency Detection Based on Sequential Probability	
			Ratio in State-Domain	84
		4.4.3	PL Calculation Based on Maximum Eigenvalue against Multi-Biases	86
		4.4.4	Multi-Fault Mapping Matrix Determination	91
	4.5	Simula	ntion Verification Experiment	91
		Silliula		
		4.5.1	Simulation Condition Setting	91
			Simulation Condition Setting	91 94
	4.6	4.5.1 4.5.2		

Re	feren	ce	12
	B.2	INMS Error-State Space Modeling	12
	B.1	INMS Operating Principles	12
В	Erro	or-State Space Model for INMS	12
A	Gau	ssian Approximation Filter Based on Bayes Rule	12
	6.2	Recommendations	11
	6.1	Conclusions	11
6	Con	clusions and Recommendations	11
	5.5	Summary	11
		5.4.3 Analysis of State Integrity Monitoring Results	11
		5.4.2 Analysis of Robust MNCM Adaptation Results	10
		5.4.1 Analysis of Robust State Estimation Results	10
	5.4	Verification Experiment Results and Analysis	10
	5.3	In-Vehicle Validation Scheme and Parameterization	10
	5.2	In-Vehicle Experiment Platform Construction	10
	5.1	Introduction	10

List of Figures

1.1	Intelligent vehicles in adverse urban environment	1
1.2	Inertial-based multiple sensors navigation system	1
1.3	The relationship between HPL, HPE, and HAL	10
1.4	The block diagram of the research content of the thesis	14
1.5	Connection between the different research contents	15
2.1	Adaptive kernel size and corresponding measurement weights for MMSE	
	and MCC	32
2.2	The trajectory of the carrier and the corresponding kinematic parameters .	37
2.3	Sensor noise and probability density distribution	39
2.4	Comparison of existing and proposed adaptive kernel size method	41
2.5	Cumulative probability distribution for the adaptive kernel size of the pro-	
	posed method	42
2.6	Horizontal position ARMSE corresponding to different tuning parameters	43
2.7	Attitude and heading estimation RMSE	44
2.8	Velocity estimation RMSE	45
2.9	Position estimation RMSE	45
2.10	Horizontal position estimation RMSE and its cumulative probability dis-	
	tribution	46
2.11	Horizontal position error ARMSE for each filter under different noises	47
2.12	Time consuming for each filtering cer of different filters	47
3.1	The relationship between the log-likelihood function, the KLD and the	
	lower bound function	54
3.2	VB-based MNCM estimation with measurement outliers interference	56
3.3	Structure of the proposed RSVBA	57
3.4	The relationship between the MNCM a priori and a posteriori IW distribu-	
	tions	61
3.5	Online smoothing RTS structure for INMS systems	63
3.6	Example of sensors noise	67
3.7	MNCM estimation of GNSS	69
3.8	MNCM estimation of OD and POLA	69
3.9	RMSE of MNCM estimation for GNSS	70

3.10	RMSE of MNCM estimation for OD and POLA	70
3.11	ARMSE of MNCM estimation for GNSS with different periods	71
3.12	ARMSE of MNCM estimation for OD and POLA with different periods .	71
3.13	Correntropy for each measurement in different cases	73
3.14	Cumulative probability distribution of correntropy for each measurement .	73
3.15	Position error for different adaptation methods	74
4.1	HPL calculation principle	77
4.2	Center and non-center Chi-square probability distribution	78
4.3	The relationship between HPL, HPE, and HAL	80
4.4	The diagram of the proposed method	83
4.5	Testing statistics for state consistency within sliding windows	86
4.6	The relationship of PL for multiple fault-biases, eigenvalue, and the non-	
	central parameter	89
4.7	Example of sensor noise for case 1	92
4.8	Example of sensor noise of case 2	93
4.9	IM Stanford diagram	94
4.10	HPL and HPE in case 1	95
4.11	Cumulative probability distribution of difference between HPL and HPE	
	in case 1	96
4.12	Stanford diagram of case 1	97
4.13	HPL and HPE in case 2	98
4.14	Cumulative probability distribution of difference between HPL and HPE	
	in case 2	98
4.15	Stanford diagram of case 2	99
5.1	In-vehicle experiment platform	102
5.2	Reference movement trajectory of in-vehicle experiment	105
5.3	Velocity and attitude of reference system	105
5.4	Attitude errors in vehicle-based experiment	106
5.5	Velocity errors in vehicle-based experiment	106
5.6	Position errors in vehicle-based experiment	107
5.7	HPE and its cumulative probability distribution	107
5.8	RMSE radar diagram of navigation parameters	108
5.9	RMSE of HPE for different estimation methods	108
5.10	MNCM estimation of GNSS	109
5.11	MNCM estimation of OD and POLA	110
5.12	Comparison of MNCM estimate with actual noise	110

5.13	HPE of different adaptation methods	111
5.14	RMSE of HPE for different adaptation methods	111
5.15	HPL and HPE	112
5.16	Cumulative probability distribution of HPL and HPE difference	112
5.17	Stanford diagram of IM	113
6.1	Future technical work	120
B.1	Operating framework for INMS	125

List of Tables

2.1	FLOPs for the main filtering parameters	36
2.2	Specifications of sensors	38
2.3	Navigation parameter estimation ARMSE in simulation	46
3.1	FLOPs for the main adaptation parameters	66
3.2	ARMSE of MNCM estimation	72
4.1	Indicators for each IM method of Case 1	96
4.2	Indicators for each IM method of Case 2	99
5.1	Nominal specifications for sensors	103
5.2	Navigation parameter estimation RMSE	108
5.3	Indicators for each IM method	111

List of Abbreviations

In this thesis, bold characters are used to represent vector and matrix variables, and italic characters are used to represent scalar variables. The main abbreviations are listed as follows.

List of main abbreviations

Abbreviation	Complete Definition
ARMSE	Averaged Root Mean Square Error
CKF	Cubature Kalman Filter
DOF	Degrees of Freedom
EKF	Extended Kalman Filter
EMSE	Estimated State Mean Square Error Matrix
FDE	Fault Detection and Exclusion
FLOPs	Floating-Point Operations
GAF	Gaussian Approximation Filters
GNSS	Global Navigation Satellite System
GWI	Gaussian Weighted Integral
HAL	Horizontal Alarm Limit
HMI	Hazardous Misleading Information
HMKF	Huber's M-estimation-Based Kalman Filter
HPE	Horizontal Position Error
HPL	Horizontal Protection Level
IM	Integrity Monitoring
IMU	Inertial Measurement Unit
INMS	Inertial-based Multi-Sensors Integrated System
ISUF	Improved Sampling Points Center-Based Resampling
1301	Free Update Framework
IW	Inverse Wishart
KF	Kalman Filter

Abbreviation	Complete Definition
KSIM	KF Sequential-Based IM
MC	Monte Carlo Test
MCC	Maximum Correntropy Criteria
MMSE	Minimum Mean Square Error
MNCM	Measurement Noise Covariance Matrix
MRCKF	MCC-Based RFU Cubature Kalman Filter
MSIM	Multi-Fault Sequential Integrity Monitoring
MSE	Mean Square Error
OD	Odometer
ORA	Outlier-Robust Adaptation
PDF	Probability Density Distribution Function
PE	Position Error
PL	Protection Level
PLR	Protection Level Reliability
POLA	Polarizer Camera
RAIM	Receiver Autonomous Integrity Monitoring
RFCKF	RFU-Based Cubature Kalman Filter
RFU	Resampling-Free Update
RMSE	Root Mean Square Error
RSIM	Robust Sequential Integrity Monitoring
RSTKF	Robust Student's t-Based Kalman Filter
SHA	Sage-Husa Adaptation
SINS	Strapdown Inertial Navigation System
STD	Standard Deviation
SUF	Sampling Points Center-Based Resampling
501	Free Update Framework
VB	Variational Bayesian
VBA	Variational Bayesian Adaptation
WLS	Weighted Least Squares

Chapter 1

Introduction

1.1 Research Background and Motivation

With the swift development of intelligent transportation systems, autonomous driving has attracted much attention, serving as a key technology for intelligent vehicle applications. In urban environments, the complex road conditions and dense buildings present greater challenges for route navigation and planning for intelligent vehicles. This further increases the dependency of autonomous driving on positioning and navigation services, and places higher demands on the accuracy, reliability, and safety of navigation systems. The global navigation satellite system (GNSS) is indispensable for autonomous driving to provide efficient positioning and navigation services with the advantages of low-cost, high-accuracy, and all-day availability [1, 2]. However, in dense urban areas, such as urban canyons and viaducts (as shown in Fig. 1.1), it is challenging to fulfill the demand for high-accuracy navigation and positioning due to the susceptibility of the satellite signal to be blocked.

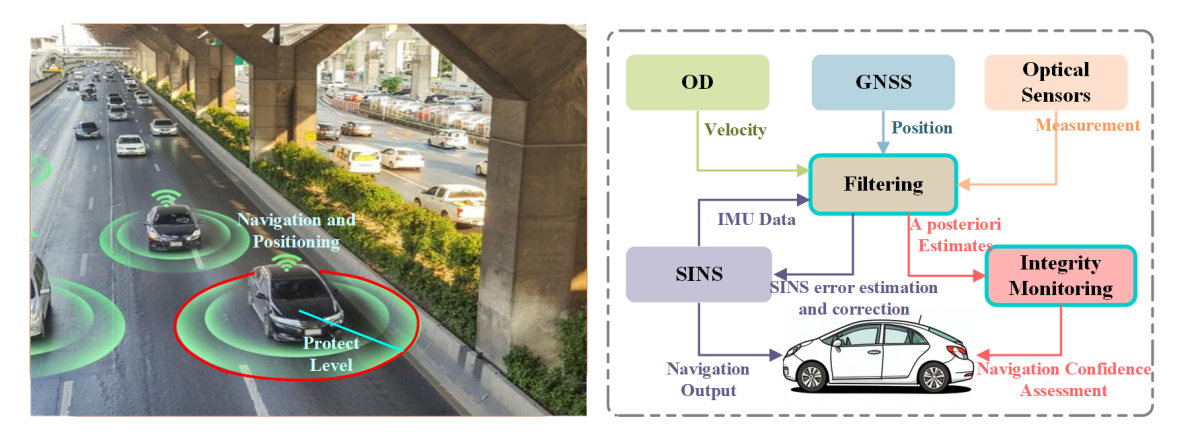


Figure 1.1: Intelligent vehicles in adverse **Figure 1.2:** Inertial-based multiple sensors urban environment navigation system

With a strap-down inertial navigation system (SINS) serving as the host system, SINS/-GNSS integration can effectively overcome the shortcomings of poor environmental applicability of GNSS and enhance the reliability of the navigation system. However, due to the accumulation of errors in SINS, the integration of SINS/GNSS is still unable to provide

reliable positioning services in adverse urban areas with frequent GNSS rejections. An inertial-based multiple-sensor integrated system (INMS) is an effective complement to the SINS/GNSS. Based on the multi-source information fusion technique, INMS utilizes the redundant data collected from several sensors to ensure positioning accuracy and improve the robustness of the system in the adverse urban scene [3, 4, 5]. Therefore, INMS has become an important research direction in autonomous driving [6].

Currently, INMS of intelligent vehicles (as shown in Fig. 1.2 and Appendix B for operating principles) is often constructed based on SINS composed of an inertial measurement unit (IMU) as the host system, equipped with such GNSS, odometer (OD), optical sensors, e.g., polarizer camera (POLA). INMS fuses the data from each sensor to correct the SINS and provides highly accurate and reliable positioning services in adverse urban areas. Although multiple sensors provide more redundant data, it also presents new challenges. As the number and types of INMS sensors increase, so does the likelihood of data errors and outlier interference in urban areas. For example, GNSS can be affected by the frequent multi-path reflection effect, the odometers can be affected by uneven road conditions, and optical sensors can be interfered with by light sources. These interference tend to result in a heavily non-Gaussian distributed noise. The existing robust estimation methods for non-Gaussian noise rely on the multivariate Gaussian approximation assumption for state vectors. In addition, the existing non-stationary sensor noise statistical identification method does not take into account the interference of outliers. As a result, the estimation accuracy and robustness cannot be guaranteed in this case, which limits the performance of navigation and positioning of intelligent vehicles.

Furthermore, while pursuing high-accuracy positioning for high-level autonomous driving, it is also necessary to effectively quantitatively evaluate the confidence of the position solution and indicate the potential risks of estimation uncertainty. Integrity is a representative indicator of the confidence of the state estimate. When the position information is unreliable due to data errors or outlier interference, the integrity monitoring (IM) can ensure that the vehicle can react quickly and switch to a safe driving mode (e.g., manual driving, reducing speed). Thus, IM reduces the potential risk of accidents (e.g., route deviation or collision) caused by inaccurate position and improves the navigation safety of intelligent vehicles. However, the majority of current IM methods for INMS are based on GNSS developed for aviation applications. The multi-failure, non-Gaussian integrity monitoring issues of INMS caused by the heavier-tailed distribution and higher outlier rate of noise in urban applications have received little research attention. It cannot effectively monitor the position integrity and cannot guarantee the navigation safety of intelligent vehicles.

Based on the above analysis, the navigation reliability and safety issues faced by INMS in urban environments hinder the development of higher-level autonomous driving. To this end, the thesis focuses on the requirements of high-accuracy robust state estimation and autonomous integrity monitoring for intelligent vehicles in urban environments. The thesis proposes a robust state estimation algorithm, a robust noise adaptation algorithm, and an autonomous integrity monitoring algorithm to address the issues of state estimation under mismatched noise assumptions, noise adaptation under outlier interference, and position confidence assessment, respectively. The research allows the advantageous complementation of multiple sensors and redundant information fusion, thereby improving the navigation accuracy and reliability of the intelligent vehicle navigation system. Furthermore, the research includes experimental verification of theoretical studies, as well as demonstrations of the proposed algorithms' practical significance for INMS.

1.2 Review of Related Research

1.2.1 Inertial-based Navigation State Estimation

INMS takes the SINS navigation parameter error as the primary state vector and constructs a state prediction model based on the error propagation equation. Furthermore, the system's state is estimated using the measurement information of external sensors to correct the navigation parameters. Therefore, as an essential branch of information fusion, the state estimator plays a critical role in INMS. Kalman Filter (KF) is a widely applicable state estimator. Based on Bayes' rule, KF achieves the optimal state estimation in the sense of the minimum mean square error (MMSE) criterion by combining a priori state and measurement information [7]. By its reliable estimation accuracy and economic computational efficiency, KF has been widely used in the navigation field [8, 9, 10]. However, the application conditions of KF are only applicable when the system model is linear, and the sensor noise is stationary with an accurately known statistical distribution, which makes the state estimation performance not guaranteed in practical applications due to nonlinear-mapping observation and unexpected outliers interference. Therefore, many filter variants and improved algorithms based on the KF framework have been developed to solve the navigation state estimation problem for different application scenarios and requirements.

(1) Nonlinear state estimation with non-resampling updates

In practical engineering, the navigation sensors' noise distribution is generally modeled by Gaussian distribution. Since the Gaussian model is enclosed under linear mapping, i.e., it has the same probability density distribution function (PDF) after linear mapping, the KF can provide the optimal estimate solution under the linear Gaussian model. However, in multiple sensor applications, due to the different observation principles of sensors, the measurement may map nonlinearly to the state, which leads to a nonlinear system model. Furthermore, since the Gaussian distribution is non-closed under the nonlinear mapping, it is infeasible to calculate the analytic optimal solution for nonlinear cases as the closed-form Gaussian distribution is violated by nonlinear mapping [11]. Although the model can be linearised with lesser error assumption, it is not applicable in adverse urban areas because the state estimation accuracy cannot be guaranteed, and error assumptions cannot be met. Moreover, since INMS adopts the feedback correction, larger state estimate errors also degrade the linearization accuracy of the model in adverse urban areas. Therefore, many Gaussian approximation filters (GAF) were developed for nonlinear closed-form solutions by linearizing models or numerical-integration approaches [12, 13]. The details are as follows.

As an extension of KF, the extended KF (EKF) achieves nonlinear state estimation through the first-order linearization of the nonlinear model and is widely used due to its simplicity and computational efficiency [14, 15, 16]. Nevertheless, the linearization-induced higher-order truncation error and weak convergence limit the application of EKF to INMS in adverse urban areas. Furthermore, in the case of the coupling between measurement and the high-dimensional state of INMS, it is challenging to derive the Jacobi matrix, which also increases the implementation burden. In light of the considerations above, Gaussian weighted integral (GWI) filters were devised on the foundation of approximate state distributions as opposed to approximate models [17, 18, 19, 20]. In GWI, the state PDF is approximated by the weighted integration of a series of deterministic sampling points, demonstrating superior convergence stability and filtering accuracy compared to EKF. Among the numerous GWI filters, the cubature Kalman filter (CKF) has been developed for high-dimensional systems and has attracted widespread attention for computational cost-effectiveness with sufficient accuracy and numerical stability [21, 22, 23].

However, as with other GWI-based filters, CKF depends on the resampling operation. Under Gaussian assumption, the resampling operation is carried out to renew the sampling points for recursively calculating Gaussian moments (i.e., mean and covariance) at each filtering period. Although the resampling operation maintains the closed Gaussian property of the state distribution, keeping the availability of analytic solutions, it only spreads the Gaussian moments and discards the high-order non-Gaussian information contained in the sampling points PDF [24], limiting the performance of GAF in INMS.

Inspired by the non-resampling method in particle filtering [25], some resampling-free

update (RFU) strategies for GWI have been proposed to overcome the drawbacks of resampling. The research introduced a pure propagation unscented Kalman filter [26], which directly modifies the sampling points to incorporate additive noise without resampling operation. While this approach preserves the higher-order moments of the state PDF, it is computationally intractable as it requires solving an additional continuous Riccati equation. Then, another RFU framework was presented in [27], which modifies the sampling points by a transformation matrix without solving the Riccati equation, ensuring computational efficiency while avoiding the resampling operation under Gaussian assumption.

Moreover, as an alternative to the modification of sampling points through matrix transformation, a study [28] presented sampling points error-based resampling-free update framework (SUF) inspired by the work [29]. The SUF introduces the posterior error matrix formulated by the linear transformation of state prediction residual to modify the sampling points. Compared to the method in [27], SUF is more computationally efficient as it does not require posterior updating for all sampling points. Further, several SUF-based variant filters have been successively developed by its robust estimation against suboptimal observation through more accurately capturing the state estimate mean square error matrix (EMSE) by reusing the diffused sampling points[30]. Moreover, by extending the SUF to account for the likelihood approximation error, an improved SUF (ISUF) was proposed in [31], where the posterior error matrix of sampling points is corrected by the measurement error matrix in addition to the state prior error matrix. With more accurate capture of a higher-order moment of state PDF, some ISUF-based filters have been developed to improve the estimation performance and robustness [32, 33].

While ISUF avoids the Gaussian reconstruction of state distribution to keep the high-order moments, it also tends to yield a significant deviation of the non-closed state distribution from the Gaussian assumption after multiple nonlinear propagations. This occurs because the nonlinear mapping breaks the closure property of state PDF (i.e., maintains the same PDF form after mapping). As a result, the heavy non-Gaussian property of state distribution compromises the estimation optimality of the MMSE in ISUF under the Gaussian assumptions, thereby degrading the estimation performance. Furthermore, ISUF requires multiple triangular (Cholesky) decompositions of the state covariance matrix. Due to the INMS state unit, the difference in the eigenvalues of the covariance matrix is too large (e.g., the velocity error differs from the gyro constant-bias covariance eigenvalue by a factor of 10⁸), which tends to cause matrix singularities and reduces the numerical stability of the Cholesky decomposition.

(2) Robust state estimation for non-Gaussian noise

Reliable state estimation is critical for navigation systems. However, measurements are often disturbed by unexpected outliers in non-open dense urban areas, leading to the noise following a non-Gaussian heavy-tailed distribution (i.e., the tailed probability of the noise is higher than that of a standard Gaussian distribution). For example, in urban canyons and viaducts, the propagation of navigation satellite signals is susceptible to multi-path effects, thus inducing non-Gaussian heavy-tailed distribution noise. In this case, measurement noise does not satisfy the Gaussian distribution condition of KF, which leads to degradation of the state estimation performance. Outlier elimination is efficient when dealing with prominent outliers that deviate significantly from the overall data distribution. However, in the case of smaller outliers with high frequency, it tends to loss of available measurement information, affecting the accuracy of statistical analysis and modeling. The robust filtering method dynamically adjusts the weights of the measurement information according to outlier magnitude by adopting a robust optimization criterion or introducing a robustness metric. In the case of prominent outliers, the weight is reduced to zero to eliminate the interference completely. In contrast, in the case of smaller outliers, the weight is decreased to a lesser extent to retain more useful information. Therefore, robust filtering can adapt to various dynamic scenarios and noise types, thereby improving the adaptability and reliability of the navigation system.

Many robust filters have been proposed to achieve robust state estimation, such as particle filtering, Huber's M-estimation-based Kalman filter (HMKF), robust student's *t* distribution-based Kalman filter (RSTKF), and its related variants. Particle filtering can approximate arbitrary noise distributions by sequential Monte Carlo methods, but it is inevitably limited by the computational burden under INMS high-dimensional systems [34, 35]. The HMKF constructs the Huber cost function to ensure the boundary of the filter residual to attenuate the outlier's interference on the state estimation by minimizing the L1 and L2 norm [36, 37]. However, the HMKF cost function value does not drop down, which retains the weight of poorer-quality measurement information and reduces the state estimation accuracy. The RSTKF models the measurement noise disturbed by anomalies with the Student's *t* distribution [38, 39, 40, 41]. However, in order to maintain the closed form of the *t* distribution of the posterior probability distribution, the RSTKF captures only the first-two orders of the moment information of the state posterior distribution and loses the higher-order moment information.

Information-theoretic learning has recently gained more attention due to its efficacy in robust state estimation. The correntropy can capture the high-order moments as an optimization cost for local similarity measures (MMSE optimization criterion used by KF captures only second-order moments) [42, 43]. The maximum correntropy criteria (MCC)

is used to replace MMSE as the optimal criterion for designing the maximum correntropy Kalman filter (MCKF) that exhibits more robustness to impulsive non-Gaussian noise due to its truncation effect [44]. However, MCKF must Cholesky decompose EMSE, which is susceptible to numerical instability in INMS due to excessive disparity between EMSE eigenvalues. Thus, this prompts some variants to execute recursion based on the square-root form of the covariance matrix [45]. In another derivation idea, MCC is used to combine weighted least squares (WLS) to form the MCC-filter [46], where the correntropy is calculated by the squared Mahalanobis distance, which avoids the decomposition of the covariance matrix and the numerical stability is guaranteed, and further variations on non-linear state estimation are developed [45, 47].

Although the feasibility of MCC-based filters for resisting outliers has been demonstrated, the selection of kernel size limits the implementation in practical engineers. MCC with a wrong kernel size fails to improve robustness against outliers and may even cause filtering divergence [48, 49]. Therefore, some adaptive methods are proposed for adjusting the kernel size online through the filtering parameters related to the innovation term or state error covariance matrix [50, 51, 52]. Although these methods can optimize the kernel size, the correctness of the kernel size cannot be guaranteed if the filter has a larger initial state error or has not yet converged. The present adaptive factor construction method can effectively keep the kernel size within the correctness range [53]. However, the decreasing properties of adaptive kernel size tend to cause excessive convergence under the continuous disturbance of outliers, i.e., the kernel size continuously converges to a small value, which can lead to a loss of adjustability of the kernel size for various noises.

(3) Adaptive state estimation for non-stationary noise

A filter's robust estimation performance depends on accurate prior statistical knowledge of the noise, which can be effectively represented by the measurement noise covariance matrix (MNCM). However, in practical INMS applications, MNCM is usually unknown or time-varying due to the variable measurement environment external to the sensors. An incorrect MNCM not only reduces state estimation accuracy due to model-actual mismatch but also affects the detection of outliers by the filter, deteriorating the robustness against outliers. Also, it interferes with the effective monitoring of navigation integrity. Therefore, it is necessary to estimate the MNCM adaptively online.

Many adaptive filters have been developed to estimate the MNCM [54, 55, 56]. The Sage-Husa based adaptive filter (SHA) is an approximate covariance matching method that obtains optimal estimates of the MNCM based on the maximum posterior criterion [57]. However, SHAKF does not guarantee that the MNCM estimates converge to the true value,

nor does the positive definition, leading to filtering divergence. The variational Bayesian-based adaptive filter (VBA) models the diagonal elements of the MNCM using an inverse gamma distribution. By employing the variational approximation, it achieves online joint estimation of the MNCM diagonal elements and the state vector [58]. Furthermore, a VB method based on the Inverse Wishart (IW) distribution is proposed to estimate the non-diagonal noise covariance matrix [54, 58, 59]. This method uses the IW distribution as the conjugate prior for the MNCM and utilizes the state estimation mean and mean square error matrix to obtain more accurate MNCM estimates. Additionally, to further improve the estimation performance of the MNCM, a sliding window-based VB variant has been proposed [60, 61]. This method employs the RTS fixed-interval smoother to obtain the smoothed posterior distribution of the state vector and uses a variational approximation to compute the MNCM, thereby avoiding the single-point iteration of VB and achieving better estimation accuracy.

Existing adaptive filtering methods can achieve effective estimation of MNCM under Gaussian noise. However, when the measurements are disturbed to outliers, the measurement noise exhibits a non-Gaussian heavy-tailed distribution, and the adaptive methods based on the Gaussian assumption cannot estimate the MNCM accurately. Inaccurate MNCM estimates, in turn, affect the robust filter's ability to suppress outliers and monitor the integrity of the navigation state. Therefore, it is necessary to mitigate the effect of measurement outliers on the MNCM estimation. The literature [62, 63] addresses this issue by removing outliers to reduce their interference with the VB adaptive method. However, in dense urban areas with frequent disturbances, such as frequent turbulence or satellite signal occlusion, the occurrence of measurement anomalies is high. Removing outliers can lead to the loss of valuable information, changing the original information distribution characteristics and affecting the accuracy of MNCM estimation.

Robust enhancement methods can adapt to various dynamic scenarios and noise types. However, current robust enhancement methods for measurement outliers primarily focus on state estimation, with less attention paid to the adaptive estimation of MNCM. A robust MNCM adaptive method is proposed based on a Gaussian-Gamma mixture distribution [64], which models the heavy-tailed measurement likelihood PDF using a Gaussian-Gamma mixture distribution to address the issue of inaccurate MNCM estimation in the presence of measurement anomalies. However, this distribution requires pre-specifying the number of Gamma mixture components, and each component needs different tuning parameters. Given that the measurement noise types and anomaly disturbance intensities of the INMS system vary across different dynamic scenarios, a noise distribution relying on fixed model parameters is not applicable for non-Gaussian noise MNCM estimation

in the INMS. Additionally, an outlier-robust adaptation method (ORA) is proposed[65]. Unlike the approach of modeling non-Gaussian noise, ORA constructs a hybrid cost function based on statistical similarity measures and maximizes the hybrid cost function as an optimization criterion to achieve MNCM estimation under outlier disturbances. However, ORA adopts a Gaussian conjugate IW distribution to model the MNCM, which cannot accurately characterize the covariance matrix of non-Gaussian noise, thereby failing to ensure robust MNCM estimation accuracy.

1.2.2 Navigation Autonomous Integrity Monitoring

The INMS plays a crucial role in autonomous driving by providing accurate positioning solutions. However, in challenging urban areas (such as urban canyons and tunnels), it is intractable to guarantee estimation accuracy for INMS due to outlier contamination [66]. For autonomous driving, while striving for high accuracy, it also needs to effectively assess the confidence of positioning information to ensure that the vehicle system responds promptly and switches to a safe (such as manual) driving mode when positioning information is unreliable, thus ensuring the safe navigation and reducing the potential accident risk caused by inaccurate positioning information. Integrity is a representative indicator for assessing the confidence of positioning estimation [67, 68, 69, 70]. Initially, integrity monitoring techniques were extensively researched and developed for aviation applications with extremely high positioning safety requirements. Subsequently, due to the increased demand for positioning reliability in the intelligent transportation sector, integrity monitoring techniques have also gradually gained attention in the field of autonomous driving [71, 72, 73]. IM includes fault detection and exclusion (FDE) and the horizontal protection level (HPL) calculation. After eliminating measurement faults by FDE, the HPL is calculated as a quantitative indicator to assess the confidence level of the position solution [74, 75]. As a statistical upper limit of horizontal position error (HPE), HPL sets up a safety boundary around the vehicle, meeting a certain integrity risk probability. Once HPL exceeds the horizontal alarm limit (HAL), i.e., the maximum tolerated positioning error, the system will issue an alarm to the user in time [76, 77]. The relationship between HPL, HPE, and HAL is shown in Fig. 1.3.

As the KF is an indispensable component of INMS, the KF-based IM has gained attention in recent years [78, 73]. The IM approach depends on reliable HPL calculations. Based on the definition of HPL, it is feasible that taking the filtering EMSE to characterize the position estimation effect, which gives rise to the k-Sigma method [79, 80, 81]. In k-Sigma, the root EMSE of sequential KF is regarded as the standard deviation of HPE that is approximated as a Gaussian distribution [80]. Then, the HPL is obtained by scaling

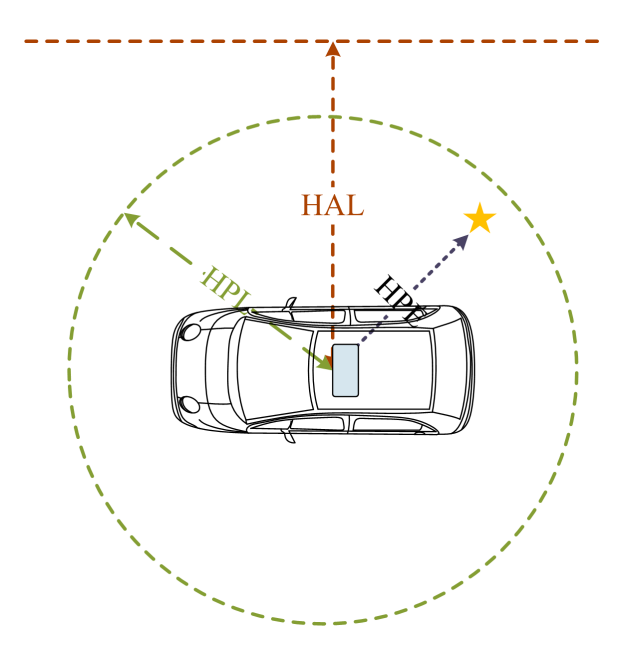


Figure 1.3: The relationship between HPL, HPE, and HAL

root EMSE using a quantile corresponding to a specific confidence region. Although the k-Sigma is simple to execute, in challenging urban areas, the Gaussian distribution models fail to accurately characterize tail error disturbed by unexpected outliers, resulting in a non-consistency in estimation and HPL failing to overbound the position error (PE). To cope with the problem, the KF integrated HPL method based on Student's *t* distribution is proposed [81, 82, 83]. The estimated HPE is modeled dynamically as a zero-mean multivariate *t*-distribution. The HPL is then calculated by the independent propagation and integration of the *t*-distributed-based HPE for each epoch. Although the assumption of thick-tailed distribution is more reasonable in adverse GNSS scenarios compared to Gaussian distribution in urban, it is computationally intractable to update the tuning parameters and maintain the closure of the *t*-distribution in each epoch.

Inspired by receiver autonomous integrity monitoring (RAIM), the approach to determine HPL by overbounding HPE instead of characterizing the distribution of HPE has been a focus of research in KF-based IM [84, 85, 86]. RAIM is a classical method in GNSS for ensuring aviation safety to assess the reliability of receiver positioning results [87, 88, 89]. RAIM determines the measurement source most susceptible to fault missed detection based on the maximum slope, which is the ratio of the statistically independent estimated HPE to the detection statistic. The upper limit of the HPE caused by fault missed detection is then used as an HPL to overbound the actual HPE. Based on the RAIM, a KF sequential-based IM (KSIM) is developed [90, 91]. KSIM reconstructs the state-space model of the sequential filter into a regression model, and then the HPL is determined by the maximum slope and the minimum detectable bias. However, since the HPL of RAIM is subject to

the number of hypothesized fault biases (i.e., outliers) in missed detection, the single-fault hypothesis developed for GNSS aviation applications is not applicable in INMS in urban due to its susceptibility to frequent multiple outliers, leading to HPL does not effectively reflect HPE.

To assess the confidence level of the position estimates in multiple fault scenarios, a multi-fault bias hypothesis-based IM is proposed [92]. However, the approach is still not applied to INMS since it is designed for optimization rather than sequential filtering principles. In addition, as with other IM variants extended from RAIM for aviation scenarios, it does not account for the interference of unexpected outliers on the protection level (PL) in challenging environments, which is crucial for the positioning safety of the vehicle. Moreover, the advanced receiver autonomous integrity monitoring (ARAIM) based on the solution separation is also developed into a KF-based integrated navigation system [93, 94, 95]. The ARAIM applies a consistency check with the multiple-stage filters in the position domain. HPL is determined by assigning the integrity risk between the main filter and each sub-filter, enabling the monitoring with multiple fault scenarios. However, since a prior probability of fault occurrences needs to be specified, it is hardly applicable to the kinematic in-vehicle positioning because the likelihood of outliers occurring is unavailable in different environments. In addition, the number of parallel sub-filters increases with the hypothesized fault biases (outliers) and measurement sources, which leads to a heavy computation burden (e.g., $n^{sf} = C_n^1 + ... + C_n^m$ with maximum hypothesized faults m and measurement sources n).

1.3 Research Objectives and Contributions

According to the above research review, there are still research gaps to achieve high-accuracy robust state estimation and autonomous integrity monitoring of INMS in dense urban areas, which are summarised below:

(1) Gap 1: Optimality and robustness of resampling-free filtering for INMS state estimation cannot be guaranteed in urban environments.

The heavy non-Gaussian noise degrades the performance of robust state estimation methods that rely on the Gaussian approximation assumption in dense urban areas.

The RFU-based filter can eliminate the Gaussian approximation assumption and prevent the loss of higher order moment information caused by the Gaussian reconstruction, thereby improving the estimation performance. However, the nonlinear mapping violates the non-closure property, causing the state distribution to deviate significantly from the Gaussian approximation assumption after a few nonlinear mappings. This deviation renders the MMSE based on the Gaussian assumption inapplicable in resampling-free filters, preventing optimal state estimation. The MCC optimal criterion can effectively captures higher-order moment information, fully exploits the non-Gaussian moment information in the RFU filter, ensures the optimality of the RFU estimation, and improves the robustness of the estimation. However, the performance of MCC is limited by its tuning parameter, i.e., the kernel size. An appropriate kernel size would reduce the filter estimation performance or even cause it to diverge. Therefore, how to ensure the optimality of non-resampling filter estimation while optimally tuning the MCC tuning parameters is a challenge to improve the accuracy of INMS state estimation in urban areas.

(2) Gap 2: MNCM cannot be estimated accurately by existing adaptive filters due to the outlier interference in urban environments.

Robust INMS state estimation and reliable integrity monitoring are dependent on accurate knowledge of MNCM. In INMS applications, the MNCM is typically unknown or time-varying due to the variable measurement conditions outside the sensors. Existing adaptive filters can accurately estimate the MNCM under Gaussian noise. However, in dense urban areas, frequent signal blocks and outliers frequently result in non-Gaussian heavy-tailed noise distributions, so the MNCM cannot be estimated accurately. An inaccurate MNCM can reduce robust state estimation accuracy due to model-actual mismatch and interfere with effective integrity monitoring. Outlier elimination techniques cannot ensure effective noise adaptation. In contrast, robust enhancement methods can prevent the loss of valuable information and improve noise adaptation performance. However, the Gaussian conjugate Inverse Wishart (IW) distribution used in existing robust noise-adaptive methods does not accurately represent the MNCM of non-Gaussian noise, resulting in suboptimal robust MNCM estimation under outlier disturbances. Therefore, how to accurately estimate the MNCM in the presence of measurement outliers is a challenge to ensure the state estimation performance and effective integrity monitoring of INMS.

(3) Gap 3: Existing IM methods cannot calculate reliable HPL due to the severe outlier interference in urban environments.

Integrity monitoring methods for filtering sequential framework in INMS are extensions of the RAIM methods developed for aviation applications in GNSS, which rely on the assumption of a maximum number of missing detection biases. Unlike aviation applications, where the low failure rate of satellites allows a single-fault assumption to satisfy integrity risk requirements, the increasing number and types of INMS sensors raise the likelihood of data errors and outlier disturbances, rendering the single-fault assumption inapplicable for INMS in urban areas. Furthermore, in the presence of outliers, the Gaussian assumption used by existing IM methods cannot accurately characterize the actual noise distribution, making it impossible to compute reliable HPL for assessing position reliability. Therefore, how to compute reliable HPL under severe outlier interference in urban areas is a challenge to monitor navigation integrity and ensure navigation safety.

This thesis aims to fill the research gaps mentioned above. The main contributions of the thesis are summarized as follows.

- (1) A robust resampling-free filtering algorithm based on MCC is proposed. First, a kernel size optimization method of MCC is designed, and an objective function of the resampling-free estimation framework is constructed based on the MCC, which effectively utilizes the higher-order moment information of non-Gaussian state and measurement noise, ensures the resampling-free estimation optimality, improves the robustness against heavy noise-Gaussian noise. Finally, the algorithm can improve navigation estimation accuracy under heavy mismatched noise assumptions in urban areas.
- (2) A robust noise adaptation algorithm is proposed based on a smoothing variational approximation. First, a joint variational approximation analytical solution of the MNCM and smoothing state is derived. Then, the inverse scale matrix of the IW distribution is reconstructed based on the correntropy matrix to suppress the interference of measurement outliers on the MNCM estimation. Finally, the algorithm achieves robust noise adaptation in the presence of outlier disturbances.
- (3) A sequential IM method is proposed based on the assumptions of multiple fault biases missing detection. First, an estimation consistency factor in state domain is calculated using the sequential probability ratio over sliding windows. Then, a horizontal protection level calculation method is designed based on the maximum eigenvalue under multi-fault assumptions. Finally, the algorithm can quantitatively evaluate the confidence of the position solution and improve navigation safety.

1.4 Structure of the Thesis

The thesis focuses on the requirements for high accuracy, robust state estimation, and autonomous integrity monitoring for intelligent vehicles in urban areas. The thesis proposes a robust state estimation algorithm, a robust noise adaptation algorithm, and an autonomous integrity monitoring algorithm to improve the navigation accuracy and safety of the intelligent vehicle by advantageous complementation of multiple sensors and redundant information fusion. The block diagram outlining the research content is shown in Fig. 1.4, and the correlation between each content is illustrated in Fig. 1.5. The main research content can be summarized as follows:

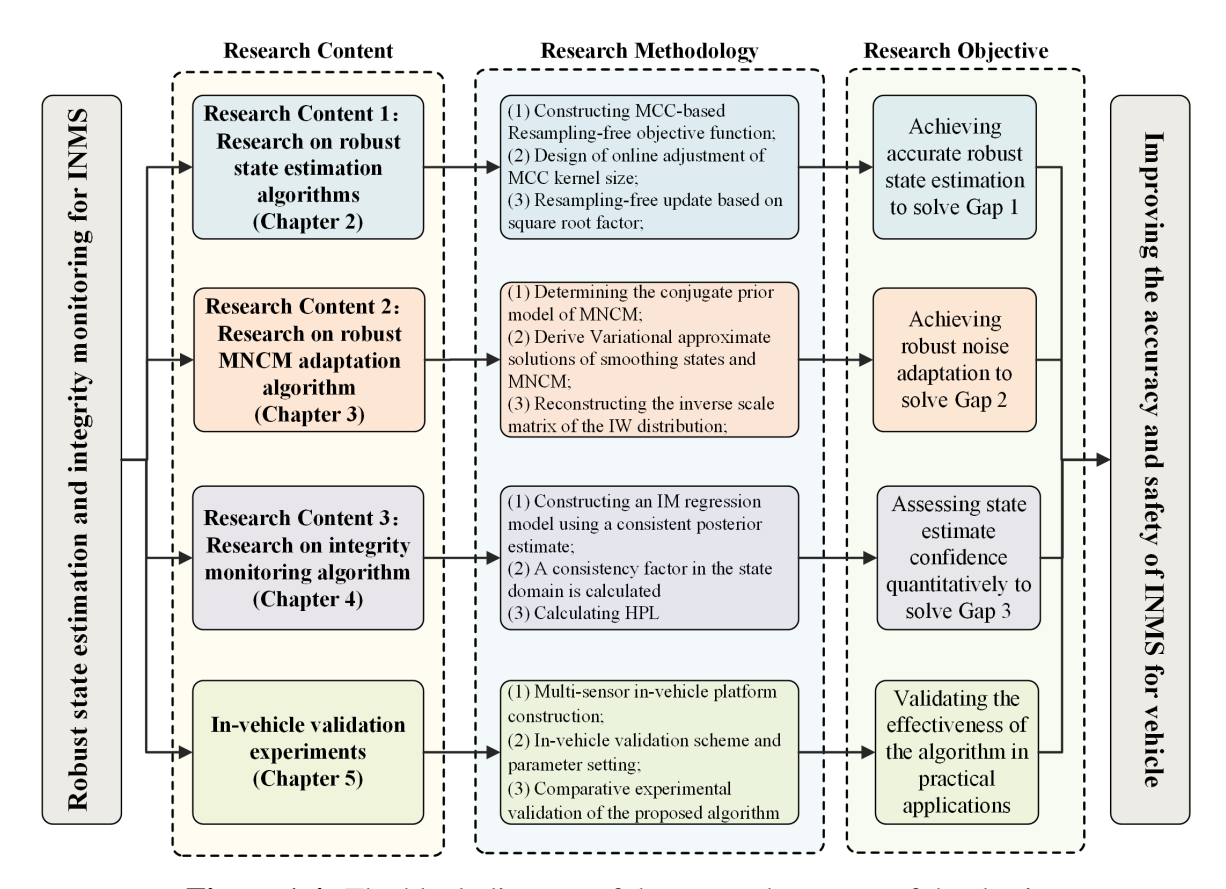


Figure 1.4: The block diagram of the research content of the thesis

• Chapter 2: Research on robust state estimation algorithms. To address the problem of INMS state estimation performance degradation due to the mismatched noise assumptions in urban areas, a robust resampling-free filter based on the adaptive kernel-sizes MCC is proposed. The cost function of the non-resampling estimation framework is constructed based on the maximum correntropy criterion, which effectively exploits the non-Gaussian moments of the state distribution caused by the nonclosed mapping, ensuring the resampling-free estimation optimality and preventing

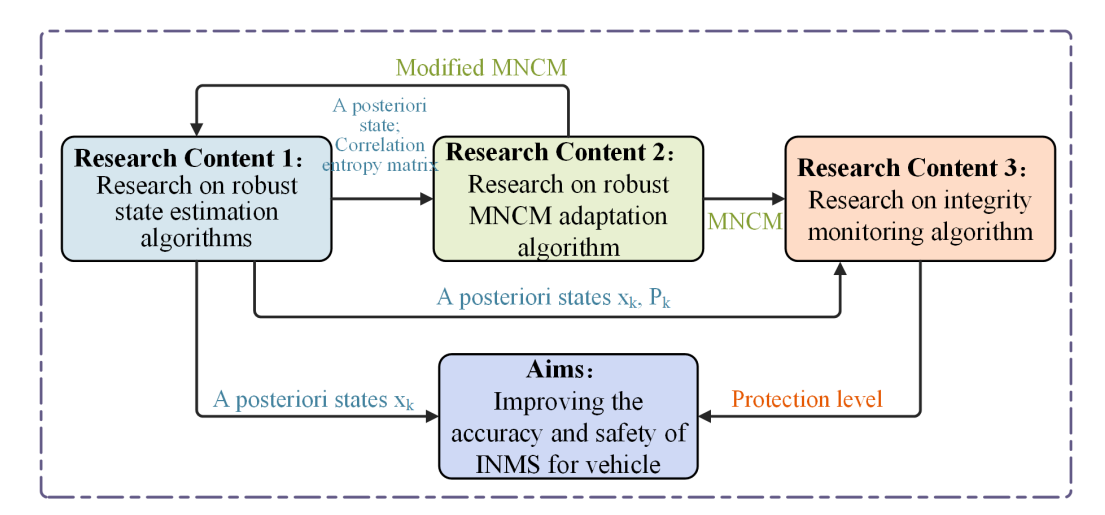


Figure 1.5: Connection between the different research contents

the loss of the higher-order moment information from Gaussian reconstruction. Then, an adaptive method for kernel size of correntropy is developed to realize the online optimal adjustment of kernel size and ensure robustness against outliers. Finally, simulation experiments are conducted to verify the effectiveness of the proposed robust estimation method.

- Chapter 3: Research on robust MNCM adaptation algorithm. To suppress the interference of outliers on the MNCM estimation in urban areas, a robust noise adaptation algorithm based on a smoothing variational approximation is proposed. The IW distribution is used as the conjugate prior model of the MNCM, and a joint variational approximate analytical solution for the MNCM and smoothing state is derived. Then, the inverse scale matrix of the IW distribution is reconstructed based on the correntropy matrix to suppress the interference of measurement outliers on the MNCM estimation. The proposed method is validated by simulation experiments. Finally, simulation experiments are conducted to verify the effectiveness of the proposed noise adaptation method.
- Chapter 4: Research on autonomous integrity monitoring algorithm. To monitor the navigation integrity for INMS in urban areas, a sequential IM method based on multiple fault bias missing detection assumption is proposed. The IM dynamic regression model is constructed by a consistent posterior estimate provided by the proposed robust filter. A consistency factor in state domain is calculated using the sequential probability ratio over sliding windows. Under the multi-fault missing detection assumption, the horizontal protection level is calculated based on the maximum eigenvalue combined with the consistency factor to quantitatively assess the confidence of the position solution. Finally, simulation experiments are conducted to verify the

effectiveness of the proposed IM method.

- Chapter 5: INMS algorithm validation experiment. Based on the above research, the performance of the proposed robust state estimation, robust noise adaptation, and autonomous integrity monitoring algorithms for practical applications are validated through in-vehicle experiments equipped with the multiple sensors platform.
- Chapter 6: Conclusion and recommendations. The conclusions of the research are drawn, including findings and contributions. Moreover, the recommendations are given for future research work.

Chapter 2

Robust State Estimation Algorithm for INMS Noise Assumption Mismatch

2.1 Introduction

The state estimation under the traditional Kalman filter framework relies on a Gaussian noise distribution assumption. However, in adverse urban areas, the interference from outliers can cause noise to exhibit a heavy-tailed non-Gaussian distribution. For example, GNSS can be affected by the frequent multi-path reflection effect; the odometers can be affected by uneven road conditions. This results in a mismatch between the actual noise probability distribution and the system noise model, i.e., the noise assumption mismatch. On the one hand, the noise assumption mismatch makes the MMSE optimal estimation criterion relying on a Gaussian distribution inapplicable, which reduces the state estimation method's performance. On the other hand, the noise assumption mismatch disrupts the state Gaussian reconstruction process of the filter under Gaussian assumptions, which reduces the covariance matrix propagation accuracy, resulting in non-consistency of the estimation. The MCC optimal criterion effectively captures higher-order moment information, fully exploits the non-Gaussian moment information in the RFU filter, ensures the optimality of the RFU estimation, and improves the estimation's robustness. However, the MCC's performance is limited by its tuning parameter, the kernel size. An appropriate kernel size would reduce the filter estimation performance or even cause it to diverge.

This chapter presents a robust state estimation algorithm to address the problem of INMS state estimation performance degradation due to noisy assumption mismatch in urban areas. First, the problem of state estimation for INMS is formulated. The principle of RFU-based filters is illustrated, and its limitation in INMS is analyzed. Then, a robust resampling-free filter based on the adaptive kernel-sizes MCC is proposed. The cost function of the RFU framework is constructed based on the MCC, which effectively exploits the non-Gaussian moments of the non-closed state distribution, ensuring the resampling-free estimation optimality and preventing the loss of the higher-order moment information from the Gaussian reconstruction. An adaptive method for MCC kernel size is developed

to achieve online optimal adjustment of kernel size and ensure robustness against outliers. Finally, the effectiveness of the proposed method is verified by simulation experiments.

2.2 Analysis of the INMS State Estimation Problem

This section presents the state estimation issue in INMS. The CKF under the Gaussian approximation assumption is given, and the numerical integration accuracy is analyzed in the high-dimensional INMS model, which induces the significance of the resampling-free filtering. First, a discrete-time stochastic dynamic system is considered as

$$\begin{cases} \mathbf{x}_{k} = \mathbf{f}_{k}(\mathbf{x}_{k-1}) + \mathbf{w}_{k-1} \\ \mathbf{z}_{k} = \mathbf{h}_{k}(\mathbf{x}_{k}) + \mathbf{v}_{k} \end{cases}$$
 (2.1)

where $\mathbf{x}_k \in \mathbb{R}^n$ and $\mathbf{z}_k \in \mathbb{R}^m$ are the state vector and the measurement vector at discretetime step k, respectively; $\mathbf{f}_k(\cdot) : \mathbb{R}^n \Rightarrow \mathbb{R}^n$ and $\mathbf{h}_k(\cdot) : \mathbb{R}^n \Rightarrow \mathbb{R}^m$ are the state dynamic function and measurement function, respectively; $\mathbf{w}_{k-1} \sim \mathrm{N}(\mathbf{0}, \mathbf{Q}_{k-1})$ and $\mathbf{v}_k \sim \mathrm{N}(\mathbf{0}, \mathbf{R}_k)$ are the uncorrelated process and measurement noise with known covariance matrix \mathbf{Q}_{k-1} and \mathbf{R}_k , respectively.

To calculate the posterior state PDF, i.e., $p(\mathbf{x}_k \mid \bar{\mathbf{z}}_k)$ with $\bar{\mathbf{z}}_k = \{\mathbf{z}_j, 1 \le j \le k\}$, the states and measurement are assumed as Gaussian distributions for ensuring analytical solutions in closed form, then the joint PDF of state and measurement vector is calculated as [96, 97]

$$p(\mathbf{x}_{k}, \mathbf{z}_{k} \mid \bar{\mathbf{z}}_{k-1}) = N\left(\begin{bmatrix} \mathbf{x}_{k} \\ \mathbf{z}_{k} \end{bmatrix}; \begin{bmatrix} \hat{\mathbf{x}}_{k|k-1} \\ \hat{\mathbf{z}}_{k|k-1} \end{bmatrix}, \begin{bmatrix} \mathbf{P}_{k|k-1} & \mathbf{P}_{k|k-1}^{xz} \\ (\mathbf{P}_{k|k-1}^{xz})^{\mathrm{T}} & \mathbf{P}_{k|k-1}^{zz} \end{bmatrix}\right)$$
(2.2)

where the prior state mean $\hat{\mathbf{x}}_{k|k-1}$ and covariance matrix $\mathbf{P}_{k|k-1}$ are the Gaussian (i.e., the first-two orders) moments of $p(\mathbf{x}_k \mid \bar{\mathbf{z}}_{k-1})$; The predicted measurement $\hat{\mathbf{z}}_{k|k-1}$ and covariance matrix $\mathbf{P}_{k|k-1}^{zz}$ are the Gaussian moments of $p(\mathbf{z}_k \mid \bar{\mathbf{z}}_{k-1})$; $\mathbf{P}_{k|k-1}^{xz}$ is the cross-covariance matrix of state and measurement, i.e., $\mathbf{P}_{k|k-1}^{xz} = \mathrm{E}[\tilde{\mathbf{x}}_{k|k-1}\tilde{\mathbf{z}}_{k|k-1}^{T}]$, where $\tilde{\mathbf{x}}_{k|k-1}$ and $\tilde{\mathbf{z}}_{k|k-1}$ are the prior state and the measurement estimation error.

Then, according to the Bayesian rule, the posterior state PDF $p(\mathbf{x}_k \mid \mathbf{\bar{z}}_k)$ is approximated as a Gaussian distribution and formulated based on Eq. (2.2) as follows [98] (Derivation details are given in the Appendix A):

$$p\left(\mathbf{x}_{k} \mid \bar{\mathbf{z}}_{k}\right) = \frac{p\left(\mathbf{x}_{k}, \mathbf{z}_{k} \mid \bar{\mathbf{z}}_{k-1}\right)}{p\left(\mathbf{z}_{k} \mid \bar{\mathbf{z}}_{k-1}\right)} \approx N\left(\mathbf{x}_{k}; \hat{\mathbf{x}}_{k}, \mathbf{P}_{k}\right). \tag{2.3}$$

*/

The calculation of N (\mathbf{x}_k ; $\mathbf{\hat{x}}_k$, \mathbf{P}_k) relies on some conditional variable PDF that needs to be obtained through GWI, such as $\mathbf{\hat{x}}_{k|k-1}$. Since the analytical solution of GWI is generally computationally intractable, the numerical integration rule is used to approximate the GWI, which is formulated in a uniform form as

$$\int_{\mathbb{R}^n} \mathbf{u}(\mathbf{x}_k) \mathbf{N}(\mathbf{x}_k; \hat{\mathbf{x}}_k, \mathbf{P}_k) d\mathbf{x} \approx \sum_{i=1}^{n_s} w^{(i)} \mathbf{u}(\mathbf{x}_k^{(i)})$$
(2.4)

where $\mathbf{x}^{(i)}$ and $w^{(i)}$ are the sampling points and the corresponding weights, respectively; n_s is the number of sampling points. In the spherical-radial cubature rule, the number of cubature points is $n_s = 2n$; The weight is $w^{(i)} = \{1/n_s, 1 \le i \le n_s\}$; The sampling points (referred as cubature points) are generated as [99, 100]

$$\mathbf{x}_{k}^{(i)} = \operatorname{chol}(\mathbf{P}_{k}) \, \boldsymbol{\xi}_{i} + \hat{\mathbf{x}}_{k}, \text{ for } i = 1, \cdots, n_{s}$$
 (2.5)

where \mathbf{P}_k denotes the state mean square error matrix; $\mathrm{chol}(\cdot)$ denotes the lower triangular matrix calculated by Cholesky decomposition; $\boldsymbol{\xi}^{(i)}$ denotes the *i*-th column of $\boldsymbol{\xi} = \sqrt{n} \left[\mathbf{I}_n - \mathbf{I}_n \right]$ with the *n*-dimensional identity matrix \mathbf{I}_n . The implementation of CKF is formulated in Algorithm 1.

Algorithm 1: One-time step implementation of CKF

```
Input: \hat{\mathbf{x}}_{k-1}, \mathbf{P}_{k-1}, \mathbf{Q}_{k-1}, \mathbf{R}_k
```

Output: $\hat{\mathbf{x}}_k, \mathbf{P}_k$

1:
$$\mathbf{x}_{k-1}^{(i)} = \operatorname{chol}(\mathbf{P}_{k-1})_{s,i} + \hat{\mathbf{x}}_{k-1}$$
, for $i = 1, \dots, n_s$

2:
$$\hat{\mathbf{x}}_{k|k-1} = \sum_{i=1}^{n_s} w^{(i)} \mathbf{f}_k(\mathbf{x}_{k-1}^{(i)})$$

3:
$$\mathbf{P}_{k|k-1} = \sum_{i=1}^{n_s} w^{(i)} \mathbf{f}_k(\mathbf{x}_{k-1}^{(i)}) \mathbf{f}_k(\mathbf{x}_{k-1}^{(i)})^{\mathrm{T}} - \hat{\mathbf{x}}_{k|k-1} \hat{\mathbf{x}}_{k|k-1}^{\mathrm{T}} + \mathbf{Q}_{k-1}$$

4:
$$\mathbf{x}_{k|k-1}^{(i)} = \operatorname{chol}\left(\mathbf{P}_{k|k-1}\right)$$
 , $i+\hat{\mathbf{x}}_{k|k-1}$, for $i=1,\cdots,n_s$

5:
$$\hat{\mathbf{z}}_{k|k-1} = \sum_{i=1}^{N} w^{(i)} \mathbf{h}_k \left(\mathbf{x}_{k|k-1}^{(i)} \right)$$

6:
$$\mathbf{P}_{k|k-1}^{zz} = \sum_{i=1}^{N} w^{(i)} \mathbf{h}_{k} \left(\mathbf{x}_{k|k-1}^{(i)} \right) \mathbf{h}_{k} \left(\mathbf{x}_{k|k-1}^{(i)} \right)^{\mathrm{T}} - \hat{\mathbf{z}}_{k|k-1} \hat{\mathbf{z}}_{k|k-1}^{\mathrm{T}} + \mathbf{R}_{k}$$

7:
$$\mathbf{P}_{k|k-1}^{xz} = \sum_{i=1}^{N} w^{(i)} \mathbf{x}_{k|k-1}^{(i)} \mathbf{h}_k \left(\mathbf{x}_{k|k}^{(i)} \right)^{\mathrm{T}} - \hat{\mathbf{x}}_{k|k-1} \hat{\mathbf{z}}_{k|k-1}^{\mathrm{T}}$$

8:
$$\mathbf{G}_k = \mathbf{P}_{k|k-1}^{xz} (\mathbf{P}_{k|k-1}^{zz})^{-1}$$

9:
$$\hat{\mathbf{x}}_k = \hat{\mathbf{x}}_{k|k-1} + \mathbf{G}_k \left(\mathbf{z}_k - \hat{\mathbf{z}}_{k|k-1} \right)$$

10:
$$\mathbf{P}_k = \mathbf{P}_{k|k-1} - \mathbf{G}_k \mathbf{P}_{k|k-1}^{zz} \mathbf{G}_k^{\mathrm{T}}$$

The estimation accuracy of CKF is analyzed qualitatively based on the propagation of

cubature points in the high-dimensional INMS model. The subscript moment k is omitted from the following analysis for simplicity of presentation. Considering a general function $\mathbf{h}(\cdot)$, there are

$$\hat{\mathbf{z}} = \int_{\mathbb{R}^n} \mathbf{h}(\mathbf{x}) \mathbf{N}(\mathbf{x}; \hat{\mathbf{x}}, \mathbf{P}) d\mathbf{x} \approx \sum_{i=1}^{n_s} w^{(i)} \mathbf{h}(\mathbf{x}^{(i)})$$
(2.6)

A multivariate Taylor series expansion of the cubature point $\mathbf{x}^{(i)}$ in Eq. (2.6) at $\hat{\mathbf{x}}$ gives

$$\mathbf{h}(\mathbf{x}^{(i)}) = \mathbf{h}(\hat{\mathbf{x}}) + \sum_{l=1}^{\infty} \frac{1}{l!} \mathbf{D}_{\mathbf{e}_{l}}^{l} \mathbf{h}$$
 (2.7)

where $\mathbf{D}_{\mathbf{e}_i}^l \mathbf{h} = \left[\sum_{j=1}^n \mathbf{e}_{i,j} \frac{\partial}{\partial \mathbf{x}_j} \right]^l \mathbf{h}(\mathbf{x}) \Big|_{\mathbf{x} = \hat{\mathbf{x}}}$; $\mathbf{e}_i = \mathbf{x}^{(i)} - \hat{\mathbf{x}} = \operatorname{chol}(\mathbf{P}) \boldsymbol{\xi}_i$; $\partial/\partial \mathbf{x}_j$ is the partial derivative of j-th element of the \mathbf{x} ; l is the expansion order of the Taylor series. As seen from Eq. (2.5), the sampling locations of the cubature points are symmetrically distributed around $\hat{\mathbf{x}}$, so bringing Eq. (2.7) into Eq. (2.6), the state mean and covariance matrix propagated through the cubature points are denoted as

$$\begin{cases}
\hat{\mathbf{z}}_{ct} = \mathbf{h}(\hat{\mathbf{x}}) + \frac{1}{2} \left(\nabla^{T} \mathbf{P} \nabla \right) \mathbf{h}(\mathbf{x}) \big|_{\mathbf{x} = \hat{\mathbf{x}}} + \mathbf{r}_{m}(n) \\
\mathbf{P}_{ct} = \mathbf{H}(\hat{\mathbf{x}}) \mathbf{P} \mathbf{H}^{T}(\hat{\mathbf{x}}) - \frac{1}{4} \left(\nabla^{T} \mathbf{P} \nabla \right) \mathbf{h}(\mathbf{x}) \big|_{\mathbf{x} = \hat{\mathbf{x}}} \left[\left(\nabla^{T} \mathbf{P} \nabla \right) \mathbf{h}(\mathbf{x}) \big|_{\mathbf{x} = \hat{\mathbf{x}}} \right]^{T} + \mathbf{r}_{cov}(n)
\end{cases} (2.8)$$

where $\nabla^{T} = [\partial/\partial \mathbf{x}_{1} \cdots \partial/\partial \mathbf{x}_{n}]$; $\mathbf{H}(\hat{\mathbf{x}}) = \partial \mathbf{h}/\partial \mathbf{x}^{T}\big|_{\mathbf{x}=\hat{\mathbf{x}}}$; $\mathbf{r}_{m}(n)$ is a Taylor series higher order term (greater than or equal to the fourth order), denoted by

$$\mathbf{r}_{\mathrm{m}}(n) = \frac{1}{2n} \sum_{i=1}^{n_{s}} \sum_{l=2}^{\infty} \frac{1}{(2l)!} \mathbf{D}_{\mathbf{e}_{i}}^{2l} \mathbf{h} = n^{l-1} \sum_{i=1}^{n_{s}} \sum_{l=2}^{\infty} \left[\frac{1}{(2l)!} \sum_{j=1}^{n} \mathbf{P}^{l}(i,j) \right]$$
(2.9)

where $\mathbf{P}^l(i,j)$ is the covariance of j-th element of $\mathbf{e}_{i,j}$; $\mathbf{r}_{cov}(n)$ is the sum of higher order terms in the Taylor series expansion, denoted by

$$\mathbf{r}_{\text{cov}}(n) = \frac{1}{4} \operatorname{E} \left[\mathbf{D}_{\mathbf{e}}^{2} \mathbf{h} \left(\mathbf{D}_{\mathbf{e}}^{2} \mathbf{h} \right)^{\mathrm{T}} \right] + \frac{1}{2 \times 3!} \operatorname{E} \left[\mathbf{D}_{\mathbf{e}}^{2} \mathbf{h} \left(\mathbf{D}_{\mathbf{e}}^{3} \mathbf{h} \right)^{\mathrm{T}} \right] + \cdots$$
(2.10)

Furthermore, the actual state mean and covariance matrix are denoted as [101, 102]

$$\begin{cases}
\hat{\mathbf{z}}_{t} = \mathbf{h}(\hat{\mathbf{x}}) + \frac{1}{2} \left(\nabla^{T} \mathbf{P} \nabla \right) \mathbf{h}(\mathbf{x}) \Big|_{\mathbf{x} = \hat{\mathbf{x}}} + E \left[\frac{\mathbf{D}_{\delta \mathbf{x}}^{4} \mathbf{h}}{4!} + \frac{\mathbf{D}_{\delta \mathbf{x}}^{6} \mathbf{h}}{6!} + \cdots \right] \\
\mathbf{P}_{t} = \mathbf{H}(\hat{\mathbf{x}}) \mathbf{P} \mathbf{H}^{T}(\hat{\mathbf{x}}) - \frac{1}{4} \left(\nabla^{T} \mathbf{P} \nabla \right) \mathbf{h}(\mathbf{x}) \Big|_{\mathbf{x} = \hat{\mathbf{x}}} \left[\left(\nabla^{T} \mathbf{P} \nabla \right) \mathbf{h}(\mathbf{x}) \Big|_{\mathbf{x} = \hat{\mathbf{x}}} \right]^{T} - \mathbf{r}_{tcov}(n)
\end{cases} (2.11)$$

where $\mathbf{r}_{\text{tcov}}(n) = \mathbb{E}\left[\sum_{i=1}^{\infty} \sum_{j=1}^{\infty} \frac{1}{(2i)!(2j)!} \left(\mathbf{D}_{\delta \mathbf{x}}^{2i} \mathbf{h}\right) \left(\mathbf{D}_{\delta \mathbf{x}}^{2i} \mathbf{h}\right)^{\text{T}}\right] + \mathbb{E}\sum_{i=2}^{\infty} \sum_{j=2}^{\infty} \left(\mathbf{D}_{\delta \mathbf{x}}^{i} \mathbf{h}\right) \left(\mathbf{D}_{\delta \mathbf{x}}^{i} \mathbf{h}\right)^{\text{T}}; \ \delta \mathbf{x} \text{ is the expansion point } \hat{\mathbf{x}} \text{ offset from the actual mean.}$

Comparing the Taylor expansion of the state means and covariances based on the propagation of cubature points in Eq. (2.8) with their actual values in Eq. (2.11), it can be given that:

- (1) The state mean $\hat{\mathbf{z}}_{ct}$ based on the cubature transformation introduces an approximation error starting from the higher-order term $\mathbf{r}_{m}(n)$. Similarly, the state covariance $\hat{\mathbf{P}}_{ct}$ introduces approximation errors from the higher order terms $\mathbf{r}_{cov}(n)$. Since $\mathbf{r}_{m}(n)$ and $\mathbf{r}_{cov}(n)$ are proportional to the exponential of the system dimension n, the approximation error increases with the system dimension. For the high-dimensional system of INMS (n = 18 for the model), a large approximation error occurs, resulting in a degradation of the filtering accuracy.
- (2) In the cubature transformation process, the posterior analytical solution is obtained by assuming that the state follows a Gaussian distribution. Furthermore, the cubature points $\mathbf{x}^{(i)}$ are tied to the coordinate axes by ξ_i , which results in a cubature point distribution that retains only the Gaussian moment, discards the available non-Gaussian higher-order moment information, destroys the original state probability distribution, and limits the state estimation performance.

2.3 Resampling-Free Gaussian Approximation Filter

To overcome the above mentioned limitations of GAF, the section introduces the resampling-free filtering and analyzes its problems in INMS.

2.3.1 RFU Based on the Center Matrix of the Cubature Points

(1) **Brief Principle:** The principle of resampling-free update is given [25]. First, the sampling point centre matrix is defined as Eq. (2.12). The sampling point is updated by the centre matrix rather than regeneration based on Gaussian assumptions.

$$\tilde{\mathbf{X}} = \left[\mathbf{x}^{(1)} - \hat{\mathbf{x}} \cdots \mathbf{x}^{(n_s)} - \hat{\mathbf{x}} \right]. \tag{2.12}$$

In detail, the prior center matrix is denoted as $\tilde{\mathbf{X}}^-$ with covariance matrix \mathbf{P}^- . The posterior center matrix is denoted as $\tilde{\mathbf{X}}^+$ with covariance matrix \mathbf{P}^+ . According to the definitions of $\tilde{\mathbf{X}}^+$ and $\tilde{\mathbf{X}}^-$, there are

$$\begin{cases} \tilde{\mathbf{X}}^{+}\mathbf{w} = \tilde{\mathbf{X}}^{-}\mathbf{w} = 0 \\ \mathbf{P}^{-} = \tilde{\mathbf{X}}^{-}\mathbf{W} (\tilde{\mathbf{X}}^{-})^{\mathrm{T}} \\ \mathbf{P}^{+} = \tilde{\mathbf{X}}^{+}\mathbf{W} (\tilde{\mathbf{X}}^{+})^{\mathrm{T}} = \mathbf{P}^{-} + \mathbf{R} \end{cases}$$
(2.13)

where $\mathbf{W} = \operatorname{diag}(\mathbf{w})$ denotes the diagonal matrix; \mathbf{w} is a vector constructed by the weights of each cubature point, i.e., $\mathbf{w} = [w^{(1)} \cdots w^{(n_s)}]^T$; \mathbf{R} is the uncertainty due to random noise.

To update the posterior sampling points sets, a posterior centre matrix needs to be calculated based on the known prior centre matrix in a recursive process. Consider the relationship between them as

$$\tilde{\mathbf{X}}^+ = \mathbf{E}\tilde{\mathbf{X}}^- \tag{2.14}$$

Taking Eq. (2.14) into Eq. (2.13) yields

$$\mathbf{E}\mathbf{L}^{-}(\mathbf{L}^{-})^{\mathrm{T}}\mathbf{E}^{\mathrm{T}} = \mathbf{L}^{+}(\mathbf{L}^{+})^{\mathrm{T}}$$
(2.15a)

$$\mathbf{P}^{+} = \mathbf{E}\tilde{\mathbf{X}}^{-}\mathbf{W} \left(\mathbf{E}\tilde{\mathbf{X}}^{-}\right)^{\mathrm{T}} = \mathbf{E} \left(\mathbf{P}^{-}\right) \mathbf{E}^{\mathrm{T}}$$
(2.15b)

where $L \in \{L^+, L^-\}$ denote the lower triangular matrix of $P \in \{P^+, P^-\}$. Thus, E can be calculated as

$$\mathbf{E} = \mathbf{L}^{+} \mathbf{M} (\mathbf{L}^{-})^{-1} = \operatorname{chol} (\mathbf{P}^{-} + \mathbf{R}) \mathbf{M} \operatorname{chol} (\mathbf{P}^{-})^{-1}$$
(2.16)

where **M** denotes any orthogonal matrix, i.e., $\mathbf{M}\mathbf{M}^T = \mathbf{I}$. Once $\tilde{\mathbf{X}}^+$ is obtained using **E** in Eq. (2.14), a posterior sample point set is updated according to Eq. (2.12) to avoid regenerating based on Gaussian assumption.

(2) **RFU Filter:** Based on the above principle, a RFU-based filter is proposed [103]. The posterior state centre matrix $\tilde{\mathbf{X}}_k$ is calculated by the prior centre matrix $\tilde{\mathbf{X}}_{k|k-1}$ and measurement centre matrix $\tilde{\mathbf{Z}}_{k|k-1}$. In detail, the posterior error matrix at time-step k is calculated as

$$\tilde{\mathbf{X}}_k = \alpha_k \mathbf{E}_k \tilde{\mathbf{X}}_{k|k-1} - \alpha_k \mathbf{G}_k \tilde{\mathbf{Z}}_{k|k-1}$$
(2.17)

where the prior state and measurement error matrix are calculated as

$$\tilde{\vartheta}_{k|k-1} = \left[\vartheta_{k|k-1}^{(1)} - \hat{\vartheta}_{k|k-1} \cdots \vartheta_{k|k-1}^{(n_s)} - \hat{\vartheta}_{k|k-1} \right], \tag{2.18}$$

where $\vartheta \in \{\mathbf{x}, \mathbf{z}\}$; \mathbf{E}_k and α_k are calculated by

$$\mathbf{E}_{k} = \operatorname{chol}\left(\mathbf{P}_{k|k-1}\right) \operatorname{chol}\left(\mathbf{P}_{k|k-1} - \mathbf{Q}_{k-1}\right)^{-1} \tag{2.19a}$$

$$\alpha_k = \operatorname{chol}(\mathbf{P}_k) \, \mathbf{M}_k \, \operatorname{chol}(\mathbf{P}_k - \mathbf{G}_k \mathbf{R}_k \mathbf{G}_k^{\mathrm{T}})^{-1}$$
(2.19b)

where the term $\mathbf{P}_k - \mathbf{G}_k \mathbf{R}_k \mathbf{G}_k$ denotes the posterior covariance matrix without the effect of additive measurement noise; A particular solution can be obtained by setting \mathbf{M}_k as the identity matrix \mathbf{I}_n . Then, the cubature points are modified by the posterior error matrix as

$$\mathbf{x}_{k}^{(i)} = \hat{\mathbf{x}}_{k} + \tilde{\mathbf{X}}_{i,k}, \text{ for } i = 1, \dots, n_{s}.$$
 (2.20)

The updated posterior cubature points are used to input the recursive filtering for the next time-step and remove the dependence on Gaussian assumption, retaining the informative high-order moments contained in the original state distribution.

2.3.2 Limitations Analysis for RFU in INMS

Although ISUF removes the dependence on Gaussian assumption through a non-resampling operation, it still has the following limitations in INMS:

- (1) It still adopts the MMSE based on the Gaussian assumption as the optimal estimation criterion to fuse the a priori state and measurement information in the posterior updating process. However, since the nonlinear mapping violates the closure property of the state PDF without Gaussian reconstruction, it tends to produce a significant deviation of the state distribution from the Gaussian assumption after multiple nonlinear propagations. This results in a severely non-Gaussian distribution and renders the MMSE inapplicable in resampling-free filters, thus preventing estimation optimality.
- (2) To compute the posterior error matrix, multiple Cholesky decompositions of the EMSE are performed in Eq. (2.19). However, without Gaussian reconstruction, the differences in state magnitudes in INMS can lead to significant gaps between eigenvalues of EMSE (e.g., a factor of 10⁸ between velocity error and gyro zero-bias covariance eigenvalues), making the EMSE matrix singular. Cholesky decomposition in this case can lead to numerical instability or even filter divergence.

2.4 Robust RFU Filter Based on Maximum Correntropy Criterion

To address the limitations of RFU in INMS, the section proposes a robust resampling-free filtering algorithm based on MCC. First, the definition of MCC is given. Then, an RFU filtering framework based on MCC is constructed, and the kernel size adjustment method of MCC is proposed. Finally, the theoretical performance of the proposed algorithm is analyzed.

2.4.1 Maximum Correntropy Criterion

The correntropy is a metric of similarity between two variables. Given two random variables $\mathbf{x}, \mathbf{y} \in \mathbb{R}^n$ with the joint probability distribution $p(\mathbf{x}, \mathbf{y})$, the correntropy is defined

as:

$$C(\mathbf{x}, \mathbf{y}) = E[\boldsymbol{\varpi}(\mathbf{x}, \mathbf{y})] = \int_{\mathbb{R}^n} \boldsymbol{\varpi}(\mathbf{x}, \mathbf{y}) \, \mathrm{d}p(\mathbf{x}, \mathbf{y})$$
(2.21)

where $E[\cdot]$ is the expectation operator; \$(x,y) denotes the kernel function satisfying the Mercer theory. The Gaussian kernel is chosen as the kernel function due to its infinite approximation ability to a nonlinear model, which is expressed as [42, 43]:

$$\boldsymbol{\varpi}(\mathbf{x}, \mathbf{y}) = G_{\boldsymbol{\sigma}}(\mathbf{x} - \mathbf{y}) = \exp\left(-\frac{\|\mathbf{x} - \mathbf{y}\|_{\mathbf{W}}^2}{2\sigma^2}\right)$$
(2.22)

where $G_{\sigma}(\cdot) \in (0,1]$ is positive and bounded; $\sigma > 0$ is the kernel size. $\|\cdot\|_{\mathbf{W}}^2 = (\cdot)^{\mathrm{T}}\mathbf{W}(\cdot)$ denotes the squared-weighted Mahalanobis distance with \mathbf{W} as the weights matrix. Generally, $p(\mathbf{x}, \mathbf{y})$ is computationally intractable, and only a finite amount of data is available. So the correntropy is calculated by the mean of a sample.

$$C(\mathbf{x}, \mathbf{y}) = \frac{1}{n_s} \sum_{i=1}^{n_s} G_{\sigma} \left(\mathbf{x}^{(i)} - \mathbf{y}^{(i)} \right)$$
 (2.23)

where $\{\mathbf{x}^{(i)}, \mathbf{y}^{(i)}\}_{i=1}^{n_s}$ is the n_s samples drawn from $p(\mathbf{x}, \mathbf{y})$. Then taking the Taylor series expansion of the Gaussian kernel function:

$$C(\mathbf{x}, \mathbf{y}) = \sum_{n=0}^{\infty} \frac{(-1)^n}{2^n \sigma^{2n} n!} E\left[(\mathbf{x} - \mathbf{y})^{2n} \right]$$
 (2.24)

The correntropy is a weighted sum of all even-order moments of the variable $\mathbf{x} - \mathbf{y}$, so the high-order information of the data can be captured. Since the correntropy is a metric of similarity, the robust state estimation can be achieved by maximizing the correntropy as an optimization criterion. The cost function of can be formulated as

$$J_{\text{MCC}}(\mathbf{x}) = \sum_{i=1}^{n_f} G_{\sigma}(\mathbf{z}_i - \mathbf{h}_i(\mathbf{x}))$$
 (2.25)

where $\mathbf{z}_i = \mathbf{h}_i(\mathbf{x}^t) + \mathbf{v}_i$ denotes the measurment; \mathbf{x}^t is the actual state vector. The state optimal estimate is obtained by maximizing the objective function, i.e.

$$\hat{\mathbf{x}} = \underset{\mathbf{x}}{\operatorname{arg\,max}} J_{\text{MCC}}(\mathbf{x}) = \underset{\mathbf{x}}{\operatorname{arg\,max}} \sum_{i=1}^{n_f} G_{\sigma}(\mathbf{z}_i - \mathbf{h}_i(\mathbf{x}))$$
(2.26)

MCC-based filtering can effectively capture the higher-order moments information of the residual $\mathbf{r}_i = \mathbf{z}_i - \mathbf{h}_i(\mathbf{x})$. In addition, in the presence of outliers, the effect of larger

deviations on the correntropy will be weakened by the thresholding effect of the negative exponential term based on the kernel size σ , which avoids a state estimation contamination.

2.4.2 A RFU Filtering Framework Based on MCC

The MCC is adopted as the optimization criterion to construct an objective function to exploit the non-Gaussian moments, and an RFU based on the square-root factor of the posterior centre matrix is devised, which ensures the estimation optimality and improves the robustness of the estimation. The details of the derivation are as follows. The implementation of the proposed MCC-based RFU framework CKF (MRCKF) is formulated in the Algorithm 2

(1) Time Update

Time update computes state a priori. Modifying the sampling points based on the posterior centre matrix as

$$\mathbf{x}_{k-1}^{(i)} = \hat{\mathbf{x}}_{k-1} + \tilde{\mathbf{X}}_{i,k-1}, \text{ for } i = 1, \dots, n_s$$
 (2.27)

Propagating cubature points and calculating the prior state mean.

$$\hat{\mathbf{x}}_{k|k-1} = \frac{1}{n_s} \sum_{i=1}^{n_s} \chi_{k|k-1}^{(i)} = \frac{1}{n_s} \sum_{i=1}^{n_s} \mathbf{f}_k(\mathbf{x}_{k-1}^{(i)})$$
 (2.28)

Then, the propagating cubature points error matrix is given as

$$\mathbf{L}_{k|k-1} = \begin{bmatrix} \chi_{k|k-1}^{(1)} - \hat{\mathbf{x}}_{k|k-1} & \cdots & \chi_{k|k-1}^{(n_s)} - \hat{\mathbf{x}}_{k|k-1} \end{bmatrix}$$
 (2.29)

where state covariance matrix is obtained by $\mathbf{P}_{k|k-1} = \frac{1}{n_s} \mathbf{L}_{k|k-1} \mathbf{L}_{k|k-1}^{\mathrm{T}} + \mathbf{Q}_{k-1}$. To avoid the Cholesky decomposition, it is supposed to operate directly on $\mathbf{L}_{k|k-1}$. Therefore, based on the matrix decomposition rules, the square-root factors of $\mathbf{P}_{k|k-1}$ can be calculated by QR decomposition of $\mathbf{L}_{k|k-1}$ as

$$\mathbf{D}_{k|k-1} = \frac{1}{\sqrt{n_s}} \operatorname{qr}\left(\mathbf{L}_{k|k-1}^{\mathrm{T}}\right) \tag{2.30a}$$

$$\mathbf{S}_{k|k-1} = \frac{1}{\sqrt{n_s}} \operatorname{qr}\left(\left[\mathbf{L}_{k|k-1}, \sqrt{n_s} \mathbf{S}_k^q\right]^{\mathrm{T}}\right)$$
(2.30b)

where $qr(\cdot)$ denotes the lower triangular matrix calculated by QR decomposition with better numerical stability; \mathbf{S}_k^q is the square-root factor of the process noise covariance matrix,

i.e., $\mathbf{Q}_k = \mathbf{S}_k^q (\mathbf{S}_k^q)^{\mathrm{T}}$; $\mathbf{D}_{k|k-1}$ and $\mathbf{S}_{k|k-1}$ are the square-root factor of the covariance matrix without and with process noise, respectively. Then, the scaling matrix is calculated as

$$\mathbf{E}_{k} = \mathbf{S}_{k|k-1} \mathbf{D}_{k|k-1}^{-1} = \operatorname{qr}\left(\left[\mathbf{L}_{k|k-1}, \sqrt{n_{s}} \mathbf{S}_{k}^{q}\right]^{\mathrm{T}}\right) \operatorname{qr}\left(\mathbf{L}_{k|k-1}^{\mathrm{T}}\right)^{-1}$$
(2.31)

Since the model uncertainty is not considered, $\mathbf{L}_{k|k-1}$ is scaled by \mathbf{E}_k to incorporate the process noise as

$$\tilde{\mathbf{X}}_{k|k-1} = \mathbf{E}_k \mathbf{L}_{k|k-1}. \tag{2.32}$$

(2) Measurement Update

Modifying the prior state cubature points based on $\tilde{\mathbf{X}}_{k|k-1}$ as

$$\mathbf{x}_{k|k-1}^{(i)} = \hat{\mathbf{x}}_{k|k-1} + \tilde{\mathbf{X}}_{i,k|k-1}, \text{ for } i = 1, \dots, n_s$$
 (2.33)

Propagating prior cubature points $\mathbf{z}_{k|k-1}^{(i)} = \mathbf{h}_k(\mathbf{x}_{k|k-1}^{(i)})$ and calculating the predicted measurement mean $\hat{\mathbf{z}}_{k|k-1}$. Then, the measurement error matrix is calculated as

$$\tilde{\mathbf{Z}}_{k|k-1} = \begin{bmatrix} \mathbf{z}_{k|k-1}^{(1)} - \hat{\mathbf{z}}_{k|k-1} & \cdots & \mathbf{z}_{k|k-1}^{(n_s)} - \hat{\mathbf{z}}_{k|k-1} \end{bmatrix}.$$
 (2.34)

The square-root factor of the predicted measurement covariance matrix is calculated as

$$\mathbf{P}_{k|k-1}^{\hat{z}\hat{z}} = \frac{1}{n_s} \tilde{\mathbf{Z}}_{k|k-1} \tilde{\mathbf{Z}}_{k|k-1}^{\mathrm{T}}$$
 (2.35)

The cross-covariance matrix is calculated as

$$\mathbf{P}_{k|k-1}^{xz} = \frac{1}{n_s} \tilde{\mathbf{X}}_{k|k-1} \tilde{\mathbf{Z}}_{k|k-1}^{\mathrm{T}}$$

$$(2.36)$$

Instead of MMSE, the MCC is then adopted as the optimal criterion. The cost function is constructed as

$$J_{\text{MCC}}(\mathbf{x}_{k}) = G_{\sigma} \left(\left\| \mathbf{x}_{k} - \hat{\mathbf{x}}_{k|k-1} \right\|_{\mathbf{P}_{k|k-1}}^{2} \right) + G_{\sigma} \left(\left\| \mathbf{z}_{k} - \mathbf{h} \left(\mathbf{x}_{k} \right) \right\|_{\mathbf{R}_{k}^{-1}}^{2} \right)$$
(2.37)

where the kernel function $G_{\sigma}(\cdot)$ is generally chosen as Gaussian kernel by its infinite approximation ability in Eq. (2.22). Then, the optimal state estimate in the sense of MCC

is calculated by maximizing the objective function as

$$\hat{\mathbf{x}}_k = \underset{\mathbf{x}_k}{\arg\max} J_{\text{MCC}}(\mathbf{x}_k) \tag{2.38}$$

Solving the optimization problem by taking the derivative of Eq. (2.37) as

$$\frac{\partial J_{\text{MCC}}(\mathbf{x}_{k})}{\partial \mathbf{x}_{k}} = G_{\sigma}\left(\mathbf{x}_{k}^{\text{md}}\right) \frac{\partial \mathbf{x}_{k}^{\text{md}}}{\partial \mathbf{x}_{k}} + G_{\sigma}\left(\mathbf{z}_{k}^{\text{md}}\right) \frac{\partial \mathbf{z}_{k}^{\text{md}}}{\partial \mathbf{x}_{k}} = 0$$
(2.39)

where $\mathbf{x}_{k}^{\mathrm{md}} = \left\|\mathbf{x}_{k} - \hat{\mathbf{x}}_{k|k-1}\right\|_{\mathbf{P}_{k|k-1}^{-1}}^{2}$; $\mathbf{z}_{k}^{\mathrm{md}} = \left\|\mathbf{z}_{k} - \mathbf{h}\left(\mathbf{x}_{k}\right)\right\|_{\mathbf{R}_{k}^{-1}}^{2}$. Then, rearranging it yields

$$G_{\sigma}\left(\mathbf{x}_{k}^{\text{md}}\right) \frac{\partial \left[\left(\mathbf{x}_{k} - \hat{\mathbf{x}}_{k|k-1}\right)^{\text{T}} \mathbf{P}_{k|k-1}^{-1} \left(\mathbf{x}_{k} - \hat{\mathbf{x}}_{k|k-1}\right)\right]}{\partial \mathbf{x}_{k}} + G_{\sigma}\left(\mathbf{z}_{k}^{\text{md}}\right) \frac{\partial \left[\left(\mathbf{z}_{k} - \mathbf{h}\left(\mathbf{x}_{k}\right)\right)^{\text{T}} \mathbf{R}_{k}^{-1} \left(\mathbf{z}_{k} - \mathbf{h}\left(\mathbf{x}_{k}\right)\right)\right]}{\partial \mathbf{x}_{k}} = 0$$
(2.40)

Based on the rules of matrix derivation operations, the following equation holds

$$G_{\sigma}\left(\mathbf{x}_{k}^{\mathrm{md}}\right)\left(\mathbf{x}_{k}-\hat{\mathbf{x}}_{k|k-1}\right)^{\mathrm{T}}\mathbf{P}_{k|k-1}^{-1}=G_{\sigma}\left(\mathbf{z}_{k}^{\mathrm{md}}\right)\left(\mathbf{z}_{k}-\mathbf{h}\left(\mathbf{x}_{k}\right)\right)^{\mathrm{T}}\mathbf{R}_{k}^{-1}\frac{\partial\mathbf{h}\left(\mathbf{x}_{k}\right)}{\partial\mathbf{x}_{k}}$$
(2.41)

Transform Eq. (2.41), it can be obtained as

$$\mathbf{x}_{k} = \mathbf{g}\left(G_{\sigma}\left(\mathbf{x}_{k}^{\text{md}}\right), G_{\sigma}\left(\mathbf{z}_{k}^{\text{md}}\right), \hat{\mathbf{x}}_{k|k-1}, \mathbf{z}_{k}\right)$$
(2.42)

According to Eq. (2.42), the optimal solution involves the fixed-point iterations of state \mathbf{x}_k . Denoting \mathbf{x}_k^t as the solution at the fixed-point iteration count t, then expanding $\mathbf{h}(\mathbf{x}_k)$ by Taylor series at the iteration state $\hat{\mathbf{x}}_k^t$, it can be obtained as follows

$$\mathbf{P}_{k|k-1}^{-1}\left(\mathbf{x}_{k}-\hat{\mathbf{x}}_{k}^{t}\right)G_{\sigma}\left(\mathbf{x}_{k}^{\mathrm{md}}\right)=\left(\mathbf{H}_{k}\right)^{\mathrm{T}}\mathbf{R}_{k}^{-1}\left(\tilde{\mathbf{z}}_{k}^{t}-\mathbf{H}_{k}\left(\mathbf{x}_{k}-\hat{\mathbf{x}}_{k}^{t}\right)\right)G_{\sigma}\left(\mathbf{z}_{k}^{\mathrm{md}}\right)$$
(2.43)

where $\tilde{\mathbf{z}}_k^t$ denotes the measurement innovation term, i.e., $\tilde{\mathbf{z}}_k^t = \mathbf{z}_k - \mathbf{h}\left(\hat{\mathbf{x}}_k^t\right)$; \mathbf{H}_k denotes the Jacobian matrix of measurement function $\mathbf{h}_k\left(\cdot\right)$ at state vector $\hat{\mathbf{x}}_k^t$. Then, Eq. (2.43) is rearranged as

$$\mathbf{I}_{k}^{p}\mathbf{x}_{k} = \left(\mathbf{H}_{k}\right)^{\mathrm{T}}\mathbf{R}_{k}^{-1}G_{\sigma}\left(\left(\mathbf{z}_{k}^{t}\right)^{\mathrm{md}}\right)\tilde{\mathbf{z}}_{k}^{t} + \mathbf{I}_{k}^{p}\hat{\mathbf{x}}_{k|k-1}$$
(2.44)

where $\mathbf{I}_{k}^{p} = \mathbf{P}_{k|k-1}^{-1} G_{\sigma} \left(\mathbf{x}_{k}^{\text{md}} \right) + \left(\mathbf{H}_{k} \right)^{\text{T}} \mathbf{R}_{k}^{-1} G_{\sigma} \left(\mathbf{z}_{k}^{\text{md}} \right) \mathbf{H}_{k}$. By rearranging Eq. (2.44), it can be obtained as

$$\hat{\mathbf{x}}_k^{t+1} = \hat{\mathbf{x}}_{k|k-1} + \mathbf{G}_k \tilde{\mathbf{z}}_k^t, \tag{2.45}$$

where filter gain is calculated as

$$\mathbf{G}_{k} = \mathbf{P}_{k|k-1} G_{\sigma} \left(\mathbf{x}_{k}^{\text{md}} \right)^{-1} \mathbf{H}_{k}^{\text{T}} \left(\mathbf{H}_{k} \mathbf{P}_{k|k-1} G_{\sigma} \left(\mathbf{x}_{k}^{\text{md}} \right)^{-1} \mathbf{H}_{k}^{\text{T}} + \mathbf{R}_{k} G_{\sigma} \left(\mathbf{z}_{k}^{\text{md}} \right)^{-1} \right)^{-1}$$
(2.46)

Generally, the prior state mean has sufficient accuracy in INMS due to a more accurate SINS error modeling. Thus, the fixed-point iteration is performed only to calculate the measurement correntropy to improve robustness. So G_k is calculated by

$$\mathbf{G}_{k} = \mathbf{P}_{k|k-1}^{xz} \mathbf{C}_{k}^{z} \left(\mathbf{P}_{k|k-1}^{\hat{z}\hat{z}} \mathbf{C}_{k}^{z} + \mathbf{R}_{k} \right)^{-1}, \tag{2.47}$$

where the correntropy matrix is calculated as

$$\mathbf{C}_{k}^{z} = \operatorname{diag}\left[G_{\sigma}\left(\left\|\tilde{\mathbf{z}}_{1,k}^{t}\right\|_{\mathbf{R}_{1,k}^{-1}}^{2}\right), ..., G_{\sigma}\left(\left\|\tilde{\mathbf{z}}_{m,k}^{t}\right\|_{\mathbf{R}_{m,k}^{-1}}^{2}\right)\right]$$
(2.48)

where $\mathbf{R}_{j,k}$ is the j-th diagonal element of \mathbf{R}_k ; $\tilde{\mathbf{z}}_{j,k}^t$ is the j-th element of $\tilde{\mathbf{z}}_k^t$.

Once the solution $\hat{\mathbf{x}}_k^{t+1}$ is obtained by Eq. (2.45), it is brought into Eq. (2.33) for the next iteration. At the end of the iteration, the square-root factor of the error matrix without and with additive measurement noise is calculated separately as

$$\mathbf{D}_{k} = \frac{1}{\sqrt{n_{s}}} \operatorname{qr} \left(\left[\tilde{\mathbf{X}}_{k|k-1} - \mathbf{G}_{k} \tilde{\mathbf{Z}}_{k|k-1} \right]^{\mathrm{T}} \right)$$
 (2.49a)

$$\mathbf{S}_{k} = \frac{1}{\sqrt{n_{s}}} \operatorname{qr}\left(\left[\tilde{\mathbf{X}}_{k|k-1} - \mathbf{G}_{k}\tilde{\mathbf{Z}}_{k|k-1}, \sqrt{n_{s}}\,\mathbf{G}_{k}\mathbf{S}_{k}^{r}\right]^{\mathrm{T}}\right)$$
(2.49b)

where \mathbf{S}_k^r denotes the square-root factor of the measurement noise covariance matrix, i.e., $\mathbf{R}_k = \mathbf{S}_k^r (\mathbf{S}_k^r)^{\mathrm{T}}$. Then, the weighting factor α_k is calculated as

$$\alpha_k = \mathbf{S}_k \mathbf{D}_k^{-1}. \tag{2.50}$$

Then, the state posterior error matrix is calculated for the next period of cubature points update as

$$\tilde{\mathbf{X}}_k = \alpha_k \tilde{\mathbf{X}}_{k|k-1} - \alpha_k \mathbf{G}_k \tilde{\mathbf{Z}}_{k|k-1}. \tag{2.51}$$

Input: $\hat{\mathbf{x}}_0, \mathbf{P}_0, \mathbf{Q}_k, \mathbf{R}_k$; Number of iterations N_m

Algorithm 2: One-time step implementation of proposed MRCKF

Output: $\hat{\mathbf{x}}_k$, $\tilde{\mathbf{X}}_k$ /* Time Update */ 1: $\mathbf{x}_{k-1}^{(i)} = \hat{\mathbf{x}}_{k-1} + \tilde{\mathbf{X}}_{i,k-1}$, for $i = 1, \dots, n_s$ 2: $\hat{\mathbf{x}}_{k|k-1} = \frac{1}{n_s} \sum_{i=1}^{n_s} \chi_{k|k-1}^{(i)} = \frac{1}{n_s} \sum_{i=1}^{n_s} \mathbf{f}_k(\mathbf{x}_{k-1}^{(i)})$ 3: $\mathbf{L}_{k|k-1} = \begin{bmatrix} \chi_{k|k-1}^{(1)} - \hat{\mathbf{x}}_{k|k-1} & \cdots & \chi_{k|k-1}^{(n_s)} - \hat{\mathbf{x}}_{k|k-1} \end{bmatrix}$ 4: $\mathbf{E}_k = \mathbf{S}_{k|k-1} \mathbf{D}_{k|k-1}^{-1} = \operatorname{qr}\left(\left[\mathbf{L}_{k|k-1}, \sqrt{n_s} \mathbf{S}_k^q\right]^{\mathrm{T}}\right) \operatorname{qr}\left(\mathbf{L}_{k|k-1}^{\mathrm{T}}\right)^{-1}$ 5: $\tilde{\mathbf{X}}_{k|k-1} = \mathbf{E}_k \mathbf{L}_{k|k-1}$ /* Measurement Update */ 6: $\mathbf{x}_k^t = \hat{\mathbf{x}}_{k|k-1}$ 7: **for** $i_t = [1:N_m]$ **do** $\mathbf{x}_{k|k-1}^{(i)} = \mathbf{x}^t + \tilde{\mathbf{X}}_{i,k|k-1}, \text{ for } i = 1, \cdots, n_s$ $\hat{\mathbf{z}}_{k|k-1} = \frac{1}{2n} \sum_{i=1}^{2n} \mathbf{z}_{k|k-1}^{(i)} \frac{1}{2n} \sum_{i=1}^{2n} \mathbf{h}_k(\mathbf{x}_{k|k-1}^{(i)})$ 10: $\tilde{\mathbf{Z}}_{k|k-1} = \begin{bmatrix} \mathbf{z}_{k|k-1}^{(1)} - \hat{\mathbf{z}}_{k|k-1} & \cdots & \mathbf{z}_{k|k-1}^{(n_s)} - \hat{\mathbf{z}}_{k|k-1} \end{bmatrix}$ 11: $\mathbf{P}_{k|k-1}^{\hat{z}\hat{z}} = \frac{1}{n_s} \tilde{\mathbf{Z}}_{k|k-1} \tilde{\mathbf{Z}}_{k|k-1}^{\mathrm{T}}$ 12: $\left\| \mathbf{C}_{k}^{z} = \operatorname{diag} \left[G_{\sigma} \left(\left\| \mathbf{\tilde{z}}_{1,k}^{t} \right\|_{\mathbf{R}_{1,k}^{-1}}^{2} \right), ..., G_{\sigma} \left(\left\| \mathbf{\tilde{z}}_{m,k}^{t} \right\|_{\mathbf{R}_{m,k}^{-1}}^{2} \right) \right]$

15: **end**

16:
$$\mathbf{D}_{k} = \frac{1}{\sqrt{n_{s}}} \operatorname{qr} \left(\left[\tilde{\mathbf{X}}_{k|k-1} - \mathbf{G}_{k} \tilde{\mathbf{Z}}_{k|k-1} \right]^{\mathrm{T}} \right)$$
17:
$$\mathbf{S}_{k} = \frac{1}{\sqrt{n_{s}}} \operatorname{qr} \left(\left[\tilde{\mathbf{X}}_{k|k-1} - \mathbf{G}_{k} \tilde{\mathbf{Z}}_{k|k-1}, \sqrt{n_{s}} \mathbf{G}_{k} \mathbf{S}_{k}^{r} \right]^{\mathrm{T}} \right)$$
18:
$$\alpha_{k} = \mathbf{S}_{k} \mathbf{D}_{k}^{-1}$$
19:
$$\tilde{\mathbf{X}}_{k} = \alpha_{k} \tilde{\mathbf{X}}_{k|k-1} - \alpha_{k} \mathbf{G}_{k} \tilde{\mathbf{Z}}_{k|k-1}$$

13: $\mathbf{G}_{k} = \mathbf{P}_{k|k-1}^{xz} \mathbf{C}_{k}^{z} \left(\mathbf{P}_{k|k-1}^{\hat{z}\hat{z}} \mathbf{C}_{k}^{z} + \mathbf{R}_{k} \right)^{-1}$ 14: $\mathbf{\hat{x}}_{k}^{t+1} = \mathbf{\hat{x}}_{k|k-1} + \mathbf{G}_{k} \left(\mathbf{z}_{k} - \mathbf{\hat{z}}_{k|k-1}^{t} \right)$

2.4.3 Adaptive Method for Correntropy Kernel Sizes

The performance of MCC is affected by the kernel size σ . For the same innovation term, a smaller σ results in a smaller eigenvalue of \mathbf{C}_k^z , leading to a reduction of the gain \mathbf{G}_k , which can effectively improve robustness against outliers. However, the filtering performance will be degraded or even diverge in Gaussian noise. Therefore, an appropriate kernel size is critical to balance filter robustness and accuracy. Some adaptive kernel

size methods have been proposed. However, these methods suffer from the excessive convergence of kernel size in INMS. Hence, an adaptive kernel size adjustment method for different noise cases is proposed. First, a theorem is given as follows:

Theorem 2.1. In the presence of outliers, the kernel size has to satisfy an upper bound for the MCC to outperform the MMSE in estimation accuracy.

Proof. The state mean square error based on MCC and MMSE are compared in [104]. The actual state EMSE of MCC is smaller than that of MMSE and has better estimation accuracy when the following conditions are satisfied:

$$\mathbf{R}_k^{\mathsf{t}} \geqslant \mathbf{P}_{\hat{z}\hat{z},k|k-1} + 2\mathbf{R}_k \tag{2.52a}$$

$$\mathbf{R}_{k}^{t} \leqslant \left(\mathbf{C}_{k}^{z}\right)^{-1} \mathbf{P}_{\hat{z}\hat{z}, k|k-1} \mathbf{C}_{k} + 2\mathbf{R}_{k} \left(\mathbf{C}_{k}^{z}\right)^{-1}$$
(2.52b)

where \mathbf{R}_k^t denotes the true measurement noise covariance matrix, which is different from \mathbf{R}_k used by the filter due to the unmodeled outliers. The heavy-tailed distribution caused by outlier interference is simplified to a Gaussian distribution with a larger noise variance to enable subsequent derivation. Then, in the measurement-specific conditions, the *j*-th diagonal element of Eq. (2.52) is extracted and rearranged as follows:

$$\mathbf{P}_{jj,\hat{z}\hat{z},k|k-1} + 2\mathbf{R}_{j,k}G_{\sigma_{j,k}} \left(\left\| \mathbf{\tilde{z}}_{j,k} \right\|_{\mathbf{R}_{j,k}^{-1}}^{2} \right)^{-1} \geqslant \mathbf{R}_{j,k}^{t}$$
 (2.53)

Eq. (2.53) is rearranged to obtain as follows:

$$G_{\sigma_{j,k}}\left(\left\|\tilde{\mathbf{z}}_{j,k}\right\|_{\mathbf{R}_{j,k}^{-1}}^{2}\right) \leqslant \frac{2\mathbf{R}_{j,k}}{\mathbf{R}_{j,k}^{t} - \mathbf{P}_{jj,\hat{z}\hat{z},k|k-1}}$$
(2.54)

Take the negative logarithm of the Eq. (2.54)

$$\frac{\left\|\tilde{\mathbf{z}}_{j,k}\right\|_{\mathbf{R}_{j,k}^{-1}}^{2}}{2\sigma_{j,k}^{2}} \geqslant -\ln\left(\frac{2\mathbf{R}_{j,k}}{\mathbf{R}_{j,k}^{t} - \mathbf{P}_{jj,\hat{z}\hat{z},k|k-1}}\right) \tag{2.55}$$

Since $g = \frac{2\mathbf{R}_{j,k}}{\mathbf{R}'_{j,k} - \mathbf{P}_{jj,\hat{x},k|k-1}} \le 1$, $\ln(g)$ is non-positive, thus Eq. (2.55) can be rearranged as follows:

$$\sigma_{j,k} \leqslant \sqrt{\frac{\left\|\tilde{\mathbf{z}}_{j,k}\right\|_{\mathbf{R}_{j,k}^{-1}}^{2}}{-2\ln(g)}}$$
(2.56)

Therefore, for MCC to outperform MMSE with respect to EMSE, the kernel size must satisfy an upper bound. As the kernel size exceeds the upper bound, the estimation accuracy of MCC decreases due to the weakened robustness to outliers. This is also consistent with the aforementioned theoretical conclusion of kernel size, i.e., MCC degradation to MMSE occurs when the kernel size is too large.

According to Theorem 2.1, the kernel size should be tuned based on the upper bound. However, the upper bound of the right term of Eq. (2.56) cannot be calculated quantitatively because the equivalent MNCM subject to outlier perturbations is unknown. Therefore, to achieve the measurement-specific outlier processing, the kernel size is adjusted by:

$$\sigma_{j,k} = \lambda_{j,k} \cdot \sigma_{\text{max}}, \text{ for } j = 1, 2, \dots, m$$
 (2.57)

where $\lambda_{j,k}$ is the adaptive factor for the *j*-th element of measurement at time-step *k*, i.e., $\mathbf{z}_{j,k}$; σ_{\max} is the setting maximum kernel size (i.e., the upper bound).

According to the definition of the adaptive kernel size, the kernel size can be kept within a reasonable range by restricting the range of $\lambda_{j,k}$, so the adaptive factor must be designed to be appropriately adapted to different noises. Inspired by the chi-squared test, the relationship between the innovation term and its covariance matrix $\mathbf{P}_{zz,k|k-1}$ is considered. $\alpha_{j,k}$ is first formulated as:

$$\alpha_{j,k} = \frac{\mathbf{P}_{zz,k|k-1}}{\left(\tilde{\mathbf{z}}_{j,k}\right)^2} \tag{2.58}$$

where $\mathbf{P}_{jj,zz,k|k-1}$ is the *j*-th diagonal element of the innovation covariance matrix $\mathbf{P}_{zz,k|k-1} = \mathbf{P}_{\hat{z}\hat{z},k|k-1} + \mathbf{R}_k$; $\tilde{\mathbf{z}}_{j,k}$ is the *j*-th element of innovation term $\tilde{\mathbf{z}}_k$, i.e., $\tilde{\mathbf{z}}_{j,k} = \mathbf{z}_{j,k} - \hat{\mathbf{z}}_{j,k|k-1}$. Then the adaptive factor $\lambda_{j,k}$ is calculated by

$$\lambda_{j,k} = 1 - \exp\left(-\alpha_{j,k}\right) \tag{2.59}$$

where $\lambda_{j,k} \in (0,1)$ is positive and bounded. Taking $\lambda_{j,k}$ into Eq. (2.57) to obtain the adaptive kernel size. Then, the correntropy matrix in Eq. (2.48) is reconstructed based on adaptive kernel sizes as

$$\mathbf{C}_{k}^{z} = \operatorname{diag}\left[G_{\sigma_{1,k}}\left(\|\tilde{\mathbf{z}}_{1,k}\|_{\mathbf{R}_{1,k}^{-1}}^{2}\right), ..., G_{\sigma_{m,k}}\left(\|\tilde{\mathbf{z}}_{m,k}\|_{\mathbf{R}_{m,k}^{-1}}^{2}\right)\right]$$
(2.60)

Remark: The proposed adjustment method is analyzed numerically. Fig. 2.1 shows the adaptive kernel size adjustment curve and the corresponding SMD (i.e., measurement weights). As can be seen from Fig. 2.1 that

- (1) Without large outliers disturbances, the residual $\tilde{\mathbf{z}}_{j,k}^2$ is smaller. In this case, the kernel width is kept at a large value, and the measurement weight of MCC is basically the same as that of the MMSE, maintaining a good estimation accuracy. Conversely, in the presence of the outliers, $\tilde{\mathbf{z}}_{j,k}^2$ are large, resulting in smaller kernel size and SMD to suppress the interference of the contaminated measurements on the state estimation.
- (2) The adaptive kernel size is insensitive to the choice of tuning parameter σ_{max} . Suppose σ_{max} is set larger, the innovation $\tilde{\mathbf{z}}_{j,k}$ will be large due to insufficient outlier suppression, which will lead to a decrease in $\lambda_{j,k}$. As a result, the kernel size does not increase as σ_{max} , and becomes smaller to resist the interference of outliers. Therefore, the proposed method is more stable and convenient in selecting the tuning parameter.

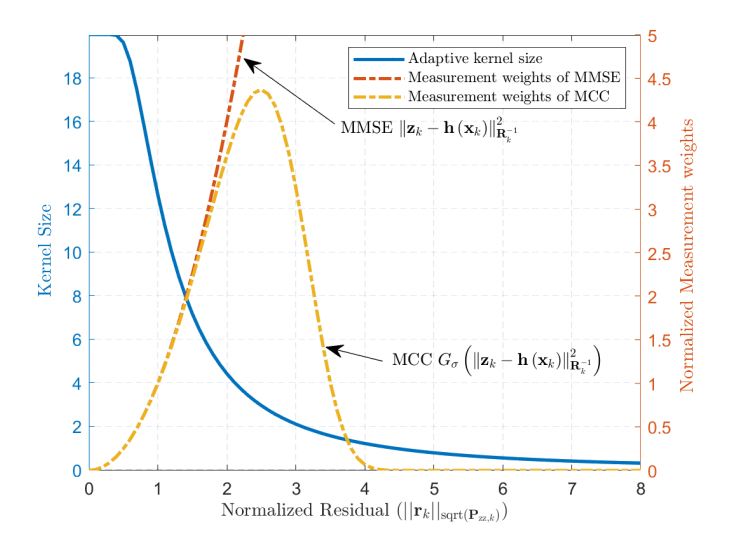


Figure 2.1: Adaptive kernel size and corresponding measurement weights for MMSE and MCC

2.4.4 Algorithm Performance and Complexity Analysis

(1) Estimation accuracy analysis

The estimation accuracy of the proposed RFU framework-based CKF is analyzed. First, the prior cubature points are updated based on Eq. (2.31) to Eq. (2.33) as

$$\mathbf{x}_{k|k-1}^{(i)} = \hat{\mathbf{x}}_{k|k-1} + \mathbf{S}_{k|k-1} \mathbf{D}_{k|k-1}^{-1} \left(\mathbf{f}_k(\mathbf{x}_{k-1}^{(i)}) - \hat{\mathbf{x}}_{k|k-1} \right)$$
(2.61)

Arranging the above equation gives

$$\mathbf{x}_{k|k-1}^{(i)} = \hat{\mathbf{x}}_{k|k-1} + \mathbf{S}_{k|k-1} \lambda_k^{(i)}$$
(2.62)

where $\lambda_k^{(i)} = \mathbf{D}_{k|k-1}^{-1}(\mathbf{f}_k(\mathbf{x}_{k-1}^{(i)}) - \hat{\mathbf{x}}_{k|k-1})$. In addition, the posterior cubature points are updated based on Eq. (2.51) as

$$\mathbf{x}_{k}^{(i)} = \hat{\mathbf{x}}_{k} + \tilde{\mathbf{X}}_{i,k-1} = \hat{\mathbf{x}}_{k} + \alpha_{k} \tilde{\mathbf{X}}_{i,k|k-1} - \alpha_{k} \mathbf{G}_{k} \tilde{\mathbf{Z}}_{i,k|k-1}$$

$$= \hat{\mathbf{x}}_{k} + \alpha_{k} \left(\mathbf{x}_{k|k-1}^{(i)} - \hat{\mathbf{x}}_{k|k-1} \right) - \alpha_{k} \mathbf{G}_{k} \left(\mathbf{z}_{k|k-1}^{(i)} - \hat{\mathbf{z}}_{k|k-1} \right)$$
(2.63)

Then, taking Eq. (2.47) into Eq. (2.63), there gives

$$\mathbf{x}_k^{(i)} = \hat{\mathbf{x}}_k + \mathbf{S}_k \, \boldsymbol{\theta}_k^{(i)} \tag{2.64}$$

where

$$\theta_k^{(i)} = \mathbf{D}_k^{-1} \left(\mathbf{x}_{k|k-1}^{(i)} - \hat{\mathbf{x}}_{k|k-1} \right) - \mathbf{D}_k^{-1} \mathbf{P}_{k|k-1}^{xz} \mathbf{C}_k^z \times \left(\mathbf{P}_{k|k-1}^{\hat{z}\hat{z}} \mathbf{C}_k^z + \mathbf{R}_k \right)^{-1} \left(\mathbf{h}_k \left(\mathbf{x}_{k|k-1}^{(i)} \right) - \hat{\mathbf{z}}_{k|k-1} \right)$$
(2.65)

Then, the GWI based on the sampling points is calculated. In terms of prior estimation as an example, taking a Taylor expansion of $\mathbf{f}_k(\cdot)$ at the mean $\hat{\mathbf{x}}_k$ for $\mathbf{x}_k^{(i)}$ as

$$\mathbf{f}_{k}(\mathbf{x}_{k}^{(i)}) = \mathbf{f}(\hat{\mathbf{x}}_{k}) + \sum_{l=1}^{\infty} \frac{1}{l!} \mathbf{D}_{\mathbf{e}_{i}}^{l} \mathbf{f}_{k}$$
(2.66)

where $\mathbf{D}_{\mathbf{e}_{i}}^{l}\mathbf{f}_{k} = \left[\sum_{j=1}^{n}\mathbf{e}_{i,j}\frac{\partial}{\partial\mathbf{x}_{j}}\right]^{l}\mathbf{f}_{k}(\mathbf{x})\Big|_{\mathbf{x}=\hat{\mathbf{x}}_{k}}$; $\mathbf{e}_{i}=\mathbf{x}_{k}^{(i)}-\hat{\mathbf{x}}_{k}=\mathbf{S}_{k}\boldsymbol{\theta}_{k}^{(i)}$; l is the order of the Taylor expansion; $\partial/\partial\mathbf{x}_{j}$ is the partial derivation of j-th element of the vector \mathbf{x}_{k} . The mean of GWI is then calculated as

$$\hat{\mathbf{x}}_{k|k-1} = E\left[\sum_{i=1}^{n_s} w^{(i)} \mathbf{f}_k \left(\mathbf{x}_k^{(i)}\right)\right] = \mathbf{f}(\hat{\mathbf{x}}) + \frac{1}{2n} \sum_{i=1}^{n_s} \mathbf{D}_{\mathbf{e}_i} \mathbf{f}_k + \mathbf{y}_k^{(2)} + \frac{1}{2n} \sum_{i=1}^{n_s} \mathbf{D}_{\mathbf{e}_i}^3 \mathbf{f}_k + \mathbf{y}_k^{(\text{hom})}$$
(2.67)

where $\mathbf{y}_k^{(2)} = \frac{1}{2n} [\nabla^T \mathbf{S}_k (\sum_{i=1}^{n_s} \boldsymbol{\theta}_k^{(i)} \boldsymbol{\theta}_k^{(i)^T}) \mathbf{S}_k^T \nabla] \mathbf{f}(\hat{\mathbf{x}})$ is the second-order term in the Taylor expansion; The high-order term is denoted as $\mathbf{y}_k^{(\text{hom})} = \frac{1}{2n} \sum_{i=1}^{n_s} \sum_{l=4}^{\infty} \frac{1}{l!} \mathbf{D}_{\mathbf{e}_i}^l \mathbf{f}_k$. In addition, the mean of CKF with symmetrical sampling points is given as

$$\hat{\mathbf{x}}_{k|k-1}^{s} = \mathbf{f}(\hat{\mathbf{x}}) + \mathbf{y}_{k}^{s(2)} + \frac{1}{2n} \sum_{i=1}^{n_{s}} \sum_{l=4}^{\infty} \frac{1}{l!} \mathbf{D}_{\mathbf{e}_{i}^{s}}^{l} \mathbf{f}_{k}$$
 (2.68)

where
$$\mathbf{y}_k^{\mathrm{s}(2)} = \frac{1}{2n} [\nabla^{\mathrm{T}} \mathbf{S}_k (\sum_{i=1}^{n_s} \boldsymbol{\xi}^{(i)} \boldsymbol{\xi}^{(i)}^{\mathrm{T}}) \mathbf{S}_k^{\mathrm{T}} \nabla] \mathbf{f}(\hat{\mathbf{x}}).$$

In the resampling process, ξ_i is constrained to the unit axis, leading cubature points cannot capture the higher-order moment of state PDF. Conversely, as can be seen from Eq. (2.62) and Eq. (2.65), the calcualtion of $\lambda^{(i)}$ and $\theta^{(i)}$ depends on the nonlinear model $\mathbf{f}_k(\cdot)$, $\mathbf{h}_k(\cdot)$ and the correntropy matrix \mathbf{C}_k^z with higher-order moment of measurement.

Furthermore, comparing the Eq. (2.67) and Eq. (2.68), due to the symmetry of the sampling point locations, $\hat{\mathbf{x}}_{k|k-1}^{s}$ offsets the odd order of the Taylor expansion term. On the contrary, $\hat{\mathbf{x}}_{k|k-1}$ preserves odd-order terms due to the asymmetry of the sampling points. Thus, the cubature point set preserves more model and measurement information and has higher estimation accuracy.

(2) Estimation consistency analysis

The estimation consistency is defined as the quantitative conformity of the filter mean square error (MSE) and the actual MSE of state vector [105], which is essential for subsequent integrity monitoring approaches. Therefore, the estimation consistency of the proposed filter is analyzed, and the theorem is given as follows.

Theorem 2.2. In the absence of outliers, the consistency for state a posteriori of MRCKF is comparable to those of MMSE. However, in the presence of fault-biases, MRCKF provides more consistent state a posteriori estimates than MMSE.

Proof. (1) In the absence of outliers, the consistency of state estimation of different methods is compared with an accurate MNCM. The state EMSE at time-step k is denoted as

$$\mathbf{P}_{k}^{\text{mc}} = \mathbf{E}\left[\tilde{\mathbf{x}}_{k}\tilde{\mathbf{x}}_{k}^{\text{T}}\right] = \mathbf{E}\left[\left(\mathbf{x}_{k} - \hat{\mathbf{x}}_{k}\right)\left(\mathbf{x}_{k} - \hat{\mathbf{x}}_{k}\right)^{\text{T}}\right]$$

$$= \mathbf{P}_{k|k-1} - \mathbf{G}_{k}^{\text{mc}}\left(\mathbf{P}_{k|k-1}^{\hat{z}\hat{z}} + \mathbf{R}_{k}\right)\left(\mathbf{G}_{k}^{\text{mc}}\right)^{\text{T}}$$
(2.69)

To linearize $\mathbf{h}_k(\cdot)$ for tractable analysis, the EMSE can be expressed as

$$\mathbf{P}_{k}^{\text{mc}} = (\mathbf{I} - \mathbf{G}_{k}^{\text{mc}} \mathbf{H}_{k}) \mathbf{P}_{k|k-1} (\mathbf{I} - \mathbf{G}_{k}^{\text{mc}} \mathbf{H}_{k})^{\text{T}} + \mathbf{K}_{k} \mathbf{R}_{k} \mathbf{K}_{k}^{\text{T}}$$
(2.70)

where G_k^{mc} is the filtering gain of MRCKF. Further, the EMSE inverse matrix can be expressed based on the matrix inversion lemma as

$$(\mathbf{P}_k^{\text{mc}})^{-1} = (\mathbf{P}_{k|k-1})^{-1} + \mathbf{H}_k^{\text{T}} \mathbf{C}_k^z \mathbf{R}_k^{-1} \mathbf{H}_k$$
 (2.71)

Then, the EMSE inverse matrix of the MMSE-based filter is computed. The filter has the same a priori update as the MRCKF and thus has the same Jacobi matrix \mathbf{H}_k . Therefore, the EMSE inverse matrix is expressed as

$$(\mathbf{P}_k^{\text{me}})^{-1} = (\mathbf{P}_{k|k-1})^{-1} + \mathbf{H}_k^{\text{T}} \mathbf{R}_k^{-1} \mathbf{H}_k$$
 (2.72)

The difference between the inverse EMSE matrices of the two filters is expressed as

$$\left(\mathbf{P}_{k}^{\text{mc}}\right)^{-1} - \left(\mathbf{P}_{k}^{\text{sf}}\right)^{-1} = \mathbf{H}_{k}^{\text{T}} \left(\mathbf{C}_{k}^{z} \mathbf{R}_{k}^{-1} - \mathbf{R}_{k}^{-1}\right) \mathbf{H}_{k}$$
(2.73)

In the absence of outliers, the smaller innovation term makes the correntropy matrix \mathbf{C}_k^z close to a unit matrix, then $\mathbf{C}_k^z\mathbf{R}_k^{-1} - \mathbf{R}_k^{-1} \approx \mathbf{0}$. Thus, $\mathbf{P}_k^{\text{mc}} \approx \mathbf{P}_k^{\text{me}}$, i.e., the consistency for state a posteriori of MRCKF is comparable to those of MMSE.

(2) In the presence of outliers, the estimation consistency of different methods is compared. First, the actual noise covariance matrix is equivalently referred to as \mathbf{R}_k^t . Then, according to Eq. (2.69), the actual state MSE is calculated as

$$\mathbf{P}_{k}^{\text{tmc}} = \mathbf{P}_{k|k-1} - \mathbf{G}_{k}^{\text{mc}} \left(\mathbf{P}_{k|k-1}^{\hat{z}\hat{z}} + \mathbf{R}_{k}^{\text{t}} \right) (\mathbf{G}_{k}^{\text{mc}})^{\text{T}}$$
(2.74)

The state MSE error can be calculated as

$$\Delta \mathbf{P}_{k}^{\text{mc}} = \mathbf{P}_{k}^{\text{mc}} - \mathbf{P}_{k}^{\text{tmc}} = \mathbf{G}_{k}^{\text{mc}} \Delta \mathbf{R}_{k} \left(\mathbf{G}_{k}^{\text{mc}} \right)^{\text{T}}$$
(2.75)

where $\Delta \mathbf{R}_k = \mathbf{R}_k^t - \mathbf{R}_k$. In the same way, the MSE estimation error of the MMSE-based filter is expressed as

$$\Delta \mathbf{P}_{k}^{\text{me}} = \mathbf{P}_{k}^{\text{me}} - \mathbf{P}_{k}^{\text{tme}} = \mathbf{G}_{k}^{\text{me}} \Delta \mathbf{R}_{k} \left(\mathbf{G}_{k}^{\text{me}} \right)^{\text{T}}$$
(2.76)

where $\mathbf{P}_k^{\mathrm{sf}}$ and $\mathbf{P}_k^{\mathrm{tsf}}$ denotes the estimated MSE and actual MSE of state respectively. $\mathbf{G}_k^{\mathrm{sf}}$ is filter gain. Then, the difference between the MSE estimation errors of the two filters is expressed as

$$\delta \mathbf{P}_{k} = \Delta \mathbf{P}_{k}^{\text{mc}} - \Delta \mathbf{P}_{k}^{\text{me}} = \mathbf{G}_{k}^{\text{mc}} \Delta \mathbf{R}_{k} (\mathbf{G}_{k}^{\text{mc}})^{\text{T}} - \mathbf{G}_{k}^{\text{me}} \Delta \mathbf{R}_{k} (\mathbf{G}_{k}^{\text{me}})^{\text{T}}$$
(2.77)

Extract the j-th diagonal matrix element of $\delta \mathbf{P}_k$ for comparison as

$$\delta \mathbf{P}_{j} = \Delta \mathbf{P}_{k,j}^{\text{mc}} - \Delta \mathbf{P}_{k,j}^{\text{me}} = \left(\mathbf{s} \left(\mathbf{G}_{k,j}^{\text{mc}} \right) - \mathbf{s} \left(\mathbf{G}_{k,j}^{\text{me}} \right) \right) \Delta \mathbf{R}_{k}^{\text{d}}$$
(2.78)

where $\mathbf{G}_{k,j}^{\mathrm{sf}}$ and $\mathbf{G}_{k,j}^{\mathrm{mc}}$ denotes the *j*-th column vector of the filter gain; $\mathbf{s}(\cdot) \in \mathbb{R}^{1 \times m}$ is the vector constructed from the squares of each element of the vector; $\Delta \mathbf{R}_k^{\mathrm{d}} \in \mathbb{R}^{m \times 1}$ is a vector constructed from the diagonal elements of $\Delta \mathbf{R}_k$, i.e., $\Delta \mathbf{R}_k^{\mathrm{d}} = \mathrm{diag}(\Delta \mathbf{R}_k)$.

According to Eq. (2.78), in the presence of unmodeled outliers, the measurement noise usually follows a heavy-tailed distribution with second-order moments \mathbf{R}_k^t larger than the

nominal matrix \mathbf{R}_k , which causes each element of $\Delta \mathbf{R}_k^d$ to be greater than 0. Meanwhile, due to the amplification of the \mathbf{C}_k^z for \mathbf{R}_k , the each element of $\mathbf{s}(\mathbf{G}_{k,j}^{\mathrm{mc}})$ are reduced. Therefore, $\delta \mathbf{P}_j$ will be less than 0, i.e., $\Delta \mathbf{P}_{k,j}^{\text{mc}}$ will be less than $\Delta \mathbf{P}_{k,j}^{\text{sf}}$, which means that MRCKF provides more consistent a posteriori state estimates than the MMSE filter.

(3) Computational complexity analysis

The computational complexity of the proposed MRCKF is analyzed in term of the floating-point operations (FLOPs). The following operations are equivalent by FLOPs: For $\mathbf{A} \in \mathbb{R}^{n \times n}$, FLOPs of \mathbf{A}^{-1} and chol(\mathbf{A}) is n^3 and $n^3/3$, respectively; For $\mathbf{A} \in \mathbb{R}^{n \times m}$, FLOPs of QR decomposition based on Householder transformation is $2nm^2 - 2/3m^3$. $\mathbf{f}_k(\cdot)$ and $\mathbf{h}_k(\cdot)$ are surrogated through the linear matrix mapping. The FLOPs for the main filtering parameters are listed in Tab. 2.1. the FLOPs of the proposed MRCKF is determined as

$$F_{MRCKF} = \frac{100}{3}n^3 + (8N_m m + 16m + 2N_m - 1)n^2 + (8N_m m^2 + 2m^2 + 2N_m m - m)n + 3N_m m^3 + 5N_m m$$
(2.79)

where N_m is the number of iterations in MCC. Further, the computation complexity with FLOPs of ISFU are given for comparison as

$$F_{ISUF} = \frac{64}{3}n^3 + (16m + 5)n^2 + (10m^2 + m)n + m^3 + m^2 + m$$
 (2.80)

$F_{ISUF} = \frac{64}{3}n^3 + (16m+5)n^2 + (10m^2 + m)n + m^3 + m^2 + m $ (2)	2.80)
---	-------

Parameter	FLOPs	Parameter	FLOPs
$\mathbf{x}_{k-1}^{(i)}$	$2n^2$	$\mathbf{\tilde{Z}}_{k k-1}$	2mn
$\mathbf{x}_{k k-1}^{(i)}$	$4n^3-2n^2$	$\mathbf{P}_{k k-1}^{xz}$	$4mn^2$
$\mathbf{\hat{x}}_{k k-1}$	$2n^2$	$\mathbf{P}_{k k-1}^{\hat{z}\hat{z}}$	$4m^2n$
$\mathbf{L}_{k k-1}$	$2n^2$	\mathbf{C}_z	5 <i>m</i>
$\mathbf{E}_{k k-1}$	$35/3n^3$	\mathbf{G}_k	$4m^2n - 2mn + 3m^3$
$ ilde{\mathbf{X}}_{k k-1}$	$4n^3-2n^2$	$\mathbf{\hat{x}}_k$	2mn
$\mathbf{x}_{k k-1}^{(i)}$	$2n^2$	\mathbf{S}_k	$10/3n^3 + 6mn^2 + 2nm^2$
$\mathbf{z}_{k k-1}^{(i)}$	$4mn^2 - 2mn$	\mathbf{D}_k	$10/3n^3 + 4mn^2$
$\hat{f z}_{k k-1}$	2mn	$\tilde{\mathbf{X}}_k$	$4n^3 - 2n^2 + 6mn^2 - mn$

Table 2.1: FLOPs for the main filtering parameters

The computational complexity of ISUF and the proposed MRCKF are both $O(n^3)$ and $O(m^3)$. The computational complexity of MRCKF is higher than that of ISUF due to the QR decomposition and fixed-point iteration. However, due to the high accuracy of the state model constructed with the SINS error equations in INMS, the initial state in the fixed-point iteration is more accurate, allowing the iterations to quickly converge to an optimal solution in a few cycles, reducing the computational burden.

2.5 Simulation Verification Experiment

This section presents a verification of the proposed algorithm through simulation experiments. First, the simulation conditions are established, including the maneuvering trajectory, sensor specifications and noise distribution, filter parameters, and performance evaluation indexes. The INMS filter model is constructed in Appendix B. Finally, the simulation results of the proposed algorithm are analyzed.

2.5.1 Simulation Condition Setting

(1) Maneuvering Track: The initial kinematic state of the carrier is set. Initial position latitude $L=45.73^\circ$, longitude $\lambda=126.63^\circ$, altitude $h=149.05\,\mathrm{m}$; Initial velocity $0\,\mathrm{m/s}$; Initial horizontal attitude $\theta=0^\circ$, $\gamma=0^\circ$, and the initial heading is $\psi=-10^\circ$. Initial misalignment angle is set to $\phi_e=30'$, $\phi_n=30'$, $\phi_u=180'$. Then, the carrier motion is simulated, and the trajectory and kinematic parameters are shown in Fig. 2.2.

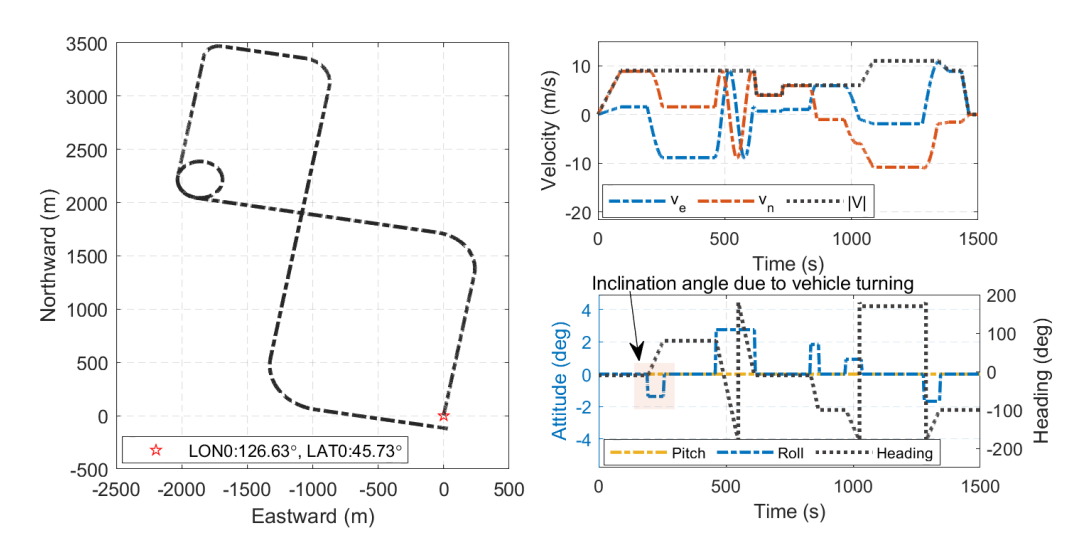


Figure 2.2: The trajectory of the carrier and the corresponding kinematic parameters

(2) Sensor Specification and Noise: According to the kinematic parameters, the specific force, angular velocity, forward velocity, heading, etc., are obtained through the

inverse SINS algorithm. Then, the sensor output is simulated based on the observation model. The specification parameter settings of each sensor are shown in Tab. 2.2.

Sensor	Specification	Index		
IMU -	Gyro constant bias	10°/h		
	Angular random walk	$1^{\circ}\sqrt{h}$		
	Acc. constant bias	200 μg		
	Velocity random walk	$20\mu\mathrm{g}/\sqrt{\mathrm{Hz}}$		
Odometer	Scale factor error	0.01		
	Installation error	[60';60';180']		
	Velocimetry accuracy	1%		
GNSS	Horizontal positioning accuracy	5 m (1σ)		
Polarizer	Heading accuracy	1° (1σ)		

Table 2.2: Specifications of sensors

In order to verify the proposed algorithm's effectiveness in noise assumption mismatch, the sensors are simulated to be disturbed by different types of non-Gaussian noise. First, the GNSS and odometer are disturbed by outliers. The noise exhibit a heavy-tailed distribution, and the probability density are denoted as

$$p\{\mathbf{w}_k\} = (1 - p_{\text{disb}}) N(0, \mathbf{R}_k) + p_{\text{disb}} N(0, 25 \mathbf{R}_k)$$
 (2.81)

where $p_{\rm disb}$ denotes the probability of outliers disturbances; $\mathbf{R}_k = {\rm diag} \left(\mathbf{r}_k\right)^2$ are the noise covariance matrix. In terms of GNSS, it is disturbed by outliers with probability $p_{\rm disb} = 0.2$ during the simulation from 200 s to 700 s; and with probability $p_{\rm disb} = 0.4$ during the simulation from 1000 s to 1300 s. In addition, $\mathbf{r}_k = [5\text{m} 5\text{m}]$ denotes the standard deviation of the GNSS latitude and longitude noise based on the sensor specification. OD is subject to the probability $p_{\rm disb} = 0.05$ for the outlier interference. $\mathbf{r}_k^{\rm od} = 0.01\,\mathbf{v}_{\rm od}$ based on the sensor specification, where $\mathbf{v}_{\rm od}$ is the odometer velocity.

Further, the polarized heading is affected not only by the sensor noise but also by the external horizontal inclination and solar elevation angle, and so on. Therefore, the sensor noise is modeled based on the Markov process [106, 107, 108], and the probability distribution is expressed as follows.

$$p\left\{\mathbf{w}_{k}\right\} = \left(1 - p_{\text{disb}}\right) N_{\text{mr}}\left(0, t_{\text{au}}, \mathbf{R}_{k}\right) + p_{\text{disb}} N_{\text{mr}}\left(0, 9\,\mathbf{R}_{k}\right)$$
(2.82)

where $N_{mr}(t,\Sigma)$ is a first-order Markov process sequence with correlation time t and covariance Σ . The correlation time is set to $t_{au}=10$ s, and the heading noise variance is set $\mathbf{R}_k=1\,\mathrm{deg}^2$ based on the sensor specification. According to the noise distribution settings, the noise and probability density distribution are shown in Fig. 2.3.

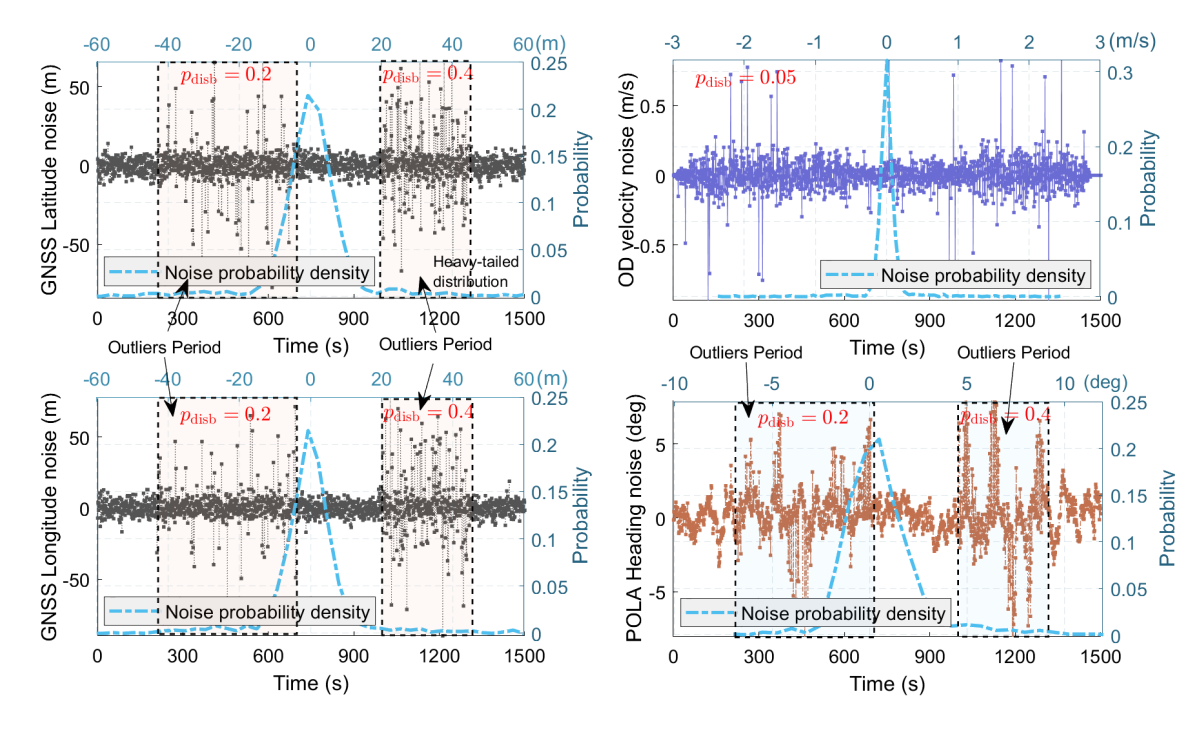


Figure 2.3: Sensor noise and probability density distribution

(3) Filter Settings: The system state is estimated by a filter based on the model established in Appendix B. The time update frequency of the filter is set to 100 Hz, the same as the IMU output frequency; the measurement update frequency of the GNSS position is set to 1 Hz; the measurement update frequency of the odometer velocity is set at 10 Hz; and the measurement update frequency of the polarizer heading is set to 1 Hz.

The proposed MRCKF is compared with the following existing classical methods mentioned in the research review to verify the effectiveness: 1) CKF; 2) RFU-Cubature Kalman Filter (RFCKF), i.e., ISUF framework [31] combined with CKF; 3) RSTKF [38]; 4) HMKF [36]; 5) MCKF [45, 109] that adopts the proposed kernel size adaptive method. The tuning parameters of the above filters are set empirically as follows: The degree-of-freedom in the RSTKF is set to $\sigma = 6$; the tuning parameter in the HMCKF is set to $\tau = 1.345$; the upper bound on the kernel size is set to $\tau = 1.345$; the upper bound is the upper bound of the upper bound of the upper bound is t

initial state mean-square error matrix P_k of the above filter are set as follows

$$\mathbf{P}_{k} = \operatorname{diag}\left(\left[\phi_{k} \ \delta \mathbf{v}_{k} \ \delta \mathbf{p}_{k} \ \varepsilon \ \nabla \ \delta \mathbf{x}_{k}^{\operatorname{od}}\right]^{\mathrm{T}}\right)^{2}$$
(2.83a)

$$\mathbf{Q}_{k} = \operatorname{diag}\left(\left[\boldsymbol{\varepsilon}_{r} \ \nabla_{r} \ \mathbf{0}_{1\times9}\right]^{T}\right)^{2} \tag{2.83b}$$

$$\mathbf{R}_{k} = \operatorname{diag}\left(\left[\mathbf{r}_{k}^{\text{gnss}} \ \mathbf{r}_{k}^{\text{od}} \ \mathbf{r}_{k}^{\text{pola}}\right]^{\mathrm{T}}\right)^{2}$$
(2.83c)

where $\varepsilon_{\rm r} = [1^{\circ}\sqrt{\rm h}\ 1^{\circ}\sqrt{\rm h}\ 1^{\circ}\sqrt{\rm h}]^{\rm T}; \nabla_{\rm r} = [20\,\mu{\rm g}/\sqrt{\rm Hz}\ 20\,\mu{\rm g}/\sqrt{\rm Hz}\ 20\,\mu{\rm g}/\sqrt{\rm Hz}]^{\rm T}; \phi_k = [30'\ 30'\ 180']^{\rm T}; \delta\mathbf{v}_k = [0.1\,{\rm m/s}\ 0.1\,{\rm m/s}\ 0.1\,{\rm m/s}]^{\rm T}; \delta\mathbf{p}_k = [10\,{\rm m}\ 10\,{\rm m}\ 10\,{\rm m}]^{\rm T}; \varepsilon = [10^{\circ}/{\rm h}\ 10^{\circ}/{\rm h}\ 10^{\circ}/{\rm h}]^{\rm T}; \nabla = [200\,\mu{\rm g}\ 200\,\mu{\rm g}\ 200\,\mu{\rm g}]^{\rm T}; \delta\mathbf{x}_k^{\rm od} = [60'\ 0.1\ 180']^{\rm T}; \mathbf{r}_k^{\rm gnss} = [5\ 5\ {\rm m}]^{\rm T}; \mathbf{r}_k^{\rm od} = 0.1\,{\rm m/s}; \mathbf{r}_k^{\rm pola} = 1\,{\rm deg}.$

(4) Evaluation Indicators: To compare the state estimation performance of the proposed filter and other filters, 30 Monte Carlo (MC) tests are performed in this simulation to eliminate the randomness of the experiment results (the sensor noise varies for each MC simulation). The root mean square error (RMSE) and the averaged root mean square error (ARMSE), which are usually based on the results of multi-group MC tests, are used as evaluation metrics of the state estimation accuracy[103, 65, 110], which is defined as

$$RMSE_k = \sqrt{\frac{1}{N_{mc}} \sum_{s=1}^{N_{mc}} (\hat{\mathbf{x}}_k^s - \mathbf{x}_k^s)^2}$$
 (2.84a)

ARMSE =
$$\sqrt{\frac{1}{N_t N_{\text{mc}}} \sum_{k=1}^{N_t} \sum_{s=1}^{N_{\text{mc}}} (\hat{\mathbf{x}}_k^s - \mathbf{x}_k^s)^2}$$
 (2.84b)

where N_{mc} is the number of MC trials; N_{t} is the total number of states; $\hat{\mathbf{x}}_{k}^{s}$ and \mathbf{x}_{k}^{s} are the estimated state and the actual state at time-step k, respectively.

In addition, when comparing and analyzing the simulation results: i) Since the attitude and velocity errors are integrated into the position error, the position estimation can reflect the overall estimation effect to some extent. Therefore, the simulation analysis focuses on the RMSE (or ARMSE) of the horizontal position to reflect the estimation performance of different filtering algorithms; ii) To more intuitively compare the estimation effects of different filters, the percentage increase in ARMSE is used as a relative comparison indicator. For example, if x is p% higher than y, then $p = abs(x - y)/y \times 100\%$.

2.5.2 Simulation Results and Analysis

This section verifies the proposed algorithm. Since the kernel size is employed in the robust RFU filtering framework, the proposed adaptive kernel size method is initially validated. Next, the proposed robust RFU filtering framework is validated.

(1) Analysis and validation of the proposed adaptive kernel size method

Fig. 2.4 shows the adaptive kernel size of the existing and proposed adjustment methods, where the existing Methods 1 and 2 are proposed in [52] and [53], respectively. The noise characteristics for GNSS latitude are similar to those for longitude, so the analysis of its adaptive kernel size is not included here. The cumulative probability distribution of the adaptive kernel size of the proposed method is shown in Fig. 2.5 . In addition, the influence of the tuning parameter of the proposed adaptive kernel size method (i.e., the upper bound σ_{max}) is analyzed. Fig. 2.6 shows the ARMSE of the horizontal position estimation of the MRCKF with different upper bounds σ_{max} . Meanwhile, the results of the horizontal position estimation of the MRCKF with different fixed kernel sizes are also shown in Fig. 2.6 .

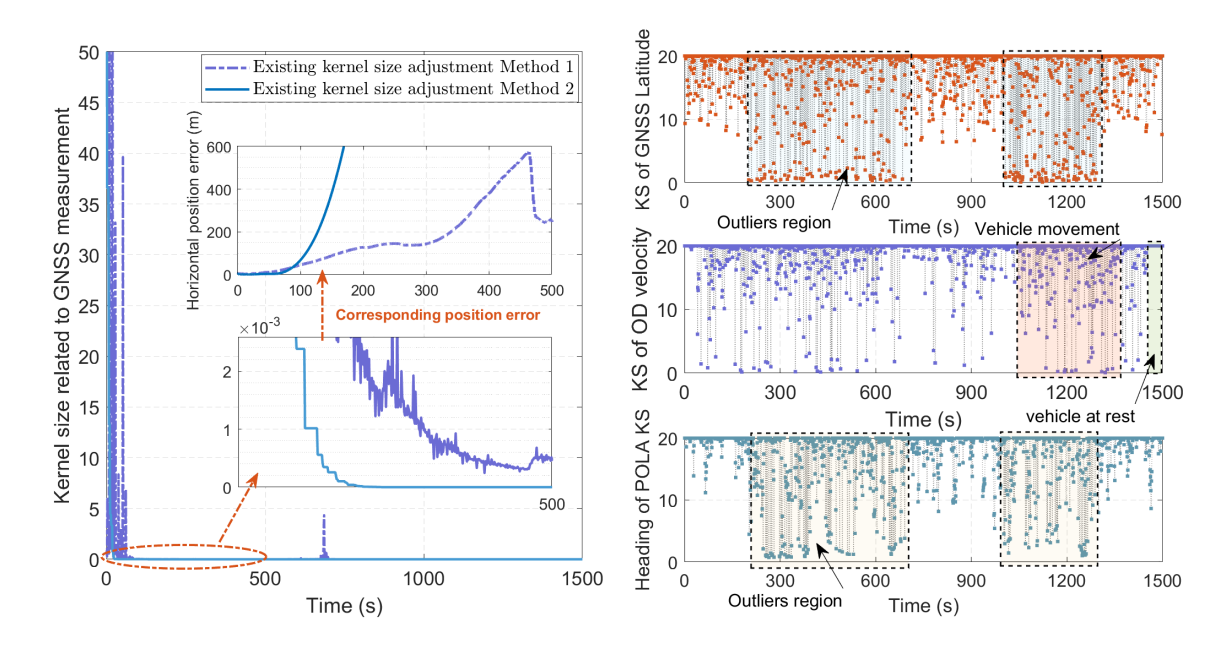


Figure 2.4: Comparison of existing and proposed adaptive kernel size method

As can be seen from Fig. 2.4, due to the direct use of the state mean square error (MSE) of the filter, the kernel size in the existing Method 1 quickly converges to a smaller value before the MSE has fully converged during the initial filtering phase. Similarly,

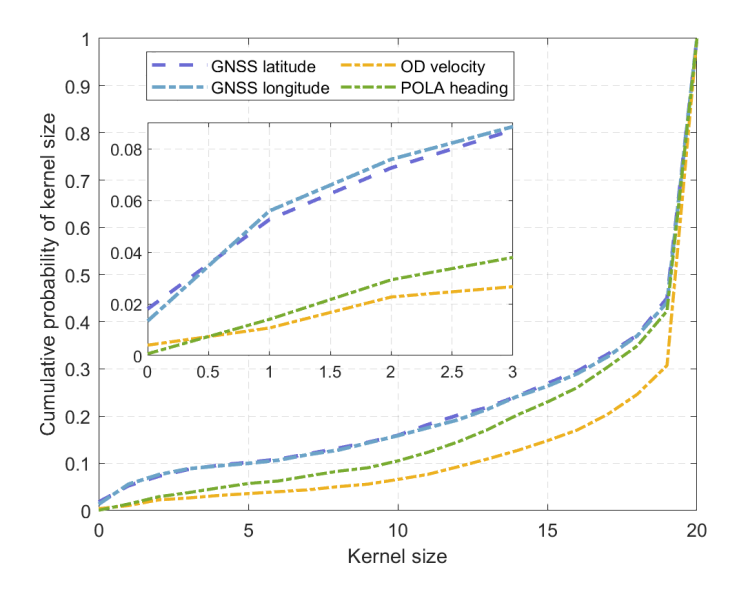


Figure 2.5: Cumulative probability distribution for the adaptive kernel size of the proposed method

in Method 2, the kernel size also converges quickly and remains small due to the monotonically decreasing adjustment of the adaptive factor, leading to the problem of overconvergence. This over-convergence problem causes the kernel size to lose its subsequent adjustment capability, which reduces the weight of useful measurement information in the state estimation, ultimately resulting in the divergence of the filter estimation. In contrast, the proposed method can effectively adjust the kernel size according to different noise cases, thus avoiding the over-convergence problem. For example, due to the vehicle velocity affecting the magnitude of odometer measurement noise, the OD is not disturbed by measurement outliers when the vehicle is stationary (e.g., from 1450 s to 1500 s). At this time, the corresponding kernel size remains large (close to the upper bound), which ensures the estimation accuracy. Conversely, when the vehicle is in motion (e.g., from 1100 s to 1300 s, when the vehicle velocity is at its maximum), the OD is frequently perturbed by significant measurement outliers, resulting in a smaller kernel size to enhance the robustness against outliers. Similarly, in the presence of GNSS and POLA outliers, the kernel size also generally decreases to suppress outliers interference.

In addition, the cumulative probability distribution of the adaptive kernel width is analyzed. As shown in Fig. 2.5, for the proposed adaptive kernel size method, the smaller kernel widths (generally less than 3) for each measurement are on the order of 10^{-2} throughout the experiment, which is consistent with the actual outlier interference settings. Furthermore, the cumulative probability of smaller kernel size values for GNSS measurements is higher than that for OD and POLA, indicating that GNSS is relatively more frequently

subjected to significant outlier interference, which is consistent with the set probabilities and magnitudes of outliers for each measurement. Therefore, the result further validates the effectiveness of the proposed adaptive kernel size method.

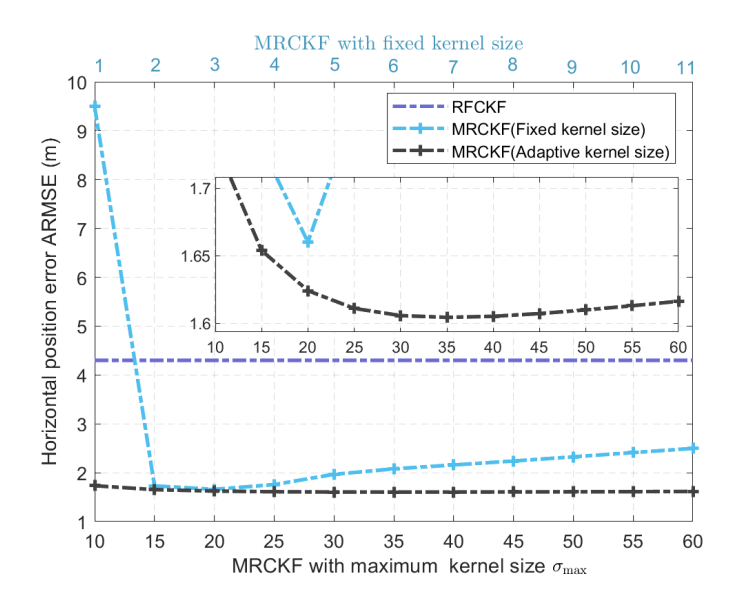


Figure 2.6: Horizontal position ARMSE corresponding to different tuning parameters

Furthermore, an analysis of the effect of the tuning parameters on the proposed adaptive kernel size method was performed. As shown in Fig. 2.6, different kernel sizes significantly affect the estimation performance without the online kernel size optimization. Both excessively large and tiny kernel sizes would reduce the filter estimation accuracy, with an ARMSE range (difference between the maximum and minimum values) reaching 7.834 m. In contrast, the choice of the kernel size upper bound σ_{max} slightly impacts the estimation performance of the proposed filter. Within the interval [10, 60], the estimation accuracy remains relatively stable, with an ARMSE range of 0.129 m. This stability is due to the fact that when σ_{max} is set larger, it leads to insufficient suppression of outliers by the MCC. Consequently, the innovation will inevitably be disturbed and increase. However, the increase in innovation will cause the adaptive factor $\lambda_{j,k}$ to decrease, which prevents the adaptive kernel size from increasing with σ_{max} , and will maintain a relatively small kernel size to suppress the outliers interference on state estimation to some extent. Therefore, the proposed filter demonstrates good stability and convenience in selecting the tuning parameters.

(2) Analysis and validation of the proposed robust RFU filter

Fig. 2.7, Fig. 2.8, and Fig. 2.9 show the RMSE of the vehicle's attitude, velocity, and position estimated by various filters, respectively. Considering that the horizontal position

error can reflect the overall state estimation performance, Fig. 2.10 presents the RMSE of horizontal position estimation and its cumulative probability distribution. Additionally, the ARMSE of each navigation parameter throughout the simulation is listed in Tab. 2.3 . Further, Fig. 2.11 provides the horizontal position ARMSE in different simulation intervals to analyze the estimation performance for various noise cases. In addition, Fig. 2.12 shows the computation time for each filtering epoch for the different filters.

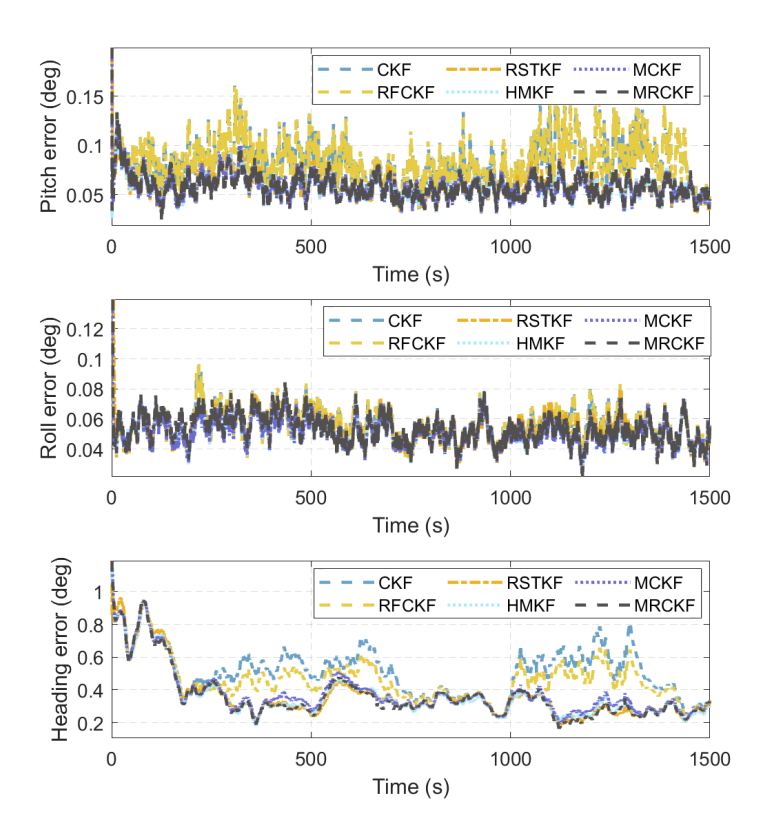


Figure 2.7: Attitude and heading estimation RMSE

As can be seen from Fig. 2.7 to Fig. 2.11 and Tab. 2.3, the heading and position navigation parameters ARMSE of the RFCKF are smaller than CKF, indicating that the estimation accuracy of RFCKF is improved to a certain extent over CKF. This improvement is due to the fact that, unlike CKF, which discards non-Gaussian higher-order moment information during Gaussian reconstruction, RFCKF removes the Gaussian assumption by resampling-free update, thereby avoiding the loss of higher-order moment information in the original state distribution caused by Gaussian reconstruction. As a result, RFCKF exhibits better estimation accuracy compared to CKF in the case of Gaussian assumption mismatch induced by the INMS nonlinear measurement function mapping.

Then, as shown in Fig. 2.11, compared to CKF and RFCKF, the navigation parameter errors of the robust filters RSTKF and HMKF are significantly reduced in the presence of

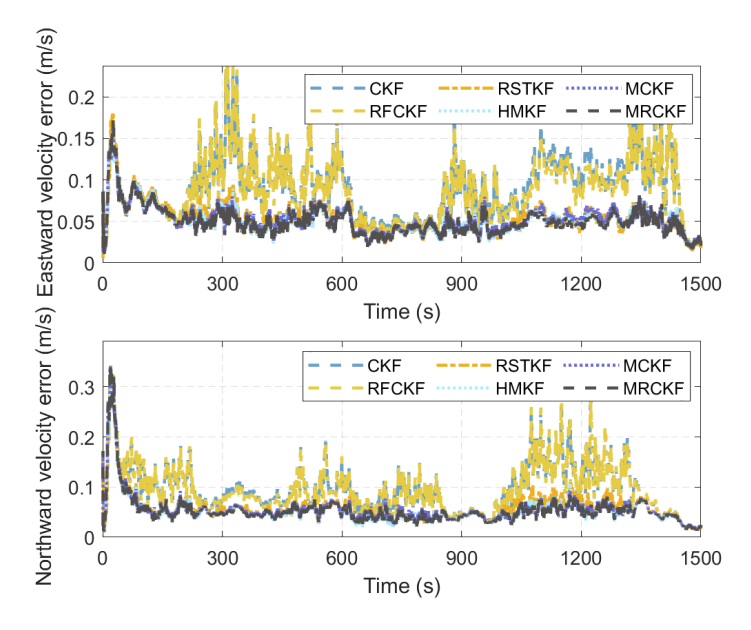


Figure 2.8: Velocity estimation RMSE

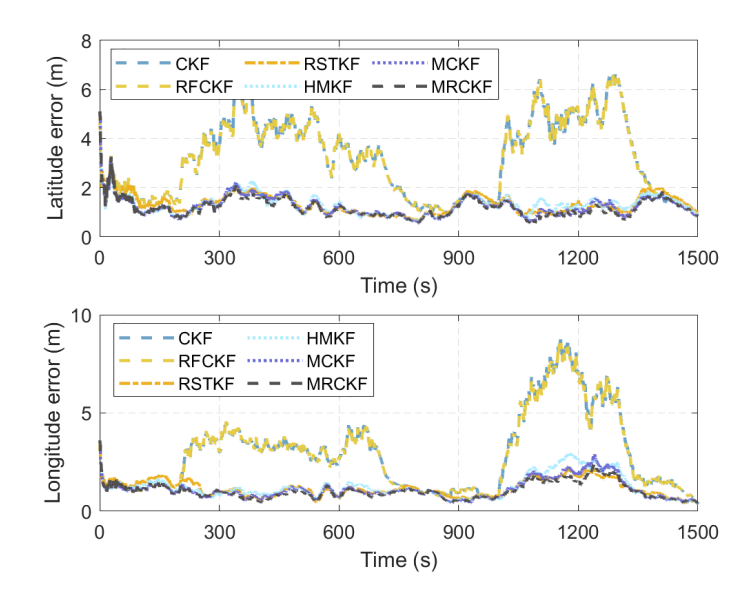


Figure 2.9: Position estimation RMSE

outliers, indicating that the robust filters effectively suppress the interference of measurement outliers on state estimation. Due to the truncation effect of the MCC based proposed adaptive kernel size method, the horizontal position ARMSE of MCKF (1.899 m) is lower than that of RSTKF (1.955 m) and HMKF (2.115 m) during the outlier interference interval. Furthermore, MRCKF based on MCKF, through the resampling-free framework based on adaptive MCC, not only enhances the robustness of the estimation, but also more effectively utilizes the higher-order moment information in the sampling points distribution and measurement data. This results in a reduction of the horizontal position ARMSE to

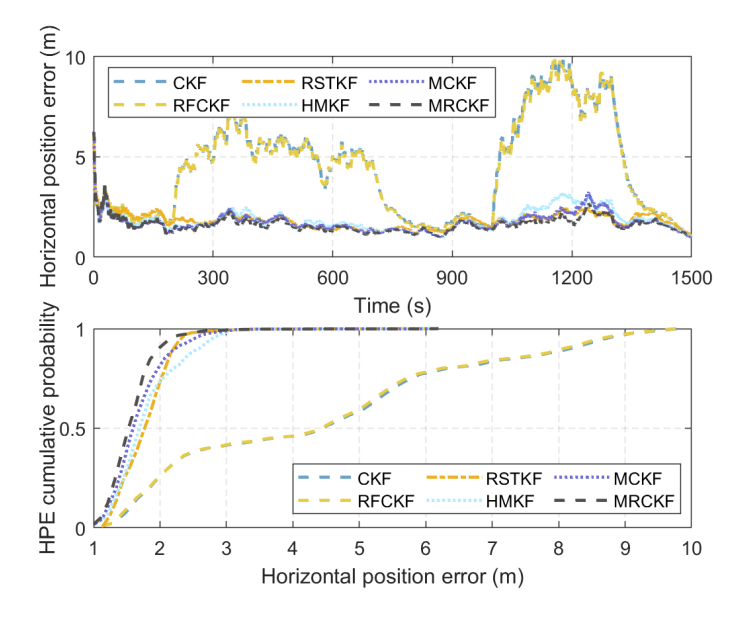


Figure 2.10: Horizontal position estimation RMSE and its cumulative probability distribution

1.684 m during the simulation interval with outlier interference, which is a reduction of 13.9%, 20.4%, and 11.3% compared to RSTKF, HMKF, and MCKF, respectively. Additionally, the cumulative probability of the horizontal position error of MRCKF within 2 m throughout the simulation is the highest at 90.2%, compared to 74.8% for RSTKF, 74.8% for HMKF, and 82.1% for MCKF. Therefore, the above analysis verifies the effectiveness of the proposed improved robust RFU framework-based MRCKF.

In addition, in the outlier interference cases, the position ARMSE of CKF and RFCKF based on the MMSE resampling-free update framework are 6.431 m and 6.370 m, respectively. The accuracy improvement of RFCKF over CKF is relatively small. However,

ARMSE	Pitch	Roll	Heading	Vel.E.	Vel.N.	Lati.	Longi.	HPE
	(deg)	(deg)	(deg)	(m/s)	(m/s)	(m)	(m)	(m)
CKF	0.083	0.056	0.515	0.090	0.095	3.570	3.532	5.021
RFCKF	0.083	0.056	0.465	0.088	0.093	3.541	3.487	4.964
RSTKF	0.059	0.053	0.365	0.053	0.057	1.393	1.235	1.863
HMKF	0.058	0.052	0.365	0.052	0.053	1.366	1.348	1.916
MCKF	0.058	0.052	0.380	0.052	0.053	1.310	1.218	1.791
MRCKF	0.058	0.052	0.363	0.049	0.050	1.248	1.107	1.657

Table 2.3: Navigation parameter estimation ARMSE in simulation

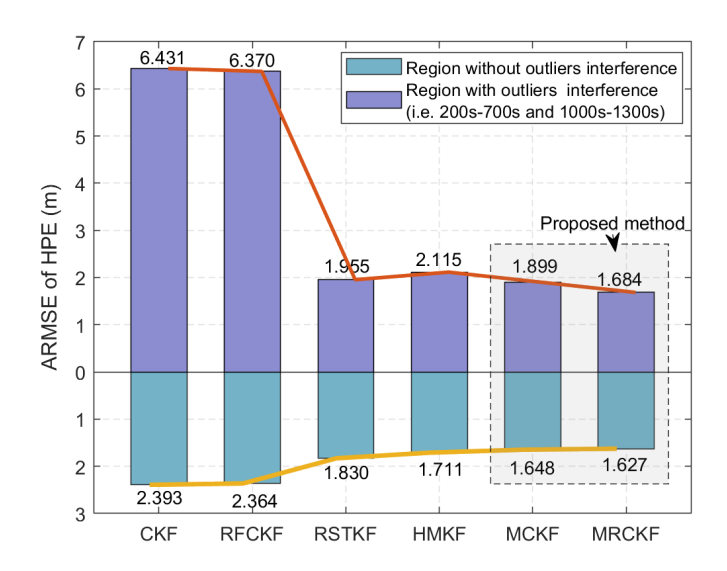


Figure 2.11: Horizontal position error ARMSE for each filter under different noises

through the proposed resampling-free update framework, MRCKF improves the estimation accuracy by 11.3% compared to MCKF, indicating a higher degree of performance improvement. It is shown that with the MCC optimization criteria, the non-Gaussian moment information retained by the resampling-free update is more effectively utilized, which further validates the effectiveness of the proposed MCC-based resampling-free update framework.

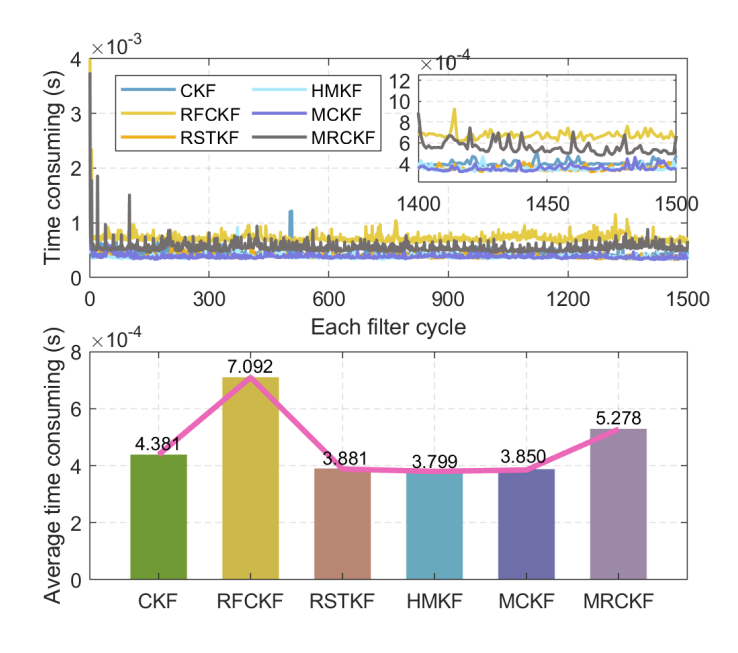


Figure 2.12: Time consuming for each filtering cer of different filters

Finally, Fig. 2.12 visually quantifies the computational burden of different filters. As

shown in Fig. 2.12, under the current computer hardware configuration (CPU Intel Core i7-12700H), although the MRCKF based on the proposed RFU framework has a higher time consumption compared to other filters (except RFCKF), it still meets real-time computational requirements. It is noteworthy that, unlike the theoretical complexity analysis based on FLOPs, the computational time includes both the computational complexity of the filter and data quality factors (e.g., longer decomposition time of the state mean square error matrix under outlier interference). Therefore, the time consumption of MCKF combined with the proposed kernel size adaptive method is lower compared to CKF.

2.6 Summary

This chapter addresses the problem of INMS state estimation performance degradation due to the mismatched noise assumptions in urban areas. First, the principles of navigation state estimation and resampling-free filtering are formulated. Then, a robust RFU filter based on the adaptive kernel-sizes MCC is proposed to address the limitations of RFU in INMS. The cost function of the resampling-free estimation framework is constructed based on the MCC, which effectively exploits the non-Gaussian moments of the non-closed state distribution, ensuring the optimality of the resampling-free estimation and preventing the loss of the higher-order moment information from the Gaussian reconstruction. An adaptive kernel size method is developed to realize the online optimal adjustment of the kernel size while maintaining robustness against outliers.

Finally, simulation experiments validate the proposed adaptive kernel size method and the robust MCC-based RFU filter. The experimental results indicate that: 1). Compared to existing methods, the proposed adaptive kernel size method can effectively adjust the kernel size for different noise cases while avoiding the over-convergence problem. Furthermore, the cumulative distribution probability of smaller kernel sizes is consistent with the outlier occurrence probability settings. Within the interval of kernel size upper bound [10, 60], the range of position ARMSE for MRCKF is 0.129 m, maintaining relatively stable estimation accuracy. It exhibits good stability in tuning parameter selection, validating the effectiveness of the proposed adaptive kernel size method; 2). In the presence of outliers (not the whole experiment), the position ARMSE of proposed MRCKF is reduced by 13.9%, 20.4%, and 11.3% compared to the existing robust RSTKF, HMKF and MCKF, respectively. Additionally, the cumulative probability of position estimation error within 2 m throughout the simulation is 90.2%, which is higher than RSTKF (74.8%), HMKF (74.8%), and MCKF (82.1%), indicating better robust estimation performance. It validates the effectiveness of the proposed robust MCC-based RFU framework.

Chapter 3

Robust Noise Adaptation Algorithm for Measuring Outliers Interference

3.1 Introduction

As a crucial factor affecting autonomous driving performance, navigation reliability and safety are technically subject to system-state robust estimation and integrity monitoring. Both techniques rely on accurately known prior knowledge of sensor noise, i.e., MNCM. In INMS applications, the MNCM is typically unknown or time-varying due to the variable measurement conditions outside the sensors. Existing adaptive filters can accurately estimate the MNCM under Gaussian noise. However, frequent signal blocks and outliers result in non-Gaussian heavy-tailed noise distributions in dense urban areas, so the MNCM cannot be estimated accurately. An inaccurate MNCM can reduce robust estimation accuracy due to model-actual mismatch and interfere with effective integrity monitoring, potentially severely impacting autonomous driving function. Outlier elimination techniques cannot ensure effective noise adaptation. In contrast, robust enhancement methods can prevent the loss of valuable information and improve noise adaptation performance. However, the Gaussian conjugate IW distribution used in existing robust noise-adaptive methods does not accurately represent the MNCM of non-Gaussian noise, resulting in suboptimal robust MNCM estimation under outlier disturbances.

This chapter presents a robust noise adaptation algorithm to suppress outlier interference in the MNCM estimation. First, the problem of INMS noise adaptation is formulated. The joint variational approximation principle is introduced, and its limitation in INMS is analyzed. Then, a robust variational approximation adaptation algorithm based on MCC is proposed. A joint variational approximation analytical solution for the MNCM and smoothing state is derived. The inverse scale matrix of the IW distribution is reconstructed based on the correntropy matrix to suppress the interference of measurement outliers on the MNCM estimation. Finally, simulation experiments are conducted to verify the effectiveness of the proposed method.

3.2 Analysis of the INMS Noise Adaptation Problem

In INMS, the inertial navigation error is generally used as the primary state vector to construct the system model. Since the state kinetic model built by the inertial navigation error equations is relatively accurate, the process noise has little effect on the estimation performance. Due to computational efficiency and coupling issues, only the measurement noise of the external sensors is usually concerned. However, the performance of each external sensor is affected by the observation environment, resulting in a difference between the nominal specifications of the sensor and its actual measurement accuracy in practical applications. When reflected in the system state-space model, this difference implies that the MNCM is unknown or time-varying. Therefore, this section analyzes the impact of MNCM errors on state estimation and integrity monitoring. For simplicity, the linear KF is used as an example to facilitate the analysis process, which does not affect the qualitative analysis results.

First, the nominal and actual MNCM are denoted as \mathbf{R}_k and \mathbf{R}_k^t at time-step k, respectively. The relationship is expressed as $\mathbf{R}_k = \mathbf{R}_k^t + \Delta \mathbf{R}_k$, where $\Delta \mathbf{R}_k$ is the MNCM error. Then, the KF filter gain is redefined as

$$\mathbf{G}_{k} = \mathbf{P}_{k|k-1} \mathbf{H}_{k}^{\mathrm{T}} \left(\mathbf{H}_{k} \mathbf{P}_{k|k-1} \mathbf{H}_{k}^{\mathrm{T}} + \mathbf{R}_{k}^{\mathrm{t}} + \Delta \mathbf{R}_{k} \right)^{-1}$$
(3.1)

Assuming $\mathbf{N}_k = \mathbf{H}_k \mathbf{P}_{k|k-1} \mathbf{H}_k^{\mathrm{T}} + \mathbf{R}_k^{\mathrm{t}}$, it can be obtained according to the principle of matrix inversion as follows

$$(\mathbf{N}_k + \Delta \mathbf{R}_k)^{-1} = \mathbf{N}_k^{-1} - \mathbf{C}_k \tag{3.2}$$

where $\mathbf{C}_k = (\mathbf{N}_k + \Delta \mathbf{R}_k)^{-1} \Delta \mathbf{R}_k \mathbf{N}_k^{-1}$. Thus, Eq. (3.1) is rearrange as

$$\mathbf{G}_{k} = \mathbf{P}_{k|k-1} \mathbf{H}_{k}^{\mathrm{T}} \left(\mathbf{N}_{k}^{-1} - \mathbf{C}_{k} \right) = \mathbf{G}_{k}^{\mathrm{t}} + \Delta \mathbf{G}_{k}^{\mathrm{t}}$$
(3.3)

where $\Delta \mathbf{G}_k^{\mathrm{t}} = -\mathbf{P}_{k|k-1}\mathbf{H}_k^{\mathrm{T}}\mathbf{C}_k$. The posterior mean of the state is calculated as

$$\hat{\mathbf{x}}_k = \hat{\mathbf{x}}_{k|k-1} + \mathbf{G}_k^{\mathsf{t}} \tilde{\mathbf{z}}_k + \Delta \mathbf{G}_k \tilde{\mathbf{z}}_k \tag{3.4}$$

As a result, the posterior state estimation error caused by $\Delta \mathbf{R}_k$ is formulated as

$$\Delta \hat{\mathbf{x}}_k = -\mathbf{P}_{k|k-1} \mathbf{H}_k^{\mathrm{T}} \left(\mathbf{N}_k + \Delta \mathbf{R}_k \right)^{-1} \Delta \mathbf{R}_k \mathbf{N}_k^{-1} \tilde{\mathbf{z}}_k$$
(3.5)

Furthermore, the effect of $\Delta \mathbf{R}_k$ on the posterior EMSE \mathbf{P}_k is analyzed. If $\mathbf{P}_k =$

 $(\mathbf{I} - \mathbf{G}_k^{\mathsf{t}} \mathbf{H}_k) \mathbf{P}_{k|k-1} - (\Delta \mathbf{G}_k \mathbf{H}_k) \mathbf{P}_{k|k-1} = \mathbf{P}_k^{\mathsf{t}} + \Delta \mathbf{P}_k$, then the EMSE error caused by $\Delta \mathbf{R}_k$ is calculated as follows

$$\Delta \mathbf{P}_k = \mathbf{P}_{k|k-1} \mathbf{H}_k^{\mathrm{T}} (\mathbf{N}_k + \Delta \mathbf{R}_k)^{-1} \Delta \mathbf{R}_k \mathbf{N}_k^{-1} \mathbf{H}_k \mathbf{P}_{k|k-1}$$
(3.6)

Then, the covariance matrix of the innovation term at time-step k is calculated as

$$\mathbf{P}_{k+1}^{zz} = \mathbf{H}_{k+1} \mathbf{F}_{k+1} \left(\mathbf{P}_k + \Delta \mathbf{P}_k \right) \mathbf{F}_{k+1}^{\mathrm{T}} \mathbf{H}_{k+1}^{\mathrm{T}} + \mathbf{R}_k^{\mathrm{t}} + \Delta \mathbf{R}_k$$
(3.7)

Assuming $\Theta_{k+1} = \mathbf{H}_{k+1} \mathbf{F}_{k+1} \mathbf{P}_{k|k-1} \mathbf{H}_k^{\mathrm{T}}$, then the covariance matrix error of the innovation term is expressed as

$$\Delta \mathbf{P}_{k+1}^{zz} = \Theta_{k+1} \left(\mathbf{N}_k + \Delta \mathbf{R}_k \right)^{-1} \Delta \mathbf{R}_k \mathbf{N}_k^{-1} \Theta_{k+1}^{\mathrm{T}} + \Delta \mathbf{R}_k$$
 (3.8)

As can be seen from Eq. (3.5) and Eq. (3.8), through the recursive propagation of the filter, the MNCM error $\Delta \mathbf{R}_k$ induces not only state estimation errors $\Delta \hat{\mathbf{x}}_k$, but also innovation covariance errors $\Delta \mathbf{P}_{k+1}^{zz}$. Although different robust filters operate on varying principles, most rely on the consistency of the innovation covariance matrix for outlier detection [111]. Therefore, MNCM errors reduce not only the accuracy of state estimation but also the robustness. In addition, these errors affect the reliable navigation integrity monitoring. Consequently, it is necessary to estimate the MNCM while estimating the state.

3.3 Variational Bayes Based Noise Adaptation Method

This section first presents the principle of Bayesian variational approximation estimation for the joint inference of the state and MNCM, and then analyzes the limitations of the method in INMS.

3.3.1 Conjugate distribution selection and joint variational approximation

The variational approximation method is a technique that utilizes prior and measurement information to derive the joint PDF analytical solution for states and unknown parameters (referring to MNCM in this study) [112]. Specifically, since the analytical solution

for the joint posterior PDF $p(\mathbf{x}, \rho | \mathbf{z})$ is computationally intractable, the variational distribution with free factored form $q(\mathbf{x}, \rho)$ is conducted to approximate the joint posterior PDF, i.e., $q(\mathbf{x}, \rho) \approx p(\mathbf{x}, \rho | \mathbf{z})$, where ρ is an unknown parameter. To achieve the approximate calculation above, the following steps are carried out:

(1) First, choose a reasonable PDF. Since \mathbf{R}_k is estimated jointly with \mathbf{x}_k , it is necessary to choose a prior probability distribution for \mathbf{R}_k . The prior conjugate distribution of the likelihood function ensures that the posterior distribution of the unknown parameters after Bayesian inference has the same probability density form as the a priori so that an analytical posterior solution can be obtained. Therefore, the prior distribution of the MNCM is generally chosen as the conjugate distribution of the likelihood function. In INMS, the probability distribution of the likelihood function $p(\mathbf{z}_k \mid \mathbf{x}_k, \mathbf{R}_k)$ follows a Gaussian distribution. Hence, its conjugate prior distribution, the Inverse Wishart (IW) distribution, is adopted as the model for the MNCM. The probability density function is expressed as follows [113, 114, 115].

$$IW(\Sigma; \nu, \Psi) = \frac{|\Psi|^{\frac{\nu}{2}} |\Sigma|^{-\frac{(\nu+m+1)}{2}}}{2^{\frac{\nu m}{2}} \Gamma_m(\frac{\nu}{2})} \exp\left\{-\frac{1}{2} \operatorname{tr}\left(\Psi \Sigma^{-1}\right)\right\}$$
(3.9)

where v is the degree of freedom (DOF); Ψ is the inverse scale matrix; $\operatorname{tr}(\cdot)$ is the trace of a matrix; $\Gamma_d(\cdot)$ denotes the gamma function. For IW, there is $\operatorname{E}[\Sigma] = \Psi/v$. Thus, $p(\mathbf{R}_k \mid \mathbf{z}_{1:k-1})$ is modeled by IW distribution as follows

$$p\left(\mathbf{R}_{k} \mid \mathbf{z}_{1:k-1}\right) = \text{IW}\left(\mathbf{R}_{k}; \hat{u}_{k|k-1}, \hat{\mathbf{U}}_{k|k-1}\right)$$
(3.10)

- (2) Then, the joint probability density is approximated by a variational factor. Since the state \mathbf{x} and the unknown parameters ρ are coupled, it is necessary to decouple the joint probability density to solve for the state vector independently \mathbf{x} and nd the parameters ρ . The variational approximation method assumes that the probability distributions between the state and the unknown parameters are independent. According to the mean-field theory, the joint probability density function can be approximated as the product of the variational factors of each parameter [54, 116], i.e., $p(\mathbf{x}, \rho) \approx q(\mathbf{x}) q(\rho)$, and solving the problem of coupling the calculation of the joint posterior PDF.
- (3) Finally, compute the posterior variational approximate PDF for each parameter. To achieve the approximation of $q(\mathbf{x}, \rho)$ to $p(\mathbf{x}, \rho | \mathbf{z})$, it is necessary to quantitatively evaluate the degree of approximation between $q(\mathbf{x}, \rho)$ and $p(\mathbf{x}, \rho | \mathbf{z})$. The Kullback-Leibler divergence (KLD) is a metric that quantitatively assesses the similarity of two probability

distributions. Thus, the KLD is used to quantitatively evaluate the degree of approximation between $q(\mathbf{x}, \rho)$ and $p(\mathbf{x}, \rho | \mathbf{z})$, and the corresponding objective function is constructed by minimizing the KLD, which is expressed as [60]

$$\{\hat{q}(\mathbf{x}), \hat{q}(\boldsymbol{\rho})\} = \underset{\{q(\mathbf{x}), q(\boldsymbol{\rho})\}}{\operatorname{arg\,min\,KLD}} \left(q(\mathbf{x})q(\boldsymbol{\rho})||p(\mathbf{x}, \boldsymbol{\rho} \mid \mathbf{z})\right)$$
(3.11)

where KLD (\cdot) denotes the KLD. Then, KLD $(q(\mathbf{x})q(\rho)||p(\mathbf{x},\rho\mid\mathbf{z}))$ is expressed as

$$KLD(q(\mathbf{x})q(\rho) \parallel p(\mathbf{x}, \rho \mid \mathbf{z})) = \iint q(\mathbf{x})q(\rho) \log \frac{q(\mathbf{x})q(\rho)}{p(\mathbf{x}, \rho \mid \mathbf{z})} d\mathbf{x} d\rho$$
(3.12)

Since the joint probability density $p(\mathbf{x}, \boldsymbol{\rho} | \mathbf{z})$ is unavailable, the log-likelihood function is calculated first according to the Bayesian rule as

$$\log p(\mathbf{z}) = \log \frac{p(\mathbf{x}, \rho, \mathbf{z})}{p(\mathbf{x}, \rho \mid \mathbf{z})} = \iint q(\mathbf{x}) q(\rho) \log \frac{p(\mathbf{x}, \rho, \mathbf{z})}{p(\mathbf{x}, \rho \mid \mathbf{z})} d\mathbf{x} d\rho$$

$$= \iint q(\mathbf{x}) q(\rho) \log \frac{p(\mathbf{x}, \rho, \mathbf{z})}{q(\mathbf{x}) q(\rho)} d\mathbf{x} d\rho + \iint q(\mathbf{x}) q(\rho) \log \frac{q(\mathbf{x}) q(\rho)}{p(\mathbf{x}, \rho \mid \mathbf{z})} d\mathbf{x} d\rho$$

$$= F(q(\mathbf{x}) q(\rho)) + \text{KLD}(q(\mathbf{x}) q(\rho) \mid\mid p(\mathbf{x}, \rho \mid \mathbf{z}))$$
(3.13)

where $F(q(\mathbf{x})q(\rho))$ denotes the lower bound of the variance dispersion function, which can be further expressed as

$$F(q(\mathbf{x})q(\rho)) = \iint q(\mathbf{x})q(\rho)\log\frac{p(\mathbf{x},\rho,\mathbf{z})}{q(\mathbf{x})q(\rho)}d\mathbf{x}d\rho$$

$$= \iint q(\mathbf{x})q(\rho)\log p(\mathbf{x},\rho,\mathbf{z})d\mathbf{x}d\rho - \iint q(\mathbf{x})q(\rho)\log q(\mathbf{x})\log q(\rho)d\mathbf{x}d\rho \qquad (3.14)$$

$$= \iint q(\mathbf{x})q(\rho)\log p(\mathbf{x},\rho,\mathbf{z})d\mathbf{x}d\rho - \int q(\mathbf{x})\log q(\mathbf{x})d\mathbf{x} - \int q(\rho)\log q(\rho)d\rho$$

Since the log-likelihood function $\log p(\mathbf{z})$ is a constant term that is independent of $q(\mathbf{x})$ and $q(\rho)$, when $F(q(\mathbf{x})q(\rho))$ is maximized, $\mathrm{KLD}(q(\mathbf{x})q(\rho)||p(\mathbf{x},\rho|\mathbf{z}))$ is minimized according to Eq. (3.13). Therefore, it can be further transformed into the following optimization problem

$$\{\hat{q}(\mathbf{x}), \hat{q}(\boldsymbol{\rho})\} = \underset{\{q(\mathbf{x}), q(\boldsymbol{\rho})\}}{\arg\max} F(q(\mathbf{x})q(\boldsymbol{\rho}))$$
(3.15)

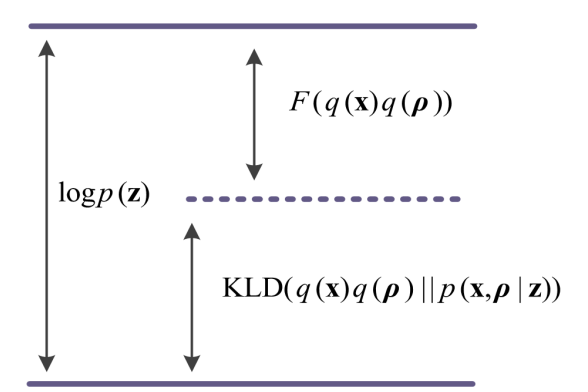


Figure 3.1: The relationship between the log-likelihood function, the KLD and the lower bound function

To solve the optimization problem in Eq. (3.15), the following logarithmic density function is defined

$$\begin{cases} \log \tilde{p}(\mathbf{x}) = \int q(\boldsymbol{\rho}) \log p(\mathbf{x}, \boldsymbol{\rho}, \mathbf{z}) d\boldsymbol{\rho} + c_{\mathbf{x}} \\ \log \tilde{p}(\boldsymbol{\rho}) = \int q(\mathbf{x}) \log p(\mathbf{x}, \boldsymbol{\rho}, \mathbf{z}) d\mathbf{x} + c_{\boldsymbol{\rho}} \end{cases}$$
(3.16)

Compute $q(\mathbf{x})$ such that $F(q(\mathbf{x})q(\rho))$ is maximized. Taking $\log \tilde{p}(\mathbf{x})$ into Eq. (3.14) gives that

$$F(q(\mathbf{x})q(\boldsymbol{\rho})) = \int q(\mathbf{x})\log\tilde{p}(\mathbf{x})d\mathbf{x} - \int q(\mathbf{x})\log q(\mathbf{x})d\mathbf{x} - c_{x}$$

$$= -\int q(\mathbf{x})\log\frac{q(\mathbf{x})}{\tilde{p}(\mathbf{x})}d\mathbf{x} - c_{x}$$

$$= -\text{KLD}(q(\mathbf{x}) \parallel \tilde{p}(\mathbf{x})) - c_{x}$$
(3.17)

where $c_x = \int q(\rho) \log q(\rho) d\rho$ is a constant term. Since KLD $(\cdot) \ge 0$, in order to maximize $F(q(\mathbf{x})q(\rho))$, it is necessary to make KLD $(q(\mathbf{x}) \parallel \tilde{p}(\mathbf{x})) = 0$, i.e., $q(\mathbf{x}) = \tilde{p}(\mathbf{x})$. Therefore, the logarithmic density function of $q(\mathbf{x})$ is expressed as

$$\log q(\mathbf{x}) = \int q(\rho) \log p(\mathbf{x}, \rho, \mathbf{z}) d\rho$$
 (3.18)

Furthermore, to maximize $F(q(\mathbf{x})q(\rho))$ with respect to $q(\rho)$, bring $\log \tilde{p}(\rho)$ into Eq. (3.14) to obtain

$$F(q(\mathbf{x})q(\rho)) = \int q(\rho)\log\tilde{p}(\rho)d\rho - \int q(\rho)\log q(\rho)d\rho - c_{p}$$

$$= -\int q(\mathbf{x})\log\frac{q(\rho)}{\tilde{p}(\rho)}d\rho - c_{p}$$

$$= -\text{KLD}(q(\rho) \parallel \tilde{p}(\rho)) - c_{p}$$
(3.19)

where $c_p = \int q(\mathbf{x}) \log q(\mathbf{x}) d\mathbf{x}$ is a constant term. Similarly, it is necessary $q(\rho) = \tilde{p}(\rho)$ for maximum $F(q(\mathbf{x})q(\rho))$. Hence, the logarithmic density function of $q(\rho)$ is expressed as

$$\log q(\rho) = \int q(\mathbf{x}) \log p(\mathbf{x}, \rho, \mathbf{z}) d\mathbf{x}$$
 (3.20)

From Eq. (3.18) and Eq. (3.20), it can be seen that the state vector and the unknown parameters are coupled with each other, and the analytical solution cannot be calculated directly. Therefore, a fixed-point iteration is necessary. Based on the aforementioned variational inference principle, Alg. 3 provides an MNCM estimation method based on variational Bayesian. For the specific derivation, refer to the literature [117].

Algorithm 3: One-time step implementation of VB

Input: $\hat{\mathbf{x}}_{k-1}, \mathbf{P}_{k-1}, u_{k-1}, \mathbf{U}_{k-1}$

Output: $\hat{\mathbf{x}}_k, \mathbf{P}_k, u_k, \mathbf{U}_k$

1: Calculate the prior state mean $\hat{\mathbf{x}}_{k|k-1}$ and MSE $\mathbf{P}_{k|k-1}$

2:
$$\hat{u}_{k|k-1} = \rho (\hat{u}_{k-1} - m - 1) + m + 1$$

3:
$$\hat{\mathbf{U}}_{k|k-1} = \rho \hat{\mathbf{U}}_{k-1}$$

4: **for**
$$i = [1:N]$$
 do

5:
$$\mathbf{A}_{k}^{(i)} = \left(\mathbf{z}_{k} - \mathbf{h}_{k} \left(\mathbf{x}_{k}^{(i)}\right)\right) \left(\mathbf{z}_{k} - \mathbf{h}_{k} \left(\mathbf{x}_{k}^{(i)}\right)\right)^{\mathrm{T}} + \mathbf{H}_{k} \mathbf{P}_{k}^{(i)} \mathbf{H}_{k}^{\mathrm{T}}$$
6:
$$\hat{u}_{k}^{(i)} = \hat{u}_{k|k-1} + 1, \hat{\mathbf{U}}_{k}^{(i)} = \mathbf{A}_{k}^{(i)} + \hat{\mathbf{U}}_{k|k-1}$$
7:
$$\hat{\mathbf{R}}_{k}^{(i)} = \hat{\mathbf{U}}_{k}^{(i)} \left(\hat{u}_{k}^{(i)} - m - 1\right)^{-1}$$
8: Using $\hat{\mathbf{R}}_{k}^{(i)}$ to update the posterior state $\hat{\mathbf{x}}_{k}^{(i)}$ and $\mathbf{P}_{k}^{(i)}$

9: end

10:
$$\hat{\mathbf{x}}_k = \hat{\mathbf{x}}_k^{(N)}, \mathbf{P}_k = \mathbf{P}_k^{(N)}, \hat{u}_k = \hat{u}_k^{(N)}, \hat{\mathbf{U}}_k = \hat{\mathbf{U}}_k^{(N)}$$

3.3.2 Limitations Analysis for VB in INMS

Although the VB adaptive method can achieve joint online estimation of the MNCM and state, there are still the following limitations in INMS applications:

(1) Outliers interfere with MNCM estimation. In INMS, as the number and types of external sensors increase, the probability of outliers occurrence and data errors also increases. Although robust filtering can mitigate outliers disturbance on state estimation, the likelihood function cannot follow the Gaussian distribution in the presence of outliers, and the IW cannot serve as the corresponding conjugate prior distribution.

In this case, modeling MNCM with IW distribution will lead to the inability to accurately compute the inverse scale matrix $\hat{\mathbf{U}}_k$, which will affect the estimation effect of MNCM. Inaccurate MNCM will further deteriorate the next VB iteration, and also interfere with state robustness estimation and integrity monitoring. Fig. 3.2 shows the MNCM estimation based on VB under the outliers interference.

(2) The historical information is not fully exploited. In Alg. 3, the state variables and MNCM are coupled, so fixed-point iteration is used to achieve joint estimation, which increases the computational burden. More importantly, VB uses only the current measurement information to repeat the iteration, discarding the historical data. Considering that the MNCM of the INMS sensor changes slowly, historical measurements and a posteriori state estimation over a period of time can be used to estimate the MNCM more accurately and smoothly.

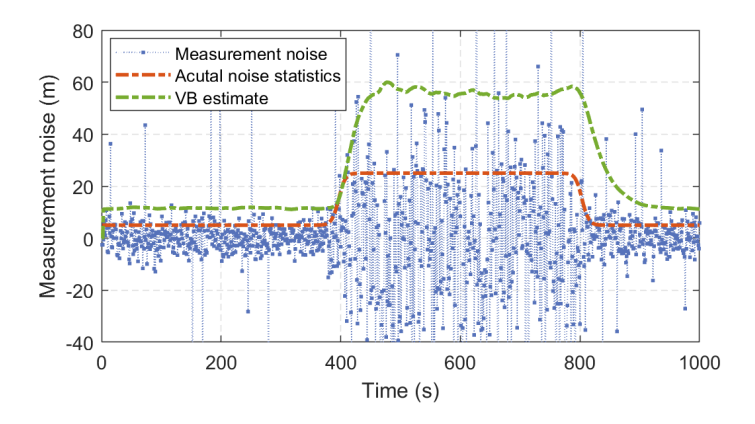


Figure 3.2: VB-based MNCM estimation with measurement outliers interference

3.4 Robust Smooth VB Noise Adaptation Based on MCC

To address the aforementioned issues, this section proposes a robust smooth variational Bayesian adaptation (RSVBA) method. First, the analytical form of the smoothed posterior state and MNCM joint variational approximation is derived. Then, the inverse scale matrix of the IW distribution is reconstructed based on the correntropy matrix to suppress the interference of measurement outliers on the MNCM estimation. Finally, the theoretical performance of the proposed adaptation method is analyzed. The specific structure of the proposed method is shown in Fig. 3.3.

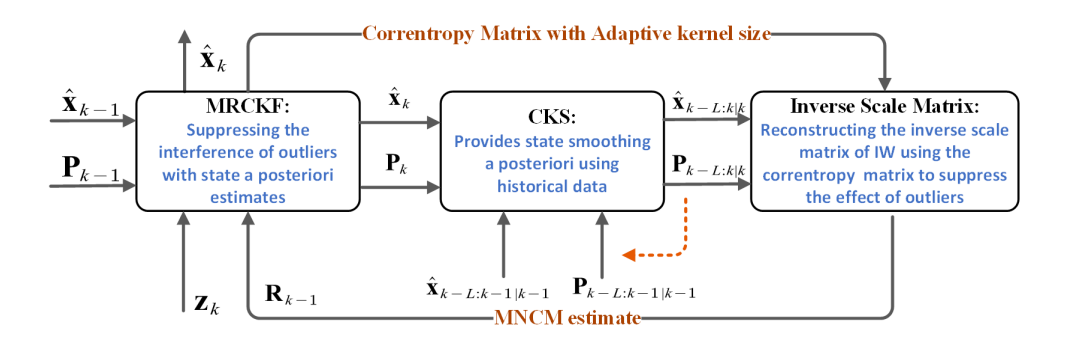


Figure 3.3: Structure of the proposed RSVBA

3.4.1 MNCM and Smoothing State Joint Variational Approximation

To make full use of historical data (including measurement and a posterior state), the variational approximation of the joint probability density of MNCM and the smoothed posterior state in the fixed interval [k-L,k] is solved. The mean of the probability distribution of the MNCM in the interval [k-L,k] is expressed as \mathbf{R}_k^L . Considering that the actual engineering MNCM generally changes slowly, \mathbf{R}_k^L can be regarded as the smoothed value of the MNCM in the fixed interval obtained using historical data. To get the analytical solution of the joint PDF of the smoothed posterior state and the MNCM $p\left(\mathbf{x}_{k-L:k}, \mathbf{R}_k^L \mid \mathbf{z}_{1:k}\right)$, it is approximated by the variational form according to the mean-field theory as follows

$$p\left(\mathbf{x}_{k-L:k}, \mathbf{R}_{k}^{L} \mid \mathbf{z}_{1:k}\right) \approx q\left(\mathbf{x}_{k-L:k}\right) q\left(\mathbf{R}_{k}^{L}\right)$$
(3.21)

The optimal solution is obtained by minimizing the KLD between the actual joint probability distribution and the approximated variational factor, i.e.

$$\left\{\hat{q}\left(\mathbf{x}_{k-L:k}\right),\hat{q}\left(\mathbf{R}_{k}^{L}\right)\right\} = \underset{\left\{q\left(\mathbf{x}_{k-L:k}\right),q\left(\mathbf{R}_{k}^{L}\right)\right\}}{\operatorname{arg\,min\,KLD}} \left(q\left(\mathbf{x}_{k-L:k}\right)q\left(\mathbf{R}_{k}^{L}\right) \parallel p\left(\mathbf{x}_{k-L:k},\mathbf{R}_{k}^{L} \mid \mathbf{z}_{1:k}\right)\right)$$
(3.22)

Then, based on Eq. (3.18) and Eq. (3.20), the optimal solution of Eq. (3.22) satisfies the following equation

$$\begin{cases} \log q(\vartheta) = \mathbf{E}_{\Xi^{(-\vartheta)}} \left[\log p\left(\Xi, \mathbf{z}_{1:k}\right) \right] + c_{\vartheta} \\ \text{s.t.} \quad \Xi \triangleq \left\{ \mathbf{x}_{k-L:k}, \mathbf{R}_{k}^{L} \right\} \end{cases}$$
(3.23)

where Ξ represents the set consisting of $\mathbf{x}_{k-L:k}$ and \mathbf{R}_k^L ; ϑ represents any element in Ξ ; $\Xi^{(-\vartheta)}$ denotes the elements of the set Ξ other than ϑ ; c_ϑ is a constant independent of ϑ . Since the variational factors $q(\mathbf{x}_{k-L:k})$ and $q(\mathbf{R}_k^L)$ are coupled, they are solved by fixed-point iteration. First, according to the conditional independence of the Gaussian-IW state

space model, the joint probability distribution $p(\Xi, \mathbf{z}_{1:k})$ can be decomposed as follows

$$p\left(\mathbf{\Xi}, \mathbf{z}_{1:k}\right) = \prod_{i=k-L}^{k} p\left(\mathbf{z}_{k} \mid \mathbf{x}_{i}, \mathbf{R}_{k}^{L}\right) p\left(\mathbf{x}_{i} \mid \mathbf{z}_{1:k-1}\right) p\left(\mathbf{R}_{k}^{L} \mid \mathbf{z}_{1:k-1}\right) p\left(\mathbf{z}_{1:k-1}\right)$$
(3.24)

According to Eq. (3.10), taking MNCM PDF into Eq. (3.24) gives

$$p\left(\mathbf{\Xi}, \mathbf{z}_{1:k}\right) = \prod_{i=k-L}^{k} N\left(\mathbf{z}_{i}; \mathbf{h}_{i}\left(\mathbf{x}_{i}\right), \mathbf{R}_{k}^{L}\right) N\left(\mathbf{x}_{i}; \hat{\mathbf{x}}_{i|i-1}, \mathbf{P}_{i|i-1}\right) IW\left(\mathbf{R}_{k}; \hat{u}_{k|k-1}, \hat{\mathbf{U}}_{k|k-1}\right) p\left(\mathbf{z}_{1:k-1}\right)$$
(3.25)

Further, taking the logarithm of $p(\Xi, \mathbf{z}_{1:k})$, the log-density function is expressed as

$$\log p\left(\Xi, \mathbf{z}_{1:k}\right) = \sum_{i=k-L}^{k} \log N\left(\mathbf{z}_{i}; \mathbf{h}_{i}\left(\mathbf{x}_{i}\right), \mathbf{R}_{k}^{L}\right) + \log N\left(\mathbf{x}_{i}; \hat{\mathbf{x}}_{i|i-1}, \mathbf{P}_{i|i-1}\right) + \log IW\left(\mathbf{R}_{k}; \hat{\mathbf{u}}_{k|k-1}, \hat{\mathbf{U}}_{k|k-1}\right) + \log p\left(\mathbf{z}_{1:k-1}\right)$$
(3.26)

Expand Eq. (3.26) to get

$$\log p\left(\Xi, \mathbf{z}_{1:k}\right) = \sum_{i=k-L}^{k} \log \left((2\pi)^{-\frac{m}{2}} \left| \mathbf{R}_{k}^{L} \right|^{-\frac{1}{2}} \right) - \frac{1}{2} \left(\mathbf{z}_{i} - \left(\mathbf{h}_{i} \left(\mathbf{x}_{i} \right) \right) \right)^{\mathrm{T}} \left(\mathbf{R}_{k}^{L} \right)^{-1} \left(\mathbf{z}_{i} - \left(\mathbf{h}_{i} \left(\mathbf{x}_{i} \right) \right) \right)$$

$$+ \log \left(\left(2\pi \right)^{-\frac{n}{2}} \left| \mathbf{P}_{i|i-1} \right|^{-\frac{1}{2}} \right) - \frac{1}{2} \left(\mathbf{x}_{i} - \hat{\mathbf{x}}_{i|i-1} \right)^{\mathrm{T}} \mathbf{P}_{i|i-1}^{-1} \left(\mathbf{x}_{i} - \hat{\mathbf{x}}_{i|i-1} \right)$$

$$+ \log \left(\frac{\left| \hat{\mathbf{U}}_{k|k-1} \right|^{\frac{\hat{u}_{k|k-1}}{2}} \left| \mathbf{R}_{k}^{L} \right|^{-\frac{(\hat{u}_{k|k-1}+m+1)}{2}}}{2} \right) - \frac{1}{2} \operatorname{tr} \left(\hat{\mathbf{U}}_{k|k-1} \left(\mathbf{R}_{k}^{L} \right)^{-1} \right) + c_{\Xi}$$

$$(3.27)$$

Rearranging the index term in the above equation gives

$$\log p\left(\mathbf{\Xi}, \mathbf{z}_{1:k}\right) = (L+1)\left(\left(-\frac{m}{2}\right)\log(2\pi) + \left(-\frac{1}{2}\right)\log\left(\left|\mathbf{R}_{k}^{L}\right|\right)\right) + (L+1)\left(-\frac{n}{2}\right)\log(2\pi)$$

$$+ \sum_{i=k-L}^{k} \left(-\frac{1}{2}\left(\mathbf{z}_{i} - \mathbf{h}_{i}\left(\mathbf{x}_{i}\right)\right)^{\mathsf{T}}\left(\mathbf{R}_{k}^{L}\right)^{-1}\left(\mathbf{z}_{i} - \mathbf{h}_{i}\left(\mathbf{x}_{i}\right)\right)\right) + \left(-\frac{1}{2}\right)\log\left(\left|\mathbf{P}_{i|i-1}\right|\right)$$

$$+ \sum_{i=k-L}^{k} \left(-\frac{1}{2}\left(\mathbf{x}_{i} - \hat{\mathbf{x}}_{i|i-1}\right)^{\mathsf{T}}\mathbf{P}_{i|i-1}^{-1}\left(\mathbf{x}_{i} - \hat{\mathbf{x}}_{i|i-1}\right)\right)$$

$$+ \left(\frac{-\left(\hat{u}_{k|k-1} + m + 1\right)}{2}\right)\log\left(\left|\mathbf{R}_{k}\right|\right) + \log\left(\frac{\left|\hat{\mathbf{U}}_{k|k-1}\right|^{\frac{\hat{u}_{k|k-1}}{2}}}{2^{\frac{m\hat{u}_{k|k-1}}{2}}}\mathbf{\Gamma}_{m}\left(\frac{\hat{u}_{k|k-1}}{2}\right)\right)$$

$$+ \left(-\frac{1}{2}\operatorname{tr}\left(\hat{\mathbf{U}}_{k|k-1}\left(\mathbf{R}_{k}^{L}\right)^{-1}\right)\right) + c_{\mathbf{\Xi}}$$
(3.28)

Eq. (3.28) can be arranged as follows

$$\log p\left(\mathbf{\Xi}, \mathbf{z}_{1:k}\right) = -\frac{1}{2} \left(L + \hat{u}_{k|k-1} + m + 2\right) \log \left(\left|\mathbf{R}_{k}^{L}\right|\right) - \frac{1}{2} \operatorname{tr}\left(\hat{\mathbf{U}}_{k|k-1}(\mathbf{R}_{k}^{L})^{-1}\right) - \frac{1}{2} \sum_{i=k-L}^{k} \left\{ \left(\mathbf{x}_{i} - \hat{\mathbf{x}}_{i|i-1}\right)^{\mathrm{T}} \mathbf{P}_{i|i-1}^{-1} \left(\mathbf{x}_{i} - \hat{\mathbf{x}}_{i|i-1}\right) + \log \left(\left|\mathbf{P}_{i|i-1}\right|\right) \right\} - \frac{1}{2} \sum_{i=k-L}^{k} \left(\mathbf{z}_{i} - \mathbf{h}_{i}\left(\mathbf{x}_{i}\right)\right)^{\mathrm{T}} \left(\mathbf{R}_{k}^{L}\right)^{-1} \left(\mathbf{z}_{i} - \mathbf{h}_{i}\left(\mathbf{x}_{i}\right)\right) + c_{\blacksquare}$$
(3.29)

where c_{Ξ} is a constant term independent of the set Ξ , and is expressed as

$$c_{\Xi} = \log p\left(\mathbf{z}_{1:k-1}\right) - \frac{L}{2}(m+n)\log(2\pi) + \log\left(\frac{\left|\hat{\mathbf{U}}_{k|k-1}\right|^{\frac{\hat{u}_{k|k-1}}{2}}}{2^{\frac{m\hat{u}_{k|k-1}}{2}}\Gamma_{m}(\frac{\hat{u}_{k|k-1}}{2})}\right)$$
(3.30)

Then, by taking Eq. (3.29) into Eq. (3.23) and letting $\vartheta = \mathbf{x}_{k-L:k}$ gives

$$\log q\left(\mathbf{x}_{k-L:k}\right) = -\frac{1}{2}\left(L + \hat{u}_{k|k-1} + m + 2\right) \operatorname{E}\left[\log\left(\left|\mathbf{R}_{k}^{L}\right|\right)\right] - \frac{1}{2}\operatorname{E}\left[\operatorname{tr}\left(\hat{\mathbf{U}}_{k|k-1}(\mathbf{R}_{k}^{L})^{-1}\right)\right]$$
$$-\frac{1}{2}\log\left(\left|\mathbf{P}_{i|i-1}\right|\right) - \frac{1}{2}\sum_{i=k-L}^{k}\left\{\left(\mathbf{x}_{i} - \hat{\mathbf{x}}_{i|i-1}\right)^{\mathsf{T}}\mathbf{P}_{i|i-1}^{-1}\left(\mathbf{x}_{i} - \hat{\mathbf{x}}_{i|i-1}\right)\right\}$$
$$-\frac{1}{2}\sum_{i=k-L}^{k}\left(\mathbf{z}_{i} - \mathbf{h}_{i}\left(\mathbf{x}_{i}\right)\right)^{\mathsf{T}}\operatorname{E}\left[\left(\mathbf{R}_{k}^{L}\right)^{-1}\right]\left(\mathbf{z}_{i} - \mathbf{h}_{i}\left(\mathbf{x}_{i}\right)\right) + c_{\mathbf{x}}$$
(3.31)

Simplifying the above equation gives

$$\log q\left(\mathbf{x}_{k-L:k}\right) = -\frac{1}{2} \sum_{i=k-L}^{k} \left(\mathbf{z}_{i} - \mathbf{h}_{i}\left(\mathbf{x}_{i}\right)\right)^{\mathrm{T}} \mathrm{E}\left[\left(\mathbf{R}_{k}^{L}\right)^{-1}\right] \left(\mathbf{z}_{i} - \mathbf{h}_{i}\left(\mathbf{x}_{i}\right)\right)$$

$$-\frac{1}{2} \sum_{i=k-L}^{k} \left\{\left(\mathbf{x}_{i} - \hat{\mathbf{x}}_{i|i-1}\right)^{\mathrm{T}} \mathbf{P}_{i|i-1}^{-1} \left(\mathbf{x}_{i} - \hat{\mathbf{x}}_{i|i-1}\right)\right\} + c_{\mathbf{x}}$$
(3.32)

where $\mathbf{E}^{(i+1)}\left[\mathbf{R}_{k}^{-1}\right]$ is calculated according to the mean definition in the IW distribution as

$$E\left[\left(\mathbf{R}_{k}^{L}\right)^{-1}\right] = \hat{u}_{k}^{L}\left(\hat{\mathbf{U}}_{k}^{L}\right)^{-1} \tag{3.33}$$

Then, the exponential operation is performed on Eq. (3.32), and $q(\mathbf{x}_{k-L:k})$ is calculated as

$$q\left(\mathbf{x}_{k-L:k}\right) \propto \prod_{i=k-L}^{k} N\left(\mathbf{z}_{i}; \mathbf{h}_{i}\left(\mathbf{x}_{i}\right), \mathbf{R}_{k}^{L}\right) N\left(\mathbf{x}_{i}; \hat{\mathbf{x}}_{i|i-1}, \mathbf{P}_{i|i-1}\right)$$
(3.34)

According to the principle of maximum a posteriori estimation, there is

$$q\left(\mathbf{x}_{k-L:k}\right) = N\left(\mathbf{x}_{k-L:k}; \hat{\mathbf{x}}_{k-L:k|k}, \mathbf{P}_{k-L:k|k}\right)$$
(3.35)

where the posterior smooth state vector $\hat{\mathbf{x}}_{k-L:k|k}$ and its covariance matrix $\mathbf{P}_{k-L:k|k}$ are obtained by the smooth estimator RTS. Then, Eq. (3.29) is substituted into Eq. (3.23), and let $\vartheta = \mathbf{R}_k$, there is

$$\log q\left(\mathbf{R}_{k}^{L}\right) = -\frac{1}{2}\left(L + \hat{u}_{k|k-1} + m + 2\right)\log\left(\left|\mathbf{R}_{k}^{L}\right|\right) - \frac{1}{2}\operatorname{tr}\left(\left(\sum_{i=k-L}^{k}\mathbf{A}_{i} + \hat{\mathbf{U}}_{k|k-1}\right)\left(\mathbf{R}_{k}^{L}\right)^{-1}\right) - \frac{1}{2}\sum_{i=k-L}^{k}\operatorname{E}\left[\log\left(\left|\mathbf{P}_{i|i-1}\right|\right)\right] - \frac{1}{2}\sum_{i=k-L}^{k}\operatorname{E}\left[\left(\mathbf{x}_{i} - \hat{\mathbf{x}}_{i|i-1}\right)^{\mathrm{T}}\mathbf{P}_{i|i-1}^{-1}\left(\mathbf{x}_{i} - \hat{\mathbf{x}}_{i|i-1}\right)\right] + c_{\mathbf{R}}$$

$$(3.36)$$

where

$$\mathbf{A}_{i} = \mathbf{E}\left[\left(\mathbf{z}_{i} - \mathbf{h}_{i}\left(\mathbf{x}_{i}\right)\right)\left(\mathbf{z}_{i} - \mathbf{h}_{i}\left(\mathbf{x}_{i}\right)\right)^{\mathrm{T}}\right]$$

$$= \mathbf{E}\left[\left(\mathbf{z}_{i} - \mathbf{h}_{i}\left(\hat{\mathbf{x}}_{i|k}\right) + \mathbf{h}_{i}\left(\hat{\mathbf{x}}_{i|k}\right) - \mathbf{h}_{i}\left(\mathbf{x}_{i}\right)\right)\left(\mathbf{z}_{i} - \mathbf{h}_{i}\left(\hat{\mathbf{x}}_{i|k}\right) + \mathbf{h}_{i}\left(\hat{\mathbf{x}}_{i|k}\right) - \mathbf{h}_{i}\left(\mathbf{x}_{i}\right)\right)^{\mathrm{T}}\right]$$

$$= \left(\mathbf{z}_{i} - \mathbf{h}_{i}\left(\hat{\mathbf{x}}_{i|k}\right)\right)\left(\mathbf{z}_{i} - \mathbf{h}_{i}\left(\hat{\mathbf{x}}_{i|k}\right)\right)^{\mathrm{T}} + \mathbf{H}_{i}\mathbf{E}\left[\left(\mathbf{x}_{i} - \hat{\mathbf{x}}_{i|k}\right)\left(\mathbf{x}_{i} - \hat{\mathbf{x}}_{i|k}\right)^{\mathrm{T}}\right]\mathbf{H}_{i}^{\mathrm{T}}$$

$$= \tilde{\mathbf{z}}_{i}^{\mathrm{S}}\left(\tilde{\mathbf{z}}_{i}^{\mathrm{S}}\right)^{\mathrm{T}} + \mathbf{H}_{i}\mathbf{P}_{i|k}\mathbf{H}_{i}^{\mathrm{T}}$$

$$(3.37)$$

where $\tilde{\mathbf{z}}_i^{\mathrm{s}} = \mathbf{z}_i - \mathbf{h}_i(\hat{\mathbf{x}}_{i|k})$; \mathbf{H}_i represents the Jacobian matrix of the measurement function \mathbf{h}_k expanded at $\hat{\mathbf{x}}_{i|k}$. Due to the conjugate distribution property, $q(\mathbf{R}_k^L)$ also follows an IW distribution, and its PDF is expressed as

$$q\left(\mathbf{R}_{k}^{L}\right) = \text{IW}\left(\mathbf{R}_{k}^{L}; \hat{u}_{k}^{L}, \hat{\mathbf{U}}_{k}^{L}\right) \tag{3.38}$$

where \hat{u}_k^L and $\hat{\mathbf{U}}_k^L$ are calculated from $q\left(\mathbf{x}_{k-L:k}\right)$ as

$$\begin{cases} \hat{u}_{k}^{L} = \hat{u}_{k|k-1}^{L} + L + 1\\ \hat{\mathbf{U}}_{k}^{L} = \hat{\mathbf{U}}_{k|k-1}^{L} + \sum_{i=k-L}^{k} \mathbf{A}_{i} \end{cases}$$
(3.39)

3.4.2 IW distribution Reconstruction Based on Correntropy for GNSS latitude Matrix

The previous section provided the analytical solution for the variational approximation of MNCM. In this section, a robust posterior estimation of the MNCM is performed based on this solution. First, the prior IW distribution parameters of the MNCM are calculated. Then, the posterior IW distribution of the MNCM is updated, and the inverse scale matrix is reconstructed based on the corresponding correntropy matrix. The relationship between the prior and posterior IW distributions of the MNCM is shown in Fig. 3.4.

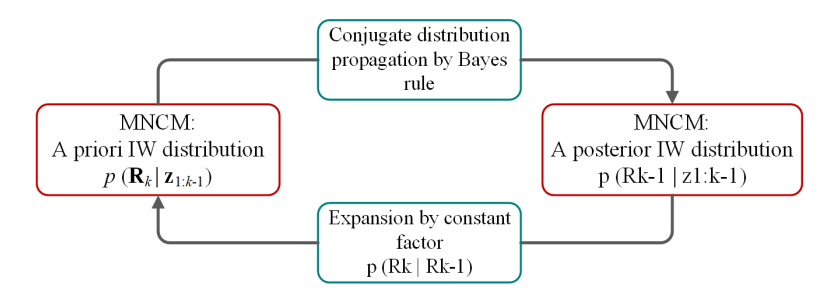


Figure 3.4: The relationship between the MNCM a priori and a posteriori IW distributions

(1) **Determine a priori IW distribution**: First, the a priori IW distribution of MNCM is updated. In recursive filtering, the PDF of the MNCM at the previous time step is assumed to follow an IW distribution given by

$$q\left(\mathbf{R}_{k-1}^{L}\right) = \text{IW}\left(\mathbf{R}_{k-1}^{L}; \hat{u}_{k-1}^{L}, \hat{\mathbf{U}}_{k-1}^{L}\right) \tag{3.40}$$

To determine the prior distribution of \mathbf{R}_k , the prior parameters $\hat{u}_{k|k-1}$ and $\hat{\mathbf{U}}_{k|k-1}$ need to be specified. Based on the full-probability rule, $p\left(\mathbf{R}_k \mid \mathbf{z}_{1:k-1}\right)$ can be further expressed as

$$q\left(\mathbf{R}_{k|k-1}^{L}\right) = \int q\left(\mathbf{R}_{k}^{L} \mid \mathbf{R}_{k-1}^{L}\right) q\left(\mathbf{R}_{k-1}^{L}\right) d\mathbf{R}_{k-1}$$

$$= \int q\left(\mathbf{R}_{k}^{L} \mid \mathbf{R}_{k-1}^{L}\right) IW\left(\mathbf{R}_{k-1}^{L}; \hat{u}_{k-1}, \hat{\mathbf{U}}_{k-1}\right) d\mathbf{R}_{k-1}$$

$$= IW\left(\mathbf{R}_{k|k-1}^{L}; \hat{u}_{k|k-1}^{L}, \hat{\mathbf{U}}_{k|k-1}^{L}\right)$$
(3.41)

where $q\left(\mathbf{R}_{k}^{L} \mid \mathbf{R}_{k-1}^{L}\right)$ is the dynamic model of the MNCM. The model needs to be able to make the prior $q\left(\mathbf{R}_{k|k-1}^{L}\right)$ follow an IW distribution. Since the MNCM changes slowly in practical engineering, the prior propagation of the MNCM is performed using constant coefficients. Therefore, the dynamic parameters of the prior IW distribution $\hat{u}_{k|k-1}^{L}$ and $\hat{\mathbf{U}}_{k|k-1}^{L}$ are calculated as follows

$$\hat{u}_{k|k-1}^L = \rho \hat{u}_{k-1}^L \tag{3.42a}$$

$$\hat{\mathbf{U}}_{k|k-1}^L = \rho \hat{\mathbf{U}}_{k-1}^L \tag{3.42b}$$

where $\rho \in [0.9, 1]$ is a time-varying expansion factor of the MNCM.

(2) **Determine a posterior IW distribution:** First, the IW inverse scale matrix is updated. Based on the measurements at multiple moments within a fixed interval and the posterior state, the Cubature Kalman Smoother (CKS) is used to compute the variational

approximation of the smoothed posterior state $q(\mathbf{x}_{k-L:k})$, which is denoted as

$$\mathbf{P}_{xx,k|k-1} = \frac{1}{n_s} \sum_{i=1}^{n_s} \mathbf{x}_{k-1}^{(i)} \mathbf{x}_{k|k-1}^{(i)T} - \hat{\mathbf{x}}_{k-1} \hat{\mathbf{x}}_{k|k-1}^{T}$$
(3.43a)

$$\mathbf{G}_{i-1}^{s} = \mathbf{P}_{xx,i|i-1}\mathbf{P}_{i|i-1}^{-1}$$
(3.43b)

$$\hat{\mathbf{x}}_{i-1|k}^{s} = \hat{\mathbf{x}}_{i-1} + \mathbf{G}_{j-1}^{s} \left(\hat{\mathbf{x}}_{i|k}^{s} - \hat{\mathbf{x}}_{i|i-1} \right)$$
(3.43c)

$$\mathbf{P}_{i-1|k}^{s} = \mathbf{P}_{i-1} + \mathbf{G}_{i-1}^{s} \left(\mathbf{P}_{i|k}^{s} - \mathbf{P}_{i|i-1} \right) (\mathbf{G}_{i-1}^{s})^{\mathrm{T}}$$
(3.43d)

Then, according to Eq. (3.37), the parameters \mathbf{A}_i are calculated using the smooth mean $\hat{\mathbf{x}}_{k-L:k|k}$ and covariance matrix $\mathbf{P}_{k-L:k|k}$ of $q(\mathbf{x}_{k-L:k})$. Meanwhile, the correntropy matrix based on the adaptive kernel size is used to eliminate outliers interference.

$$\mathbf{A}_{i}^{c} = \mathbf{C}_{i}^{z} \tilde{\mathbf{z}}_{i}^{s} \left(\tilde{\mathbf{z}}_{i}^{s}\right)^{\mathrm{T}} \left(\mathbf{C}_{i}^{z}\right)^{\mathrm{T}} + \mathbf{H}_{i} \mathbf{P}_{i|k} \mathbf{H}_{i}^{\mathrm{T}}$$
(3.44)

where C_i^z is the correntropy matrix based on the adaptive multi-kernel size at time-step i in MRCKF. Then, the degrees of freedom and the reconstructed inverse scale matrix of the posterior IW distribution are calculated as

$$\begin{cases} \hat{u}_{k}^{L} = \rho \hat{u}_{k-1} + L + 1 \\ \hat{\mathbf{U}}_{k}^{L} = \rho \hat{\mathbf{U}}_{k-1} + \sum_{i=k-L}^{k} \mathbf{A}_{i}^{c} \end{cases}$$
(3.45)

Further, the MNCM is calculated based on the posterior IW distribution as follows

$$\hat{\mathbf{R}}_k^L = \hat{\mathbf{U}}_k^L / \hat{u}_k^L \tag{3.46}$$

The pseudocode of the proposed RSVBA method is given in Alg. 4. RSVBA uses the smooth posterior state and measurement data in a fixed interval to improve the accuracy of MNCM estimation. In addition, it uses a correntropy matrix based on adaptive kernel sizes to suppress the outlier's interference on the IW inverse scale matrix, thereby achieving a robust estimation of MNCM in the presence of an outlier.

3.4.3 Smooth Robust Adaptation Executed in INMS

In this section, the proposed RSVBA robust adaptation method is applied to INMS. The structure of the algorithm is depicted in Fig. 3.5. In INMS, the state posterior is initially computed by MRCKF, which not only corrects the navigation parameters but also

Algorithm 4: One-time step implementation of RSVBA

Input:
$$\hat{\mathbf{x}}_{k-1}$$
, \mathbf{P}_{k-1} , \mathbf{z}_k , \hat{u}_{k-1}^L , \mathbf{U}_{k-1}^L
Output: $\hat{\mathbf{x}}_k$, \mathbf{P}_k , \hat{u}_k^L , \mathbf{U}_k^L
/* Forward robust filtering */

1: $[\hat{\mathbf{x}}_k, \mathbf{P}_k, \mathbf{G}_k, \mathbf{C}_k^z,] = \mathrm{MRCKF}[\hat{\mathbf{x}}_{k-1}, \mathbf{P}_{k-1}, \mathbf{z}_k, \hat{u}_{k-1}^L, \mathbf{U}_{k-1}^L]$
/* Backward smoothing */

2: for $j = [k:-1:k-L]$ do
3: $|\mathbf{G}_{i-1}^s = \mathbf{P}_{xx,i|i-1}\mathbf{P}_{i|i-1}^{-1}$
4: $\hat{\mathbf{x}}_{i-1|k}^s = \hat{\mathbf{x}}_{i-1} + \mathbf{G}_{j-1}^s(\hat{\mathbf{x}}_{i|k}^s - \hat{\mathbf{x}}_{i|i-1})$
5: $|\mathbf{P}_{i-1|k}^s = \mathbf{P}_{i-1} + \mathbf{G}_{i-1}^s(\mathbf{P}_{i|k}^s - \mathbf{P}_{i|i-1})(\mathbf{G}_{i-1}^s)^T$
6: end

/* MNCM robust estimator */

7: $\mathbf{A}_i^c = \mathbf{C}_i^c \tilde{\mathbf{z}}_i^s(\tilde{\mathbf{z}}_i^s)^T(\mathbf{C}_i^c)^T + \mathbf{H}_i \mathbf{P}_{i|k} \mathbf{H}_i^T$
8: $\mathbf{A}_k = \sum_{i=k-L}^k \mathbf{A}_i^c$
9: $\hat{u}_{k|k-1}^L = \rho \hat{u}_{k-1}^L, \hat{\mathbf{U}}_{k|k-1}^L = \rho \hat{\mathbf{U}}_{k-1}^L$
10: $\hat{u}_k^L = \hat{u}_{k|k-1}^L + L + 1$
11: $\hat{\mathbf{U}}_k^L = \hat{u}_{k|k-1}^L + \sum_{i=k-L}^k \mathbf{A}_i^c$
12: $\hat{\mathbf{R}}_k = \hat{\mathbf{U}}_k^L / \hat{u}_k^L$

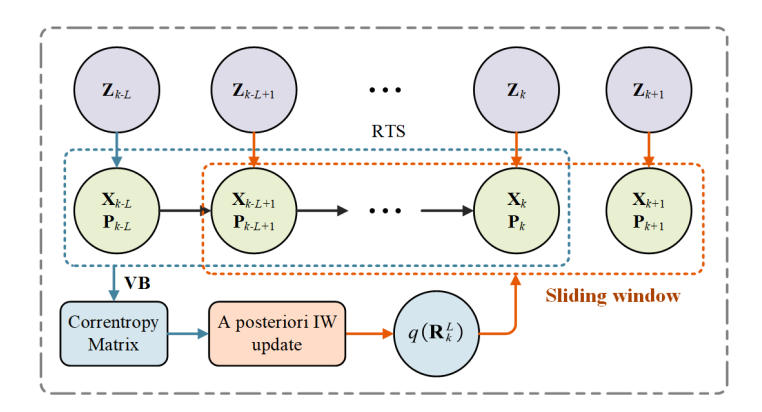


Figure 3.5: Online smoothing RTS structure for INMS systems

provides data to RSVBA for sliding window MNCM estimation. Subsequently, the MNCM estimated by RSVBA is used for subsequent state estimation and integrity monitoring. In RSVBA, the measurement matrix can be derived using the post-statistical linearization method, avoiding the calculation of the Jacobian matrix. Specifically, based on the definition of the state prediction covariance $\mathbf{P}_{k,k-1}$ and the cross-covariance matrix $\mathbf{P}_{xz,k,k-1}$ in

MRCFK, the following relationship holds

$$\mathbf{P}_{k,k-1} = \mathbf{E}\left[\left(\mathbf{x}_k - \hat{\mathbf{x}}_k \right) \left(\mathbf{x}_k - \hat{\mathbf{x}}_k \right)^{\mathrm{T}} \right]$$
 (3.47a)

$$\mathbf{P}_{xz,k,k-1} = \mathbf{E}\left[\left(\mathbf{x}_k - \hat{\mathbf{x}}_k \right) \left(\mathbf{z}_k - \hat{\mathbf{z}}_k \right)^{\mathrm{T}} \right] \triangleq \mathbf{P}_{k,k-1} \mathbf{H}_k^{\mathrm{T}}$$
(3.47b)

Then, the pseudo-measurement matrix is calculated as

$$\mathbf{H}_k = \mathbf{P}_{xz}^{\mathrm{T}} \mathbf{P}_{k,k-1}^{-1} \tag{3.48}$$

3.4.4 Algorithm Performance and Complexity Analysis

(1) MNCM estimation stability analysis

The numerical stability of the proposed adaptation method is analyzed. First, according to Eq. (3.45), the posterior mean of the MNCM based on the IW distribution in the interval [k-L,k] is calculated as [103]

$$\hat{\mathbf{R}}_{k} = \frac{\hat{\mathbf{U}}_{k}^{L}}{\hat{\mu}_{k}^{L}} = \frac{\rho \hat{\mathbf{U}}_{k-1} + \sum_{i=k-L}^{k} \mathbf{A}_{i}^{c}}{\rho \hat{\mu}_{k-1} + L + 1} = \frac{\rho \hat{\mathbf{U}}_{k-1} + \mathbf{A}_{s}^{c}}{\rho \hat{\mu}_{k-1} + L + 1}$$
(3.49)

In addition, assuming the last cycle $\hat{\mathbf{R}}_{k-1} = \hat{\mathbf{U}}_{k-1}^L / \hat{u}_{k-1}^L$ in the interval [k-L-1,k-1], then substituting it into Eq. (3.49) gives

$$\hat{\mathbf{R}}_{k} = \frac{\rho \hat{u}_{k-1}^{L} \hat{\mathbf{R}}_{k-1} + \mathbf{A}_{s}^{c}}{\rho \hat{u}_{k-1}^{L} + L + 1}$$
(3.50)

Furthermore, according to Eq. (3.42a) and Eq. (3.45), \hat{u}_{k-1}^L is expressed as

$$\hat{u}_{k-1}^{L} = \rho^{k-1}\hat{u}_{0}^{L} + \rho^{k-2}(L+1) + \dots + \rho(L+1) + (L+1)$$
(3.51)

Rearrange it to get

$$\hat{u}_{k-1}^{L} = \rho^{k-1}\hat{u}_{0}^{L} + \frac{1 - \rho^{k-1}}{1 - \rho}(L+1)$$
(3.52)

Bringing Eq. (3.52) into Eq. (3.50) gives

$$\hat{\mathbf{R}}_k = \frac{g(\boldsymbol{\rho}, k) \,\hat{\mathbf{R}}_{k-1} + \mathbf{A}_s^c}{g(\boldsymbol{\rho}, k) + L + 1}$$
(3.53)

where $g(\rho,k) = \rho^k \hat{u}_0^L + \frac{\rho - \rho^k}{1 - \rho} (L + 1)$. From Eq. (3.53), it can be obtained

$$\lim_{k \to +\infty} g(\rho, k) = \rho / (1 - \rho) \tag{3.54}$$

Based on Eq. (3.53) and Eq. (3.54), $g(\rho,k)$ is actually the weighting factor for $\hat{\mathbf{R}}_{k-1}$ and \mathbf{A}_s^c . Once the filter converges, $g(\rho,k)$ is a monotonically increasing function of the MNCM expansion coefficient ρ , which means that the influence of the previous estimate $\hat{\mathbf{R}}_{k-1}$ on the current $\hat{\mathbf{R}}_k$ can be controlled by ρ . The smaller ρ , the less influence $\hat{\mathbf{R}}_{k-1}$ has on $\hat{\mathbf{R}}_k$. Conversely, the larger ρ , the more $\hat{\mathbf{R}}_{k-1}$ is used. Furthermore, there is

$$\eta_k = \frac{g(\rho, k)}{g(\rho, k) + L + 1} \tag{3.55}$$

$$\mathbf{B}_{k} = \frac{\mathbf{A}_{s}^{c}}{g\left(\boldsymbol{\rho}, k\right) + L + 1} \tag{3.56}$$

Then Eq. (3.53) is re-expressed as follows

$$\hat{\mathbf{R}}_k = \eta_k \hat{\mathbf{R}}_{k-1} + \mathbf{B}_k \tag{3.57}$$

 $\hat{\mathbf{R}}_k$ can be denoted by the initial MNCM $\hat{\mathbf{R}}_0$ as

$$\hat{\mathbf{R}}_k = \left(\prod_{i=1}^k \eta_i\right) \hat{\mathbf{R}}_0 + \sum_{i=1}^k \left(\prod_{j=i+1}^k \eta_j\right) \mathbf{B}_i$$
 (3.58)

Since $C_i^z \in (0, I)$ in Eq. (3.44), $A_i^c > 0$ and $B_i > 0$. In addition, due to $\eta_i \in (0, 1)$, the MNCM estimate $\hat{\mathbf{R}}_k > 0$ is positive definite in the current interval. Therefore, the numerical stability of the MNCM estimated by the proposed adaptive method is guaranteed.

(2) Computational complexity analysis

This section uses FLOPs to analyze the computational complexity of the proposed RSVBA. The equivalent FLOPs for several matrix operations involved are given in Chapter 2. The FLOPs required for the main parameters of the proposed method are given in Tab. 3.1. According to Tab. 3.1, the FLOPs of the RSVBA is calculated as follows

$$F_{RSVBA} = 7Ln^3 + (4Lm + 2L - 2m)n^2 + (L - 2Lm)n$$

$$-6mn + 2m^3 + (2L + 6)m^2 + (L + 13)m$$
(3.59)

According to the above FLOPs analysis, the computational complexity of RSVBA is $O(n^3)$ and $O(m^3)$. However, due to the fixed-interval smoothing operation, the FLOPs of RSVBA are approximately proportional to the fixed-interval size L, so the computational complexity of the proposed filter increases linearly with L. Therefore, it is generally recommended to choose the sliding window size L in the range [5,20] to achieve a more appropriate computational efficiency and estimation accuracy.

Parameter	FLOPs	Parameter	FLOPs		
$\mathbf{G}_{i-1}^{\mathrm{s}}$	$3n^3-n^2$	$\hat{\mathbf{x}}_{i-1 k}^{\mathrm{s}}$	$2n^2 + n$		
$\mathbf{P}_{i-1 k}^{\mathrm{s}}$	$4n^3$	$\hat{\mathbf{R}}_k$	m^2		
$\hat{\mathbf{U}}_{k k-1}^{L}$	m^2	$\hat{\mathbf{U}}_k^L$	$(L+1)m^2$		
\mathbf{A}_{i}^{c}	$2mn^2 + 2m^2n - mn + 4m^3 - 3m^2 - m$				

Table 3.1: FLOPs for the main adaptation parameters

3.5 Simulation Verification Experiment

3.5.1 Simulation Condition Setting

The vehicle trajectory and sensors specifications in the simulation are the same as those in the section 2.5.1. Then, the sensor noise, filter parameters, and evaluation metrics are set as follows.

- (1) Sensor Noise Settings: To verify the effectiveness of the proposed RSVBA for time-varying MNCM estimation, different sensor noise magnitudes and distributions are set for various periods. An example of sensor noise is shown in Fig. 3.6 (the noise varies in different MC simulations). The specific noise settings are as follows.
 - **Period 1**: From 0 s to 500 s, the sensors are not disturbed by outliers. The probability distribution of the sensor noise is given by

$$p\left(\mathbf{w}_{\text{p1}}^{\text{gnss}}\right) = N\left(0, \mathbf{R}_{k}^{\text{gnss}}\right), p\left(\mathbf{w}_{\text{p1}}^{\text{od}}\right) = N\left(0, \mathbf{R}_{k}^{\text{od}}\right), p\left(\mathbf{w}_{\text{p1}}^{\text{pola}}\right) = N_{\text{mr}}\left(0, t_{\text{au}}, \mathbf{R}_{k}^{\text{pola}}\right)$$
(3.60)

where GNSS positioning noise covariance matrix $\mathbf{R}_k^{\mathrm{gnss}} = \mathrm{diag}\left(\mathbf{r}_k^{\mathrm{gnss}}\right)^2$, according to the sensor specifications, there are $\mathbf{r}_k^{\mathrm{gnss}} = [5\text{m} 5\text{m}]$; OD velocity noise variance $\mathbf{R}_k^{\mathrm{od}} = \mathrm{diag}\left(\mathbf{r}_k^{\mathrm{od}}\right)^2$ with $\mathbf{r}_k^{\mathrm{od}} = 0.01\,\mathbf{v}_{\mathrm{od}}$ based on sensor specifications; POLA heading noise variance $\mathbf{R}_k^{\mathrm{pola}} = (\mathbf{r}_k^{\mathrm{pola}})^2$ with $\mathbf{r}_k^{\mathrm{pola}} = 1\,\mathrm{deg}$ and the related time $t_{\mathrm{au}} = 10\,\mathrm{s}$.

• **Period 2**: GNSS, odometer, and POLA are subject to outliers interference during the simulation from 500 s to 1000 s. The noise probability distribution is given by

$$\begin{cases}
p\left(\mathbf{w}_{p2}^{gsod}\right) = (1 - p_{disb}) N\left(0, \mathbf{R}_{k}^{gsod}\right) + p_{disb} N\left(0, 25 \mathbf{R}_{k}^{gsod}\right) \\
p\left(\mathbf{w}_{p2}^{pola}\right) = (1 - p_{disb}) N_{mr}\left(0, t_{au}, \mathbf{R}_{k}^{pola}\right) + p_{disb} N_{mr}\left(0, t_{au}, 9 \mathbf{R}_{k}^{pola}\right)
\end{cases}$$
(3.61)

where $\mathbf{w}_{p2}^{gsod} = [\mathbf{w}_{p2}^{gnss} \ \mathbf{w}_{p2}^{od}]^T$; $\mathbf{R}_k^{gsod} = \text{diag}([\mathbf{r}_k^{gnss} \ \mathbf{r}_k^{od}])^2$; $p_{disb} = 0.1$ indicates the likelihood of outliers interference.

• **Period 3**: Within 1000 s to 1500 s, the accuracy of GNSS and the POLA decreases due to observation blockage, and the noise standard deviation increases to three times the nominal value, i.e., $\mathbf{R}_k^{\text{gsod}} = \text{diag}\left(\left[3\mathbf{r}_k^{\text{gnss}} \ 3\mathbf{r}_k^{\text{od}}\right]\right)^2$. In addition, each sensor is disturbed by outliers. Thus, the probability density distribution is denoted as follows

$$\begin{cases}
p\left(\mathbf{w}_{p3}^{gsod}\right) = (1 - p_{disb}) \, N\left(0, \mathbf{R}_{k}^{gsod}\right) + p_{disb} \, N\left(0, 25\mathbf{R}_{k}^{gsod}\right) \\
p\left(\mathbf{w}_{p3}^{pola}\right) = (1 - p_{disb}) \, N_{mr}\left(0, t_{au}, 9\mathbf{R}_{k}^{pola}\right) + p_{disb} \, N_{mr}\left(0, t_{au}, 9\mathbf{R}_{k}^{pola}\right)
\end{cases}$$
(3.62)

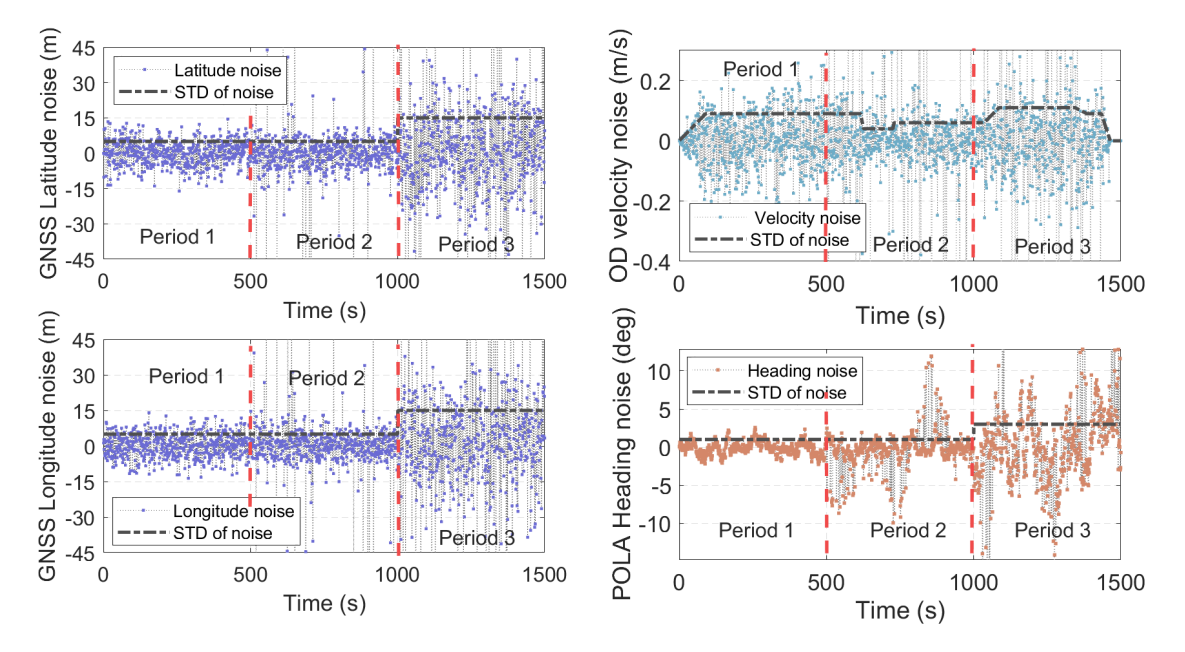


Figure 3.6: Example of sensors noise

(2) Adaptation Methods: The proposed RSVBA is compared with the following existing classical methods to verify its effectiveness: 1) SHA; 2) VBA; 3) ORA[65]. The tuning parameters for the above methods are empirically specified as follows: In the Sage-Husa method, the MNCM initial is $\mathbf{R}_0 = \text{diag}([5\text{m } 5\text{m } 0.05\text{m/s } 1\text{deg}])^2$, and the damping factor is set to b = 0.95; in VBA, the initial of the degree of freedom parameter is $u_k = 10$, the initial of the inverse scaling matrix is $U_k = (u_k - m - 1) \mathbf{R}_0$ and the expansion

coefficient $\rho = 0.95$. ORA uses the square-root similarity function, and the degree of freedom parameters are set to $\omega = 5$ and $\tau_R = 2$. The sliding window size in the proposed RSVBA is set to 10.

(3) Evaluation Indicators: To compare the performance of the proposed method with other methods, 30 MC trials were performed in this simulation to eliminate the randomness of the simulation results (the sensor noise is different in each MC simulation). The root mean square (RMS) is used as the estimation result of MNCM, and the RMSE and ARMSE are used as the evaluation indicators of the estimation accuracy. The RMS is defined as

$$\mathbf{r}_k^{\text{RMS}} = \sqrt{\frac{1}{N_{\text{mc}}} \sum_{s=1}^{N_{\text{mc}}} \left(\hat{\mathbf{r}}_k^s\right)^2}$$
 (3.63)

where N_{mc} is the number of MC trials; $\hat{\mathbf{r}}_k^s$ represents the MNCM estimate at time-step k of the s-th MC trial, reflected in the form of the square root of the diagonal elements, i.e., the noise standard deviation (STD).

3.5.2 Simulation Results and Analysis

The simulation is performed according to the aforementioned settings. First, the MNCM estimation results are analyzed. Then, the robust state estimation results corresponding to the MNCM estimation are analyzed.

(1) Analysis of MNCM adaptation estimation. Fig. 3.7 shows the MNCM estimation of GNSS in the form of noise standard deviations. Similarly, Fig. 3.8 shows the MNCM estimation of OD and POLA. Furthermore, Fig. 3.7 shows the RMSE of the MNCM estimation for GNSS, and Fig. 3.10 shows the RMSE of the MNCM estimation for OD and POLA. In addition, the ARMSE of the MNCM estimation for GNSS, OD and POLA at different periods are shown in Fig. 3.11 and Fig. 3.12, respectively.

As shown in Fig. 3.7 and Fig. 3.8, during period 1, when there is no interference from outliers, each adaptive method can effectively estimate the MNCM, i.e., the noise standard deviation, and achieve accurate identification of the noise statistical parameters. However, in the presence of outliers, each adaptive method exhibits different estimation effects. During period 2, the classical SHA and VBA adaptive methods cannot accurately estimate the MNCM. In detail, as shown in Fig. 3.11 and Fig. 3.12, the ARMSEs of the SHA method for MNCM estimation of GNSS latitude and longitude are 11.571 m and 11.366 m, respectively. The ARMSEs of SHA for OD and POLA MNCM estimation are 0.151m/s and 0.940 deg, respectively. VB has similar MNCM estimation effects to SHA because both

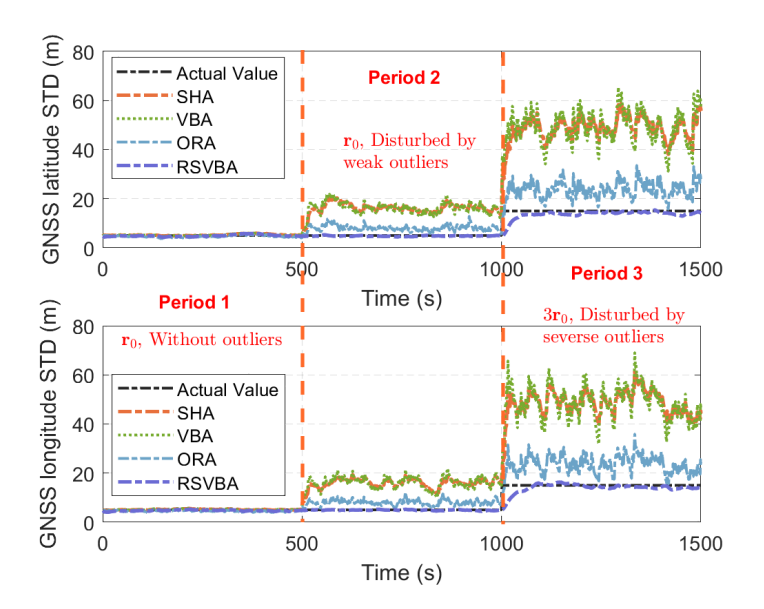


Figure 3.7: MNCM estimation of GNSS

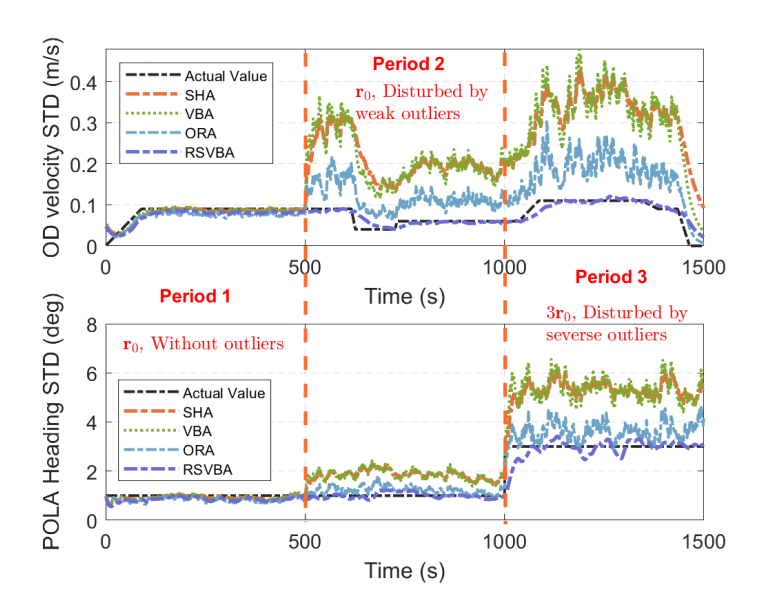


Figure 3.8: MNCM estimation of OD and POLA

SHA and VB rely on accurate noise modeling. However, measurement outliers cause the noise model to mismatch the actual noise cases, resulting in a heavy-tailed distribution of the innovation term. Thus, IW cannot be used as a conjugate prior for the likelihood function, which prevents SHA and VB from accurately identifying the noise statistics.

The ORA method, designed for handling outliers, has a better MNCM estimation effect than SHA in period 2. During this period, the ARMSEs of ORA for GNSS latitude and longitude noise standard deviation estimation are 4.125 m and 4.039 m, respectively, which are 64.4% and 64.5% lower than those of SHA. Additionally, the ARMSEs of ORA

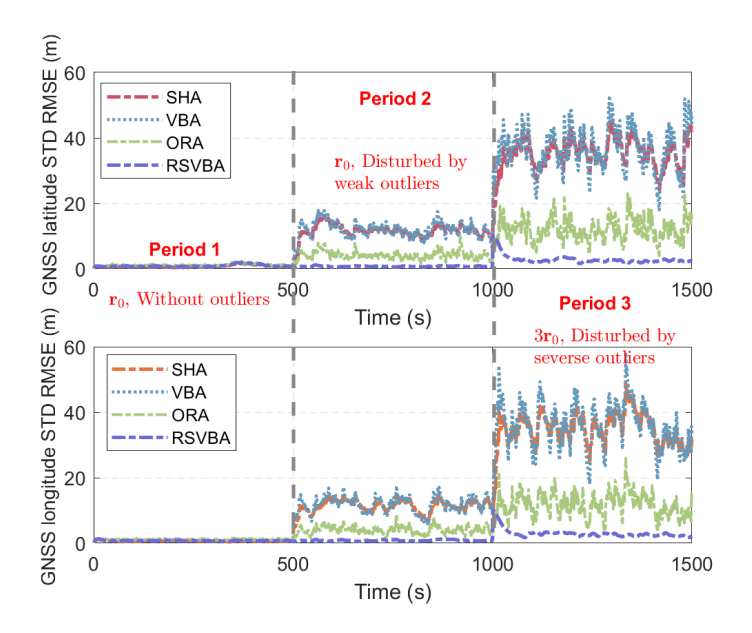


Figure 3.9: RMSE of MNCM estimation for GNSS

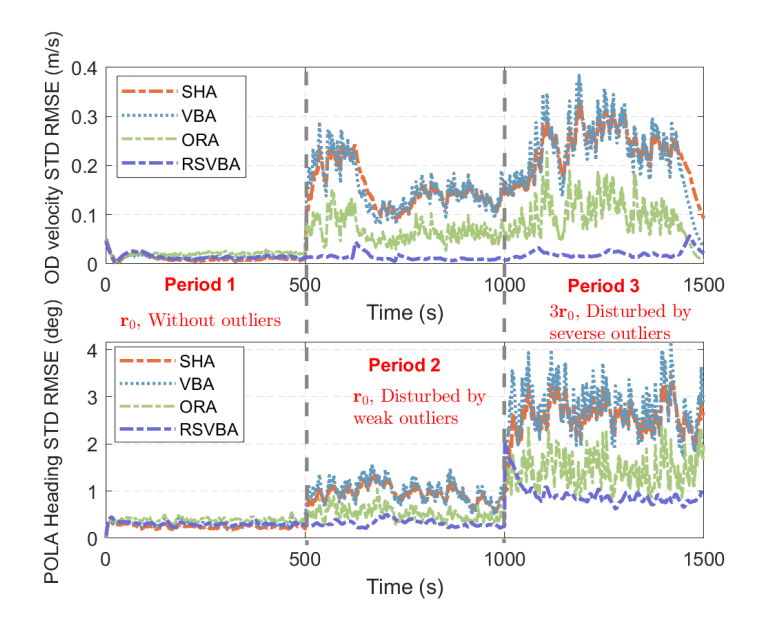


Figure 3.10: RMSE of MNCM estimation for OD and POLA

for OD velocity and POLA heading estimation are 0.067 m/s and 0.517 deg, respectively, which are 55.6% and 45.0% lower than that of SHA, respectively, indicating its robust adaptation ability to MNCM against outlier interference. Furthermore, compared with ORA, the proposed RSVBA method demonstrates superior MNCM adaptive performance under outlier interference. In period 2, the RSVBA estimates of MNCM of GNSS latitude and longitude are 0.751 m and 0.838 m, which are close to the estimation results in non-interference period 1 (0.910 m and 0.775 m), indicating that RSVBA can achieve robust

MNCM estimation under outlier interference. Similarly, for OD velocity and POLA heading in period 2, the MNCM estimates of RSVBA are 0.013 m/s and 0.315 deg, respectively, which are similar to the results of period 1 (0.015 m and 0.301 deg), confirming the robust estimation effect of RSVBA on MNCM in the presence of outliers.

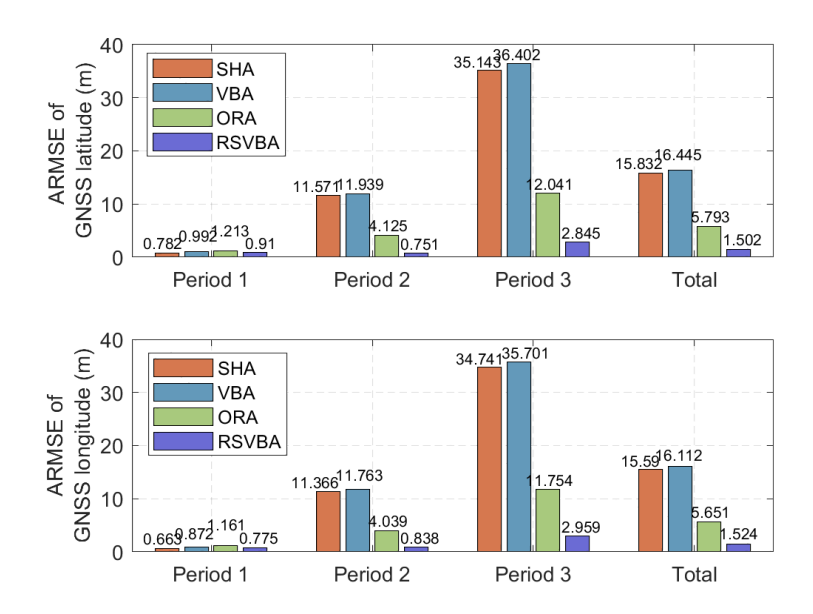


Figure 3.11: ARMSE of MNCM estimation for GNSS with different periods

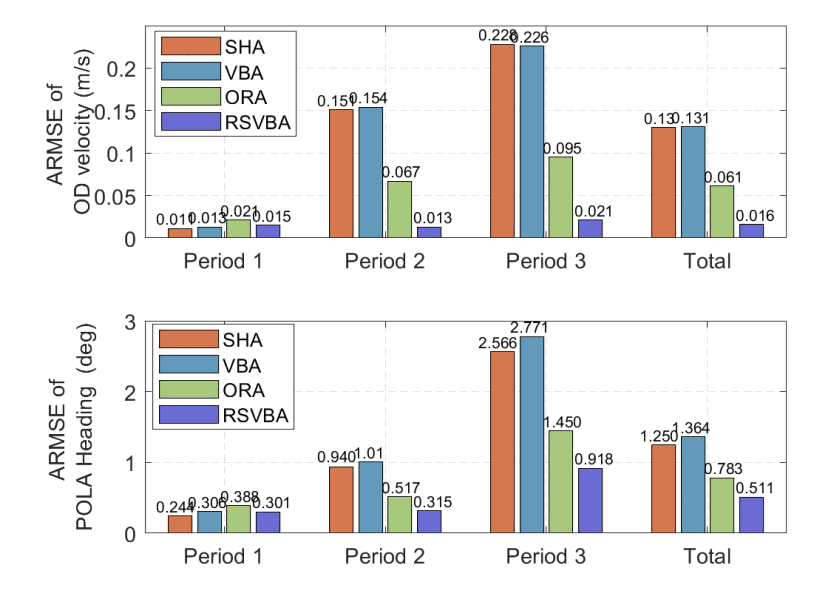


Figure 3.12: ARMSE of MNCM estimation for OD and POLA with different periods

Index	Method	Period 1	Period 2	Period 3	Total
	SHA	0.782	11.571	35.143	15.832
GNSS	VBA	0.992	11.939	36.402	16.445
Latitude (m)	ORA	1.213	4.125	12.041	5.793
	RSVBA	0.910	0.751	2.845	1.502
	SHA	0.663	11.366	34.741	15.590
GNSS	VBA	0.872	11.763	35.701	16.112
Longitude (m)	ORA	1.161	4.039	11.754	5.651
	RSVBA	0.775	0.838	2.959	1.524
	SHA	0.011	0.151	0.228	0.130
OD	VBA	0.013	0.154	0.226	0.131
Velocity (m/s)	ORA	0.021	0.067	0.095	0.061
	RSVBA	0.015	0.013	0.021	0.016
	SHA	0.244	0.940	2.566	1.250
POLA	VBA	0.306	1.010	2.771	1.364
Heading (deg)	ORA	0.388	0.517	1.450	0.783
	RSVBA	0.301	0.315	0.918	0.511

Table 3.2: ARMSE of MNCM estimation

Furthermore, during period 3, the outliers interference further increased, significantly reducing the accuracy of the SHA and VBA methods for estimating MNCM. For instance, the ARMSEs of SHA and VBA for the GNSS latitude noise standard deviation are 35.143 m and 36.402 m, respectively. The ARMSEs of SHA and VBA for POLA heading noise standard deviation are 2.566 deg and 2.771 deg, respectively. As a result, an accurate estimation of MNCM is not achievable. While the adaptation accuracy of the ORA method is improved compared to SHA and VBA, the ARMSE of the ORA method for GNSS latitude and POLA heading is 12.041 m and 1.450 deg, respectively, which still does not meet the accuracy requirements in practical applications. In comparison with other methods, the proposed RSVBA can consistently and accurately estimate MNCM even under severe outlier disturbances. Its ARMSEs for the MNCM estimation of GNSS latitude and longitude are only 2.845 m and 2.959 m, and the MNCM of OD velocity and POLA heading are 0.021 m/s and 0.918 deg, respectively, thereby achieving a more accurate estimation of MNCM.

(2) Analysis of robust state estimation corresponding to MNCM estimation. Fig. 3.13

shows the correntropy values of each measurement under three different cases: the without MNCM adaptation, VBA-based MNCM adaptation, and the proposed RSVBA robust MNCM adaptation method. The cumulative probability distribution of the corresponding correntropy values for each measurement is depicted in Fig. 3.14. The analysis focuses only on GNSS latitude due to its similar noise distribution and analysis results to GNSS longitude. Considering that the position error reflects the overall estimation performance, Fig. 3.15 presents the position estimation results corresponding to different adaptation methods.

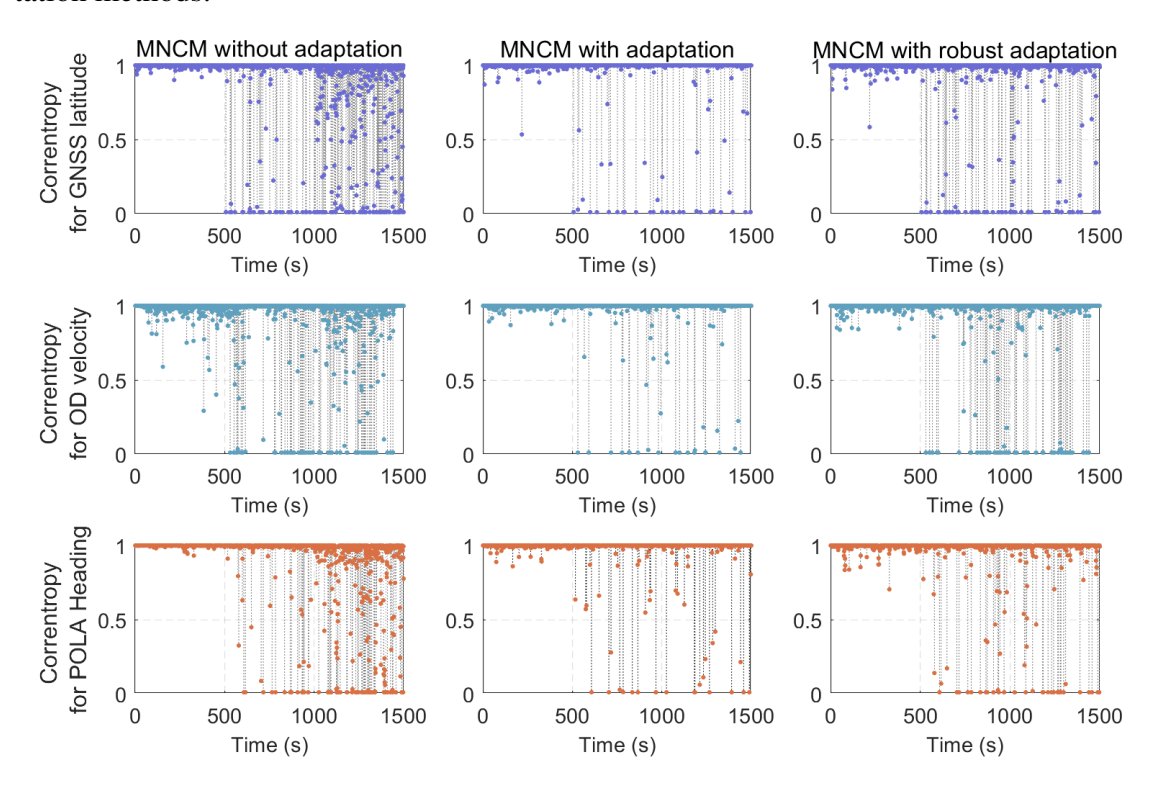


Figure 3.13: Correntropy for each measurement in different cases

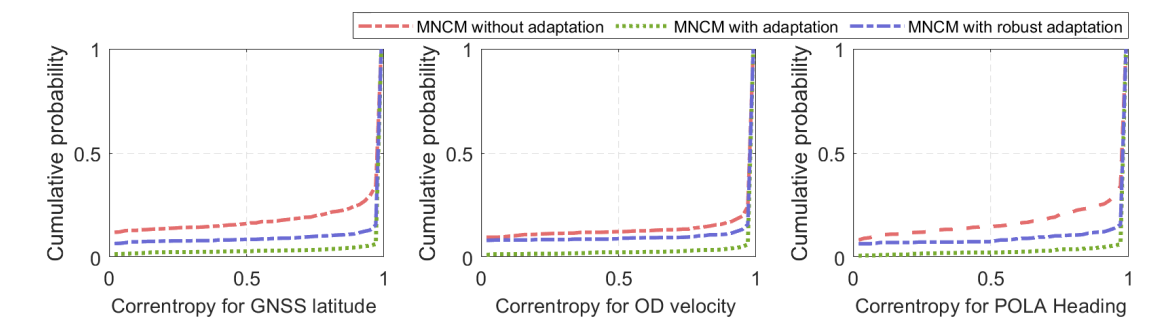


Figure 3.14: Cumulative probability distribution of correntropy for each measurement

As shown in Fig. 3.13, during period 1, when there is no outlier perturbation, the correntropy values of the measurements under different adaptation methods are close to 1, so

the measurement is fully explored to optimize the state estimation. However, if the measurement is disturbed by outliers, the correntropy values are distinct for different adaptation methods. For example, in period 3 (i.e., 1000 s to 1500 s), the correntropy without MNCM adaptation is significantly smaller overall. This is because the noise amplitude increases in period 3, but the MNCM does not adaptation and still maintains a small nominal value, resulting in a significant innovation statistical value. As a result, the measurement tends to be considered an outlier, resulting in a small correntropy value.

In contrast, in the case of MNCM adaptation, the distribution of the correntropy is significantly larger compared to the situation without MNCM adaptation. This is because the MNCM adaptation is disturbed by the outliers, leading to a larger MNCM estimate than the actual value (seen Fig. 3.7 and Fig. 3.8). The larger MNCM makes the statistics of the filtering innovation smaller, and the outliers tend to be ignored, ultimately resulting in a large correntropy. Furthermore, when employing the proposed RSVBA method to robustly estimate the MNCM, the distribution of the correlation can match the simulation setting probability for the outliers. This is due to RSVBA's ability to provide accurate MNCM estimates and utilize filtering innovation statistics to detect outliers accurately, thus calculating reliable correntropy and suppressing the interference of outliers on MNCM estimation.

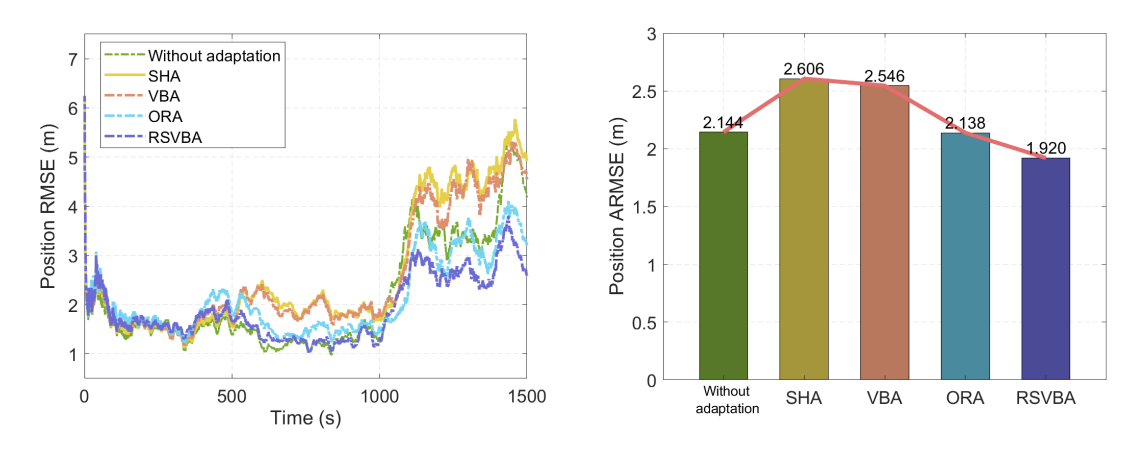


Figure 3.15: Position error for different adaptation methods

As shown in Fig. 3.15, the position ARMSE is 2.144 m without MNCM estimation. Due to the inaccurate estimation of MNCM under outlier interference, both SHA and VBA not only fail to improve the state estimation accuracy, but also decrease the robustness of position estimation. In contrast, since the interference of measurement outliers on MNCM estimation is accurately suppressed, robust adaptive MNCM estimation is achieved. The position ARMSE of RSVBA is reduced to 1.920 m, which is 26.3%, 24.6%, and 10.2%

3.6. Summary 75

lower than that of SHA (2.606 m), VBA (2.546 m), ORA (2.138 m) respectively, with better robust estimation accuracy. This verifies the effectiveness of the proposed adaptation algorithm.

3.6 Summary

This chapter presents a robust noise adaptation algorithm to suppress outlier perturbations on the MNCM estimation. First, the problem of INMS noise adaptation is formulated, and the joint variational approximation principle and its limitation in INMS are analyzed. Then, a robust variational approximation adaptation algorithm based on MCC is proposed. A joint variational approximation analytical solution for the MNCM and smoothing state is derived. The inverse scale matrix of the IW distribution is reconstructed based on the correntropy matrix to suppress the interference of measurement outliers on the MNCM estimation. Meanwhile, the performance of the proposed adaptive method is analyzed theoretically. Finally, simulation experiments are conducted to verify the effectiveness of the proposed method. The experimental results show that, compared to the SHA, VBA, and ORA methods, the proposed RSVBA has higher estimation accuracy for MNCM in the presence of outliers, and the corresponding position estimation ARMSE is reduced by 26.3%, 24.6%, and 10.2%, respectively, indicating better robust estimation accuracy. This demonstrates that the proposed RSVBA can effectively suppress the interference of measurement outliers on MNCM estimation and verifies its effectiveness.

Chapter 4

Autonomous State Integrity Monitoring Algorithm for Multiple Fault Assumption

4.1 Introduction

In addition to high-accuracy positioning, it is also necessary to effectively quantitatively evaluate the confidence of the position solution through integrity monitoring to ensure vehicle navigation safety in adverse urban areas. IM methods for filtering sequential framework in INMS are extensions of the RAIM methods developed for aviation applications in GNSS, which rely on the assumption of a maximum number of missing detection biases. Unlike aviation applications, where the low failure rate of satellites allows a single-fault assumption to satisfy integrity risk requirements, the increasing number and types of INMS sensors raise the likelihood of data errors and outlier disturbances, rendering the single-fault assumption inapplicable for INMS in urban areas. Furthermore, in the presence of outliers, the Gaussian assumption used by existing IM methods cannot accurately characterize the actual noise distribution, making it impossible to compute reliable HPL for assessing position reliability.

This chapter presents a sequential IM method based on multiple fault-missing detection assumptions to effectively assess the position estimation of INMS in urban areas. First, the integrity monitoring problem is formulated. The maximum slope-based IM is introduced, and its limitations in INMS are analyzed. Then, a sequential IM method based on multiple fault assumptions is proposed. The IM dynamic regression model is built using a consistent posterior estimate provided by the proposed robust filter. A consistency factor in the state domain is calculated using the sequential probability ratio over sliding windows. Under the multiple fault-missing detection assumption, the HPL is calculated based on the maximum eigenvalue combined with the consistency factor to quantitatively evaluate the confidence of the position solution. Finally, simulation experiments are conducted to verify the effectiveness of the proposed method.

4.2 Analysis of the INMS Integrity Monitoring Problem

IM includes the FDE process and the HPL calculation. First, the severe fault bias is eliminated through FDE. Then, the HPL is calculated as a quantitative indicator to assess the confidence level of the position solution. Therefore, as a key technique for IM, this section focuses on the analysis of horizontal protection level calculation issues. The HPL calculation principle is given in Fig. 4.1.



Figure 4.1: HPL calculation principle

(1) First, determine the relationship between the state estimation error and the detection statistics raised by the measurement noise bias. Consider the following regression observation equation as

$$\mathbf{y}_k = \mathbf{C}_k \mathbf{x}_k + \mathbf{v}_k \tag{4.1}$$

where \mathbf{y}_k is the measurement vector at time-step k; \mathbf{v}_k is the measurement noise and is assumed to follow a Gaussian distribution $\mathbf{v}_k \sim N(0, \mathbf{V}_k)$. Therefore, the state estimation can be obtained by the weighted least squares algorithm as [74]

$$\hat{\mathbf{x}}_k = \mathbf{A}_k \mathbf{y}_k = \left(\mathbf{C}_k^{\mathrm{T}} \mathbf{W}_k \mathbf{C}_k \right)^{-1} \mathbf{C}_k^{\mathrm{T}} \mathbf{W}_k \mathbf{y}_k \tag{4.2}$$

where $\mathbf{A}_k = \left(\mathbf{C}_k^{\mathrm{T}} \mathbf{W}_k \mathbf{C}_k\right)^{-1} \mathbf{C}_k^{\mathrm{T}} \mathbf{W}_k$ represents the mapping matrix from the measurement domain to the state domain; $\mathbf{W}_k = \mathbf{V}_k^{-1}$ indicates the measurement weighting matrix. Based on Eq. (4.2), the state estimation error is calculated as Eq. (4.3). This equation essentially reveals the state estimation error caused by the measurement noise bias \mathbf{v}_k .

$$\tilde{\mathbf{x}}_{k} = \hat{\mathbf{x}}_{k} - \mathbf{x}_{k} = \left(\mathbf{C}_{k}^{\mathrm{T}} \mathbf{W}_{k} \mathbf{C}_{k}\right)^{-1} \mathbf{C}_{k}^{\mathrm{T}} \mathbf{W}_{k} \left(\mathbf{y}_{k} - \mathbf{C}_{k} \mathbf{x}_{k}\right) = \mathbf{A}_{k} \mathbf{v}_{k} \tag{4.3}$$

Furthermore, the measurement residuals calculated from the state estimation are

$$\mathbf{r}_k = \mathbf{y}_k - \mathbf{C}_k \hat{\mathbf{x}}_k = \mathbf{C}_k \mathbf{x}_k + \mathbf{v}_k - \mathbf{C}_k \hat{\mathbf{x}}_k = (\mathbf{I} - \mathbf{C}_k \mathbf{A}_k) \mathbf{v}_k \tag{4.4}$$

Then, the detection statistic is calculated as

$$s_k = \mathbf{r}_k^{\mathrm{T}} \mathbf{W}_k \mathbf{r}_k = \mathbf{v}_k^{\mathrm{T}} \mathbf{S}_k \mathbf{v}_k \tag{4.5}$$

where $\mathbf{S}_k = (\mathbf{I} - \mathbf{C}_k \mathbf{A}_k)^{\mathrm{T}} \mathbf{W}_k (\mathbf{I} - \mathbf{C}_k \mathbf{A}_k)$. The relationship between the state estimation error and the detection statistics raised by the measurement noise bias is determined by Eq. (4.3) and Eq. (4.5).

(2) The minimum detectable bias is the detection statistic of the outlier bias that cannot be detected under the specified false alarm rate and missed detection rate. First, the fault detection threshold T_d is determined at a specified false alarm rate. Then, the minimum detectable bias is determined based on T_d and the specified missed detection rate. Specifically, a binary hypothesis is defined: a) The hypothesis of outlier-free in the measurement H_0 ; and b) The hypothesis of outlier bias in measurement H_1 . For different hypotheses, the statistic s_k follows different distributions, specified as follows

$$\begin{cases}
H_0: \mathbf{E}[\mathbf{v}_k] = 0, \ s_k \sim \chi^2(\nu) \\
H_1: \mathbf{E}[\mathbf{v}_k] \neq 0, \ s_k \sim \chi^2(\nu, \lambda)
\end{cases}$$
(4.6)

where $\chi^2(v)$ denotes the central chi-square distribution with v degrees of freedom; $\chi^2(v,\lambda)$ denotes the non-central chi-square distribution with v degrees of freedom and a non-central parameter $\lambda = E[\mathbf{v}_k]$.

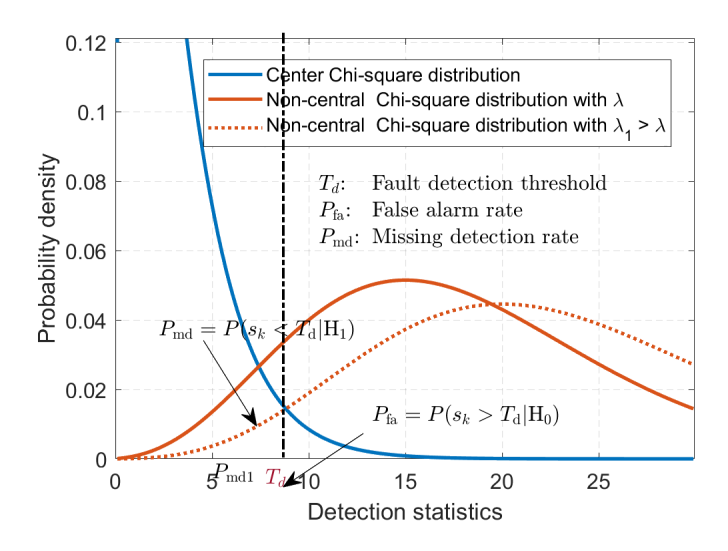


Figure 4.2: Center and non-center Chi-square probability distribution

a) Under the H_0 hypothesis, if a fault bias is detected, it refers to a false alarm. With a specified false alarm rate P_{fa} , s_k satisfies the following [77]

$$P(s_k < T_d | H_0) = \int_0^{T_d} p_{\chi^2(v)}(x) dx = 1 - P_{fa}$$
 (4.7)

where $p_{\chi^2(\nu)}(x) = \frac{1}{2^{\frac{\nu}{2}}\Gamma(\frac{\nu}{2})}x^{\frac{\nu}{2}-1}\exp\left(-\frac{1}{2}x\right)$ denotes the PDF of central chi-square distribution with degrees of freedom ν [118]; The $\Gamma(\cdot)$ is the Gamma function; $T_{\rm d}$ represents the threshold for fault detection, i.e. the quantile of $p_{\chi^2(\nu)}$ at a confidence level of $1-P_{\rm fa}$. $T_{\rm d}$ can be uniquely determined for a specified $P_{\rm fa}$.

b) Under the hypothesis of H_1 , the IM accounts for the missing detection of fault bias, i.e., these are faults that are not detected. In detail, if the measurement is disturbed by a fault bias \mathbf{f}_k , then according to Eq. (4.5), s_k is calculated as

$$s_k = (\mathbf{v}_k + \mathbf{f}_k)^{\mathrm{T}} \mathbf{S}_k (\mathbf{v}_k + \mathbf{f}_k)$$
 (4.8)

where s_k follows a non-central chi-square distribution. Then, with a specified missed detection rate P_{md} , s_k satisfies the following

$$P(s_k < T_d | H_1) = \int_0^{T_d} p_{\chi^2_{(v,\lambda)}}(x) dx = P_{md}$$
 (4.9)

where $p_{\chi^2_{(\nu,\lambda)}}(x) = \frac{1}{2} \left(\frac{x}{\lambda}\right)^{\frac{\nu-2}{4}} \exp\left[-\frac{1}{2}(x+\lambda)\right] I_{\frac{\nu}{2}-1}(\sqrt{\lambda x})$ indicating a non-central chi-square distribution PDF. The non-central parameter λ can be determined by half-search methods, etc., while $T_{\rm d}$ and $P_{\rm md}$ are specified.

- Fig. 4.2 plots the above central and non-central chi-square probability distributions. With specified $P_{\rm fa}$ and $P_{\rm md}$, the non-central chi-square distribution $p_{\chi^2_{(\nu,\lambda)}}$ and the corresponding non-central parameter λ are uniquely determined. Comparing the two non-central chi-square probability curves, once the detection statistic λ_1 is greater than λ , the corresponding missed detection rate $P_{\rm md1}$ will be less than $P_{\rm md}$, which cannot meet the specified missed detection rate. Therefore, λ essentially represents the minimum detectable bias (or the maximum undetectable bias) of missing detection.
- (3) Based on the minimum detectable bias, the maximum potential (position) error, i.e., the HPL, can be calculated under the fault missing detection assumption. Since the actual HPE is known, the HPL is used to evaluate the unknown HPE by providing a reliable range for the vehicle position and reflecting the confidence in the position solution. Fig. 4.3 shows the relationship between HPL, HPE, and HAL. As shown in Fig. 4.3, with a certain integrity risk, the position solution will generally be within the HPL boundary in case 1. If the HPL is unreliable, it may be unable to effectively overbound the HPE, i.e., the HPE is greater than the HPL in case 2, so the HPL cannot reflect the confidence of the position solution. In the worst case, the HPE exceeds the HAL, but the HPL is still less than the HAL, which will lead to hazardous misleading information (HMI) in case 3. In this case,

the position solution is not unreliable, but the system still cannot issue an alarm and switch to the safe driving mode, which seriously undermines navigation safety.

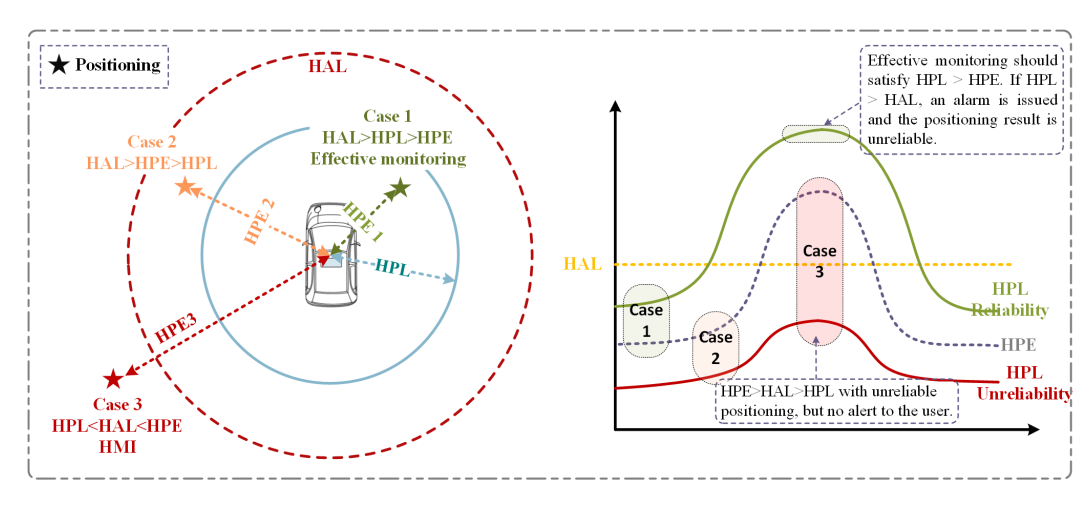


Figure 4.3: The relationship between HPL, HPE, and HAL

4.3 Integrity Monitoring Method With Biases Projections

This section presents the common integrity monitoring used in filter frames for multisensor integrated navigation. Then, the limitations of its application in INMS are analyzed.

4.3.1 Protection Level Calculation Based on Maximum Slope

The HPL calculation is the key technique in IM. In IM applied to multi-sensor integrated navigation, the HPL calculation is common based on the maximum slope method developed in RAIM. It defines the slope as the ratio of statistically independent HPE and filtering innovation detection statistics [119]. The measurement with the maximum slope is most susceptible to missing detection. Then, the HPL is calculated by the maximum slope and the maximum undetectable bias λ . Specifically, the method relies on the single-fault assumption of the observation source, i.e., there is a missed fault in observation after FDE. Assuming that there is a missed fault bias b_i in the i-th observation at moment k, and expressing the fault vector as $\mathbf{f}_k = \mathbf{T}_i^z b_i$, thus the detection statistic is calculated based on Eq. (4.5) as

$$s_k = \mathrm{E}\left[\left(\mathbf{v}_k + \mathbf{f}_k\right)^{\mathrm{T}} \mathbf{S}_k \left(\mathbf{v}_k + \mathbf{f}_k\right)\right] = \mathbf{S}_{ii,k} b_i^2$$
(4.10)

where $S_{ii,k}$ denotes the *i*-th diagonal element of S_k . Further, the HPE caused by fault bias b_i is calculated. Based on Eq. (4.3), the state estimation error induced by b_i is denoted as

$$\tilde{\mathbf{x}}_k^{\mathrm{b}} = \mathbf{A}_k \mathbf{f}_k = \mathbf{A}_k \mathbf{T}_i^{\mathrm{z}} b_i \tag{4.11}$$

In INMS, the position error vector $\tilde{\mathbf{p}}_k = \left[\delta p_k^{\rm e} \ \delta p_k^{\rm n}\right]^{\rm T}$ is obtained by

$$\tilde{\mathbf{p}}_k = \mathbf{T}_p^x \tilde{\mathbf{x}}_k^b = \mathbf{T}_p^x \mathbf{A}_k \mathbf{T}_i^z b_i \tag{4.12}$$

where \mathbf{T}_p^x denotes the mapping matrix of $\tilde{\mathbf{p}}_k$ from the state vector $\tilde{\mathbf{x}}_k^b$. Then the HPE is calculated by $\tilde{\mathbf{p}}_k$ as

$$\delta p^{b} = \sqrt{\tilde{\mathbf{p}}_{k}^{T} \tilde{\mathbf{p}}_{k}} = b_{i} \sqrt{(\mathbf{T}_{i}^{z})^{T} \mathbf{A}_{k}^{T} (\mathbf{T}_{p}^{x})^{T} \mathbf{T}_{p}^{x} \mathbf{A}_{k} \mathbf{T}_{i}^{z}} = b_{i} \sqrt{\mathbf{A}_{(p_{e},i),k}^{2} + \mathbf{A}_{(p_{n},i),k}^{2}}$$
(4.13)

where $\mathbf{A}_{(p_{\rm e},i),k}$ and $\mathbf{A}_{(p_{\rm n},i),k}$ denote the elements $(p_{\rm e},i)$ and $(p_{\rm n},i)$ of the mapping matrix \mathbf{A}_k , respectively. Then, the linear mapping ratio (i.e., the slope) between the detection statistic and potential position error caused by b_i can be obtained based on Eq. (4.10) and Eq. (4.13) as [80, 91]

$$SLOP_{i} = \sqrt{\frac{\mathbf{A}_{(p_{e},i),k}^{2} + \mathbf{A}_{(p_{n},i),k}^{2}}{\mathbf{S}_{ii,k}}}$$
(4.14)

The measurement element with the maximum slope has the smallest detection statistic, which is the most likely to be missed in FDE. Therefore, the maximum slope $SLOP_{max}$ is used to calculate the HPL. In addition, with the specified P_{fa} and P_{md} , the non-central parameter λ is uniquely determined as the maximum undetectable bias. Therefore, HPL is calculated as

$$HPL = SLOP_{\text{max}}\sqrt{\lambda}$$
 (4.15)

4.3.2 Limitations Analysis for Integrity Monitoring in INMS

The IM method based on RAIM has limitations when it comes to implementing INMS in urban areas. These limitations are as follows.

- (1) The above IM method assumes a single-fault missing case based on Eq. (4.10). However, in urban areas with an increasing number and types of INMS sensors, the likelihood of data errors and outlier interference rises, making the single-fault assumption invalid. Consequently, the IM method cannot calculate a reliable HPL for evaluating position solution confidence and monitoring navigation integrity.
- (2) The slope calculation relies on an assumption of noisy Gaussian distribution with known statistics based on Eq. (4.2) and Eq. (4.14). However, in the presence of outliers, the Gaussian assumption used by existing IM methods cannot accurately characterize the actual noise distribution, resulting in an inaccurate covariance matrix due

- to the inconsistent state a posteriori estimation. In this case, it is infeasible to calculate a reliable HPL for evaluating position solution confidence.
- (3) The HPL is mainly dominated by protecting against potential fault biases under fault-bias missed detection assumptions. Indeed, the position estimation uncertainty (i.e., MSE) during the iterations of sequential filtering also plays an important role for PL. Therefore, HPL should protect against both fault bias and position uncertainty based on estimation consistency.

4.4 Sequential Multiple Fault-Biases based Integrity Monitoring

The above common IM principle is based on the RAIM developed for aviation applications, where the HPL is mainly dominated by protecting against potential fault biases under missed detection assumptions. Indeed, position estimation uncertainty (i.e., MSE) during the iterations of sequential filtering also plays an important role for HPL. Based on the definition, the estimation consistency can reflect the characterization effect of filter-MSE on the actual PE distribution. Therefore, with higher consistency, HPL can be primarily dominated by the MSE as a statistical bound for PE. In practice, however, factors such as a mismatch of noise models due to fault interference or incorrect filter parameters can lead to poor estimation consistency, making the MSE-induced HPL fail to evaluate the actual PE. Moreover, faults are more likely to be missing-detected because the state estimate has been contaminated by outliers. Therefore, in addition to the estimation uncertainty, it is necessary to protect against PE induced by potential multi-fault further based on the consistency level. This approach, which is based on the consistency level, provides a more reliable and accurate HPL to envelop the PE while reducing the redundancy space of HPL, improving the IM availability under multi-fault assumptions. Therefore, based on this motivation, the principle of HPL calculation is formulated as [120]

$$HPL = \underset{s_{k} \in (0, T_{d})}{arg \max} \left\{ \left(\delta p^{n} | H_{0} \right) + w \left(\eta \right) \left(\delta p^{b} | H_{1} \right) \right\}$$

$$(4.16)$$

where the term $\delta p^{\rm n}$ is the MSE-induced HPL against the estimation uncertainty; $\delta p^{\rm b}$ is the HPL against the multiple fault biases. Different from aviation applications, due to the outlier disturbances and a priori state errors in challenging urban areas, the missing assumption of multiple fault biases needs to be considered for reliable HPL; $w(\cdot)$ is a weight function for $\delta p^{\rm b}$ regarding the consistency level indicator η .

Based on the above motivation, we propose a multi-biases sequential integrity monitoring method (MSIM) in the section. First, the IM dynamic regression model is constructed by a consistent posterior estimate provided by the proposed robust filter. Then, the estimation consistency in the state domain is detected based on the sequential probability ratio over sliding windows. PL is determined based on the innovation-based maximum eigenvalue under multi-fault assumption combined with the consistency factor. Fig. 4.4 shows the structure of the proposed IM method.

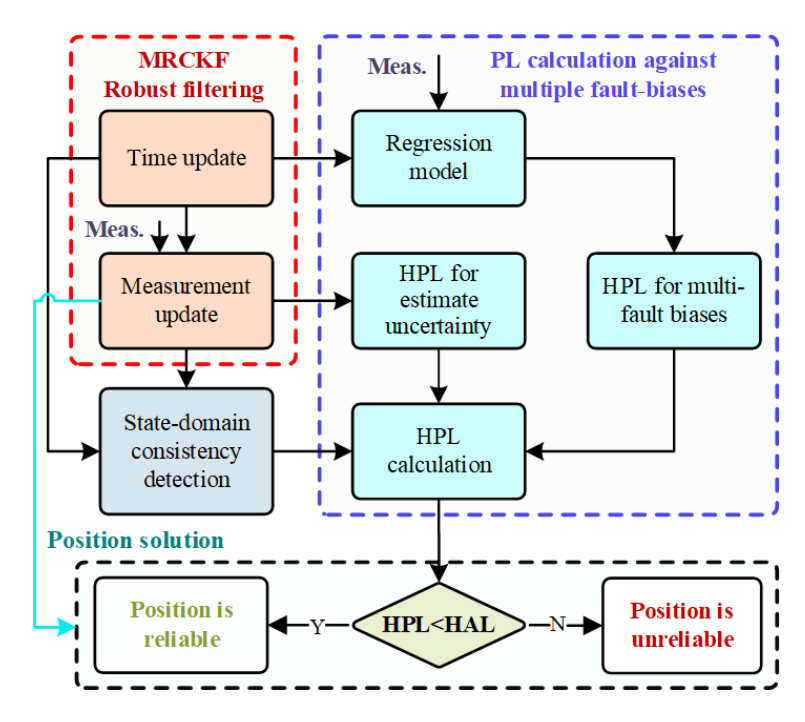


Figure 4.4: The diagram of the proposed method

4.4.1 IM Regression Model Based on Consistent Estimation

The estimation consistency is defined as the quantitative conformity of the filter MSE and the actual MSE of state vector [105], which is essential for protection level. A posterior state estimation consistency of the proposed MRCKF is analyzed in the Theorem 2.2. It is demonstrated that the MRCKF provides more consistent a posteriori estimation results. Therefore, the IM regression model is constructed based on MRCKF. Specifically, the filter-based state space model is first converted to a least-squares regression model. Consider the following discrete-time stochastic state space model as

$$\begin{cases} \mathbf{x}_k = \mathbf{f}_k(\mathbf{x}_{k-1}) + \mathbf{w}_{k-1}^x \\ \mathbf{z}_k = \mathbf{h}_k(\mathbf{x}_k) + \mathbf{w}_k^z \end{cases}$$
(4.17)

where $\mathbf{x}_k \in \mathbb{R}^n$ and $\mathbf{z}_k \in \mathbb{R}^m$ are the state and the measurement vector at discrete-time step k; $\mathbf{w}_{k-1}^x \sim \mathrm{N}(\mathbf{0}, \mathbf{Q}_{k-1})$ and $\mathbf{w}_{k-1}^z \sim \mathrm{N}(\mathbf{0}, \mathbf{R}_k)$ are the uncorrelated process and measurement noise with known covariance matrix \mathbf{Q}_{k-1} and \mathbf{R}_k , respectively. Then, the prior state mean $\hat{\mathbf{x}}_{k|k-1}$ and its covariance matrix $\mathbf{P}_{k|k-1}$ are obtained as

$$\hat{\mathbf{x}}_{k|k-1} = \int_{\mathbb{R}^n} \mathbf{f}_k(\mathbf{x}_{k-1}) \, \mathbf{N}(\hat{\mathbf{x}}_{k-1}, \mathbf{P}_{k-1}) \, d\mathbf{x}_{k-1}$$
(4.18a)

$$\mathbf{P}_{k|k-1} = \int_{\mathbb{R}^n} \mathbf{f}_k(\mathbf{x}_{k-1}) \mathbf{f}_k^{\mathrm{T}}(\mathbf{x}_{k-1}) N(\hat{\mathbf{x}}_{k-1}, \mathbf{P}_{k-1}) d\mathbf{x}_{k-1} - \hat{\mathbf{x}}_{k|k-1} \hat{\mathbf{x}}_{k|k-1}^{\mathrm{T}} + \mathbf{Q}_{k-1}$$
(4.18b)

where $N(\hat{\mathbf{x}}_{k-1}, \mathbf{P}_{k-1})$ is obtained by MRCKF. Then, the prior state estimate is regarded as an additional measurement vector, and the state space model Eq. (4.17) is constructed as a regression model for the weighted least squares form, i.e.

$$\begin{bmatrix} \mathbf{z}_k \\ \hat{\mathbf{x}}_{k|k-1} \end{bmatrix} = \begin{bmatrix} \mathbf{H}_k \\ \mathbf{I}_n \end{bmatrix} \mathbf{x}_k + \begin{bmatrix} \mathbf{w}_k^z \\ \mathbf{w}_k^x \end{bmatrix}$$
(4.19)

where \mathbf{H}_k is the Jacobi matrix expanded at $\hat{\mathbf{x}}_{k|k-1}$ for $\mathbf{h}_k(\cdot)$, which can be computed by the posterior statistical linearization method of section 3.4.3. Further, Eq. (4.19) can be expressed in the following form

$$\mathbf{y}_k = \mathbf{C}_k \mathbf{x}_k + \mathbf{v}_k \tag{4.20}$$

where $\mathbf{y}_k \in \mathbb{R}^{m+n}$ denotes the joint observation vector of a prior state and measurement at time-step k; \mathbf{v}_k is the joint observation noise, which follows the distribution as

$$\mathbf{v}_{k} \sim \mathbf{N}(0, \mathbf{V}_{k}), \ \mathbf{V}_{k} = \begin{bmatrix} \mathbf{R}_{k} & \mathbf{0} \\ \mathbf{0} & \mathbf{P}_{k|k-1} \end{bmatrix}$$
 (4.21)

4.4.2 Estimation Consistency Detection Based on Sequential Probability Ratio in State-Domain

The common method for consistency detection is to check the measurement innovation using a distribution whiteness test (e.g., chi-square test). Still, it suffers from the following problems: 1) the consistency level of the measurement domain is not equivalent to the state (position) domain of interest in IM, so it is not feasible to indirectly reflect the consistency of the position estimation through the innovation sequence [105]; 2) the chi-square test has reliable detection performance against mutation error. However, under the slowly growing error that is hardly suppressed by robust filters, the chi-square test cannot effectively detect the estimation consistency level. To this end, we propose a state-domain

consistency detection method based on the sequential probability ratio over a sliding window against challenging slowly growing errors.

First, in the presence of outliers, the measurement is modeled at time-step $i \in [k-L+1,k]$ within the sliding window as follows

$$\mathbf{z}_i = \mathbf{H}_i \, \mathbf{x}_i + \mathbf{w}_i^z + \mathbf{f}_i^z \tag{4.22}$$

where \mathbf{f}_i^z is a faults-bias. Then, based on Algorithm 4, the difference between state a priori and a posteriori is calculated as

$$d\mathbf{x}_i = \hat{\mathbf{x}}_i - \hat{\mathbf{x}}_{i|i-1} = \delta \mathbf{x}_i - \delta \mathbf{x}_{i|i-1} + \mathbf{f}_i^x$$
(4.23)

where $\mathbf{f}_i^x = \mathbf{G}_i \mathbf{f}_i^x$. Then, a sequence $\{d\mathbf{x}_i | i = k - L + 1, ..., k\}$ is used to detect consistency with computational efficiency more reliably. In case without error disturbance in the sequence (i.e., $\mathbf{f}_i^x = \mathbf{0}$), the consistency is optimal and the sequence mean is $\mathbb{E}[d\mathbf{x}] = \mathbf{0}$. Thus, $d\mathbf{x}_i$ follows a zero-mean Gaussian distribution with covariance \mathbf{P}_i^{dx} , i.e., $d\mathbf{x}_i \sim N(\mathbf{0}, \mathbf{P}_i^{dx})$. Conversely, when estimation is inconsistent due to slowly growing errors, there is

$$\mathbb{E}\left[d\mathbf{x}\right] = \bar{\mathbf{f}}_{i}^{x} \neq \mathbf{0}, \mathbb{E}\left[\left(d\mathbf{x}_{i} - \bar{\mathbf{f}}_{i}^{x}\right)^{\mathrm{T}}\left(d\mathbf{x}_{i} - \bar{\mathbf{f}}_{i}^{x}\right)\right] = \mathbf{P}_{i}^{\mathrm{dx}}$$
(4.24)

Then, a binary hypothesis is defined as 1) H_0^c : The hypothesis of consistency; 2) H_1^c : The hypothesis of inconsistency. Based on the above distribution, $d\mathbf{x}_i$ has different probability functions under different hypotheses, as follows.

$$P(\mathbf{d}\mathbf{x}_i \mid \mathbf{H}_0^{\mathrm{c}}) = \mathbf{U}_i \cdot \exp\left(-\frac{1}{2}\mathbf{d}\mathbf{x}_i^{\mathrm{T}}(\mathbf{P}_i^{\mathrm{dx}})^{-1}\mathbf{d}\mathbf{x}_i\right)$$
(4.25)

$$P(\mathbf{d}\mathbf{x}_i \mid \mathbf{H}_1^{\mathbf{c}}) = \mathbf{U}_i \cdot \exp\left(-\frac{1}{2}(\mathbf{d}\mathbf{x}_i - \bar{\mathbf{f}}_i^{\mathbf{x}})^{\mathrm{T}}(\mathbf{P}_i^{\mathrm{dx}})^{-1}(\mathbf{d}\mathbf{x}_i - \bar{\mathbf{f}}_i^{\mathbf{x}})\right)$$
(4.26)

where $\mathbf{U}_i = 2\pi^{-n_s/2} (\mathbf{P}_i^{\mathrm{dx}})^{-1/2}$; $\bar{\mathbf{f}}_i^{\mathrm{x}} = \sum_{j=k-L+1}^k \mathrm{d}\mathbf{x}_j/L$; The covariance matrix is obtained by proposed MRCKF as

$$\mathbf{P}_{k}^{\text{dx}} = \mathbb{E}\left[d\mathbf{x} d\mathbf{x}^{\text{T}} \mid \mathbf{z}_{k}\right]$$

$$= \mathbb{E}\left[\left(\mathbf{G}_{k}\left(\mathbf{z}_{k} - \hat{\mathbf{z}}_{k}\right)\right)\left(\mathbf{G}_{k}\left(\mathbf{z}_{k} - \hat{\mathbf{z}}_{k}\right)\right)^{\text{T}}\right]$$

$$= \mathbf{G}_{k}\left(\mathbf{H}_{k}\mathbf{P}_{k|k-1}\mathbf{H}_{k}^{\text{T}} + \mathbf{R}_{k}\left(\mathbf{C}_{k}^{z}\right)^{-1}\right)\mathbf{G}_{k}^{\text{T}}$$
(4.27)

Thus, the probability ratio of the two hypotheses over the sliding window is given by [121]

$$\bar{p}_{k} = \frac{P(d\mathbf{x}_{k-L+1}, \cdots, d\mathbf{x}_{k} \mid \mathbf{H}_{1}^{c})}{P(d\mathbf{x}_{k-L+1}, \cdots, d\mathbf{x}_{k} \mid \mathbf{H}_{0}^{c})} = \prod_{i=k-L+1}^{k} \frac{P(d\mathbf{x}_{i} \mid \mathbf{H}_{1}^{c})}{P(d\mathbf{x}_{i} \mid \mathbf{H}_{0}^{c})}$$
(4.28)

Furthermore, the logarithmic operation on \bar{p}_k yields

$$\bar{r}_k = |\ln(\bar{p}_k)| = \sum_{i=k-L+1}^k |\Delta r_i|$$
 (4.29)

where the ratio increment Δr_i is calculated as

$$\Delta r_i = \frac{1}{2} d\mathbf{x}_i^{\mathrm{T}} (\mathbf{P}_i^{\mathrm{dx}})^{-1} d\mathbf{x}_i - \frac{1}{2} (d\mathbf{x}_i - \bar{\mathbf{f}}_i^{\mathrm{x}})^{\mathrm{T}} (\mathbf{P}_i^{\mathrm{dx}})^{-1} (d\mathbf{x}_i - \bar{\mathbf{f}}_i^{\mathrm{x}})$$
(4.30)

The probability ratio calculation is illustrated in Fig. 4.5. Then, the consistency factor is defined as

$$\eta = \bar{r}_k \cdot T_{\text{cons}}^{-1} \tag{4.31}$$

where $T_{\rm cons}$ is the consistency detection threshold, obtained by [122]

$$T_{\rm cons} = \ln\left(\frac{1 - P_{\rm md}}{P_{\rm fa}}\right) \tag{4.32}$$

The factor η quantifies the consistency of the estimates. As η becomes smaller, the consistency of the estimates improves. Conversely, if η is greater than 1, the estimates are inconsistent, indicating that the filter MSE does not represent the actual state error distribution.

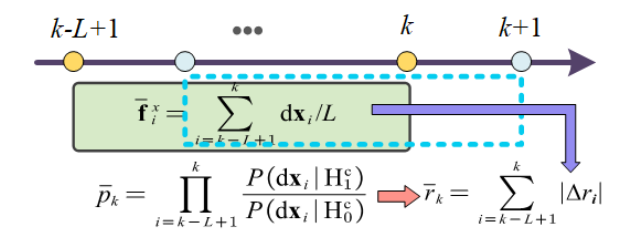


Figure 4.5: Testing statistics for state consistency within sliding windows

4.4.3 PL Calculation Based on Maximum Eigenvalue against Multi-Biases

As an upper bound on the potential HPE, the HPL is determined under the multiple fault-biases missed detection hypothesis. Based on Eq. (4.16), HPL includes protection against estimation uncertainty and multiple fault biases, which are separately calculated as follows.

(1) **HPL against estimate uncertainty:** Under the faults-free hypothesis, HPE is approximated to follow a Gaussian distribution. i.e., $\delta p_k \sim N\left(0, \mathbf{P}_{\delta p_k}\right)$, where $\mathbf{P}_{\delta p_k} \approx \left(\sigma_{\mathrm{n},k}^2 + \sigma_{\mathrm{e},k}^2\right)$,

 $\sigma_{n,k}$ and $\sigma_{e,k}$ are the standard deviation of east and north PE. In the case of consistent state estimation, the covariance of actual PE covariance is equivalent to the filter-indicated MSE. Therefore, the HPL for estimation uncertainty is calculated as

$$\delta p_k^{\rm n} = -Q^{-1} \left(\frac{P_{\rm fa}}{2} \right) \sqrt{\mathbf{P}_k^{\rm e} + \mathbf{P}_k^{\rm n}} \tag{4.33}$$

where $Q^{-1}(\cdot)$ denotes the inverse function of the normal distribution CDF that determines the quantile; $\mathbf{P}_k^{\mathrm{e}}$ and $\mathbf{P}_k^{\mathrm{n}}$ are the filter-indicated MSE of the east and north position error, respectively. In fact, δp_k^{n} can be regarded as the protection for the random noise part of the PE with error bias when subjected to outlier interference. Furthermore, the protection for the maximum PE error bias is given below.

(2) HPL against multiple fault biases: First, a mapping relationship is established between the HPE and the detection statistics caused by multi-fault biases. Then, based on the mapping relationship, the HPL is computed by a non-central parameter λ . Specifically, assuming there are r measurement error biases and denoted by $\mathbf{f}^b \in \mathbb{R}^r$, the fault vector is then denoted by

$$\mathbf{f}_k = \mathbf{T}_k^z \mathbf{f}_k^b \tag{4.34}$$

where \mathbf{T}_k^z denotes the mapping matrix from the multi-fault bias projects to the fault vector. Then, the measurement vector is denoted as

$$\mathbf{y}_k = \mathbf{C}_k \mathbf{x}_k + \mathbf{v}_k + \mathbf{f}_k \tag{4.35}$$

Based on Eq. (4.3), the state estimation error caused by outliers is

$$\tilde{\mathbf{x}}_k^{\mathrm{b}} = \mathbf{A}_k \mathbf{f}_k = \mathbf{A}_k \mathbf{T}_k^{\mathrm{z}} \mathbf{f}_k^{\mathrm{b}} \tag{4.36}$$

Thus, the position error vector $\tilde{\mathbf{p}}_k = [\delta p_k^e \ \delta p_k^n]^T$ is calculated as

$$\tilde{\mathbf{p}}_k = \mathbf{T}_p^x \tilde{\mathbf{x}}_k^b = \mathbf{T}_p^x \mathbf{A}_k \mathbf{T}_k^z \mathbf{f}_k^b \tag{4.37}$$

The HPL arising from the multiple fault biases is calculated as

$$\delta p^{b} = \sqrt{\tilde{\mathbf{p}}_{k}^{T} \tilde{\mathbf{p}}_{k}} = \sqrt{(\mathbf{f}_{k}^{b})^{T} (\mathbf{T}_{k}^{z})^{T} \mathbf{D}_{k} \mathbf{T}_{k}^{z} \mathbf{f}_{k}^{b}}$$
(4.38)

where $\mathbf{D}_k = \mathbf{A}_k^{\mathrm{T}} (\mathbf{T}_p^x)^{\mathrm{T}} \mathbf{T}_p^x \mathbf{A}_k = \mathbf{W}_k \mathbf{C}_k (\mathbf{C}_k^{\mathrm{T}} \mathbf{W}_k \mathbf{C}_k)^{-1} (\mathbf{T}_p^x)^{\mathrm{T}} \mathbf{T}_p^x (\mathbf{C}_k^{\mathrm{T}} \mathbf{W}_k \mathbf{C}_k)^{-1} \mathbf{C}_k^{\mathrm{T}} \mathbf{W}_k$. Further, the detection statistic due to the multiple fault biases is determined. According to Eq. (4.29),

the residual is calculated as

$$\mathbf{r}_k = (\mathbf{I} - \mathbf{C}_k \mathbf{A}_k) \, \mathbf{f}_k \tag{4.39}$$

Based on the established dynamic regression model, the residual \mathbf{r}_k consists of state and measurement residuals. Since the sensor outliers only interfere with the measurement, the residuals need to be extracted in \mathbf{r}_k , i.e.,

$$\mathbf{r}_{k}^{z} = \mathbf{L}_{z}\mathbf{r}_{k} \tag{4.40}$$

For example, when latitude and longitude (error) are used as the external measurement, the extraction matrix is expressed as

$$\mathbf{L}_{z} = \begin{bmatrix} 1 & 0 & \mathbf{0}_{1 \times n} \\ 0 & 1 & \mathbf{0}_{1 \times n} \end{bmatrix}_{2 \times (m+n)}$$

$$(4.41)$$

Thus, the statistic caused by the outlier disturbance is calculated as

$$s_k^z = (\mathbf{r}_k^z)^{\mathrm{T}} \mathbf{W}_k^z \mathbf{r}_k^z = (\mathbf{f}_k^{\mathrm{b}})^{\mathrm{T}} (\mathbf{T}_k^z)^{\mathrm{T}} \mathbf{S}_k^z \mathbf{T}_k^z \mathbf{f}_k^{\mathrm{b}}$$
(4.42)

where $\mathbf{W}_{k}^{z} = (\mathbf{R}_{k})^{-1}$; \mathbf{S}_{k}^{z} is calculated as

$$\mathbf{S}_{k}^{z} = (\mathbf{I} - \mathbf{C}_{k} \mathbf{A}_{k})^{\mathrm{T}} \mathbf{L}_{z}^{\mathrm{T}} \mathbf{W}_{k}^{z} \mathbf{L}_{z} (\mathbf{I} - \mathbf{C}_{k} \mathbf{A}_{k})$$
(4.43)

In addition, the non-central parameter λ can be uniquely determined with a specified P_{fa} and P_{md} by such as the half-interval search method, which is formulated as

$$\lambda = \inf \left\{ \int_0^{T_d} f_{\chi^2_{(n,\lambda)}}(x) \, \mathrm{d}x \leqslant P_{\mathrm{md}} \right\}$$
 (4.44)

where $T_{\rm d} = \sqrt{\chi_n^{-2} (1 - P_{\rm fa})}$ is a quantile corresponding $P_{\rm fa}$; $\chi_n^{-2} (\cdot)$ is the inverse chi-squared CDF with n degrees of freedom. From the previous analysis in Eq. (4.10), λ is essentially the maximum undetectable bias subject to $P_{\rm fa}$ and $P_{\rm md}$. Therefore, due to the statistical independence [80] between the HPE and the statistics value, the following constraint problem holds by Eq. (4.38) and Eq. (4.42) as

$$\begin{cases} \delta p^{b} = \max_{\mathbf{T}_{k}^{z} \in \mathbf{T}_{k}} \sqrt{(\mathbf{f}_{k}^{b})^{T} (\mathbf{T}_{k}^{z})^{T}} \mathbf{D}_{k} \mathbf{T}_{k}^{z} \mathbf{f}_{k}^{b} \\ \text{s.t.} \Rightarrow (\mathbf{f}_{k}^{b})^{T} (\mathbf{T}_{k}^{z})^{T} \mathbf{S}_{k}^{z} \mathbf{T}_{k}^{z} \mathbf{f}_{k}^{b} = \lambda \end{cases}$$

$$(4.45)$$

By offsetting the fault vector \mathbf{f}_k^b , Eq. (4.45) can be transformed into the unconstrained problem, which is

$$\delta p_k^{\mathsf{b}} = \sqrt{\Lambda_{\mathsf{max}}(\Sigma_k)} \sqrt{\lambda} \tag{4.46}$$

where $\Lambda_{\max}(\cdot)$ denotes the maximum eigenvalue; Σ_k is calculated as

$$\Sigma_k = \left(\mathbf{T}_k^z\right)^{\mathrm{T}} \mathbf{D}_k \mathbf{T}_k^z \left(\left(\mathbf{T}_k^z\right)^{\mathrm{T}} \mathbf{S}_k^z \mathbf{T}_k^z\right)^{-1}$$
(4.47)

Based on Eq. (4.46), the maximum position error under the multi-fault bias missing detection assumption, i.e., HPL, is determined by the non-central parameter λ . Fig. 4.6 shows the relationship of PL for multiple fault biases, eigenvalue, and the non-central parameter. It can be seen from Fig. 4.6 that by numerically solving for the maximum eigenvalue, PL against the multiple fault biases can be determined based on the non-central parameter λ .

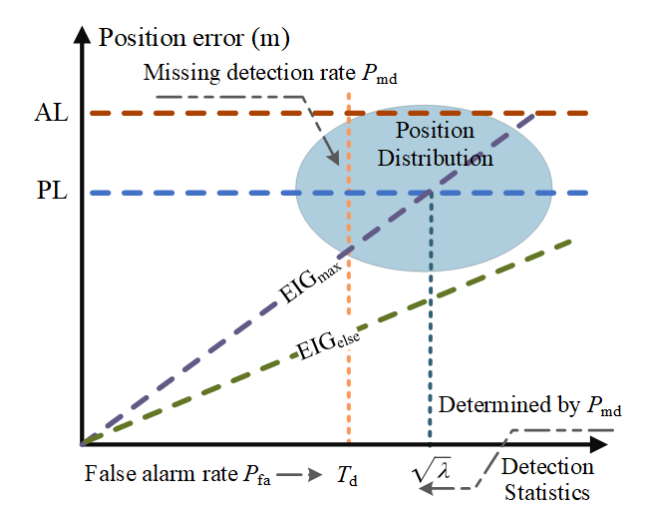


Figure 4.6: The relationship of PL for multiple fault-biases, eigenvalue, and the non-central parameter

(3) Overall HPL determination: Under the multi-fault assumption, the HPL $\delta p_k^{\rm n}$ and $\delta p_k^{\rm b}$ protect the random noise and error bias terms of the PE, respectively. Therefore, based on Eq. (4.33) and Eq. (4.46), the overall PL is obtained by combining the consistency factor η , which is given by

$$HPL = \delta p_k^{\rm n} + w(\eta) \cdot \delta p_k^{\rm b}$$
 (4.48)

where the weighting function is defined as

$$w(\eta) = \min(\eta^2, 1) \tag{4.49}$$

When the consistency factor is small, the weight of δp_k^{b} is also smaller, so HPL can be primarily dominated by the MSE-induced δp_k^{n} since the filter-indicated MSE can effectively represent the distribution of the actual position error. Conversely, as the consistency factor increases, due to unexpected non-Gaussian noise interference as well as a priori state error bias, the weight of $\delta p_k^{\rm b}$ also increases to protect against the potential bias of the HPE in addition to the protecting HPE against random noise via the MSE-induced $\delta p_k^{\rm n}$.

```
Algorithm 5: One-time step calculation of HPL
```

```
Input: \hat{\mathbf{x}}_k, \mathbf{P}_k, P_{\mathrm{fa}}, P_{\mathrm{md}}, Degrees of freedom v, Consistency factor \eta
        Output: Protection level HPL
         /* Calculate non-center parameter
                                                                                                                                                                                                                               */
  1: [\lambda, T_d] = \text{ncx2ncp}(P_{fa}, P_{md}, v)
        /* Calculate HPL
                                                                                                                                                                                                                               */
 2: \delta p_k^{\mathrm{n}} = -Q^{-1} \left( \frac{P_{\mathrm{fa}}}{2} \right) \sqrt{\mathbf{P}_k^{\mathrm{e}} + \mathbf{P}_k^{\mathrm{n}}}
 3: \mathbf{C}_k = \begin{bmatrix} \mathbf{H}_k^{\mathrm{T}} \ \mathbf{I}_n \end{bmatrix}^{\mathrm{T}}, \mathbf{W}_k = \mathrm{diag} \left( \begin{bmatrix} \mathbf{R}_k \ \mathbf{P}_{k|k-1} \end{bmatrix} \right)^{-1}
 4: \mathbf{A}_k = (\mathbf{C}_k^{\mathrm{T}} \mathbf{W}_k \mathbf{C}_k)^{-1} \mathbf{C}_k^{\mathrm{T}} \mathbf{W}_k
 5: \mathbf{D}_k = \mathbf{A}_k^{\mathrm{T}} \left( \mathbf{T}_n^{\mathrm{x}} \right)^{\mathrm{T}} \mathbf{T}_n^{\mathrm{x}} \mathbf{A}_k
 6: \mathbf{S}_{k}^{z} = (\mathbf{I} - \mathbf{C}_{k} \mathbf{A}_{k})^{\mathrm{T}} \mathbf{L}_{z}^{\mathrm{T}} \mathbf{W}_{k}^{z} \mathbf{L}_{z} (\mathbf{I} - \mathbf{C}_{k} \mathbf{A}_{k})
 7: \Sigma_k = (\mathbf{T}_k^z)^{\mathrm{T}} \mathbf{D}_k \mathbf{T}_k^z \left( (\mathbf{T}_k^z)^{\mathrm{T}} \mathbf{S}_k^z \mathbf{T}_k^z \right)^{-1}
 8: \delta p_k^{\rm b} = \sqrt{\Lambda_{\rm max}(\Sigma_k)} \sqrt{\lambda}
 9: HPL = \delta p_k^{\rm n} + \min(\eta^2, 1) \cdot \delta p_k^{\rm b}
10: Function [\lambda, T_d] = \text{ncx2ncp}(P_{fa}, P_{md}, v)
                  T_{\rm d} = {\rm chi2inv} \left(1 - P_{\rm fa}, v\right)
                  \lambda_{\min} = 0, \lambda = \lambda_{\max} = 500
12:
                  Pcdf = ncx2cdf(T<sub>d</sub>,v,\lambda)
13:
                  while abs(Pcdf - P_{md}) > 0.01P_{md} do
14:
                            if Pcdf > P<sub>md</sub> then \lambda_{\min} = \lambda;
15:
                           else \lambda_{\text{max}} = \lambda;
16:
                          \lambda = (\lambda_{max} + \lambda_{min})/2
                           Pcdf = ncx2cdf(T<sub>d</sub>,\nu,\lambda)
18:
                  end
19:
20: end
```

4.4.4 Multi-Fault Mapping Matrix Determination

In order to calculate the HPL using the equation Eq. (4.34), it is necessary to determine the number of missing faults and the corresponding mapping matrix. In the state-of-the-art methods, the number of missing faults is determined by assigning a prior fault probability to each sensor based on the integrity risk [93]. The fault mapping matrix is then determined by permutations. For example, with a missing fault r, it is necessary to compute $N_f = 1 + C_m^1 + ... + C_m^r$ permutations corresponding to the position error and choose the maximum among them as the HPL. However, in the case of INMS in urban areas, the fault prior probability of each sensor is not available due to changes in dynamic observation scenarios. Furthermore, with the increase in the number and types of INMS sensors in urban areas, so does the likelihood of data errors and outlier interference, resulting in a greater number of fault permutations and imposing a heavy computational burden.

The purpose of determining the fault mapping matrix is to find the combination of fault measurements that causes the largest position error. In GNSS, the effect of measurements on the position varies according to the satellite's spatial position. Whereas the measurement model is fixed in INMS. Therefore, the combination of measurement information can be determined based on the degree of observability of the measurement with respect to state (i.e., position error in INMS). To this end, the number of fault biases is first determined. Given the robustness against outlier of the front-end robust filtering and the accurate state a priori propagation of INMS, the faults outliers are detected by a chi-square test based on the filtering innovation term, and the detection statistic is calculated as

$$s_{i,k}^{f} = \tilde{\mathbf{z}}_{i,k}^{2} \mathbf{P}_{ii,zz}^{-1}, \text{ for } i \in [1, m]$$
 (4.50)

where $\tilde{\mathbf{z}}_{i,k}$ denotes the *i*-th element of the innovation $\tilde{\mathbf{z}}_k$; $\mathbf{P}_{ii,zz}$ is the *i*-th diagonal element of the covariance matrix of the innovation. The number of faults is determined by comparing $s_{i,k}^{\mathrm{f}}$ with the fault detection threshold T_{d} . The method determines the multi-fault mapping matrix while avoiding the permutations, thus improving the computational efficiency.

4.5 Simulation Verification Experiment

4.5.1 Simulation Condition Setting

The vehicle trajectory and sensors specifications in the simulation are the same as those in the section 2.5.1. Then, the sensor noise, IM method parameters, and evaluation metrics are set as follows.

(1) Sensor Noise Settings: Integrity monitoring focuses more on the reliability of HPL in adverse scenarios, i.e., the ability to overbound and quantitatively evaluate the HPE to ensure navigation safety. To this end, this experiment simulates a more adverse noise condition to verify the reliability of HPL. Specifically, two sets of simulation experiments with different noise types and disturbances are set up as follows.

Case 1: GNSS, OD, and POLA are disturbed by outliers during different periods. The noise probability distribution is expressed as

$$\begin{cases}
p\left(\mathbf{w}_{k}^{\text{gsod}}\right) = (1 - p_{\text{disb}}) \, \mathrm{N}\left(0, \mathbf{R}_{k}\right) + p_{\text{disb}} \, \mathrm{N}\left(0, 100 \, \mathbf{R}_{k}\right) \\
p\left(\mathbf{w}_{k}^{\text{pola}}\right) = (1 - p_{\text{disb}}) \, \mathrm{N}_{\text{mr}}\left(0, t_{\text{au}}, \mathbf{R}_{k}^{\text{pola}}\right) + p_{\text{disb}} \, \mathrm{N}_{\text{mr}}\left(0, t_{\text{au}}, 25 \, \mathbf{R}_{k}^{\text{pola}}\right)
\end{cases}$$
(4.51)

where $\mathbf{w}_k^{\mathrm{gsod}} = \left[\mathbf{w}_k^{\mathrm{gnss}} \; \mathbf{w}_k^{\mathrm{od}}\right]^{\mathrm{T}}$; $\mathbf{R}_k = \mathrm{diag}\left(\left[\mathbf{r}_k^{\mathrm{gnss}} \; \mathbf{r}_k^{\mathrm{od}}\right]\right)^2$, based on sensors specifications, there is $\mathbf{r}_k^{\mathrm{gnss}} = [5 \mathrm{m} \; 5 \mathrm{m}]$, $\mathbf{r}_k^{\mathrm{od}} = 0.01 \, \mathbf{v}_{\mathrm{od}}$; $\mathbf{R}_k^{\mathrm{pola}} = (\mathbf{r}_k^{\mathrm{pola}})^2$ is the heading noise covariance, $\mathbf{r}_k^{\mathrm{pola}} = 1 \, \mathrm{deg}$, relevant time setting $t_{\mathrm{au}} = 10 \, \mathrm{s}$; The p_{disb} denotes the probability of outlier interference, which is $p_{\mathrm{disb}} = 0.1$ for $0 \, \mathrm{s}$ to $1000 \, \mathrm{s}$ and increases to $p_{\mathrm{disb}} = 0.5$ for $1000 \, \mathrm{s}$ to $1500 \, \mathrm{s}$. An example of noise for case 1 is shown in Fig. 4.7.

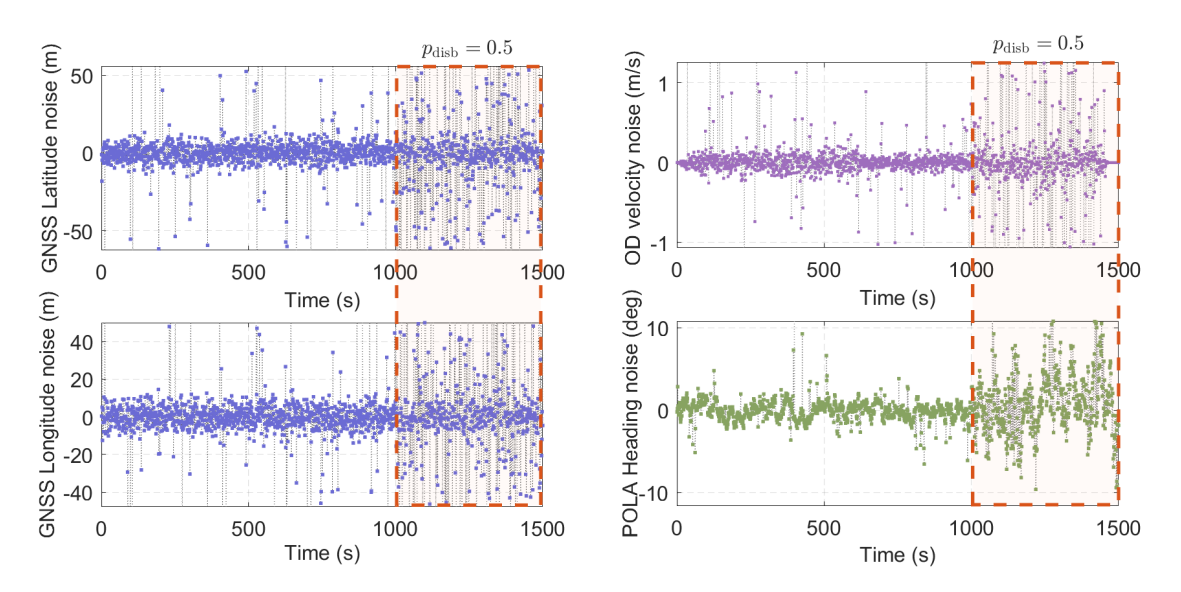


Figure 4.7: Example of sensor noise for case 1

Case 2: GNSS, OD, and POLA are disturbed by outliers during different periods, and the noise probability distribution is the same as case 1. Nevertheless, from 600 s to 900 s, GNSS and POLA are blocked and cannot provide measurement data. An example of noise for case 2 is shown in Fig. 4.8.

(2) IM Methods: The proposed MSIM is compared with the following methods to validate its effectiveness: 1) k-Sigma [80, 81], which calculates the PL directly using the state covariance matrix of CKF based on a fixed state-space model; 2) KSIM [90], which

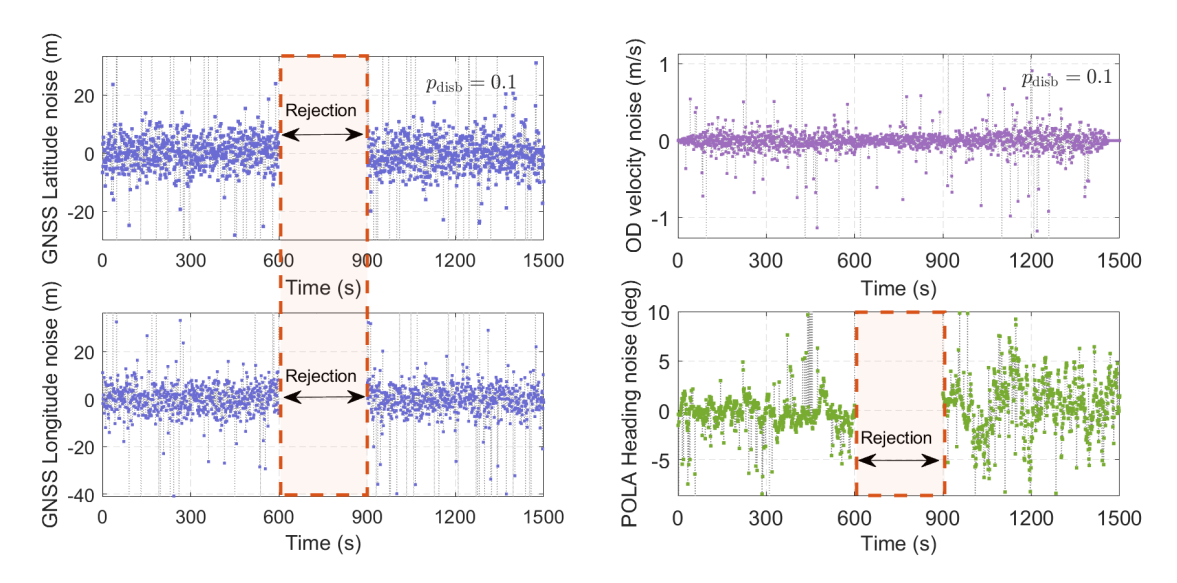


Figure 4.8: Example of sensor noise of case 2

employs a maximum slope-based single-fault hypothesis method within the filtering framework, incorporating the maximum possible position bias along with the estimation uncertainty of CKF; 3) RSIM, which utilizes the consistent state covariance matrix provided by MRCKF, applying the single-fault assumption method that combines the maximum possible position bias with the estimation uncertainty of MRCKF. The settings for the filter parameters are the same as in subsection 2.5.1. The IM parameters are then set as follows: In k-sigma, the scalar factor is set to k = 4; The false alarm rate is set to $P_{\rm fa} = 10^{-4}$; The missing detection rate is set to $P_{\rm md} = 10^{-4}$; With the specified $P_{\rm fa}$ and $P_{\rm md}$, the non-central parameter for the INMS model is $\lambda = 102.41$. In addition, the HAL for in-vehicle route navigation is set to HAL=20 m according to the U.S. Federal Radionavigation Program [123].

(3) Evaluation Indicators: In contrast to the overall error distribution concerned in state estimation accuracy, IM requires a reasonable overbound of HPL to HPE and focuses on whether HPL can effectively evaluate the position confidence. Therefore, the protection level reliability (PLR) and the probability of HMI event are used to assess the IM algorithm [124, 94]. Specifically, HPL reliability is the probability that the HPL can effectively overbound the HPE. The higher the PLR is, the more reliable the HPL is. Moreover, the HMI event refers to a case where the PE exceeds the AL, but the PL is still less than the AL, which is defined in section 4.2. In this case, the position solution is not unreliable, but the system still cannot issue an alarm and switch to the safe mode, which seriously undermines navigation safety. Therefore, the probability of HMI should be as low as possible to ensure navigation safety. Fig. 4.9 reflects the relationship of the above indicator. These indicators

are defined as

$$\begin{cases} P_{\text{PLR}} = \frac{N_{\{\text{HPL}>\text{HPE}\}}}{N_{\text{e}}} \times 100\% \\ P_{\text{HMI}} = \frac{N_{\{\text{HPE}>\text{HAL}\}\cap\{\text{HPL}<\text{HAL}\}}}{N_{\text{e}}} \times 100\% \end{cases}$$

$$(4.52)$$

where P_{PLR} and P_{HMI} are the HPL reliability and the probability of the HMI event, respectively; $N_{\{\cdot\}}$ denotes the number of cases; N_e denotes total number of epochs.

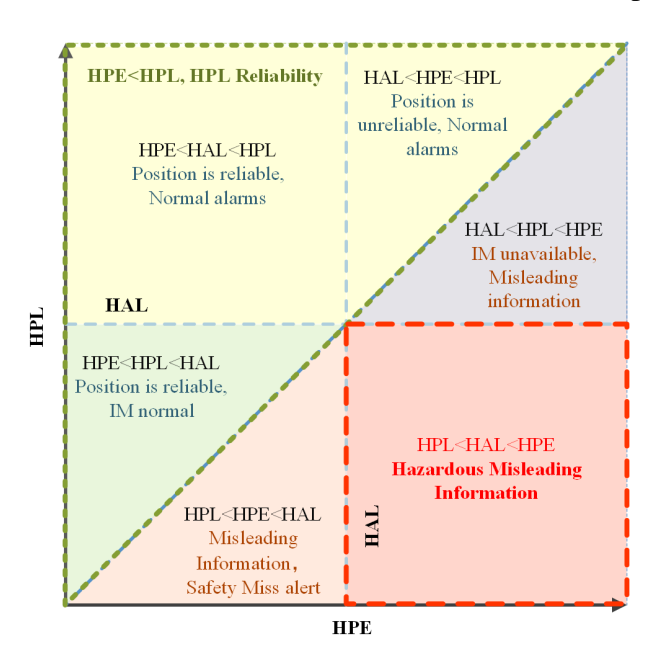


Figure 4.9: IM Stanford diagram

4.5.2 Simulation Results and Analysis

(1) Results and analysis of Case 1: Fig. 4.10 shows the HPE and HPL results of a single MC trial in case 1 to intuitively demonstrate the relationship between HPL and HPE. In addition, Fig. 4.11 shows the cumulative probability distributions of the difference between HPL and HPE (combined MC test results) for different IM methods to reflect the reliability of HPL in case 1. Fig. 4.12 plots the Stanford diagram for the different IM methods. In addition, the indicators of different IM methods are listed in Tab. 4.1.

From Fig. 4.10, in the presence of unmodeled outliers, there is an estimation inconsistency of the CKF due to the inability to incorporate the effect of the outliers on the state estimation. As a result, the HPL of the k-Sigma method cannot overbound and evaluate the HPE of the CKF, especially in the presence of severe outlier disturbances (i.e., between 1000 s and 1500 s). This means that k-Sigma cannot accurately evaluate position confidence and monitor the navigation integrity of INMS. In comparison, KSIM provides a

reliable HPL. However, KSIM only considers the maximum potential position error based on the predetermined statistical model and does not consider the impact of unmodeled outliers. Consequently, the HPL of KSIM still falls short of bounding the HPE in the presence of outliers, and the confidence of the position solution cannot be effectively evaluated.

Compared to CKF, which calculates the state MSE using a predetermined statistical model, MRCKF has improved estimation consistency by dynamically adjusting the state MSE based on external noise situations. Therefore, the HPL of RSIM based on MRCKF can efficiently exceed the HPE from 0 s to 1000 s. However, for severe outliers (1000 s to 1500 s), the RSIM method cannot effectively evaluate the HPE because it only considers the single fault missing detection. Then, MSIM provides a more reliable HPL by considering multiple fault assumptions and position estimation uncertainty. Consequently, MSIM can effectively evaluate the HPE and monitor position integrity, thereby enhancing navigation safety.

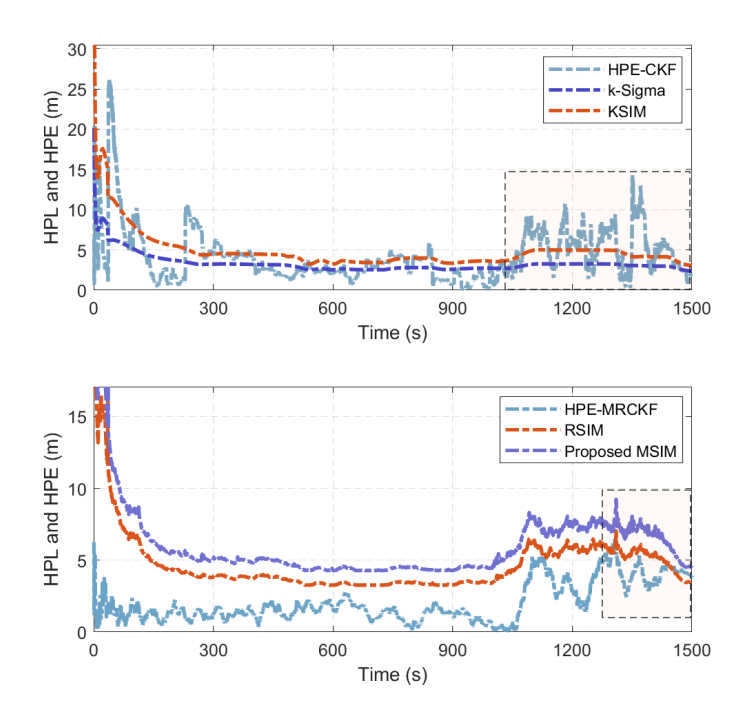


Figure 4.10: HPL and HPE in case 1

In addition, according to Fig. 4.11, different IM methods have different HPL reliability. Specifically, for the k-sigma and KSIM methods, there is a 40.12% and 25.31% probability that HPL is lower than HPE (i.e., the gray shaded area on the left), which corresponds to HPL reliabilities of 59.88% and 74.69%, respectively. This indicates that HPL

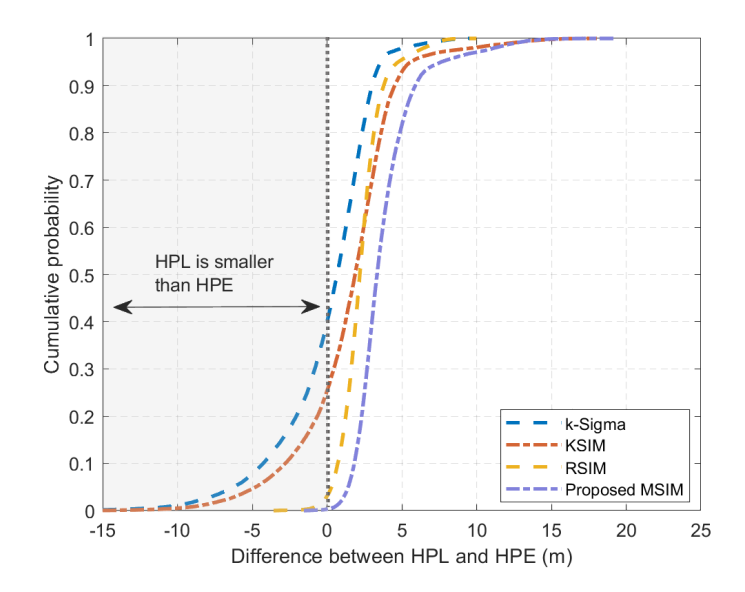


Figure 4.11: Cumulative probability distribution of difference between HPL and HPE in case 1

 Table 4.1: Indicators for each IM method of Case 1

Index	k-Sigma	KSIM	RSIM	MSIM
PLR	59.88%	74.69%	96.85%	99.62%
HMI	0.22%	0.28%	0.00%	0.00%

cannot effectively overbound HPE in evaluating the confidence of the position. In comparison, the RSIM method shows a significantly higher HPL reliability of 96.85%, but fails to effectively evaluate the HPE under severe outlier disturbances.

The proposed MSIM shows the highest HPL reliability of 99.62% throughout the MC simulation. In addition, the cumulative probability that the HPL of MSIM exceeds the HPE is maintained at 97.11% over the 10 m range. This indicates that MSIM provides a more reliable HPL in INMS applications while avoiding the problem of over-conservatism of the HPL and more effectively evaluating the confidence of the position solution. Furthermore, based on Fig. 4.12, the probability of HMI events for k-Sigma and KSIM is 0.22%, even higher in adverse urban areas, which does not meet the integrity risk requirements. In contrast, the proposed MSIM does not generate any HMI event during the whole MC simulation, which effectively realizes the integrity monitoring and ensures the positioning safety of the vehicle.

(2) Results and analysis of Case 2: Fig. 4.13 shows the HPE and HPL results from a single MC trial in case 2. Fig. 4.14 shows the cumulative probability distributions of the

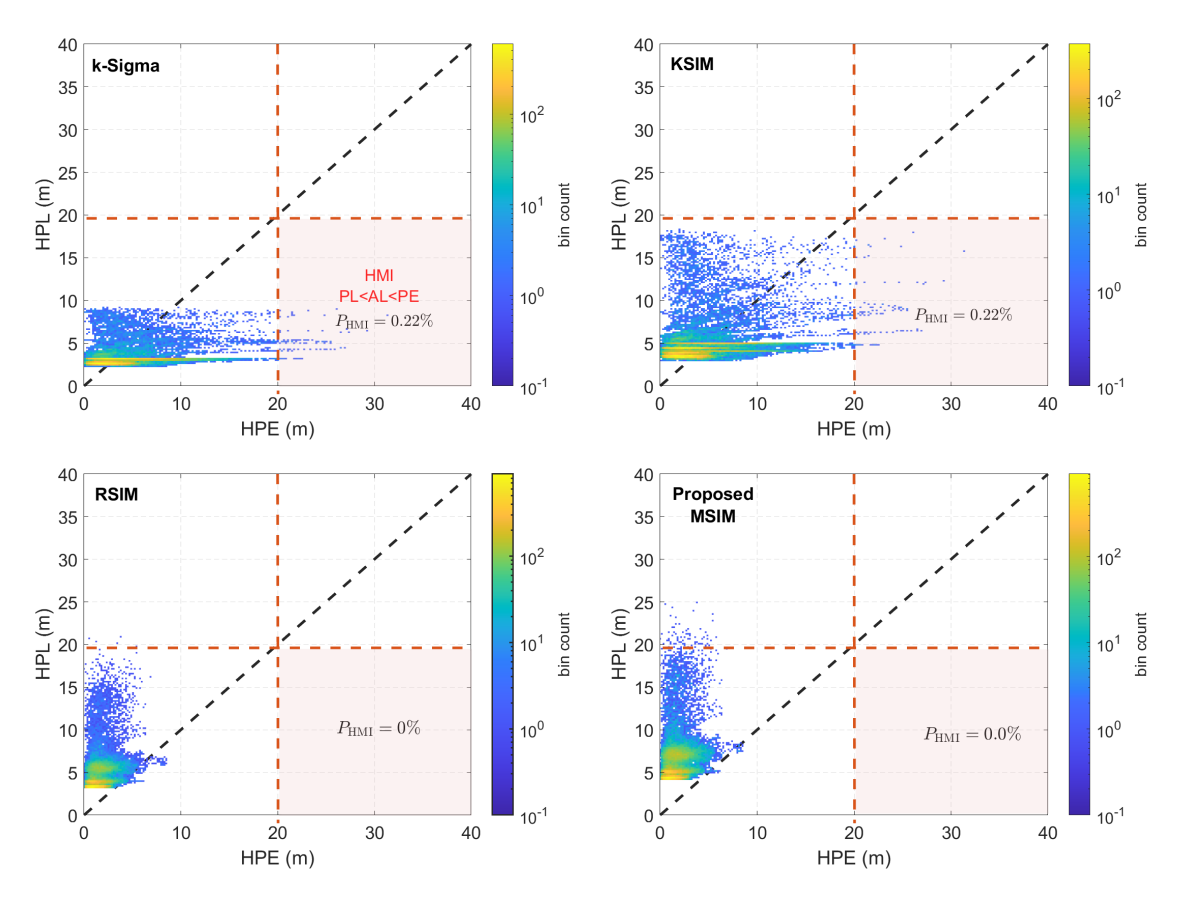


Figure 4.12: Stanford diagram of case 1

difference between HPL and HPE (combined MC trial results) for different IM methods to reflect the reliability of HPL of case 2. Fig. 4.15 shows the Stanford plot for the different IM methods. In addition, the indicators of different IM methods are listed in Tab. 4.2.

As can be seen from Fig. 4.13, in the case of GNSS and POLA rejection from 600 s to 900 s, the HPE still increases even though the spread of the position error is limited to some extent by the combination of IMU and odometer. In this case, the HPL of the k-Sigma method cannot evaluate the HPE of the CKF. Although KSIM provides a reliable HPL, it still falls short of overbounding the HPE and assessing the confidence in the position. In the case of missing GNSS and POLA data, MRCKF avoids the discarding of information caused by Gaussian reconstruction and still has better consistency than CKF. Thus, the HPL of RSIM based on MRCKF can efficiently overbound the HPE from 600 s to 900 s compared to k-Sigma and KSIM. In addition, MSIM provides a more reliable HPL by considering multiple fault assumptions and position estimation uncertainty, which improves the navigation safety of a vehicle.

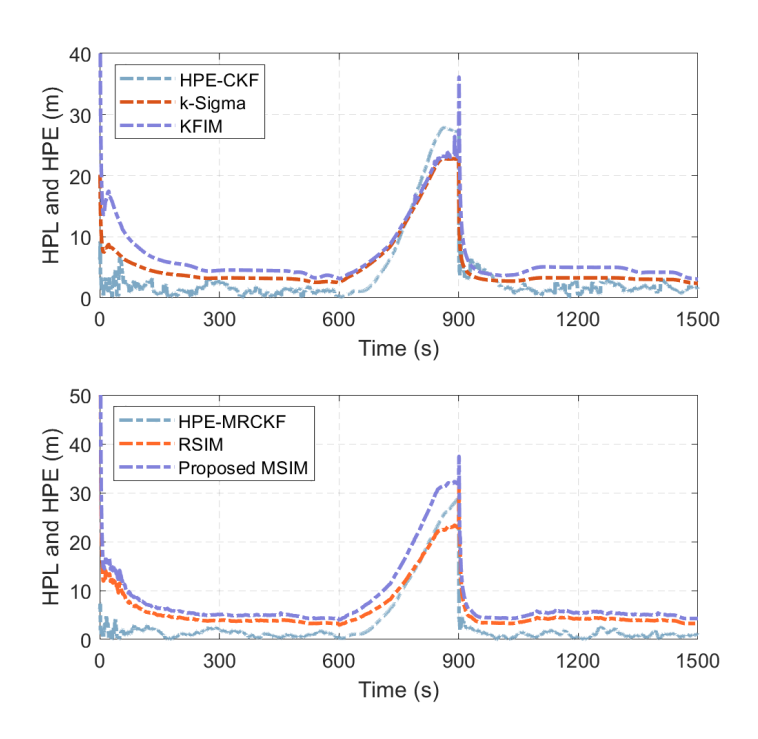


Figure 4.13: HPL and HPE in case 2

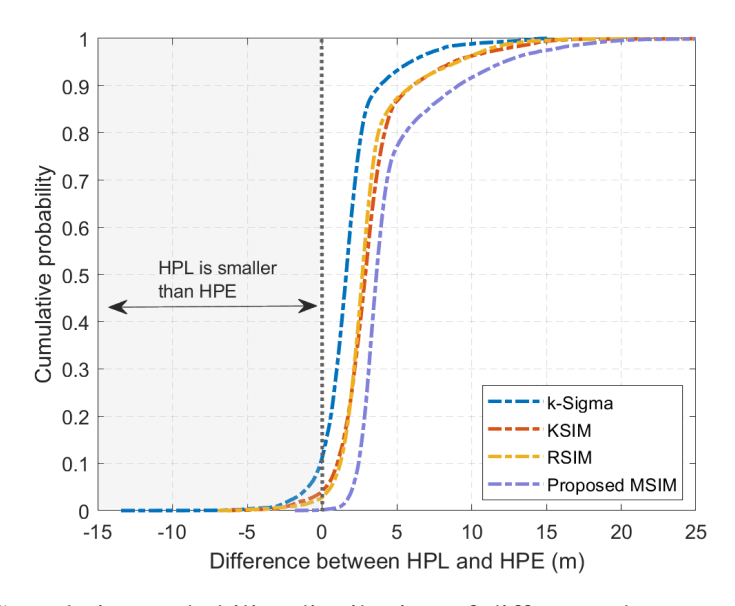


Figure 4.14: Cumulative probability distribution of difference between HPL and HPE in case 2

In addition, as shown in Fig. 4.11, different IM methods have different HPL reliability. Specifically, for the k-Sigma and KSIM methods, the reliability of HPL is 79.74% and 90.77%, respectively. This indicates that HPL cannot effectively overbound the HPE to

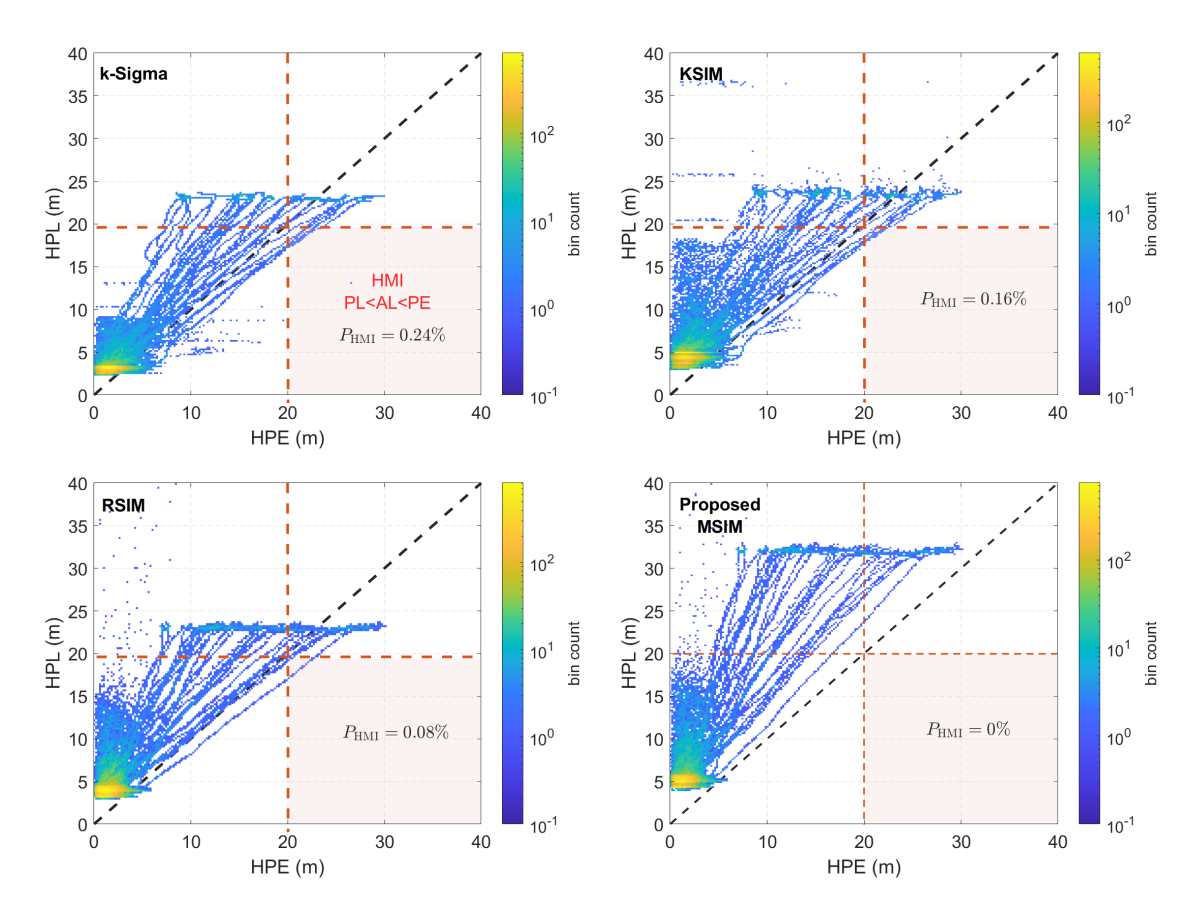


Figure 4.15: Stanford diagram of case 2

Table 4.2: Indicators for each IM method of Case 2

Index	k-Sigma	KSIM	RSIM	MSIM
PLR	79.74%	90.77%	97.36%	99.84%
HMI	0.24%	0.16%	0.08%	0.00%

evaluate the confidence of the position. In comparison, the RSIM method shows a significantly higher HPL reliability of 97.36% but cannot effectively assess the HPE under severe outlier disturbances. The proposed MSIM shows the highest HPL reliability of 99.84% throughout the MC simulation. In addition, the cumulative probability that the HPL of MSIM exceeds the HPE is maintained at 91.77% over the 10 m range. This indicates that MSIM provides a more reliable HPL in INMS applications while avoiding the problem of over-conservatism of HPL and more effectively evaluating the confidence of the position solution. Furthermore, based on Fig. 4.12, the probability of HMI events for k-Sigma, KSIM, and RSIM are respectively 0.24%, 0.16%, and 0.08%, even higher in adverse urban areas, which does not meet the requirements of integrity risk. In contrast, the proposed

MSIM does not generate any HMI event during the whole MC simulation, which effectively realizes the integrity monitoring and ensures the positioning safety of the vehicle.

4.6 Summary

This chapter presents a sequential IM method based on the assumption of multiple fault missing detection to effectively monitor the navigation integrity of INMS in urban areas. First, the integrity monitoring problem is formulated. The maximum slope-based IM is introduced, and its limitations in INMS are analyzed. Subsequently, a sequential IM method is proposed. The IM dynamic regression model is constructed by a consistent posterior estimate provided by the proposed robust filter. A consistency factor in state domain is calculated using the sequential probability ratio over sliding windows. Under the assumption of multiple fault-missing detection, the HPL is calculated based on the maximum eigenvalue to quantitatively evaluate the confidence of the position solution. Finally, simulation experiments are conducted to verify the effectiveness of the proposed IM method. The experimental results indicate that the k-Sigma, KSIM, and RSIM methods have the highest HPL reliability of 79.74%, 90.77%, and 97.36%, and the highest probability of HMI events of 0.24%, 0.22%, and 0.08% respectively, in various simulation cases, which could not satisfy the integrity risk requirements. In comparison, the proposed MSIM has an HPL reliability of over 99.62% in various simulation cases and does not generate any HMI events. This effectively evaluates the reliability of the position estimation and realizes the integrity monitoring, thus verifying the effectiveness of the proposed method.

Chapter 5

Verification Experiments for Proposed INMS Algorithms

5.1 Introduction

To address the problems of robust state estimation, accurate noise adaptation, and autonomous state integrity monitoring for INMS in dense urban areas, this thesis proposes a robust resampling-free filtering algorithm based on MCC in Chapter 2, a robust MNCM adaptation algorithm based on VB in Chapter 3, and an autonomous integrity monitoring algorithm based on the multiple fault-missing detection assumption in Chapter 4. The effectiveness of the proposed algorithms is preliminarily verified by numerical simulation experiments. Furthermore, in this chapter, an in-vehicle experiment is conducted to validate the performance of the proposed algorithms in practical engineering applications. First, an in-vehicle experimental platform is constructed, and the validation scheme is designed and parameterized. The experiment results are then analyzed.

5.2 In-Vehicle Experiment Platform Construction

A test multi-sensor navigation system is constructed by integrating the micro-electromechanical system (MEMS)-IMU, GNSS, OD, and POLA. Meanwhile, a high-precision fiber-optic gyro (FOG)-IMU with an RTK integration system serves as a reference system to provide benchmark data on navigation parameters with centimeter-level positioning accuracy. The in-vehicle experiment platform is shown in Fig. 5.1, and the nominal specifications of each sensor are listed in Tab. 5.1. During the experiment, a self-developed polarizer system was used, which achieved a heading accuracy of $1^{\circ}(1\sigma)$ in an open scene. However, the heading accuracy decreases in dense urban areas due to building obstructions, light pollution, etc.



Figure 5.1: In-vehicle experiment platform

5.3 In-Vehicle Validation Scheme and Parameterization

First, the proposed robust filtering algorithm MRCKF is validated. Then, the robust noise adaptation algorithm RSVBA is validated using the state a posteriori estimation results of MRCKF. Finally, the autonomous integrity monitoring algorithm MSIM is validated. The specific parameters of each algorithm and evaluation indices are set as follows.

(1) State Estimation Algorithm: As in the 2.5.1 subsection, the proposed MRCKF is compared with the following classical methods to verify the effectiveness: 1) CKF; 2) RFCKF; 3) RSTKF; 4) HMKF; and 5) MCKF adopting the proposed kernel size adaptive method. The tuning parameters of the above filters are set empirically as follows: The degree-of-freedom in the RSTKF is set to $\sigma = 6$; the tuning parameter in the HMCKF is set to $\gamma = 1.345$; the upper bound on the kernel size is set to $\sigma_{\text{max}} = 20$. In addition, the MNCM \mathbf{R}_k , the process noise covariance matrix \mathbf{Q}_k , and the initial state MSE \mathbf{P}_k are set as follows

$$\mathbf{P}_{k} = \operatorname{diag}\left(\left[\phi_{k} \ \delta \mathbf{v}_{k} \ \delta \mathbf{p}_{k} \ \varepsilon \ \nabla \ \delta \mathbf{x}_{k}^{\operatorname{od}}\right]^{\mathrm{T}}\right)^{2}$$
(5.1a)

$$\mathbf{Q}_{k} = \operatorname{diag}\left(\left[\boldsymbol{\varepsilon}_{r} \ \nabla_{r} \ \mathbf{0}_{1\times 9}\right]^{T}\right)^{2} \tag{5.1b}$$

$$\mathbf{R}_{k} = \operatorname{diag}\left(\left[\mathbf{r}_{k}^{\mathrm{gnss}} \ \mathbf{r}_{k}^{\mathrm{od}} \ \mathbf{r}_{k}^{\mathrm{pola}}\right]^{\mathrm{T}}\right)^{2}$$
 (5.1c)

where $\varepsilon_{\rm r} = [1^{\circ}\sqrt{\rm h} \ 1^{\circ}\sqrt{\rm h} \ 1^{\circ}\sqrt{\rm h}]^{\rm T}; \nabla_{\rm r} = [20\,\mu{\rm g}/\sqrt{\rm Hz} \ 20\,\mu{\rm g}/\sqrt{\rm Hz} \ 20\,\mu{\rm g}/\sqrt{\rm Hz}]^{\rm T}; \phi_k = [30'\ 30'\ 180']^{\rm T}; \delta\mathbf{v}_k = [0.1\,{\rm m/s}\ 0.1\,{\rm m/s}\ 0.1\,{\rm m/s}]^{\rm T}; \delta\mathbf{p}_k = [10\,{\rm m}\ 10\,{\rm m}\ 10\,{\rm m}]^{\rm T}; \varepsilon = [10^{\circ}/{\rm h}\ 10^{\circ}/{\rm h}\ 10^{\circ}/{\rm h}]^{\rm T}; \nabla = [200\,\mu{\rm g}\ 200\,\mu{\rm g}\ 200\,\mu{\rm g}]^{\rm T}; \delta\mathbf{x}_k^{\rm od} = [60'\ 0.1\ 180']^{\rm T}; \mathbf{r}_k^{\rm gnss} = [5\ 5\ {\rm m}]^{\rm T}; \mathbf{r}_k^{\rm od} = 0.1\,{\rm m/s}; \mathbf{r}_k^{\rm pola} = 1\,{\rm deg}.$

Sensor	Specification	Index	
	Gyro constant bias stability	10°/h	
MEMS-IMU	Angular random walk	$1^{\circ}\sqrt{h}$	
	Acc. constant bias stability	200 μg	
	elocity random walk yro constant bias stability ngular random walk	$20\mu g/\sqrt{Hz}$	
FOG-IMU Angular	Gyro constant bias stability	0.05°/h	
	Angular random walk	$0.005^{\circ}\sqrt{h}$	
	Acc. constant bias stability	10 μg	
	Velocity random walk	$1 \mu g / \sqrt{Hz}$	
Odamatan	Pulse number	1000	
Odometer	Resolution	$2.289e - 03 \mathrm{m/p}$	
GNSS	Horizontal positioning accuracy	5 m (1σ)	
POLA	Heading accuracy	1°(1σ)	

Table 5.1: Nominal specifications for sensors

- (2) Noise Adaptation Algorithm: The proposed RSVBA is compared with the following existing classical methods to verify its effectiveness: 1) SHA; 2) VBA; and 3) ORA. The tuning parameters for the above methods are empirically specified as follows: In the Sage-Husa method, the damping factor is set to b = 0.95, and the MNCM initial is $\mathbf{R}_0 = \text{diag}\left(\left[5\text{m } 5\text{m } 0.05\text{m/s } 1\text{deg}\right]\right)^2$; in VBA, the initial of the degree of freedom parameter is $u_k = 10$, the initial of the inverse scaling matrix is $U_k = (u_k m 1)\mathbf{R}_0$ and the expansion coefficient $\rho = 0.95$. ORA uses the square-root similarity function, and the degree of freedom parameters are set to $\boldsymbol{\sigma} = 5$ and $\tau_R = 2$. The sliding window size in the proposed RSVBA is set to 10.
- (3) Integrity Monitoring Algorithm: The proposed MSIM is compared with the following methods to validate its effectiveness: 1) k-Sigma; 2) KSIM; and 3) RSIM. The IM parameters are set as follows: In k-sigma, the scalar factor is set to k = 4; The false alarm rate is set to $P_{\rm fa} = 10^{-4}$; The missing detection rate is set to $P_{\rm md} = 10^{-4}$; With the specified $P_{\rm fa}$ and $P_{\rm md}$, the non-central parameter for the INMS model is $\lambda = 102.41$. In addition, the HAL for in-vehicle route navigation is set to HAL=20 m according to the U.S. Federal Radionavigation Program [123].

(4) Evaluation Indicators:

• For the state estimation algorithm, unlike the evaluation metrics based on multiple

Monte Carlo trials in Chapter 2, this section uses the common single-experiment RMSE as the evaluation metric, which is defined as

$$RMSE = \sqrt{\frac{1}{N_t} \sum_{k=1}^{N_t} (\hat{\mathbf{x}}_k - \mathbf{x}_k)^2}$$
 (5.2)

where N_t is the total number of states during the experiment; $\hat{\mathbf{x}}_k$ and \mathbf{x}_k are the estimated and actual states at time-step k, respectively. The results analysis focuses on the RMSE of the horizontal position to reflect the estimation performance of different filtering algorithms.

- For the noise adaptation algorithm, since the statistical characteristics of the actual non-stationary noise are unavailable, the performance of the algorithm is evaluated based on the degree of match between the MNCM estimation and the actual noise situation and the estimation effect before and after adaptation.
- For the IM algorithm, the evaluation metrics are the same as Eq. (4.52) in Section 4.5.1, i.e., the HPL reliability and HMI probability are still used for evaluation.

5.4 Verification Experiment Results and Analysis

This subsection conducts experimental validation of the proposed algorithm. The invehicle experiments are carried out based on the conditions above. Based on the collected data, this section analyses the experiment results of the robust estimation, MNCM adaptation, and integrity monitoring algorithms, respectively, verifying their effectiveness in practice engineering.

5.4.1 Analysis of Robust State Estimation Results

Fig. 5.2 shows the reference trajectory and GNSS trajectory, and also illustrates a typical dense urban area during the experiment, i.e., GNSS is blocked by the viaducts and skyscrapers. Fig. 5.3 gives the velocity and attitude parameters of the reference system. Fig. 5.4 to Fig. 5.6 show the attitude error, velocity error, and position error of the different filters, respectively. Since the HPE reflects the overall estimation performance, Fig. 5.7 shows the HPE of the vehicle and its cumulative probability distribution. In addition, Tab. 5.2 lists the RMSE of each navigation parameter for different filters. Fig. 5.8 and Fig. 5.9 show the RMSE visually through the radar diagram and histogram.

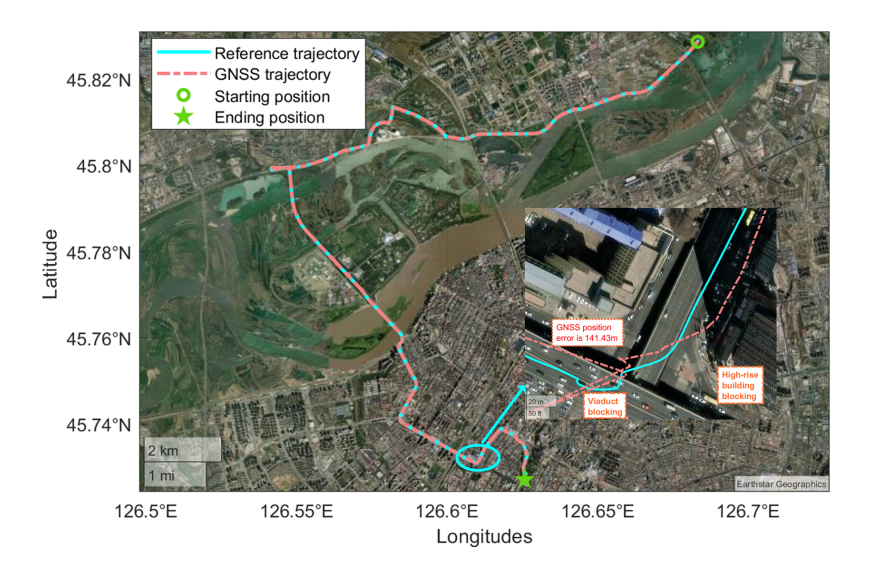


Figure 5.2: Reference movement trajectory of in-vehicle experiment

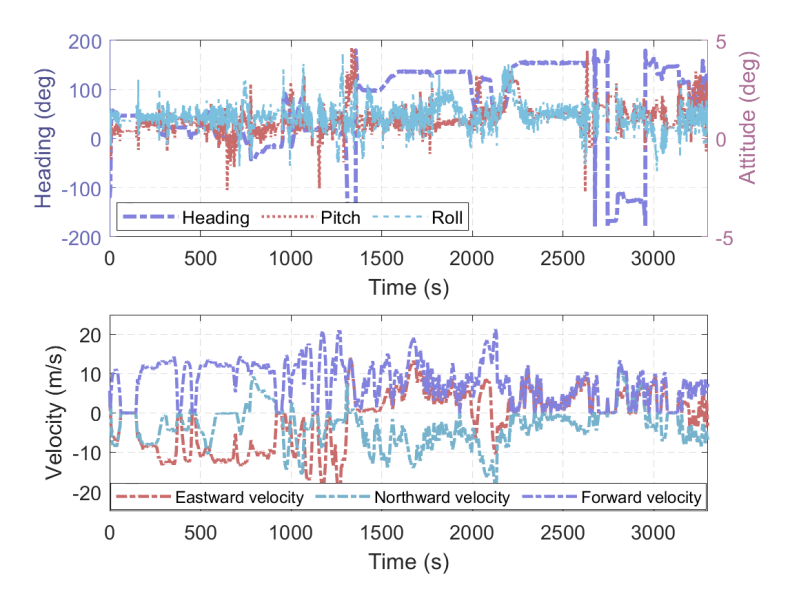


Figure 5.3: Velocity and attitude of reference system

As shown in Fig. 5.2, the maximum positioning error of GNSS is 141.43 m in the urban area blocked by the viaduct and high-rise buildings, which cannot provide effective navigation and positioning services. Fig. 5.3 shows the attitude and velocity of the vehicle experiment provided by the reference system in the navigation coordinate frame. The centimetre-level positioning accuracy of RTK and the high-precision smoothing effect of FOG-INS allow the system to provide high-precision reference information even when satellite navigation is rejected.

As shown in Fig. 5.4 to Fig. 5.7 and Tab. 5.2, by fusing redundant data from different

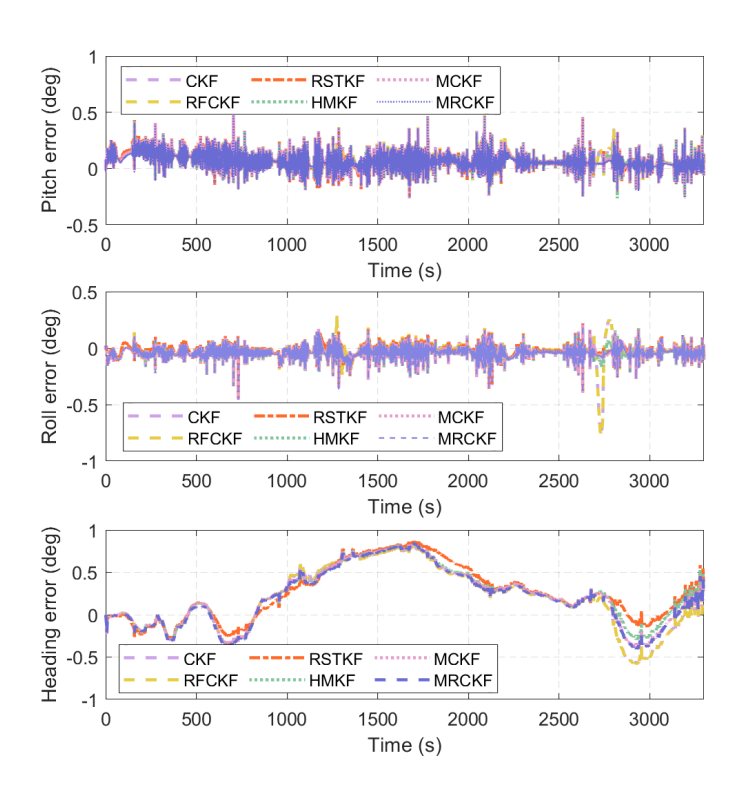


Figure 5.4: Attitude errors in vehicle-based experiment

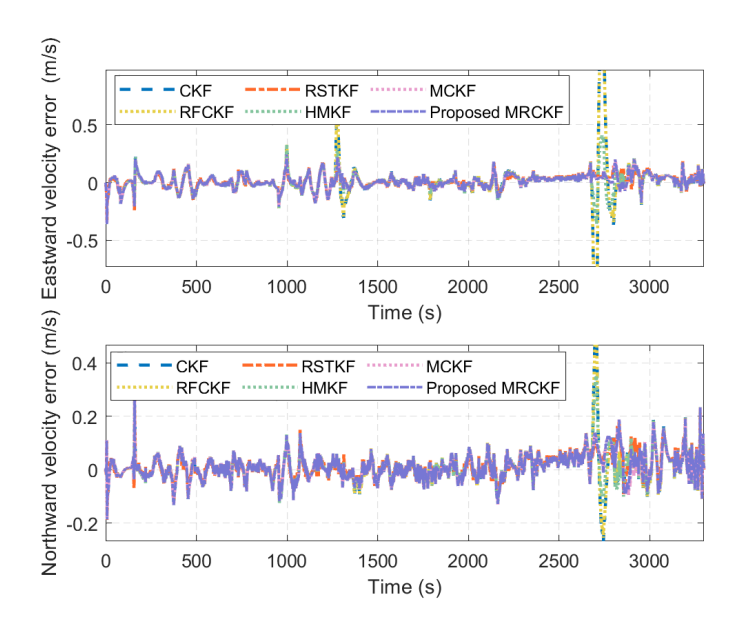


Figure 5.5: Velocity errors in vehicle-based experiment

sensors, CKF partially constrains the position, reducing the maximum positioning error to 94.380 m with an RMSE of 7.754 m. The RMSE of RFCKF for HPE is reduced to 7.653 m, demonstrating improved estimation performance compared to CKF by avoiding the loss of higher-order moments caused by Gaussian reconstruction. Furthermore, the robust filters

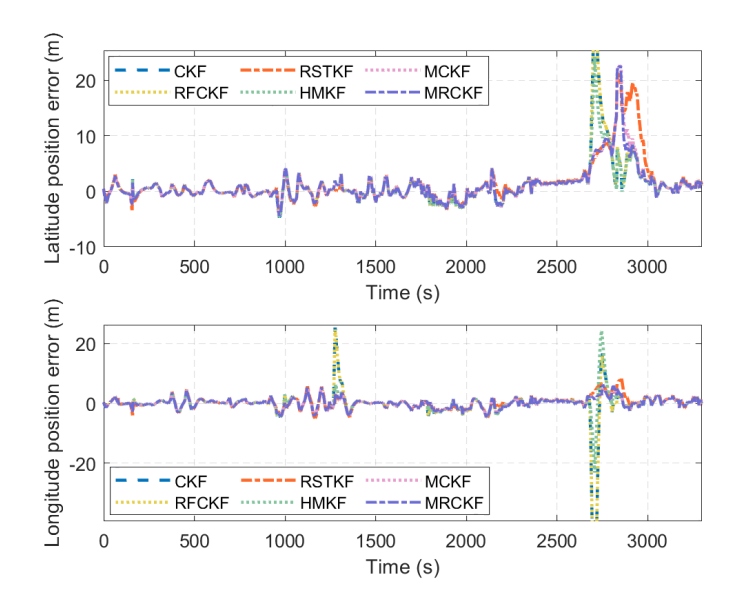


Figure 5.6: Position errors in vehicle-based experiment

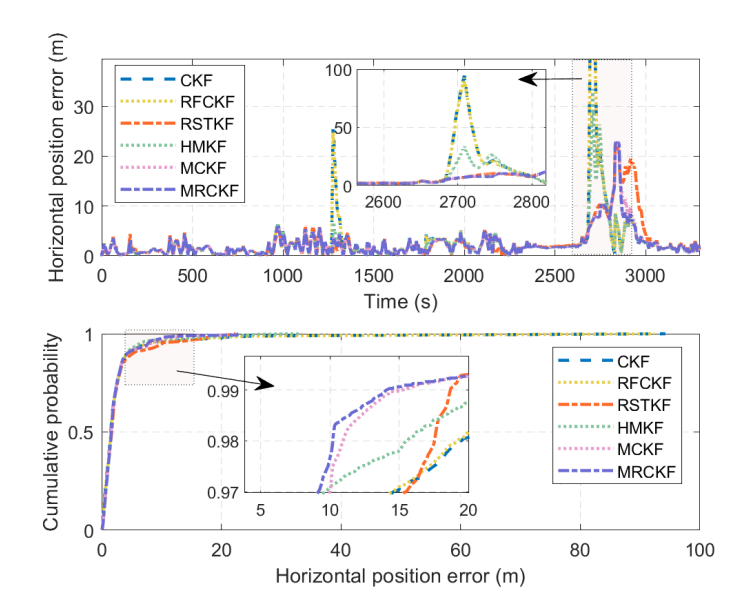


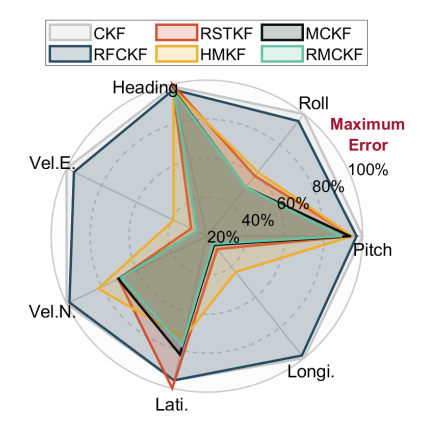
Figure 5.7: HPE and its cumulative probability distribution

RSTKF and HMKF demonstrate superior estimation performance compared to CKF and RFCKF. For instance, the RMSE of HPE for RSTKF and HMKF is 4.529 m and 4.195 m, respectively, which is reduced by 41.6% and 45.9% than that of CKF (7.754 m) and significantly improves the estimation accuracy. This improvement is attributed to the suppression of measurement outliers in state estimation by robust filtering against non-Gaussian noise, such as GNSS multipath effects caused by viaducts and high-rise buildings and outlier interference for OD data when driving over uneven roads. Moreover, with the proposed kernel size adaptive method, MCKF demonstrates superior estimation performance compared

to RSTKF and HMKF, with a position ARMSE (3.795 m), which is reduced by 16.2% and 9.5% than RSTKF and HMKF, respectively. This demonstrates the feasibility of the proposed kernel size optimal method.

ADMCE	Pitch	Roll	Heading	Vel.E.	Vel.N.	Lati.	Longi.	HPE
ARMSE	(deg)	(deg)	(deg)	(m/s)	(m/s)	(m)	(m)	(m)
CKF	0.087	0.081	0.404	0.190	0.061	3.941	6.678	7.754
RFCKF	0.084	0.077	0.397	0.182	0.060	3.937	6.563	7.653
RSTKF	0.082	0.042	0.409	0.055	0.043	4.109	1.904	4.529
HMKF	0.082	0.050	0.397	0.074	0.050	3.021	2.911	4.195
MCKF	0.081	0.048	0.395	0.049	0.043	3.380	1.725	3.795
MRCKF	0.077	0.054	0.392	0.049	0.042	3.192	1.674	3.605

Table 5.2: Navigation parameter estimation RMSE



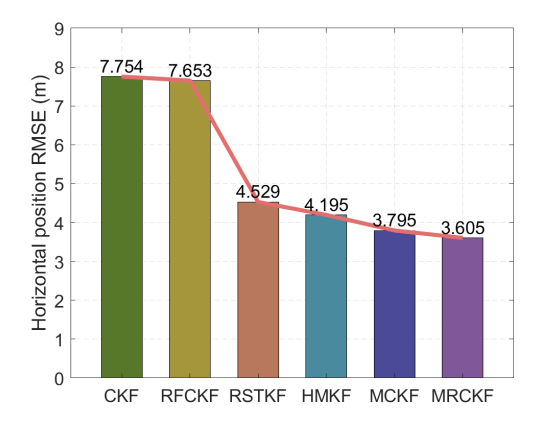


Figure 5.8: RMSE radar diagram of naviga- **Figure 5.9:** RMSE of HPE for different estition parameters mation methods

Further, as seen from Fig. 5.8 and Fig. 5.9, the proposed MRCKF has a higher overall estimation accuracy of the navigation parameters than RSTKF and HMKF. For instance, the position RMSE of MRCKF is 3.605 m, which is reduced by 20.4% and 14.1% compared to that of RSTKF and HMKF, respectively. Then, the estimation accuracy of the horizontal position of MRCKF is improved by 5.0% than MCKF. This improvement is due to the fact that MRCKF is designed by adopting the proposed adaptive MCC-RFU framework on MCFK, which captures the non-Gaussian moments in the sampling points distribution more efficiently, which results in improved estimation performance. This further demonstrates the effectiveness of the proposed enhanced robust RFU framework. Furthermore, the cumulative probability of horizontal position estimation error within 10 m for MRCKF

(97.8%) is the highest compared to that of RSTKF (94.6%), HMKF (97.1%), and MCKF (97.0%), indicating better robust estimation and further validating the effectiveness of the proposed filter algorithm in handling heavy outliers interference.

5.4.2 Analysis of Robust MNCM Adaptation Results

The robust MNCM adaptive results are analyzed to reflect the estimated MNCM in the form of noise standard deviation. Then, for assessing the accuracy of the MNCM estimates, Fig. 5.12 shows a comparison of the MNCM with the actual noise, qualitatively analyzing the MNCM estimation effect by the degree of match between them. Additionally, Fig. 5.13 and Fig. 5.14 present the position estimation errors and RMSE corresponding to the different noise adaptive methods, providing a quantitative analysis of the accuracy of the MNCM estimation of each method based on the position estimation effect.

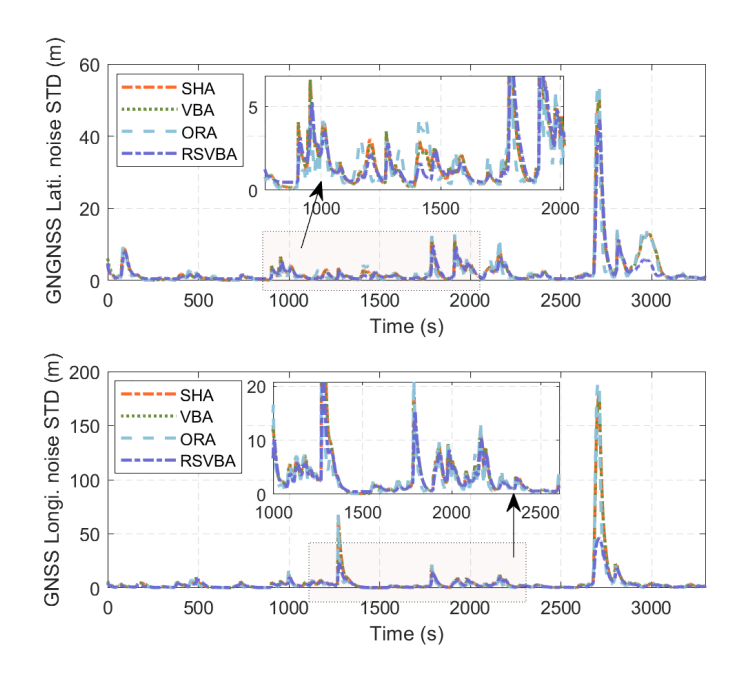


Figure 5.10: MNCM estimation of GNSS

As seen from Fig. 5.10, the estimation results of SHA, VBA, and ORA for MNCM of GNSS are relatively similar. The proposed RSVBA demonstrates smoother estimation results than other methods. This is due to the suppression of the interference of outliers for MNCM estimation and the use of sliding window VB, which combines the state-smoothing a posteriori and the historical measurement data. In addition, it can be seen from Fig. 5.12 that the MNCM of RSVBA for GNSS closely matches the actual noise. For example, around 2800 s of the experiment, as the viaduct obstructs the GNSS latitude and longitude position, the MNCM estimated by RSVBA also increases, aligning with the trend of the

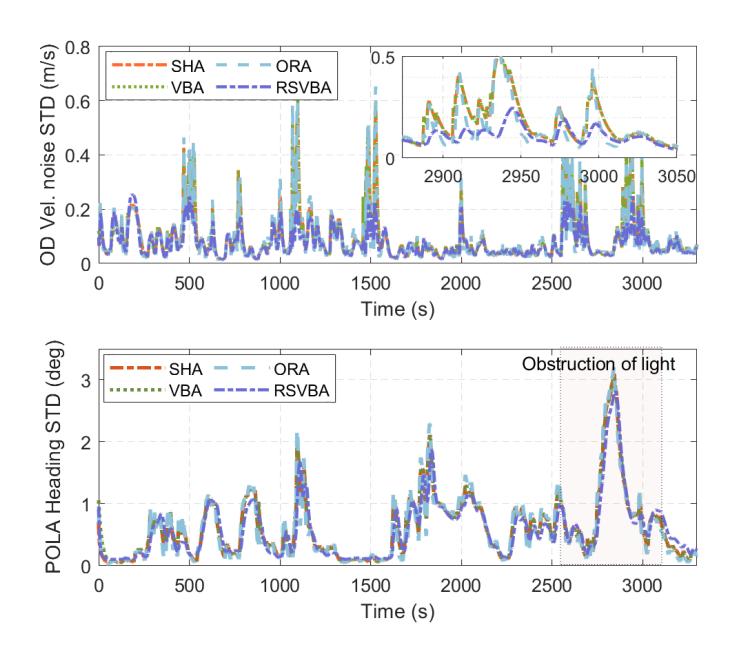


Figure 5.11: MNCM estimation of OD and POLA

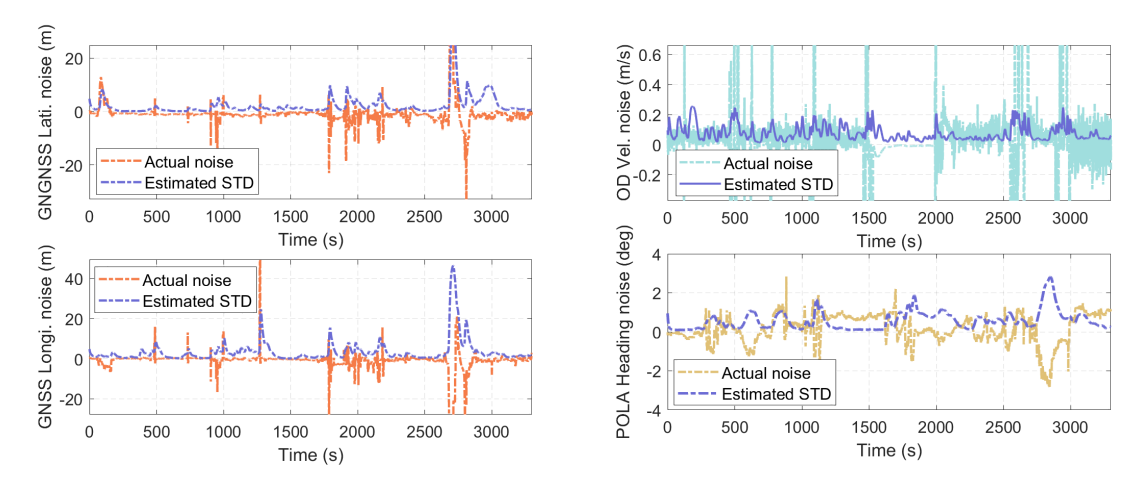
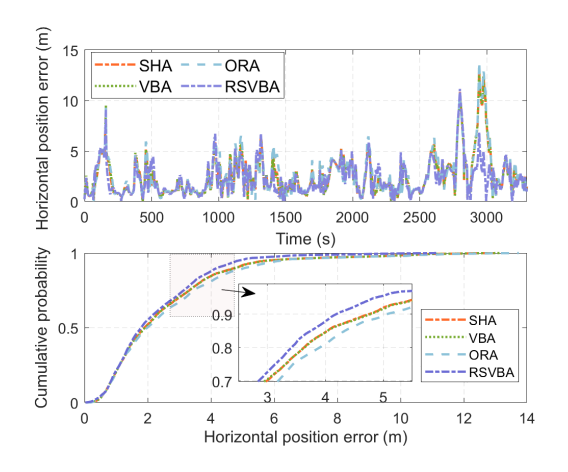


Figure 5.12: Comparison of MNCM estimate with actual noise

actual noise. Furthermore, from Fig. 5.11, the situation of MNCM estimation for POLA is similar to that of GNSS, and RSVBA provides smoother estimation results than other methods. The MNCM estimation is consistent with the actual noise. For example, from 2800 s to 3000 s, the MNCM grows as the POLA heading noise increases.

Further, the odometer is susceptible to outliers when the vehicle drives over uneven surfaces, such as speed bumps. In this case, the estimation of SHA, VBA, and ORA for MNCM of OD is disturbed by outliers from Fig. 5.11. The maximum standard deviation of the estimation noise is 0.603 m/s, 0.618 m/s, 0.652 m/s, which does not match the actual sensor noise characteristics. The estimation of MNCM of OD velocity by RSVBA is



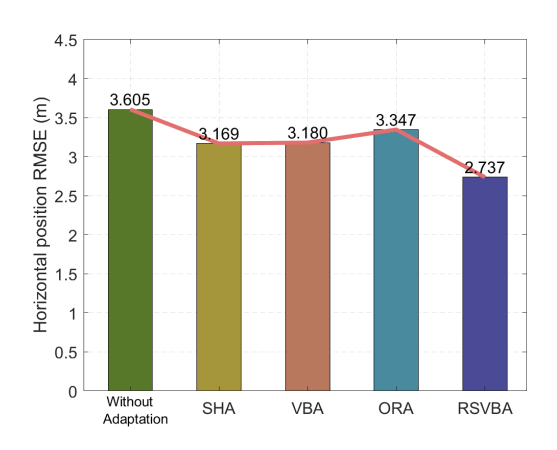


Figure 5.13: HPE of different adaptation **Figure 5.14:** RMSE of HPE for different adaptation methods

Table 5.3: Indicators for each IM method

Index	k-Sigma	KSIM	RSIM	MSIM
PLR	88.68%	93.61%	86.23%	99.85%
HMI	1.24%	1.24%	0.00%	0.00%

smoother and more consistent with the actual sensor noise than the methods. This indicates that RSVBA can effectively suppress the interference of measurement outliers on MNCM estimation and validates the effectiveness of the proposed robust adaptation method.

Furthermore, the position estimate results are used to quantitatively analyze the MNCM estimation performance of different methods. As shown in Fig. 5.13 and Fig. 5.14, the position RMSE of the MRCKF without MNCM adaptation is 3.605 m. When MNCM is estimated, the position RMSE for the SHA, VBA, and ORA is reduced to 3.169 m, 3.180 m, and 3.347 m, respectively. Further, the proposed RSVBA has a position RMSE of 2.737 m, which is reduced by 13.63%, 13.93%, and 18.23% compared to SHA, VBA, and ORA, respectively. These results demonstrate a significant improvement in estimation accuracy and validate the effectiveness of the proposed RSVBA.

5.4.3 Analysis of State Integrity Monitoring Results

Fig. 5.15 shows HPE and HPL results of different IM methods. Fig. 5.16 shows the cumulative probability distributions of the difference between HPL and HPE for different IM methods to reflect the reliability of HPL. Fig. 5.17 plots the Stanford diagram for the different IM methods. In addition, the indicators of different IM methods are listed in Tab. 5.3.

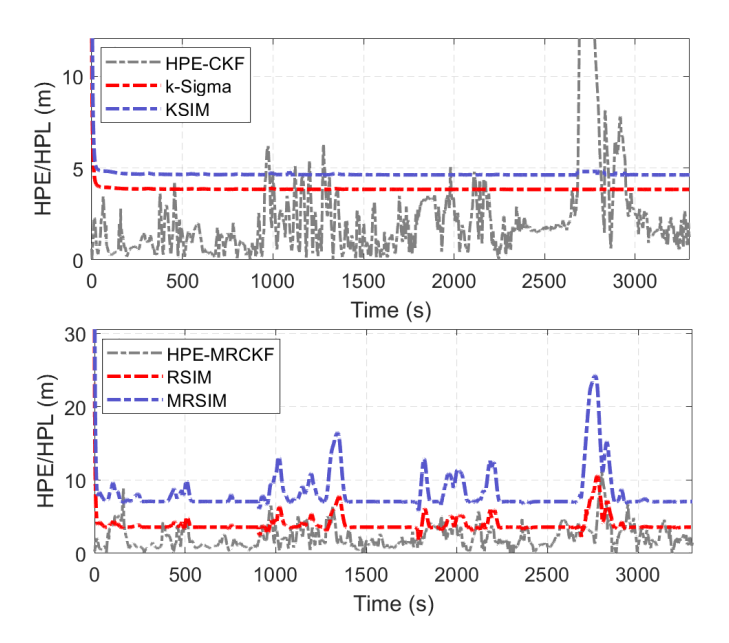


Figure 5.15: HPL and HPE

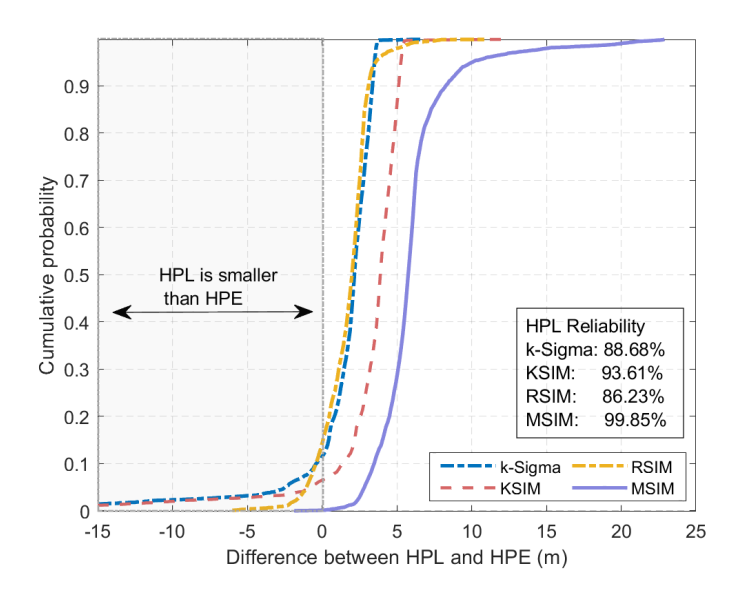


Figure 5.16: Cumulative probability distribution of HPL and HPE difference

The k-Sigma and KSIM methods rely on the a posteriori estimation results of the regular KF method. Based on Fig. 5.15 and Fig. 5.16, under a predetermined Gaussian noise model, the HPL reliability of the k-Sigma method is only 88.68%, especially in cases where GNSS is blocked (around 2800 s), the HPL reliability is even lower. Thus, k-Sigma cannot accurately evaluate the confidence of the position solution and monitor the navigation integrity due to estimation inconsistency. In comparison, KSIM provides a reliable HPL. However, KSIM only considers the maximum potential position error based on the

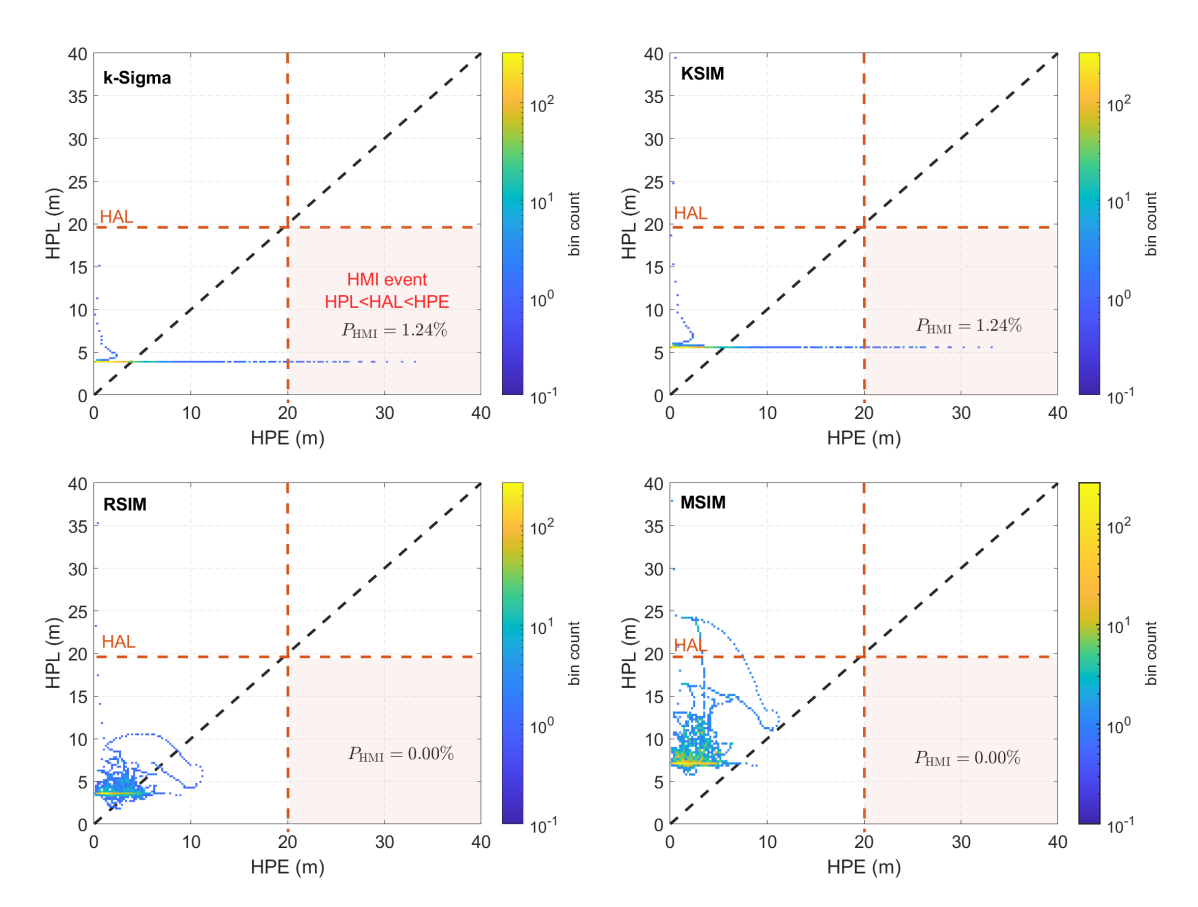


Figure 5.17: Stanford diagram of IM

predetermined statistical model and does not consider the effect of unmodeled outliers. As a result, the HPL of KSIM still falls short of bounding the HPE, and the confidence of the position solution cannot be effectively evaluated.

RSIM adopts the same single-fault assumption as KSIM. Furthermore, with the regression model constructed by the consistent a posteriori estimate of MRCKF, RSIM can dynamically adjust the protection level according to the actual noise situation. However, the single-fault assumption is not applicable well to vehicle INMS in urban areas due to frequent sensor disturbances. As a result, the HPL reliability of KSIM is only 86.23%, which cannot quantitatively assess the confidence of the position solution. Moreover, MSIM has an HPL reliability of 99.85% throughout the experiment and is higher than other existing HPL calculation methods based on a predetermined model. This demonstrates that MSIM provides a more reliable HPL by considering multiple fault assumptions with position estimation uncertainty. Consequently, MSIM can effectively evaluate the HPE and monitor position integrity, thereby enhancing navigation safety. Further, it can be seen from Fig. 4.11 that the probability of HMI events for k-Sigma and KSIM is 1.24%, even rises even higher in adverse urban areas, which does not meet the integrity risk requirements.

In contrast, the proposed MSIM does not generate any HMI event during the whole MC simulation, which effectively realizes the integrity monitoring and ensures the positioning safety of the vehicle.

5.5 Summary

In this chapter, an in-vehicle experiment is conducted using MEMS-IMU, GNSS, OD, and POLA to verify the practical performance of the proposed algorithm in adverse urban environment heavily shaded by viaducts and high-rise buildings, etc. The results of the experiment are as follows.

- (1) The proposed robust state estimation algorithm is validated. The experimental results indicate that the MMSE-based CKF and RFCKF show poor estimation effects in dense urban areas heavily shaded by viaducts and high-rise buildings subject to non-Gaussian heavy-tailed noise. Compared to the existing robust filters RSTKF, HMKF, and MCKF adopting the kernel size optimal method, the proposed MRCKF shows smaller RMSE for each navigation parameter, and the position RMSE is reduced by 20.4%, 14.1%, and 5.0%, respectively, indicating better robust estimation effect in adverse urban areas. This validates the proposed MRCKF algorithm in practical applications.
- (2) The proposed robust noise adaptation algorithm is validated. The experimental results show that compared to SHA, VBA, and ORA methods, the noise MNCM estimation of the proposed RSVBA is smoother and matches the actual sensor noise characteristics in adverse urban areas with the presence of outliers. Additionally, the position RMSE of RSVBA is reduced by 13.6%, 13.9%, and 18.2% compared to SHA, VBA, and ORA methods, respectively. This indicates that the proposed RSVBA can effectively suppress the interference of measurement outliers on MNCM estimation and achieve robust noise adaptation, thus validating the practical performance of the proposed algorithm.
- (3) The proposed autonomous integrity monitoring algorithm is validated. The experimental results show that the HPL reliability of the k-Sigma, KSIM, and RSIM methods are 88.68%, 93.61%, and 86.23%, respectively, and even lower especially in adverse urban areas. Also, the k-Sigma and KSIM suffer from the HMI events with a probability of 1.24%. In contrast, the proposed MSIM has the highest HPL reliability (99.85%) throughout the experiment and does not generate any HMI events,

5.5. Summary 115

effectively evaluating the confidence of the position solution and monitoring the integrity of the INMS. These results verify the practical performance of the proposed algorithm.

Chapter 6

Conclusions and Recommendations

The thesis focuses on the requirements for high accuracy, robust navigation, and autonomous integrity monitoring for intelligent vehicles in urban environments. The research proposes a robust state estimation algorithm, a robust noise adaptation algorithm, and an autonomous integrity monitoring algorithm to improve the navigation accuracy and safety for the intelligent vehicle by advantageous complementation of multiple sensors and redundant information fusion. Furthermore, the research includes experimental validation of theoretical studies and demonstrates the practical significance of the proposed robust estimation and integrity monitoring algorithms for INMS. The conclusions and recommendations of this thesis are summarized as follows.

6.1 Conclusions

(1) To address the problem of INMS state estimation performance degradation due to the mismatched noise assumptions in urban areas, a robust RFU state estimation algorithm based on the adaptive MCC is proposed. The cost function of the resampling-free estimation framework is constructed based on the maximum correntropy criterion, which effectively exploits the non-Gaussian moments of the state distribution caused by the nonclosed mapping, ensures the resampling-free estimation optimality and avoids the loss of the higher-order moment information from the Gaussian reconstruction. Then, an adaptive kernel size method is developed to achieve the online optimal adjustment of the kernel size while maintaining robustness against outliers. Simulation experiments validate the proposed adaptive kernel size method and the robust MCC-based RFU filter. The experimental results indicate that: a) Compared to existing methods, the proposed adaptive kernel size method can effectively adjust the kernel size for different noise cases while avoiding the over-convergence problem. Furthermore, the cumulative distribution probability of smaller kernel sizes is consistent with the outlier occurrence probability settings. Within the interval of kernel size upper bound [10, 60], the range of position ARMSE for MRCKF is 0.129 m, maintaining relatively stable estimation accuracy. It exhibits good stability in tuning parameter selection, validating the effectiveness of the proposed adaptive kernel

6.1. Conclusions

size method; b) In the presence of outliers, the position ARMSE of proposed MRCKF is reduced by 13.9%, 20.4%, and 11.3% compared to the existing robust RSTKF, HMKF and MCKF, respectively. Additionally, the cumulative probability of position estimation error within 2 m throughout the simulation is 90.15%, which is higher than RSTKF (74.8%), HMKF (74.8%), and MCKF (82.1%), indicating better robust estimation performance. It validates the effectiveness of the proposed robust MCC-based RFU framework.

- (2) To suppress the interference of outliers on the MNCM estimation in urban areas, a robust noise adaptation algorithm based on a smoothing variational approximation is proposed. The IW distribution is used as the conjugate prior model of the MNCM, and a joint variational approximate analytical solution for the MNCM and smoothing state is derived. Then, the inverse scale matrix of the IW distribution is reconstructed based on the correntropy matrix to suppress the interference of measurement outliers on the MNCM estimation. Simulation experiments validate the proposed method. The experimental results show that, compared to the SHA, VBA, and ORA methods, the proposed RSVBA has higher estimation accuracy for MNCM in the presence of outliers, and the corresponding position estimation ARMSE is reduced by 26.3%, 24.6%, and 10.2%, respectively, indicating better robust estimation accuracy. This demonstrates that the proposed RSVBA can effectively suppress the interference of measurement outliers on MNCM estimation and verifies its effectiveness.
- (3) To monitor the navigation integrity for INMS in urban areas, a sequential IM method based on multiple fault bias missing detection assumption is proposed. The IM dynamic regression model is constructed by a consistent posterior estimate provided by the proposed robust filter. A consistency factor in the state domain is calculated using the sequential probability ratio over sliding windows. Under the multiple fault-missing detection assumption, the HPL is calculated based on the maximum eigenvalue combined with the consistency factor to quantitatively evaluate the confidence of the position solution. Simulation experiments are conducted to verify the effectiveness of the proposed IM method. The experimental results indicate that the k-Sigma, KSIM, and RSIM methods have the highest HPL reliability of 79.74%, 90.77%, and 97.36%, and the highest probability of HMI events of 0.24%, 0.22%, and 0.08% respectively, in various simulation cases, which could not satisfy the integrity risk requirements. In comparison, the proposed MSIM has an HPL reliability of over 99.62% in various simulation cases and does not generate any HMI events. This effectively evaluates the reliability of the position estimation and realizes the integrity monitoring, thus verifying the effectiveness of the proposed method.
 - (4) An in-vehicle experiment is conducted using MEMS-IMU, GNSS, OD, and POLA

to validate the practical performance of the proposed robust estimation, noise adaptation, and integrity monitoring algorithm: a) The proposed robust state estimation algorithm is validated. The experimental results indicate that the MMSE-based CKF and RFCKF show poor estimation results in dense urban areas subject to non-Gaussian heavy-tailed noise. Compared to the existing robust filters RSTKF, HMKF, and MCKF adopting the kernel size optimal method, the proposed MRCKF shows smaller RMSE for each navigation parameter, and the position RMSE is reduced by 20.4%, 14.1%, and 5.0%, respectively, indicating better robust estimation effect. This validates the proposed MRCKF algorithm in practical applications; b) The proposed robust noise adaptation algorithm is validated. The experimental results show that compared to SHA, VBA, and ORA methods, the noise MNCM estimation of the proposed RSVBA is smoother and matches the actual sensor noise characteristics in adverse urban areas with the presence of outliers. Additionally, the position RMSE of RSVBA is reduced by 13.6%, 13.9%, and 18.2% compared to SHA, VBA, and ORA methods, respectively. This indicates that the proposed RSVBA can effectively suppress the interference of measurement outliers on MNCM estimation and achieve robust noise adaptation, thus validating the practical performance of the proposed algorithm; c) The proposed autonomous integrity monitoring algorithm is validated. The experimental results show that the HPL reliability of the k-Sigma, KSIM, and RSIM methods are 88.68%, 93.61%, and 86.23%, respectively, and even lower in adverse urban areas. Also, the k-Sigma and KSIM suffer from the HMI events with a probability of 1.24%. In contrast, the proposed MSIM has the highest HPL reliability (99.85%) throughout the experiment and does not generate any HMI events, effectively evaluating the confidence of the position solution and monitoring the integrity of the INMS. These results validate the practical performance of the proposed algorithm.

6.2 Recommendations

With the rapid development of the low-altitude economy and intelligent robotics, an increasing number of autonomous devices—such as drones, robots, and unmanned vehicles—are being deployed. However, the presence of severe non-Gaussian noise and highly complex nonlinear system models in challenging environments limits the effectiveness of current model-driven state estimation and integrity monitoring methods for navigation systems. Currently, data-driven intelligent methods such as reinforcement learning are advancing rapidly and have demonstrated complementary advantages over traditional model-driven approaches. Based on this background, this section first outlines the future research trends in state estimation and health monitoring methods. Then, the specific technical work

6.2. Recommendations 119

in the future will be explored, which is also illustrated in Fig. 6.1.

(1) Future Research Direction

- State estimation combining reinforcement learning and Kalman filtering. Traditional robustness enhancement and noise adaptation methods for Kalman filters tend to increase the nonlinearity of the computational process, which can undermine the reliability of state estimation. Reinforcement learning, by interacting with the environment to learn optimal strategies, can dynamically adjust key Kalman filter parameters online (such as MNCM), or directly compensate for model prediction errors. This approach effectively mitigates the Kalman filter's dependence on accurate prior models and fixed noise statistics. Consequently, in the presence of sensor anomalies, abrupt environmental changes, or system model errors, it enables more accurate estimation of states such as position, velocity, and attitude, thereby significantly improving the reliability and accuracy of navigation systems in real-world challenging scenarios. Integrating reinforcement learning with Kalman filtering is therefore of great significance for further enhancing navigation and positioning accuracy in challenging environments.
- Integrity monitoring based on data-driven by deep learning. The protection levels are calculated using regression models based on measurement projection, representing a model-driven approach to navigation integrity monitoring. However, in practical dynamic scenarios, noise distributions are often unknown, unbounded, and multimodal, and nonlinear models may fail to capture the mapping relationships accurately. As a result, relying solely on fixed models for error distribution may not provide sufficient reliability for safety-critical positioning applications. Deep learning and data-driven methods can leverage large volumes of historical and real-time data to automatically learn error characteristics in complex environments, enabling more accurate and dynamic protection level calculations as well as adaptive computation of integrity support information. Compared to traditional RAIM and solution separation-based advanced RAIM methods, these approaches offer greater adaptability, higher detection sensitivity, and lower false alarm rates. Therefore, integrity monitoring based on data-driven deep learning is of great significance for further improving the safety and reliability of navigation and positioning in challenging environments.

(2) Future Technical Work

• Integrity monitoring for vertical direction. The IM algorithm proposed in this

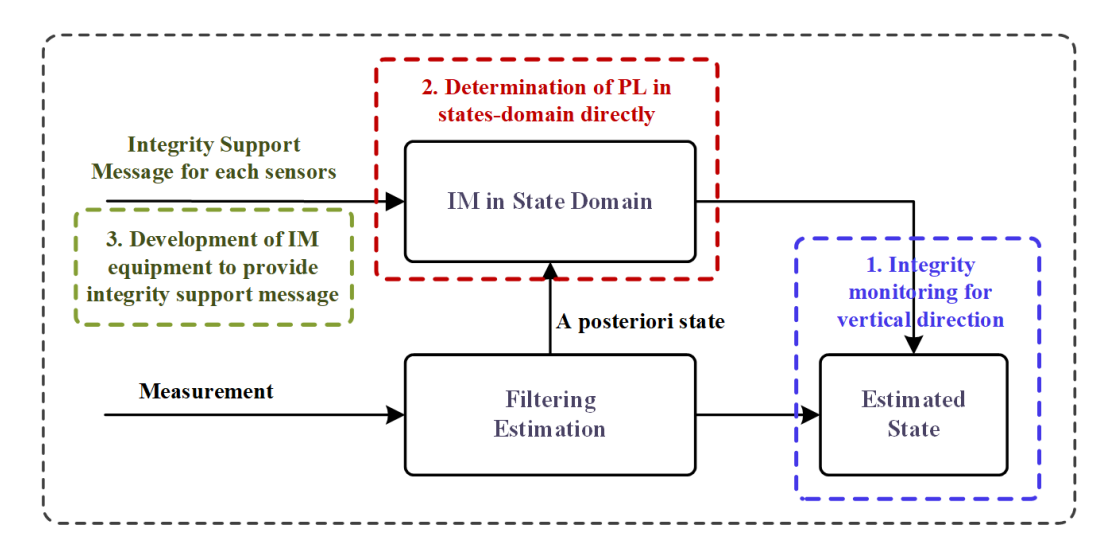


Figure 6.1: Future technical work

thesis focuses on monitoring the integrity of the horizontal position solution for invehicle applications. However, it may also be necessary to monitor the integrity of other navigation states under various application scenarios and requirements. For instance, in elevated bridges or mountainous areas, the integrity of vertical coordinates is also crucial for navigation safety. It's essential to investigate whether the same integrity monitoring mechanism and protection level calculation method can be applied to other states (e.g., vertical coordinates) in future work.

- Determination of PL in states-domain directly. In current integrity monitoring methods, PL is calculated based on projecting the hypothesized fault biases in the state domain from the measurement domain. This approach is more practical than the solution separation approach because it avoids predetermining much of the integrity support message (e.g., sensor fault probability), for which there is no available determination method for integrated navigation. Theoretically, however, the direct determination of the PL of the a posteriori states is more reasonable than the indirect mapping by measurement. The direct determination of PL should also differ from the principle of solution separation, as it eliminates the need to compute PL through multiple failure assumptions. Therefore, the direct determination of PL in the state domain without any fault assumptions is one of the future research directions for integrated navigation integrity.
- **Development of integrity monitoring equipment.** With the rapid development of autonomous vehicles and other unmanned devices, navigation safety is playing an increasingly important role. Existing advanced integrity monitoring algorithms for satellite navigation require external base stations to provide corresponding integrity

6.2. Recommendations 121

support messages, such as satellite failure rates and maximum nominal bias. However, for inertial integrated navigation systems, there are currently no mature algorithms or prototype devices that provide external integrity support messages. Therefore, it is necessary to develop integrity monitoring and corresponding matching devices in the future.

Appendix A

Gaussian Approximation Filter Based on Bayes Rule

A discrete-time stochastic dynamic system is considered as

$$\begin{cases} \mathbf{x}_{k} = \mathbf{f}_{k}(\mathbf{x}_{k-1}) + \mathbf{w}_{k-1} \\ \mathbf{z}_{k} = \mathbf{h}_{k}(\mathbf{x}_{k}) + \mathbf{v}_{k} \end{cases}$$
(A.1)

where $\mathbf{x}_k \in \mathbb{R}^n$ and $\mathbf{z}_k \in \mathbb{R}^m$ are the state vector and the measurement vector at discretetime step k, respectively; $\mathbf{f}_k(\cdot) : \mathbb{R}^n \Rightarrow \mathbb{R}^n$ and $\mathbf{h}_k(\cdot) : \mathbb{R}^n \Rightarrow \mathbb{R}^m$ are the state dynamic function and measurement function, respectively; $\mathbf{w}_{k-1} \sim \mathrm{N}(\mathbf{0}, \mathbf{Q}_{k-1})$ and $\mathbf{v}_k \sim \mathrm{N}(\mathbf{0}, \mathbf{R}_k)$ are the uncorrelated process and measurement noise with known covariance matrix \mathbf{Q}_{k-1} and \mathbf{R}_k , respectively.

To calculate the posterior state PDF, i.e., $p(\mathbf{x}_k \mid \bar{\mathbf{z}}_k)$ with $\bar{\mathbf{z}}_k = \{\mathbf{z}_j, 1 \leq j \leq k\}$, the states and measurement are assumed as Gaussian distributions for ensuring analytical solutions in closed form, then the joint PDF of state and measurement vector is calculated as

$$p\left(\mathbf{x}_{k}, \mathbf{z}_{k} \mid \bar{\mathbf{z}}_{k-1}\right) = N\left(\begin{bmatrix}\mathbf{x}_{k} \\ \mathbf{z}_{k}\end{bmatrix}; \begin{bmatrix}\hat{\mathbf{x}}_{k|k-1} \\ \hat{\mathbf{z}}_{k|k-1}\end{bmatrix}, \begin{bmatrix}\mathbf{P}_{k|k-1} & \mathbf{P}_{k|k-1}^{xz} \\ (\mathbf{P}_{k|k-1}^{xz})^{T} & \mathbf{P}_{k|k-1}^{zz}\end{bmatrix}\right)$$
(A.2)

where the prior state mean $\hat{\mathbf{x}}_{k|k-1}$ and covariance matrix $\mathbf{P}_{k|k-1}$ are the Gaussian (i.e., the first-two orders) moments of $p(\mathbf{x}_k \mid \bar{\mathbf{z}}_{k-1})$; The predicted measurement $\hat{\mathbf{z}}_{k|k-1}$ and covariance matrix $\mathbf{P}_{k|k-1}^{zz}$ are the Gaussian moments of $p(\mathbf{z}_k \mid \bar{\mathbf{z}}_{k-1})$; $\mathbf{P}_{k|k-1}^{xz}$ is the cross-covariance matrix of state and measurement. The above variables are calculated by Gaussian weighted integration and are represented as follows:

$$\hat{\mathbf{x}}_{k|k-1} = \int_{\mathbb{R}^n} \mathbf{f}_k(\mathbf{x}_{k-1}) \mathbf{N}(\mathbf{x}_{k-1} \mid \hat{\mathbf{x}}_{k-1}, \mathbf{P}_{k-1}) d\mathbf{x}_{k-1}$$
(A.3)

$$\hat{\mathbf{z}}_{k|k-1} = \int_{\mathbb{R}^n} \mathbf{h}_k(\mathbf{x}_k) \, \mathbf{N}\left(\mathbf{x}_k; \hat{\mathbf{x}}_{k|k-1}, \mathbf{P}_{k|k-1}\right) \, \mathrm{d}\mathbf{x}_k \tag{A.4}$$

$$\mathbf{P}_{k|k-1} = \int_{\mathbb{R}^n} \mathbf{f}_k\left(\mathbf{x}_{k-1}\right) \mathbf{f}_k^{\mathrm{T}}\left(\mathbf{x}_{k-1}\right) \mathrm{N}\left(\mathbf{x}_{k-1}; \hat{\mathbf{x}}_{k-1}, \mathbf{P}_{k-1}\right) \mathrm{d}\mathbf{x}_{k-1} - \hat{\mathbf{x}}_{k|k-1} \hat{\mathbf{x}}_{k|k-1}^{\mathrm{T}} + \mathbf{Q}_{k-1}$$
(A.5)

$$\mathbf{P}_{k|k-1}^{xz} = \int_{\mathbb{R}^n} \mathbf{x}_k \mathbf{h}_k^{\mathrm{T}}(\mathbf{x}_k) \, \mathbf{N}\left(\mathbf{x}_k; \hat{\mathbf{x}}_{k|k-1}, \mathbf{P}_{k|k-1}\right) \, \mathrm{d}\mathbf{x}_k - \hat{\mathbf{x}}_{k|k-1} \hat{\mathbf{z}}_{k|k-1}^{\mathrm{T}} \tag{A.6}$$

$$\mathbf{P}_{k|k-1}^{zz} = \int_{\mathbb{R}^n} \mathbf{h}_k(\mathbf{x}_k) \mathbf{h}_k^{\mathrm{T}}(\mathbf{x}_k) \mathrm{N}\left(\mathbf{x}_k; \hat{\mathbf{x}}_{k|k-1}, \mathbf{P}_{k|k-1}\right) \mathrm{d}\mathbf{x}_k - \hat{\mathbf{z}}_{k|k-1} \hat{\mathbf{z}}_{k|k-1}^{\mathrm{T}} + \mathbf{R}_k$$
(A.7)

According to the Bayes rule, the posterior state PDF $p(\mathbf{x}_k \mid \bar{\mathbf{z}}_k)$ can be obtained from $p(\mathbf{x}_k, \mathbf{z}_k \mid \bar{\mathbf{z}}_{k-1})$ and denoted under the Gaussian assumption as

$$p\left(\mathbf{x}_{k} \mid \bar{\mathbf{z}}_{k}\right) = \frac{p\left(\mathbf{x}_{k}, \mathbf{z}_{k} \mid \bar{\mathbf{z}}_{k-1}\right)}{p\left(\mathbf{z}_{k} \mid \bar{\mathbf{z}}_{k-1}\right)} = \frac{p\left(\mathbf{z}_{k} \mid \mathbf{x}_{k}\right) p\left(\mathbf{x}_{k} \mid \bar{\mathbf{z}}_{k-1}\right)}{p\left(\mathbf{z}_{k} \mid \bar{\mathbf{z}}_{k-1}\right)} \approx N\left(\mathbf{x}_{k}; \hat{\mathbf{x}}_{k}, \mathbf{P}_{k}\right)$$
(A.8)

where the posterior state estimate mean $\hat{\mathbf{x}}_k$ and the covariance matrix \mathbf{P}_k are calculated as

$$\hat{\mathbf{x}}_{k} = \hat{\mathbf{x}}_{k|k-1} + \mathbf{P}_{k|k-1}^{xz} (\mathbf{P}_{k|k-1}^{zz})^{-1} (\mathbf{z}_{k} - \hat{\mathbf{z}}_{k|k-1})$$
(A.9)

$$\mathbf{P}_{k} = \mathbf{P}_{k|k-1} - \mathbf{P}_{k|k-1}^{xz} (\mathbf{P}_{k|k-1}^{zz})^{-1} (\mathbf{P}_{k|k-1}^{xz})^{\mathrm{T}}$$
(A.10)

Appendix B

Error-State Space Model for INMS

This section constructs the error-state state-space model of the INMS. The east-north-up (ENU) geographic coordinate system is used as the navigation coordinate system (n-frame), while the IMU coordinate system and the odometer coordinate system are represented as b-frame and o-frame, respectively. The moment subscript k is omitted from the model for simplicity in presentation.

B.1 INMS Operating Principles

In INMS, the SINS is used as a host system to output navigation data at high frequencies. Other sensors provide observations to correct the INS. Firstly, SINS updates the attitude, velocity, and position information in INMS, which is formulated by Eq. (B.1).

$$\dot{\mathbf{C}}_{b}^{n} = \mathbf{C}_{b}^{n}[\boldsymbol{\omega}_{nb}^{b} \times] = \mathbf{C}_{b}^{n}[\boldsymbol{\omega}_{ib}^{b} \times] - [\boldsymbol{\omega}_{in}^{n} \times] \mathbf{C}_{b}^{n}; \tag{B.1a}$$

$$\dot{\mathbf{v}}^{n} = \mathbf{C}_{b}^{n} \mathbf{f}_{ib}^{b} - (2\omega_{ie}^{n} + \omega_{en}^{n}) \times \mathbf{v}^{n} + \mathbf{g}^{n}; \tag{B.1b}$$

$$\dot{\mathbf{p}} = \dot{\mathbf{v}}^{\mathrm{n}}; \tag{B.1c}$$

where \mathbf{C}_{b}^{n} is a direction cosine matrix of SINS corresponding to the attitude $[\theta \ \gamma \ \psi]^{\mathrm{T}}$; $\mathbf{v} = [v_{\mathrm{e}} \ v_{\mathrm{n}} \ v_{\mathrm{u}}]^{\mathrm{T}}$ are the east, north, and upward velocity error of SINS, respectively; $\mathbf{p} = [L \ \lambda \ h]^{\mathrm{T}}$ are the latitude error, longitude error and altitude error, respectively. $\boldsymbol{\omega}_{\mathrm{nb}}^{\mathrm{b}}$ is the angular velocity of the b-frame with respect to the n-frame; $[\boldsymbol{\omega}_{\mathrm{nb}}^{\mathrm{b}} \times]$ is the skew-symmetric matrix; $\boldsymbol{\omega}_{\mathrm{ib}}^{\mathrm{b}}$ is the three-axis angular velocity of IMU; $\mathbf{f}_{\mathrm{ib}}^{\mathrm{b}} = [f_x \ f_y \ f_z]^{\mathrm{T}}$ denotes the three-axis specific force of IMU; $\boldsymbol{\omega}_{\mathrm{in}}^{\mathrm{n}} = \boldsymbol{\omega}_{\mathrm{ie}}^{\mathrm{n}} + \boldsymbol{\omega}_{\mathrm{en}}^{\mathrm{n}}$, in which $\boldsymbol{\omega}_{\mathrm{ie}}^{\mathrm{n}} = [0 \ \boldsymbol{\omega}_{\mathrm{ie}} \cos L \ \boldsymbol{\omega}_{\mathrm{ie}} \sin L]^{\mathrm{T}}$, $\boldsymbol{\omega}_{\mathrm{en}}^{\mathrm{n}} = [-\frac{v_{\mathrm{n}}}{R_{\mathrm{N}} + h} \ \frac{v_{\mathrm{e}}}{R_{\mathrm{N}} + h} \tan L]^{\mathrm{T}}$; $\boldsymbol{\omega}_{\mathrm{ie}}$ is the angular velocity of the earth's rotation; $\mathbf{r}_{\mathrm{eS}}^{\mathrm{e}} = [R_{\mathrm{M}} \ R_{\mathrm{N}}]^{\mathrm{T}}$ is the local radius of the earth, R_{M} and R_{N} are the earth's radius for the meridian circle and the dodecaphragm circle, respectively.

However, due to the inherent drawback of error accumulation, it is necessary to use measurement data from external sensors such as OD, GNSS, and optical sensors to correct SINS errors in real-time. Specifically, to ensure the validity of the state minor assumption, the errors in the SINS are used to construct the main state vectors, and the state kinetic

model is developed based on the differential equations of the SINS error [74, 125]. Then, the measurements are obtained by the deviations between SINS solution and position, velocity, and heading observation data from the GNSS, odometer, and polarizer camera, and the matching measurement model is constructed. Finally, the state is estimated by a filter and is used to correct the SINS. The operating architecture is shown on Fig. B.1.

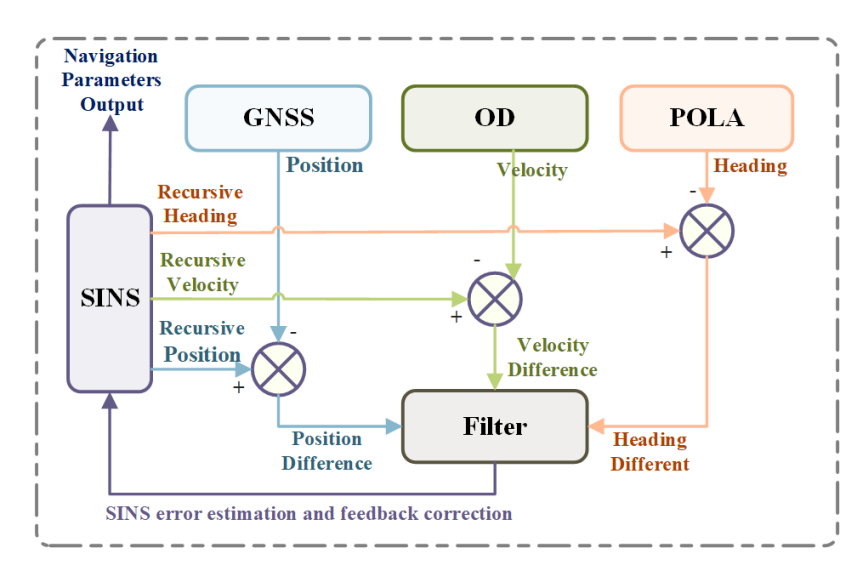


Figure B.1: Operating framework for INMS

B.2 INMS Error-State Space Modeling

(1) State-dynamic model

The differential equation for the SINS platform misalignment angle $\dot{\phi}$, velocity error $\delta \dot{\mathbf{v}}$, position error $\delta \dot{\mathbf{p}}$, and odometer mounting bias angle and scale factor error are first given as follows.

$$\dot{\phi} = -\omega_{ie}^{e} \times \phi + \mathbf{C}_{b}^{n} \varepsilon; \tag{B.2a}$$

$$\delta \dot{\mathbf{v}}^{n} = -\left(\mathbf{C}_{b}^{e} \mathbf{f}_{ib}^{b}\right) \times \phi - 2\omega_{ie}^{e} \times \delta \mathbf{v}^{n} + \frac{2g_{0}}{\mathbf{r}_{eS}^{e}} \frac{\mathbf{p}}{|\mathbf{p}|^{2}} \mathbf{p}^{T} + \mathbf{C}_{b}^{e} \nabla;$$
(B.2b)

$$\delta \dot{\mathbf{p}} = \delta \mathbf{v}; \dot{\varepsilon} = \mathbf{0}; \dot{\nabla} = \mathbf{0};$$
 (B.2c)

$$\dot{\alpha}_x = 0; \, \dot{\alpha}_z = 0; \, \delta \dot{K}_{\text{od}} = 0$$
 (B.2d)

where $\phi = [\phi_e \ \phi_n \ \phi_u]^T$ denotes the platform misalignment angle of SINS, i.e., the offset angle between the computed platform frame and the actual platform frame; $\varepsilon = [\varepsilon_x \ \varepsilon_y \ \varepsilon_z]^T$ denotes gyro constant bias in *b*-frame; $\nabla = [\nabla_x \ \nabla_y \ \nabla_z]^T$ denotes the accelerometer constant bias in *b*-frame; $\mathbf{x}_{od} = [\alpha_z \ \delta K_{od} \ \alpha_x]^T$ are odometer-related error parameters, α_x and α_z

are the installation deviation angle between the odometer frame and the IMU frame, δK_{od} is the odometer scale factor error. Construct the state vector $\mathbf{x} = [\phi \ \delta \mathbf{v} \ \delta \mathbf{p} \ \epsilon \ \nabla \ \mathbf{x}_{\text{od}}]^T$, and develope the following INMS state kinetic model based on the above differential equations:

$$\dot{\mathbf{x}} = \mathbf{F}\mathbf{x} + \mathbf{G}\mathbf{w} \tag{B.3}$$

where the state transfer matrix **F** and the noise driving matrix **G** are calculated as follows

$$\begin{split} \mathbf{F} &= \begin{bmatrix} \mathbf{F}_{avp} \ \mathbf{F}_{imu} \ \mathbf{F}_{od} \\ \mathbf{0}_{9\times 9} \ \mathbf{0}_{9\times 6} \ \mathbf{0}_{9\times 3} \end{bmatrix}; \mathbf{F}_{avp} &= \begin{bmatrix} \mathbf{F}_{aa} \ \mathbf{F}_{av} \ \mathbf{F}_{vp} \\ \mathbf{F}_{va} \ \mathbf{F}_{vv} \ \mathbf{F}_{vp} \\ \mathbf{0}_{3\times 3} \ \mathbf{F}_{pv} \ \mathbf{F}_{pp} \end{bmatrix}; \\ \mathbf{F}_{imu} &= \begin{bmatrix} -\mathbf{C}_{b}^{n} \ \mathbf{0}_{3\times 3} \\ \mathbf{0}_{3\times 3} \ \mathbf{C}_{b}^{n} \\ \mathbf{0}_{3\times 3} \ \mathbf{0}_{3\times 3} \end{bmatrix}; \mathbf{G} &= \begin{bmatrix} -\mathbf{C}_{b}^{n} \ \mathbf{0}_{3\times 3} \\ \mathbf{0}_{3\times 3} \ \mathbf{C}_{b}^{n} \\ \mathbf{0}_{12\times 3} \ \mathbf{0}_{12\times 3} \end{bmatrix}; \\ \mathbf{F}_{aa} &= \begin{bmatrix} 0 & \omega_{te} \sin L - \frac{v_{e} \tan L}{R_{N} + h} & 0 & -\frac{v_{e}}{R_{N} + h} \\ \omega_{te} \cos L + \frac{v_{e}}{R_{N} + h} & \frac{v_{e}}{R_{M} + h} & 0 \end{bmatrix}; \\ \mathbf{F}_{av} &= \begin{bmatrix} 0 & -\frac{1}{R_{M} + h} & 0 \\ \frac{1}{R_{N} + h} & 0 & 0 \\ \frac{1}{R_{N} + h} & 0 & 0 \end{bmatrix}; \mathbf{F}_{ap} &= \begin{bmatrix} 0 & 0 & 0 \\ -\omega_{te} \sin L & 0 & 0 \\ \omega_{te} \cos L + \frac{v_{e}}{R_{N} + h} & \sec^{2} L & 0 \\ \omega_{te} \cos L + \frac{v_{e} \sin L}{R_{N} + h} & 2\omega_{te} \sin L v_{u} & 0 \\ -2\omega_{te} \sin L v_{e} & 0 & 0 \\ \end{bmatrix}; \\ \mathbf{F}_{vv} &= \begin{bmatrix} 2\omega_{te} \cos Lv_{n} + \frac{v_{e} v_{n} \sec^{2} L}{R_{N} + h} + 2\omega_{te} \sin Lv_{u} & 0 \\ -2\omega_{te} \sin Lv_{e} & 0 & 0 \\ -2\omega_{te} \sin Lv_{e} & 0 & 0 \\ \end{bmatrix}; \\ \mathbf{F}_{vv} &= \begin{bmatrix} \frac{v_{n} \tan L}{R_{N} + h} - \frac{v_{u}}{R_{N} + h} & 2\omega_{te} \sin L + \frac{v_{e} \tan L}{R_{N} + h} & 2\omega_{te} \cos L + \frac{v_{e}}{R_{N} + h} \\ 2\omega_{te} \cos L + \frac{2v_{e}}{R_{N} + h} & -\frac{v_{n}}{R_{M} + h} & -\frac{v_{n}}{R_{M} + h} \\ 2\omega_{te} \cos L + \frac{2v_{e}}{R_{N} + h} & \frac{2v_{n}}{R_{M} + h} & 0 \\ \end{bmatrix}; \\ \mathbf{F}_{pv} &= \begin{bmatrix} 0 & \frac{1}{R_{M} + h} & 0 \\ \frac{R_{N} + h}{R_{N} + h} & 0 \\ 0 & 0 & 1 \end{bmatrix}; \mathbf{F}_{pp} &= \begin{bmatrix} 0 & 0 & 0 \\ \frac{v_{e} \sec L \tan L}{R_{N} + h} & 0 \\ 0 & 0 & 0 \end{bmatrix}; \mathbf{F}_{od} &= \mathbf{0}_{9 \times 3} \\ 0 & 0 & 0 \end{bmatrix}$$

(2) Measurement model

(a) GNSS position-based measurement equation: GNSS provides position $\mathbf{p}_{gnss} = [L_{gnss} \ \lambda_{gnss} \ h_{gnss}]^T$ in geographic coordinate system. In INMS, the difference between the SINS and GNSS positions is used as the measurement. Thus, the measurement equation is

constructed associated with the position error as

$$\mathbf{z}_{gnss} = \mathbf{p} - \mathbf{p}_{gnss} = \delta \mathbf{p} \tag{B.4}$$

(b) **OD velocity-based measurement equation:** Odometer provides the forward velocity of the carrier. With the odometer scale factor error $\delta K_{\rm od}$ and measurement noise $n_{\rm od}$, the odometer output $\tilde{v}_{\rm od}^{\rm o}$ is expressed as

$$\tilde{v}_{\text{od}}^{\text{o}} = \left(1 + \delta K_{\text{od}}\right) v_{\text{od}}^{\text{o}} + n_{\text{od}} \tag{B.5}$$

The installation error between the odometer and the IMU coordinate system is supposed as a smaller angle and expressed as $\alpha = [\alpha_x \ \alpha_y \ \alpha_z]^T$, thus the direction cosine matrix \mathbf{C}_0^b is formulated as

$$\mathbf{C}_{o}^{b} = \mathbf{I} - (\boldsymbol{\alpha} \times) = \begin{bmatrix} 1 & \alpha_{z} & -\alpha_{y} \\ -\alpha_{z} & 1 & \alpha_{x} \\ \alpha_{y} & -\alpha_{x} & 1 \end{bmatrix}$$
(B.6)

where $\alpha \times$ denotes the skew-symmetric matrix of α . Furthermore, the projection of odometer velocity vector $\tilde{\mathbf{v}}_{od}^{o} = \begin{bmatrix} 0 & \tilde{v}_{od}^{o} & 0 \end{bmatrix}^{T}$ in the body coordinate system is expressed as

$$\tilde{\mathbf{v}}_{\text{od}}^{\text{b}} = \mathbf{C}_{\text{o}}^{\text{b}} \tilde{\mathbf{v}}_{\text{od}}^{\text{o}} = (\mathbf{I} - (\alpha \times)) \, \tilde{\mathbf{v}}_{\text{od}}^{\text{o}} = \mathbf{v}_{\text{od}}^{\text{b}} + \begin{bmatrix} \alpha_z v_{\text{od}}^{\text{o}} \\ \delta K_{\text{od}} v_{\text{od}}^{\text{o}} \\ -\alpha_x v_{\text{od}}^{\text{o}} \end{bmatrix}$$
(B.7)

Let $\mathbf{x}_{od} = [\alpha_z \ \delta K_{od} \ \alpha_x]^T$, $\mathbf{M}_{od} = \text{diag}([v_{od}^o; v_{od}^o; -v_{od}^o])$, then the right-hand error term in Eq. (B.7) can be represented as $\delta \mathbf{v}_{od}^b = \mathbf{M}_{od}\mathbf{x}_{od}$. Subsequently, the odometer velocity $\tilde{\mathbf{v}}_{od}^b$ is projected into navagition coordinate frame by $\hat{\mathbf{C}}_b^n$ to construct the measurement equation as

$$\begin{split} \tilde{\mathbf{v}}_{od}^{n} &= \hat{\mathbf{C}}_{b}^{n} \tilde{\mathbf{v}}_{od}^{b} = (\mathbf{I} - (\phi \times)) \mathbf{C}_{b}^{n} \left(\mathbf{v}_{od}^{b} + \delta \mathbf{v}_{od}^{b} \right) \\ &= \mathbf{v}_{od}^{n} - (\phi \times) \mathbf{v}_{od}^{n} + \mathbf{C}_{b}^{n} \delta \mathbf{v}_{od}^{b} - (\phi \times) \mathbf{C}_{b}^{n} \delta \mathbf{v}_{od}^{b} \end{split} \tag{B.8}$$

After compensating for the velocity error $\delta \mathbf{v}_L = \mathbf{C}_b^n \left(\omega_{nb}^b \times\right) \mathbf{L}$ caused by the fixed level-arm, the difference between the SINS velocity $\hat{\mathbf{v}}^n$ and OD velocity $\tilde{\mathbf{v}}_{od}^n$ is used as the measurement. Thus, the measurement equation is constructed as

$$\mathbf{z}_{od} = \hat{\mathbf{v}}^{n} - \tilde{\mathbf{v}}_{od}^{n} = \delta \mathbf{v}^{n} - (\mathbf{v}_{od}^{n} \times) \phi - \mathbf{C}_{b}^{n} \mathbf{M}_{od} \mathbf{x}_{od} + (\phi \times) \mathbf{C}_{b}^{n} \mathbf{M}_{od} \mathbf{x}_{od}$$
(B.9)

(c) POLA heading-based measurement equation: Polarizer navigation system provides carrier heading information. The difference between the SINS heading ψ and POLA heading ψ_{pola} is used as measurement and constructing the corresponding measurement equation associated with INS platform misalignment angle $\phi = [\phi_e \ \phi_n \ \phi_u]$. First, the attitude is definited as $\delta \mathbf{A} = [\delta \theta \ \delta \gamma \ \delta \psi]^T$. According to the projection relationship of n-frame and b-frame, there is

$$\mathbf{C}_{\mathbf{n}}^{\mathbf{n}'}\mathbf{C}_{\mathbf{b}}^{\mathbf{n}} = \mathbf{C}_{\mathbf{b}}^{\mathbf{n}}\mathbf{C}_{\mathbf{b}'}^{\mathbf{b}} \tag{B.10}$$

where n' and b' are the computed coordinate system. $\mathbf{C}_{n}^{n'}$ and $\mathbf{C}_{b'}^{b}$ contains the skew-symmetric matrix of ϕ and μ , respectively. Thus, there is

$$[\mathbf{I} - \phi \times] \mathbf{C}_{b}^{n} = \mathbf{C}_{b}^{n} [\mathbf{I} + \mu \times]$$
 (B.11a)

$$\phi = -\mathbf{C}_b^n \mu \tag{B.11b}$$

According to the definition of the installation error angle $\dot{\mu} = \omega_{nb}^b$ and the Eulerian angular differential equation $\omega_{nb}^b = \mathbf{C}_A^\omega \cdot \dot{\mathbf{A}}$, there is $\phi = -\mathbf{C}_b^n \mathbf{C}_A^\omega \cdot \delta \mathbf{A}$ through the integration approximation. Thus, the relationship between the attitude error angle and the platform misalignment angle can be obtained as [126]

$$\delta \mathbf{A} = \begin{bmatrix} -\cos\psi & -\sin\psi & 0\\ \sin\psi/\cos\theta & -\cos\psi/\cos\theta & 0\\ -\tan\theta\sin\psi & \tan\theta\cos\psi & -1 \end{bmatrix} \cdot \phi$$
 (B.12)

where θ and ψ are the carrier pitch and heading angles, respectively. Since POLA only outputs the heading information, the measurement equation is given as

$$\mathbf{z}_{\text{pola}} = \psi - \psi_{\text{pola}} = -\tan\theta\sin\psi\phi_{\text{e}} + \tan\theta\cos\psi\phi_{\text{n}} - \phi_{\text{u}}$$
 (B.13)

Reference

- [1] Niels Joubert, Tyler GR Reid, and Fergus Noble. Developments in modern GNSS and its impact on autonomous vehicle architectures. In 2020 IEEE Intelligent Vehicles Symposium (IV), pages 2029–2036. IEEE, 2020.
- [2] Liang Chen, Fu Zheng, Xiaopeng Gong, and Xinyuan Jiang. Gnss high-precision augmentation for autonomous vehicles: Requirements, solution, and technical challenges. *Remote Sensing*, 15(6):1623, 2023.
- [3] Chao Xiang, Chen Feng, Xiaopo Xie, Botian Shi, Hao Lu, Yisheng Lv, Mingchuan Yang, and Zhendong Niu. Multi-sensor fusion and cooperative perception for autonomous driving: A review. *IEEE Intelligent Transportation Systems Magazine*, 2023.
- [4] Yuan Zhuang, Xiao Sun, You Li, Jianzhu Huai, Luchi Hua, Xiansheng Yang, Xiaoxiang Cao, Peng Zhang, Yue Cao, Longning Qi, et al. Multi-sensor integrated navigation/positioning systems using data fusion: From analytics-based to learning-based approaches. *Information Fusion*, 95:62–90, 2023.
- [5] Lisheng Xu, Haoran Zhang, Jiaole Wang, Ang Li, Shuang Song, Hongliang Ren, Lin Qi, Jason J Gu, and Max Q-H Meng. Information loss challenges in surgical navigation systems: From information fusion to AI-based approaches. *Information Fusion*, 92:13–36, 2023.
- [6] Guowei Wan, Xiaolong Yang, Renlan Cai, Hao Li, Yao Zhou, Hao Wang, and Shiyu Song. Robust and precise vehicle localization based on multi-sensor fusion in diverse city scenes. In 2018 IEEE International Conference on Robotics and Automation (ICRA), pages 4670–4677. IEEE, 2018.
- [7] Masoud Khodarahmi and Vafa Maihami. A review on Kalman filter models. *Archives of Computational Methods in Engineering*, 30(1):727–747, 2023.
- [8] Mengde Zhang, Kailong Li, Baiqing Hu, and Chunjian Meng. Comparison of Kalman filters for inertial integrated navigation. *Sensors*, 19(6):1426, 2019.
- [9] Zhenbing Qiu and Lei Guo. Improved cubature Kalman filter for spacecraft attitude estimation. *IEEE Transactions on Instrumentation and Measurement*, 70:1–13, 2020.

[10] Li Luo, Yulong Huang, Zheng Zhang, and Yonggang Zhang. A new Kalman filter-based in-motion initial alignment method for DVL-aided low-cost SINS. *IEEE Transactions on Vehicular Technology*, 70(1):331–343, 2021.

- [11] Weisong Wen, Tim Pfeifer, Xiwei Bai, and Li-Ta Hsu. Factor graph optimization for GNSS/INS integration: A comparison with the extended Kalman filter. *NAVI-GATION: Journal of the Institute of Navigation*, 68(2):315–331, 2021.
- [12] Yulong Huang, Yonggang Zhang, Bo Xu, Zhemin Wu, and Jonathon A Chambers. A new adaptive extended Kalman filter for cooperative localization. *IEEE Transactions on Aerospace and Electronic Systems*, 54(1):353–368, 2017.
- [13] Mingming Bai, Yulong Huang, Yonggang Zhang, and Guangle Jia. A novel progressive Gaussian approximate filter for tightly coupled GNSS/INS integration. *IEEE Transactions on Instrumentation and Measurement*, 69(6):3493–3505, 2019.
- [14] Iyad Hashlamon. A new adaptive extended Kalman filter for a class of nonlinear systems. *Journal of Applied and Computational Mechanics*, 6(1):1–12, 2020.
- [15] Karmvir Singh Phogat and Dong Eui Chang. Invariant extended Kalman filter on matrix Lie groups. *Automatica*, 114:108812, 2020.
- [16] Maosong Wang, Wenqi Wu, Peiyuan Zhou, and Xiaofeng He. State transformation extended Kalman filter for GPS/SINS tightly coupled integration. *GPS Solutions*, 22:1–12, 2018.
- [17] Torben Knudsen and John Leth. A new continuous discrete unscented Kalman filter. *IEEE Transactions on Automatic Control*, 64(5):2198–2205, 2018.
- [18] Tianyu Liu, Songsong Cheng, Yiheng Wei, Ang Li, and Yong Wang. Fractional central difference Kalman filter with unknown prior information. *Signal Processing*, 154:294–303, 2019.
- [19] Gaoge Hu, Bingbing Gao, Yongmin Zhong, and Chengfan Gu. Unscented kalman filter with process noise covariance estimation for vehicular ins/gps integration system. *Information Fusion*, 64:194–204, 2020.
- [20] Jianbo Shao, Wu Chen, Ya Zhang, Fei Yu, and Jingxian Wang. Adaptive maximum correntropy based robust CKF with variational Bayesian for covariance estimation. *Measurement*, 202:111834, 2022.
- [21] Ienkaran Arasaratnam and Simon Haykin. Cubature Kalman filters. *IEEE Transactions on Automatic Control*, 54(6):1254–1269, 2009.

[22] Bingbing Gao, Gaoge Hu, Yongmin Zhong, and Xinhe Zhu. Cubature Kalman filter with both adaptability and robustness for tightly-coupled GNSS/INS integration. *IEEE Sensors Journal*, 21(13):14997–15011, 2021.

- [23] Zhao Wang, Yulong Huang, Maosong Wang, Jin Wu, and Yonggang Zhang. A computationally efficient outlier-robust cubature kalman filter for underwater gravity matching navigation. *IEEE Transactions on Instrumentation and Measurement*, 71:1–18, 2022.
- [24] Guangwei Wang, Bingbo Cui, and Changyuan Tang. Robust cubature Kalman filter based on maximum correntropy and resampling-free sigma-point update framework. *Digital Signal Processing*, 126:103495, 2022.
- [25] Tiancheng Li, Miodrag Bolic, and Petar M Djuric. Resampling methods for particle filtering: classification, implementation, and strategies. *IEEE Signal Processing Magazine*, 32(3):70–86, 2015.
- [26] Ondřej Straka, Jindřich Duník, and Miroslav Šimandl. Design of pure propagation unscented Kalman filter. *IFAC Proceedings Volumes*, 47(3):5933–5938, 2014.
- [27] Ondrej Straka and Jindrich Duník. Resampling-free stochastic integration filter. In 2020 IEEE 23rd International Conference on Information Fusion (FUSION), pages 1–8. IEEE, 2020.
- [28] Bingbo Cui, Xiyuan Chen, and Xinhua Tang. Improved cubature kalman filter for gnss/ins based on transformation of posterior sigma-points error. *IEEE Transactions on Signal Processing*, 65(11):2975–2987, 2017.
- [29] Yang Tian and Yang Cheng. Novel measurement update method for quadrature-based Gaussian filters. In *AIAA Guidance*, *Navigation*, *and Control (GNC) Conference*, page 4949, 2013.
- [30] Bingbo Cui, Xiyuan Chen, Xihua Tang, Haoqian Huang, and Xiao Liu. Robust cubature Kalman filter for GNSS/INS with missing observations and colored measurement noise. *ISA Transactions*, 72:138–146, 2018.
- [31] Yulong Huang, Yanggang Zhang, Ning Li, and Lin Zhao. An improved Gaussian approximate filtering method. *Acta Automation Sinica*, 42(3):385–401, 2016.
- [32] Bingbo Cui, Xinhua Wei, Xiyuan Chen, Jinyang Li, and Lin Li. On sigma-point update of cubature Kalman filter for GNSS/INS under GNSS-challenged environment. *IEEE Transactions on Vehicular Technology*, 68(9):8671–8682, 2019.

[33] Bingbo Cui, Xinhua Wei, Xiyuan Chen, and Aichen Wang. Improved high-degree cubature Kalman filter based on resampling-free sigma-point update framework and its application for inertial navigation system-based integrated navigation. *Aerospace Science and Technology*, 117:106905, 2021.

- [34] Tsung Lin and Wan Hsieh. Robust mixture modeling using the skew t distribution. *Statistics and Computing*, 17(2):81–92, 2007.
- [35] Mingming Bai, Yulong Huang, Yonggang Zhang, and Feng Chen. A novel heavy-tailed mixture distribution based robust Kalman filter for cooperative localization. *IEEE Transactions on Industrial Informatics*, 17(5):3671–3681, 2020.
- [36] Yao Li, Lanhua Hou, Yang Yang, and Jinwu Tong. Huber's M-estimation-based cubature Kalman filter for an INS/DVL integrated system. *Mathematical Problems in Engineering*, 2020:1–12, 2020.
- [37] Tao Zou, Weixiang Zeng, Wenlin Yang, Muk Chen Ong, Yunting Wang, and Weilun Situ. An adaptive robust cubature Kalman filter based on Sage-Husa estimator for improving ship heave measurement accuracy. *IEEE Sensors Journal*, 23(9):10089–10099, 2023.
- [38] Yulong Huang, Yonggang Zhang, Ning Li, Zhemin Wu, and Jonathon A Chambers. A novel robust Student's t-based Kalman filter. *IEEE Transactions on Aerospace and Electronic Systems*, 53(3):1545–1554, 2017.
- [39] Wenshuo Li, Xin Liu, and Lei Guo. Robust particle filtering with state transition uncertainties: A student's t disturbance observer-based approach. *IEEE Transactions on Instrumentation and Measurement*, 70:1–13, 2021.
- [40] Jiangbo Zhu, Weixin Xie, and Zongxiang Liu. Student's t-based robust poisson multi-bernoulli mixture filter under heavy-tailed process and measurement noises. *Remote Sensing*, 15(17):4232, 2023.
- [41] Tao Zhang, Jian Wang, Liang Zhang, and Lin Guo. A student's T-based measurement uncertainty filter for SINS/USBL tightly integration navigation system. *IEEE Transactions on Vehicular Technology*, 70(9):8627–8638, 2021.
- [42] Badong Chen, Xi Liu, Haiquan Zhao, and Jose C Principe. Maximum correntropy Kalman filter. *Automatica*, 76:70–77, 2017.
- [43] Bo Xu, Xiaoyu Wang, Jiao Zhang, and Asghar A Razzaqi. Maximum correntropy delay Kalman filter for SINS/USBL integrated navigation. *ISA Transactions*, 117:274–287, 2021.

[44] Jingjing He, Changku Sun, Baoshang Zhang, and Peng Wang. Maximum correntropy square-root cubature Kalman filter for non-Gaussian measurement noise. *IEEE Access*, 8:70162–70170, 2020.

- [45] Xi Liu, Hua Qu, Jihong Zhao, and Pengcheng Yue. Maximum correntropy square-root cubature Kalman filter with application to SINS/GPS integrated systems. *ISA Transactions*, 80:195–202, 2018.
- [46] Reza Izanloo, Seyed Abolfazl Fakoorian, Hadi Sadoghi Yazdi, and Dan Simon. Kalman filtering based on the maximum correntropy criterion in the presence of non-Gaussian noise. In 2016 Annual Conference on Information Science and Systems (CISS), pages 500–505. IEEE, 2016.
- [47] Cheng Xu, Mengmeng Ji, Yue Qi, and Xinghang Zhou. MCC-CKF: A distance constrained Kalman filter method for indoor TOA localization applications. *Electronics*, 8(5):478, 2019.
- [48] Hongwei Wang, Wei Zhang, Junyi Zuo, and Heping Wang. Outlier-robust Kalman filters with mixture correntropy. *Journal of the Franklin Institute*, 357(8):5058–5072, 2020.
- [49] Chen Liu, Gang Wang, Xin Guan, and Chutong Huang. Robust M-estimation-based maximum correntropy Kalman filter. *ISA Transactions*, 136:198–209, 2023.
- [50] Bowen Hou, Zhangming He, Xuanying Zhou, Haiyin Zhou, Dong Li, and Jiongqi Wang. Maximum correntropy criterion Kalman filter for α -Jerk tracking model with non-Gaussian noise. *Entropy*, 19(12):648, 2017.
- [51] Seyed Fakoorian, Reza Izanloo, Azin Shamshirgaran, and Dan Simon. Maximum correntropy criterion Kalman filter with adaptive kernel size. *2019 IEEE National Aerospace and Electronics Conference*, pages 581–584, 2019.
- [52] Seyed Fakoorian, Angel Santamaria-Navarro, Brett T Lopez, Dan Simon, and Aliakbar Agha-mohammadi. Towards robust state estimation by boosting the maximum correntropy criterion kalman filter with adaptive behaviors. *IEEE Robotics and Automation Letters*, 6(3):5469–5476, 2021.
- [53] Shengxin Li, Bo Xu, Lianzhao Wang, and Asghar A Razzaqi. Improved maximum correntropy cubature Kalman filter for cooperative localization. *IEEE Sensors Journal*, 20(22):13585–13595, 2020.
- [54] Haoshen Lin and Chen Hu. Variational inference based distributed noise adaptive Bayesian filter. *Signal Processing*, 178:107775, 2021.

[55] Cheng Pan, Jingxiang Gao, Zengke Li, Nijia Qian, and Fangchao Li. Multiple fading factors-based strong tracking variational Bayesian adaptive Kalman filter. *Measurement*, 176:109139, 2021.

- [56] Peng Yun, Panlong Wu, Shan He, and Xingxiu Li. A variational Bayesian based robust cubature Kalman filter under dynamic model mismatch and outliers interference. *Measurement*, 191:110063, 2022.
- [57] Ruixin Liu, Fucheng Liu, Chunning Liu, and Pengchao Zhang. Modified sage-husa adaptive Kalman filter-based SINS/DVL integrated navigation system for AUV. *Journal of Sensors*, 2021:1–8, 2021.
- [58] Simo Sarkka and Aapo Nummenmaa. Recursive noise adaptive Kalman filtering by variational Bayesian approximations. *IEEE Transactions on Automatic Control*, 54(3):596–600, 2009.
- [59] Soheil Sadat Hosseini, Mohsin M Jamali, and Simo Särkkä. Variational Bayesian adaptation of noise covariances in multiple target tracking problems. *Measurement*, 122:14–19, 2018.
- [60] Huang Yulong. Research on high-precision state estimation methods and their applications in target tracking and cooperative localization. PhD thesis, Harbin Engineering University, 2018.
- [61] Yulong Huang, Fengchi Zhu, Guangle Jia, and Yonggang Zhang. A slide window variational adaptive Kalman filter. *IEEE Transactions on Circuits and Systems II: Express Briefs*, 67(12):3552–3556, 2020.
- [62] Hongwei Wang, Hongbin Li, Jun Fang, and Heping Wang. Robust Gaussian Kalman filter with outlier detection. *IEEE Signal Processing Letters*, 25(8):1236–1240, 2018.
- [63] Haoqing Li, Daniel Medina, Jordi Vilà-Valls, and Pau Closas. Robust variational-based Kalman filter for outlier rejection with correlated measurements. *IEEE Transactions on Signal Processing*, 69:357–369, 2020.
- [64] Hao Zhu, Guorui Zhang, Yongfu Li, and Henry Leung. An adaptive Kalman filter with inaccurate noise covariances in the presence of outliers. *IEEE Transactions on Automatic Control*, 67(1):374–381, 2021.
- [65] Mingming Bai, Yulong Huang, Yonggang Zhang, and Jonathon Chambers. Statistical similarity measure-based adaptive outlier-robust state estimator with applications. *IEEE Transactions on Automatic Control*, 67(8):4354–4361, 2022.

[66] Xuhang Liu, Xiaoxiong Liu, Yue Yang, Yicong Guo, and Weiguo Zhang. Robust variational Bayesian method-based SINS/GPS integrated system. *Measurement*, 193:110893, 2022.

- [67] Zhao Zeqian. Research on autonomous integrity monitoring method of vehicle positioning based on vehicle-vehicle cooperative assistance. Master's thesis, Beijing Jiaotong University, 2018.
- [68] Cagatay Tanil, Samer Khanafseh, Mathieu Joerger, and Boris Pervan. Sequential integrity monitoring for kalman filter innovations-based detectors. In *Proceedings* of the 31st International Technical Meeting of the Satellite Division of The Institute of Navigation (ION GNSS+ 2018), pages 2440–2455, 2018.
- [69] Mahdi Maaref and Zaher M Kassas. Autonomous integrity monitoring for vehicular navigation with cellular signals of opportunity and an IMU. *IEEE Transactions on Intelligent Transportation Systems*, 23(6):5586–5601, 2021.
- [70] Zhangjun Yu, Qiuzhao Zhang, Shubi Zhang, Nanshan Zheng, and Keqiang Liu. A state-domain robust autonomous integrity monitoring with an extrapolation method for single receiver positioning in the presence of slowly growing fault. *Satellite Navigation*, 4(1):20, 2023.
- [71] Tarek Hassan, Ahmed El-Mowafy, and Kan Wang. A review of system integration and current integrity monitoring methods for positioning in intelligent transport systems. *IET Intelligent Transport Systems*, 15(1):43–60, 2021.
- [72] Felipe A Costa de Oliveira, Frank Sill Torres, and Alberto García-Ortiz. Recent advances in sensor integrity monitoring methods—a review. *IEEE Sensors Journal*, 22(11):10256–10279, 2022.
- [73] Rui Chen and Long Zhao. Multi-level autonomous integrity monitoring method for multi-source pnt resilient fusion navigation. *Satellite Navigation*, 4(1):21, 2023.
- [74] Haitao Jiang, Tuan Li, Dan Song, and Chuang Shi. An effective integrity monitoring scheme for GNSS/INS/vision integration based on error state EKF model. *IEEE Sensors Journal*, 22(7):7063–7073, 2022.
- [75] Hao Jing, Yang Gao, Sepeedeh Shahbeigi, and Mehrdad Dianati. Integrity monitoring of GNSS/INS based positioning systems for autonomous vehicles: State-of-theart and open challenges. *IEEE Transactions on Intelligent Transportation Systems*, 23(9):14166–14187, 2022.

[76] Alexander Chernodarov, V. Monitoring and adaptive robust protection of the integrity of GNSS/SINS observations in urban environments. *IFAC-Papers OnLine*, 55(6):378–383, 2022.

- [77] Ziyue Fan and Long Zhao. Autonomous integrity of multi-source information resilient fusion navigation system: state-of-the-art and open challenges. *IEEE Transactions on Instrumentation and Measurement*, 73:1–17, 2024.
- [78] Mathieu Joerger and Boris Pervan. Kalman filter-based integrity monitoring against sensor faults. *Journal of Guidance, Control, and Dynamics*, 36(2):349–361, 2013.
- [79] Grischa Gottschalg, Matthias Becker, and Stefan Leinen. Integrity concept for sensor fusion algorithms used in a prototype vehicle for automated driving. In 2020 European Navigation Conference (ENC), pages 1–10. IEEE, 2020.
- [80] Susmita Bhattacharyya and Demoz Gebre-Egziabher. Kalman filter-based RAIM for GNSS receivers. *IEEE Transactions on Aerospace and Electronic Systems*, 51(3):2444–2459, 2015.
- [81] Grischa Gottschalg and Stefan Leinen. Comparison and evaluation of integrity algorithms for vehicle dynamic state estimation in different scenarios for an application in automated driving. *Sensors*, 21(4):1458, 2021.
- [82] Joelle Al Hage, Philippe Xu, and Philippe Bonnifait. Bounding localization errors with Student distribution for road vehicles. In *International Technical Symposium on Navigation and Timing*, 2018.
- [83] E Dominguez Tijero, L Martinez Fernandez, JI Zarzosa, J Garcia, J Ibanez-Guzman, E Stawiarski, Philippe Xu, G Avellone, F Pisoni, E Falletti, et al. High accuracy positioning engine with an integrity layer for safety autonomous vehicles. In *Proceedings of the 31st International Technical Meeting of The Satellite Division of the Institute of Navigation (ION GNSS+ 2018)*, pages 1566–1572, 2018.
- [84] Susmita Bhattacharyya and Dinesh Mute. Kalman filter-based RAIM for reliable aircraft positioning with GPS and NavIC constellations. *Sensors*, 20(22):6606, 2020.
- [85] Zhang Wenyu. Research on gnss multi-source fusion navigation and its autonomous integrity monitoring technology. Master's thesis, Nanjing University of Aeronautics and Astronautics, 2021.
- [86] Zhipeng Wang, Xin Li, Yanbo Zhu, Qiang Li, and Kun Fang. Integrity monitoring of Global Navigation Satellite System/Inertial Navigation System integrated navigation system based on dynamic fading filter optimisation. *IET Radar, Sonar &*

- Navigation, 16(3):515-530, 2022.
- [87] Sam Pullen and Mathieu Joerger. GNSS integrity and receiver autonomous integrity monitoring (RAIM). *Position, navigation, and timing technologies in the 21st century: integrated satellite navigation, sensor systems, and civil applications*, 1:591–617, 2020.
- [88] Antonio Angrisano and Salvatore Gaglione. Smartphone GNSS performance in an urban scenario with RAIM application. *Sensors*, 22(3):786, 2022.
- [89] Shizhuang Wang, Yawei Zhai, Cheng Chi, Xingqun Zhan, and Yiping Jiang. Implementation and analysis of fault grouping for multi-constellation advanced RAIM. *Advances in Space Research*, 71(11):4765–4786, 2023.
- [90] Yuting Gao, Yang Jiang, Yang Gao, and Guanwen Huang. A linear Kalman filter-based integrity monitoring considering colored measurement noise. *GPS Solutions*, 25(2):1–13, 2021.
- [91] Omar Garcia Crespillo. GNSS/INS Kalman Filter Integrity Monitoring with Uncertain Time Correlated Error Processes. Technical report, EPFL, 2022.
- [92] Chengyao Li and Steven L Waslander. Visual measurement integrity monitoring for UAV localization. In 2019 IEEE International Symposium on Safety, Security, and Rescue Robotics (SSRR), pages 22–29. IEEE, 2019.
- [93] Qian Meng and Li-Ta Hsu. Integrity monitoring for all-source navigation enhanced by Kalman filter-based solution separation. *IEEE Sensors Journal*, 21(14):15469–15484, 2020.
- [94] Vasileios Bosdelekidis, Torleiv H. Bryne, Nadezda Sokolova, and Tor A. Johansen. Navigation algorithm-agnostic integrity monitoring based on solution separation with constrained computation time and sensor noise overbounding. *Journal of Intelligent & Robotic Systems*, 106(1), 2022.
- [95] Weichuan Pan, Xingqun Zhan, and Xin Zhang. Fault exclusion method for ARAIM based on tight GNSS/INS integration to achieve CAT-I approach. *IET Radar, Sonar & Navigation*, 13(11):1909–1917, 2019.
- [96] Mevin B. Hooten, Devin S. Johnson, and Brian M. Brost. Making recursive Bayesian inference accessible. *American Statistician*, 75(2):185–194, 2021.

[97] Ximing Li, Changchun Li, Jinjin Chi, and Jihong Ouyang. Approximate posterior inference for Bayesian models: black-box expectation propagation. *Knowledge And Information Systems*, 64(9):2361–2387, 2022.

- [98] Di Ding, Kai F. He, and Qian Quan Yong Fan. A Bayesian adaptive unscented Kalman filter for aircraft parameter and noise estimation. *Journal of Sensors*, 2021:9002643–1–9002643–11, 2021.
- [99] Rudolph Merwe and Eric Wan. Gaussian mixture sigma-point particle filters for sequential probabilistic inference in dynamic state-space models. In 2003 IEEE International Conference on Acoustics, Speech, and Signal Processing, 2003. Proceedings. (ICASSP)., volume 6, pages VI–701, 2003.
- [100] Ienkaran Arasaratnam and Simon Haykin. Cubature Kalman Filters. *IEEE Transactions on Automatic Control*, 54(6):1254–1269, 2009.
- [101] Mark R Morelande and Angel F Garcia-Fernandez. Analysis of Kalman filter approximations for nonlinear measurements. *IEEE Transactions on Signal Processing*, 61(22):5477–5484, 2013.
- [102] Qingwen Meng, Xuyou Li, and Yanda Guo. An efficient gauss-seidel cubature Kalman filter. *IEEE Transactions on Circuits and Systems II: Express Briefs*, 69(3):1932–1936, 2021.
- [103] Yulong Huang, Yanggang Zhang, Ning Li, and Lin Zhao. An improved Gaussian approximate filtering method. *Acta Automation Sinica*, 42(3):385–401, 2016.
- [104] Seyed Fakoorian, Alireza Mohammadi, Vahid Azimi, and Dan Simon. Robust Kalman-type filter for non-Gaussian noise: Performance analysis with unknown noise covariances. *Journal of Dynamic Systems, Measurement, and Control*, 141(9), 2019.
- [105] Jindrich Duník and Ondrej Straka. State estimate consistency monitoring in Gaussian filtering framework. *Signal Processing*, 148:145–156, 2018.
- [106] Yu Wang, Xiao Hu, Jun Lian, and Zhi Xian. Algorithms and error analysis of bionic orientation based on polarized light. *Journal of Astronautics*, 36(2):211, 2015.
- [107] Qingfeng Dou, Tao Du, Shanpeng Wang, Jian Yang, and Lei Guo. A novel polarized skylight navigation model for bionic navigation with marginalized unscented Kalman filter. *IEEE Sensors Journal*, 22(5):4472–4483, 2021.

[108] Xin Qin, Wei Huang, Mingfei Xu, and Shuqiang Jia. Error analysis and calibration based on division-of-aperture bionic polarization navigation systems. *Optics Communications*, 569:130844, 2024.

- [109] Jianbo Shao, Wu Chen, Ya Zhang, Fei. Yu, and Jiachong Chang. Adaptive multi-kernel size-based maximum correntropy cubature Kalman filter for the robust state estimation. *IEEE Sensors Journal*, 22(20):19835–19844, 2022.
- [110] Yulong Huang, Yonggang Zhang, Bo Xu, Zhemin Wu, and Jonathon A Chambers. A new adaptive extended Kalman filter for cooperative localization. *IEEE Transactions on Aerospace and Electronic Systems*, 54(1):353–368, 2017.
- [111] Hao Zhu, Guorui Zhang, Yongfu Li, and Henry Leung. An adaptive Kalman filter with inaccurate noise covariances in the presence of outliers. *IEEE Transactions on Automatic Control*, 67(1):374–381, 2021.
- [112] Akash Kumar Dhaka, Alejandro Catalina, Manushi Welandawe, and Andersen. Challenges and opportunities in high dimensional variational inference. *Advances in Neural Information Processing Systems*, 34:7787–7798, 2021.
- [113] Dimitris G. Tzikas, Aristidis C. Likas, and Nikolaos P. Galatsanos. The variational approximation for Bayesian inference. *IEEE Signal Processing Magazine*, 25(6):131–146, 2008.
- [114] NK Schuurman, RPPP Grasman, and EL Hamaker. A comparison of inverse-wishart prior specifications for covariance matrices in multilevel autoregressive models. *Multivariate behavioral research*, 51(2-3):185–206, 2016.
- [115] Yulong Huang, Yonggang Zhang, Peng Shi, and Jonathon Chambers. Variational adaptive Kalman filter with Gaussian-inverse-Wishart mixture distribution. *IEEE Transactions on Automatic Control*, 66(4):1786–1793, 2020.
- [116] Hong Xu, Keqing Duan, Huadong Yuan, Wenchong Xie, and Yongliang Wang. Adaptive fixed-lag smoothing algorithms based on the variational Bayesian method. *IEEE Transactions on Automatic Control*, 66(10):4881–4887, 2020.
- [117] Yulong Huang, Yonggang Zhang, Zhemin Wu, Ning Li, and Jonathon Chambers. A novel adaptive Kalman filter with inaccurate process and measurement noise covariance matrices. *IEEE Transactions on Automatic Control*, 63(2):594–601, 2017.
- [118] Gauhar Rahman, Shahid Mubeen, and Abdur Rehman. Generalization of chi-square distribution. *Journal of Statistics Applications & Probability*, 4(1):119, 2015.

[119] Omar García Crespillo, Anja Grosch, Jan Skaloud, and Michael Meurer. Innovation vs residual KF based GNSS/INS autonomous integrity monitoring in single fault scenario. In *Proceedings of the 30th International Technical Meeting of the Satellite Division of the Institute of Navigation (ION GNSS+ 2017)*, pages 2126–2136, 2017.

- [120] Jianbo Shao, Fei Yu, Ya Zhang, Qian Sun, Yanyan Wang, and Wu Chen. Robust sequential integrity monitoring for positioning safety in GNSS/INS integration. *IEEE Sensors Journal*, 24(9):15145–15155, 2024.
- [121] Guangle Gao, Yongmin Zhong, Shesheng Gao, and Bingbing Gao. Double-channel sequential probability ratio test for failure detection in multisensor integrated systems. *IEEE Transactions on Instrumentation and Measurement*, 70:1–14, 2021.
- [122] Yahya Chetouani. A sequential probability ratio test (SPRT) to detect changes and process safety monitoring. *Process Safety and Environmental Protection*, 92(3):206–214, 2014.
- [123] Mark Esper, Elaine L Chao, Chad F Wolf, et al. 2019 Federal Radionavigation Plan. Technical report, United States Department of Defense, 2020.
- [124] Yuting Gao, Yang Jiang, Yang Gao, and Guanwen Huang. A linear Kalman filter-based integrity monitoring considering colored measurement noise. *GPS solutions*, 25:1–13, 2021.
- [125] Nabil Shaukat, Ahmed Ali, Muhammad Javed Iqbal, Muhammad Moinuddin, and Pablo Otero. Multi-sensor fusion for underwater vehicle localization by augmentation of rbf neural network and error-state Kalman filter. *Sensors*, 21(4):1149, 2021.
- [126] Gongmin Yan and Yu Deng. Review on practical Kalman filtering techniques in traditional integrated navigation system. *Navigation Positioning and Timing*, 7:50–64, 2020.